Poly(ethylene oxide)-based Architectures as Polymer Electrolytes for Solid-State Lithium-Metal Batteries

Zur Erlangung des akademischen Grades eines

DOKTORS DER NATURWISSENSCHAFTEN

(Dr. rer. nat.)

von der KIT-Fakultät für Chemie und Biowissenschaften
des Karlsruher Instituts für Technologie (KIT)

genehmigte
DISSERTATION
von

M.Sc. Andreas Johannes Butzelaar
aus Heilbronn

1. Referent: Prof. Dr. Patrick Théato

2. Referent: Prof. Dr. Michael Meier

Tag der mündlichen Prüfung: 07.02.2022

für Laura

Declaration of Authorship

Die vorliegende Arbeit wurde im Zeitraum von Februar 2019 bis Januar 2022 am Institut für Technische Chemie und Polymerchemie (ITCP) am Karlsruher Institut für Technologie (KIT) unter der wissenschaftlichen Betreuung von Prof. Dr. Patrick Théato angefertigt.

Ich erkläre hiermit, dass ich die vorliegende Arbeit im Rahmen der Betreuung durch Prof. Dr. Patrick Théato selbstständig verfasst und keine anderen als die angegebenen Quellen und Hilfsmittel verwendet habe. Wörtlich oder inhaltlich übernommene Stellen sind als solche kenntlich gemacht und die Satzung des Karlsruher Instituts für Technologie (KIT) zur Sicherung guter wissenschaftlicher Praxis wurde beachtet. Des Weiteren erkläre ich, dass ich mich derzeit in keinem laufenden Promotionsverfahren befinde, und auch keine vorausgegangenen Promotionsversuche unternommen habe. Die elektronische Version der Arbeit stimmt mit der schriftlichen Version überein und die Primärdaten sind gemäß Abs. A (6) der Regeln zur Sicherung guter wissenschaftlicher Praxis des KIT beim Institut abgegeben und archiviert.

Karlsruhe, den 21. Februar 2022

_____

Andreas Butzelaar

List of Publications

Publications within this Dissertation

[5] Butzelaar, A. J.; Röring, P.; Hoffmann, M.; Atik, J.; Paillard, E.; Wilhelm, M.; Winter, M.; Brunklaus, G.; Theato, P. Advanced Block Copolymer Design for Polymer Electrolytes: Prospects of Microphase Separation. *Macromolecules* **2021**, 54 (23), 11101–11112. DOI: 10.1021/acs.macromol.1c02147.

[4] Butzelaar, A. J.; Röring, P.; Mach, T. P.; Hoffmann, M.; Jeschull, F.; Wilhelm, M.; Winter, M.; Brunklaus, G.; Théato, P. Styrene-Based Poly(ethylene oxide) Side-Chain Block Copolymers as Solid Polymer Electrolytes for High-Voltage Lithium-Metal Batteries. *ACS Appl. Mater. Interfaces* **2021**, 13 (33), 39257–39270. DOI: 10.1021/acsami.1c08841.

[3] Butzelaar, A. J.; Gauthier-Jaques, M.; Liu, K. L.; Brunklaus, G.; Winter, M.; Theato, P. The power of architecture – cage-shaped PEO and its application as a polymer electrolyte. *Polym. Chem.* **2021**, 12, 4326–433. DOI: 10.1039/D1PY00490E.

[2] Butzelaar, A. J.; Schneider, S.; Molle, E.; Theato, P. Synthesis and Post-Polymerization Modification of Defined Functional Poly(vinyl ether)s. *Macromol. Rapid Commun.* **2021**, 42 (13), 2100133. DOI: 10.1002/marc.202100133.

[1] Butzelaar, A. J.; Liu, K. L.; Röring, P.; Brunklaus, G.; Winter, M.; Theato, P. A Systematic Study of Vinyl Ether-Based Poly(Ethylene Oxide) Side-Chain Polymer Electrolytes. *ACS Appl. Polym. Mater.* **2021**, 3 (3), 1573–1582. DOI: 10.1021/acsapm.0c01398.

Other Publications

[4] Hoffmann, M.; Butzelaar, A. J.; Iacob, C.; Théato, P.; Wilhelm, M. Ionogels as Polymer Electrolytes for Lithium-Metal Batteries: Comparison of Poly(ethylene glycol) diacrylate (PEGDA) and an Imidazolium-based Ionic Liquid Crosslinker. *ACS Appl. Polym. Mater.* **2022**, under revision.

[3] Khudyshkina, A. D.; Morozova, P. A.; Butzelaar, A. J.; Hoffmann, M.; Wilhelm, M.; Theato, P.; Fedotov, S. S.; Jeschull, F. Poly(ethylene oxide)-based Electrolytes for Solid-State Potassium Metal Batteries with Prussian Blue Positive Electrode. *ACS Appl. Polym. Mater.* **2022**, under revision.

[2] Frech, S.; Molle, E.; Butzelaar, A. J.; Theato, P. Ethylene-Free Synthesis of Polyethylene Copolymers and Block Copolymers. *Macromolecules* **2021**, 54 (21), 9937–9946. DOI: 10.1021/acs.macromol.1c01257.

[1] Krause, C. H.; Butzelaar, A. J.; Diddens, D.; Dong, D.; Théato, P.; Bedrov, D.; Hwang, B.-J.; Winter, M.; Brunklaus, G. Quasi-solid single ion conducting polymer electrolyte membrane containing novel fluorinated poly(arylene ether sulfonimide) for lithium metal batteries. *J. Power Sources* **2021**, 484, 229267. DOI: 10.1016/j.jpowsour.2020.229267.

Conference Contributions

[1] Polyethylenoxid basierte Architekturen als Polymerelektrolyte für Festkörperbatterien

Poster at the “FestBatt Industrietag”, October 10th, 2020.

Abstract

Polymer electrolytes (PEs) are expected to overcome most drawbacks of conventional organic liquid electrolytes, hence enabling a safer operation of next generation lithium batteries. In this regard, especially poly(ethylene oxide) (PEO) as part of solid polymer electrolytes (SPEs) is of high interest due to its low glass transition temperature (T_g), good chain flexibility, remarkable electrochemical stability against lithium-metal, low comparable costs and great solubility for conductive lithium salts. However, despite these important attributes, PEO-based SPEs often suffer from high crystallinity, which results in low ionic conductivities below its melting point due to the fact that ion transport is mainly taking place in the amorphous regions. Several approaches have been introduced to reduce crystallization and thus increase the ionic conductivity such as the introduction of plasticizers or nanofillers, or blending with other polymers. Further, alteration of the polymers' molecular architecture constitutes a sophisticated way to reduce crystallization and, therefore, displays a merging of the field of synthetic polymer chemistry and battery chemistry. Consequently, the present thesis deals with well-thought architectural approaches for PEO-based PEs as general topic while using the gained knowledge for further outgoing studies.

In a first approach, the synthesis of a systematic library of vinyl ether-based PEO side chain copolymers in order to reduce the crystallization of PEO is covered. The influence of different grafted PEO side chain lengths, the grafting density and the $[Li^+]$:[EO] ratio after mixing with lithium bis(trifluoromethanesulfonyl)imide (LiTFSI) on the T_g, the crystallinity and the resulting ionic conductivity was thoroughly examined. Herein, copolymers bearing longer PEO side chains and higher grafting densities showed higher crystallization tendencies while their T_g was reduced at the same time. Furthermore, the addition of LiTFSI reduced the crystallization, but inversely increased the T_g. Since these effects are directly impacting the ionic conductivity, it was demonstrated that these parameters need to be carefully adjusted in order to balance their influence appropriately. In this way, a fundamental view enlightening PEO side chain copolymers for their application as polymer electrolytes could be provided, laying the foundation for further studies within this thesis.

The second topic arose as a side project from the first one being based on living cationic polymerization of vinyl ethers. This technique is known for a good control over chain growth yielding polymers with well-defined molar mass distributions and low dispersities. However, the practical challenges involved in the synthesis of poly(vinyl ether)s using cationic polymerization techniques limited suitable post-polymerization modifications (PPM) *via*

chemoselective click reactions. Within this project, the successful controlled cationic polymerization of vinyl ethers bearing pendant C=C double and C≡C triple bonds using a single-component initiation and control agent under ambient conditions was achieved. Furthermore, the PPM *via* thiol-ene/-yne and copper(I)-catalyzed alkyne-azide cycloaddition (CuAAC) reaction of the obtained polymers was successfully realized demonstrating the straightforward synthesis of unprecedented functional poly(vinyl ether)s.

In the third project, for the first time the gram-scale synthesis of a four-arm *cage*-shaped PEO and its pioneering application as PE is discussed. The obtained PEs comprising low lithium salt loadings ($[Li^+]$:[EO] 1:25) showed good ionic conductivities at low temperatures due to their well suppressed crystallization by the *cage* architecture, thus without any further addition of plasticizer or structural solvent. Overall, this project could consequently contribute to unveil the great toolbox of polymer chemists to overcome crystallization issues in PEO-based PEs.

The fourth approach builds on the results of the first project dealing with the design of styrene-based PEO side chain block copolymers featuring a microphase separation and their application as SPE in high voltage lithium-metal batteries. A straightforward synthesis was established overcoming typical drawbacks of PEO block copolymers prepared by anionic polymerization or ester-based PEO side chain copolymers. Both the PEO side chain length as well as the LiTFSI content were varied and the underlying relationships were elucidated in view of polymer compositions with high ionic conductivity. Subsequently, a selected composition was subjected to further analyses including phase separated morphology, providing not only excellent self-standing films with intrinsic mechanical stability but also the ability to suppress lithium dendrite growth as well as flexibility, wettability and good contacts with the electrodes. Furthermore, a high thermal and electrochemical stability was demonstrated. To do so, linear sweep and cyclic voltammetry, lithium plating/stripping tests and galvanostatic overcharging using high voltage cathodes were conducted unveiling stable lithium-metal interfaces and a high oxidative stability of around 4.75 V. Consequently, cycling of Li||NMC622 cells did not exhibit commonly observed rapid cell failure or voltage noise typically associated with PEO-based electrolytes in Li||NMC622 cells, attributed to the high mechanical stability. Thus, a comprehensive view is provided highlighting that the combination of PEO and high voltage cathodes is not impossible *per se*.

The fifth project expands the findings of the fourth project. Here, an advanced design for PEs based on the previously studied microphase separated styrene-based PEO side chain block copolymers is described. Usually, such block copolymers are characterized by a high

mechanical stability provided by the PS domain, while the PEO-based domain features decent ionic conductivities, however, mostly only at elevated temperatures. To guarantee suitable conductivities at lower temperatures, two ionic liquids (ILs) as model plasticizers for the PEO domain were selectively implemented. Since those ILs are non-miscible with PS, the latter domain is unaffected, thus still providing a great mechanical stability. To maintain the necessary ability to form a self-standing film, the size of the PS domain was adjusted to match with the conducting PEO-based domain. For this, a series of four block copolymers with different block ratios was synthesized, thus enabling the study on the influence of different amounts of IL. Further, all derived polymer electrolytes were thoroughly characterized by thermal, morphological and electrochemical analyses. The microphase separated morphology with long-range order and a good thermal and mechanical stability, as well as the selective mixing of the ILs within the conducting domain was proven. Consequently, electrochemical impedance spectroscopy (EIS) revealed a significant increase in ionic conductivity up to two orders of magnitude in comparison to the non-plasticized control sample of project four. Even more, exhaustive studies of the lithium-ion transference number showed not only the importance of such detailed analysis for IL-containing PEs, but also the actual increase of the raw lithium-ion conductivity. Finally, full cycling in Li||$LiFePO_4$ (LFP) cells was conducted to clearly demonstrate the applicability of this approach.

In summary, the importance of macromolecular approaches within the field of battery chemistry, in particular polymer-based electrolytes, could not only be successfully demonstrated, but they were also used to overcome critical problems associated with PEO-based PEs in a sophisticated fashion, *i.e.*, crystallization issues, the dilemma regarding mechanical stability/ionic conductivity and the combination of PEO and high-voltage cathodes. Consequently, novel and groundbreaking conclusions regarding trends and behavioral tendencies of PEO-based PEs could be drawn and based upon this, the performance of respective battery materials could be significantly improved. Especially in times of raw material shortages, an ever-growing demand of energy storage materials and the trend in society towards battery-powered vehicles, smart and effective solutions for the latter could be identified, developed and realized in a straightforward fashion.

Zusammenfassung

Polymerelektrolyte (PEe) sollen die meisten Nachteile konventioneller, organischer Flüssigelektrolyte überwinden und so einen sicheren Betrieb der nächsten Generation von Lithiumakkumulatoren ermöglichen. Hierbei ist im Speziellen Poly(ethylenoxid) als fester Polymerelektrolyt von hohem Interesse auf Grund der niedrigen Glasübergangstemperatur (T_g), der guten Flexibilität, einer außerordentlichen Stabilität gegenüber metallischem Lithium, vergleichbar geringen Kosten und einer guten Löslichkeit gegenüber leitenden Lithiumsalzen. Trotz dieser hervorragenden Eigenschaften leiden PEO-basierte PEe häufig unter hoher Kristallinität, was sich in geringen ionischen Leitfähigkeiten unterhalb des Schmelzpunktes widerspiegelt, da der Transport der Ionen hauptsächlich in amorphen Regionen stattfindet. Aus diesem Grund wurden viele Ansätze entwickelt, um die Kristallinität zu verringern und somit die ionische Leitfähigkeit zu erhöhen, wie beispielsweise die Implementierung von Weichmachern oder das Mischen mit anderen Polymeren. Des Weiteren stellt die Modifikation der molekularen Architektur der Polymere mittels synthetischer Polymerchemie eine besonders ausgeklügelte Methode dar, um die Kristallinität zu verringern und schafft es dabei die Felder der Polymerchemie und Batteriechemie gekonnt zu vereinen. Dementsprechend beschäftigt sich die vorliegende Dissertation mit gut durchdachten Ansätzen für verschiedene Architekturen von PEO-basierten PEen als generelles Thema, während der erlangte Wissensschatz für weitere, hiervon ausgehende Studien genutzt wird.

In einem ersten Ansatz wurde eine systematisch aufgebaute Bibliothek von vinyletherbasierten PEO-Seitenkettencopolymeren synthetisiert, um so die Kristallinität von PEO zu reduzieren. Hierbei wurde der Einfluss der Seitenkettenlänge, der Propfdichte und des [Li^+]:[EO] Verhältnisses nach dem Mischen mit Lithiumbis(trifluormethylsulfonyl)amid (LiTFSI) auf den T_g, die Kristallinität und die daraus resultierende ionische Leitfähigkeit eingehend untersucht. Hierbei zeigen Copolymere mit längeren PEO-Seitenketten sowie höheren Propfdichten größere Kristallisationstendenzen, jedoch einen verringerten T_g. Gleichzeitig verringert die Zugabe von LiTFSI die Kristallinität, aber erhöht wiederum den T_g. Da diese Effekte jedoch direkt die ionische Leitfähigkeit beeinflussen, wurde gezeigt, dass diese Parameter genauestens abgestimmt werden müssen, um deren Einfluss entsprechend zu balancieren. Auf diese Weise konnte eine grundlegende Sicht auf PEO-Seitenkettencopolymere und deren Anwendung als PE ermöglicht werden und so die Basis für weitere Studien in dieser Thesis gelegt werden.

Das zweite Thema wurde als Nebenprojekt aus dem Ersten, basierend auf der kontrollierten kationischen Polymerisation von Vinylethern, entwickelt. Diese Technik ist bekannt für eine

gute Kontrolle über das Kettenwachstum, um so Polymere mit definierten molaren Massen und niedrigen Dispersitäten zu erhalten. Allerdings limitierten die praktischen Herausforderungen der üblichen Synthese von Poly(vinylether)n)mittels kationischer Polymerisation die Anwendung von Post-Polymerisationsmodifikationen (PPM) beispielsweise durch chemoselektiven Click-Reaktionen. Innerhalb dieses Projekts konnte die erfolgreiche kontrollierte kationische Polymerisation von Vinylethern mit anhängenden C=C Doppelbindungen und C≡C Dreifachbindungen unter Verwendung eines Einkomponenten-Initiator- und Kontrollmoleküls gezeigt werden. Des Weiteren konnte die PPM durch Thiol-En/In und CuAAC-Reaktionen und dadurch erfolgreich die unkomplizierte Synthese von neuartigen Poly(vinylether)n demonstriert werden.

Der dritte verfolgte Ansatz beschäftigt sich mit der erstmaligen Beschreibung der Synthese von vierarmigem, käfigförmigem PEO im Grammmaßstab und der wegweisenden Anwendung als PE. Die so erhaltenen PEe mit niedrigen Lithiumsalzmengen ($[Li^+]$:[EO] 1:25) zeigten gute ionische Leitfähigkeiten bei Raumtemperatur auf Grund der effektiv unterdrückten Kristallisation durch die käfigförmige Architektur; und das ohne den Zusatz von Weichmachern oder Lösungsmittel. Insgesamt konnte dieses Projekt dazu beitragen die großartige Werkzeugkiste von Polymerchemiker zu demonstrieren, um Probleme mit der Kristallinität von PEO-basierten PEen zu lösen.

Der vierte Ansatz baut auf dem ersten Projekt auf und beschäftigt sich mit dem Design von styrolbasierten PEO-Seitenkettenblockcopolymeren, die eine Mikrophasenseparation aufweisen, und deren Anwendung als PE in Hochvolt-Lithiummetallakkumulatoren. Eine unkomplizierte Synthese wurde entwickelt, die die üblichen Nachteile von PEO-Blockcopolymeren, welche mittels anionischer Polymerisation hergestellt wurden, oder esterbasierten PEO-Seitenkettencopolymeren löst. Beides, die PEO-Seitenkettenlänge und die LiTFSI-Menge wurden variiert und die zugrundeliegenden Zusammenhänge offenbart, um Zusammensetzungen mit hoher ionischer Leitfähigkeit zu erhalten. Anschließend wurde eine ausgewählte Zusammensetzung für weitere Analysen ausgewählt, inklusive phasenseparierter Morphologie, die nicht nur exzellente selbststehende Filme mit intrinsischer mechanischer Stabilität, sondern auch die Eigenschaft Lithiumdendritenwachstum zu unterdrücken, sowie Flexibilität und einen guten Kontakt zu den Elektroden ermöglicht. Des Weiteren wurden die gute thermische wie auch elektrochemische Stabilität demonstriert. Dazu wurden Lineare-Sweep-Voltammetrie und Cyclovoltammetrie, Lithiumabtragung/-abscheidungtests und galvanostatisches Überladen mit Hochvoltkathoden durchgeführt, um eine stabile Grenzfläche gegenüber metallischem Lithium und eine hohe oxidative Stabilität von ~ 4.75 V zu beweisen.

Konsequenterweise zeigten Zyklisierungen in Li||NMC622 Zellen weder das für PEO-basierte PEe typische schnelle Zellversagen noch Spannungsrauschen. So konnte ein umfassendes Verständnis erlangt werden, das gezeigt hat, dass die Kombination von PEO und Hochvoltkathoden nicht *per se* unmöglich ist.

Das fünfte Projekt erweitert die Ergebnisse des vierten Projekts. Hierzu wird ein fortgeschrittenes Design für PE beschrieben, welches auf den zuvor beschriebenen mikrophasenseparierten, styrolbasierten PEO-Seitenkettenblockcopolymeren besteht. Üblicherweise zeigen solche Blockcopolymere eine hohe mechanische Stabilität, welche von der Polystyrol (PS)-Domäne bereitgestellt wird, während die PEO basierte Domäne akzeptable ionische Leitfähigkeiten ermöglicht, allerdings nur bei höheren Temperaturen. Um brauchbare Leitfähigkeiten bei niedrigeren Temperaturen zu erreichen, wurden zwei ionische Flüssigkeiten (IFen) als Modellweichmacher selektiv in die PEO-Domäne eingebracht. Weil diese IFen nicht mit PS mischbar sind, bleibt diese Domäne davon unbeeinflusst und kann immer noch eine hervorragende mechanische Stabilität garantieren. Um jedoch die notwendige selbststehende Filmbildungseigenschaft beizubehalten, wurde die Größe der PS-Domäne entsprechend angepasst, um der leitenden, PEO-basierten Domäne zu entsprechen. Hierzu wurde eine Serie von vier Blockcopolymeren mit verschieden Blockverhältnissen synthetisiert, um den Einfluss von verschiedenen Mengen an IFen zu untersuchen. Weiter wurden alle so erhaltenen PEe eingehend mittels thermischer, morphologischen und elektrochemischer Analysemethoden untersucht. Die mikrophasenseparierte Morphologie mit Fernordnung sowie eine gute thermische und mechanische Stabilität, wie auch die selektive Mischung der IFen mit der leitenden Domäne konnte demonstriert werden. Konsequenterweise zeigte elektrochemische Impedanzspektroskopie einen signifikanten Anstieg der ionischen Leitfähigkeit um bis zu zwei Größenordnungen im Vergleich zur Referenz aus dem vierten Projekt. Des Weiteren konnten umfassende Studien der Lithiumionentransferzahl nicht nur die Wichtigkeit so detaillierter Untersuchungen für IF-enthaltende PEe beweisen, sondern auch den tatsächlichen Anstieg der Lithiumionenleitfähigkeit. Schlussendlich konnten Zyklisierungen in Li||$LiFePO_4$ Zellen klar die Anwendbarkeit des Ansatzes demonstrieren.

Zusammenfassend konnte die Signifikanz von Ansätzen zur Modifikation der Polymerarchitektur im Feld der Batteriechemie, im Besonderen bei polymerbasierten Elektrolyten, nicht nur erfolgreich gezeigt werden, sondern sie wurden auch dazu genutzt kritische Probleme von PEO-basierten PEen auf ausgeklügelte Art und Weise zu lösen, d.h. Probleme auf Grund der Kristallinität, das Dilemma zwischen mechanischer Stabilität und ionischer Leitfähigkeit, sowie die Kombination von PEO und Hochvoltkathoden.

Konsequenterweise konnten neue und wegweisende Schlüsse in Bezug auf Trends und Verhalten von PEO-basierten PEen gezogen werden und darauf aufbauend die Performanz von entsprechenden Batteriematerialien signifikant verbessert werden. Insbesondere in Zeiten von Rohstofflimitierungen, einem wachsenden Bedarf an Energiespeichermaterialien und dem Trend zu batteriebetriebenen Fahrzeugen konnten clevere und effektive Lösungen identifiziert, entwickelt und unkompliziert realisiert werden.

Table of Contents

Table of Contents

1 Introduction

The rising awareness for climate change and thus the search for environmental-friendly energy solutions is currently resulting in an enormous demand for a battery-driven society that range from mobile devices to electrical vehicles.[1,2] However, most state-of-the-art batteries still employ lithium-ion batteries (LIBs) that feature organic liquid electrolytes (OLEs) which manifests a drawback in several perspectives. On the one hand, these organic liquids are flammable, toxic and prone to leakage thus generating a huge safety issue.[3,4] On the other hand, the limited electrochemical stability and the unrestricted dendrite-growth does not allow for the use of metallic lithium electrodes, although the latter would drastically increase the available energy density.[5,6] In this regard, solid-state electrolytes (SSEs) are beneficial in terms of mechanical strength, toxicity, electrochemical stability and thermal tolerance, thus potentially eliminating the safety issues of OLE-based batteries.[7] In principle, these SSE materials can be divided into inorganic solid electrolytes and polymer electrolytes (PEs),[8] whereas the latter will be covered in the present thesis.

Even though many different advanced PEs have been introduced,[9–11] poly(ethylene oxide) (PEO) as ion conducting matrix for alkali metal salts is still among the most studied PEs despite its first report nearly 50 years ago.[12–16] PEO offers a good chain flexibility, low glass transition temperature (T_g), remarkable electrochemical stability against lithium-metal, great solubility for conductive lithium salts and comparable low costs.[17] Indeed, the first commercial PE (and also SSE) system was introduced by the Bolloré Group during the last decade featuring a cell setup consisting of a lithium-metal anode, a PEO-based polymer electrolyte and a $LiFePO_4$ cathode.[18,19] This milestone impressively demonstrates the reason for the ongoing research in PEO-based PEs.

However, despite these important attributes and great achievements, PEO-based PEs often suffer from high crystallinity, resulting in low ionic conductivities below its melting point since ion transport is mainly taking place in the amorphous domains.[20,21] Therefore, to improve the ionic conductivity at lower temperatures, different approaches can help to manufacture completely amorphous materials for enhanced ion transport, such as cross-linking,[22] the implementation of plasticizer[23,24] or nanofillers,[25] or blending with other polymers.[26] Furthermore, approaches to alter the molecular architecture, such as attaching PEO as side chain or even more complex architectures, successfully showed to inherently reduce crystallization in the absence of any additives.[27–29] Thus, this elegant route is of particular interest from a polymer chemists' point of view and, therefore, for the present thesis.

Although these approaches readily increase the ionic conductivity, polymer/battery chemists face an additional challenge, namely a dilemma regarding the correlation between ionic conductivity and mechanical stability. Generally, a higher ionic conductivity is achieved by lowering the T_g of the polymer, however resulting in a loss of mechanical stability due to the softer structure.[8,30] Conversely, a higher T_g increases the mechanical stability, but decreases the ionic conductivity. Unfortunately, a high mechanical stability is not less important than a high ionic conductivity since it is responsible for the suppression of lithium dendrite growth and prevention of short-circuits within the cells.[31]

To solve this dilemma, it is necessary to tune both properties independently from each other. For this purpose, block copolymers have demonstrated to successfully realize both a low T_g of one block being responsible for the ionic conductivity and a high mechanical stability by another block which provides rigidity.[32] Thus, this approach once more displays the great possibilities of synthetic polymer chemistry to solve challenges within PEs by adjusting the molecular architecture in a sophisticated manner. Consequently, this thesis will give an insight into the great toolbox of polymer chemists providing solutions for challenges within the field of polymer electrolytes for solid-state batteries.

2 Theoretical Background

The current chapter provides a brief introduction to the polymerization techniques used in this thesis, lithium batteries in general and polymer electrolyte-based lithium batteries in particular, while further setting the focus on PEO-based PEs.

2.1 Cationic Polymerization

These days, polymers have a broad field of application ranging from simple plastic bags or packaging to highly specialized fields such as tissue engineering, artificial joints or as component in batteries.[33–35] Thus, being able to gain control over molar mass and dispersity (*Đ*) can be crucial especially with respect to tailored applications. Among others *ionic polymerization* methods, namely *anionic* and *cationic polymerization* (AP and CP), are able to achieve this goal. Both are usually described as 'living polymerization' when certain conditions are met. This term of a 'living polymerization' was first introduced by Szwarc in 1956 and describes a polymerization with absent transfer or termination reactions as well as an initiation rate that is faster than the propagation rate enabling the creation of well-defined polymers.[36,37] Thus, the only 'truly living' polymerization technique is AP, since all other techniques only suppress transfer or termination reactions but cannot eliminate it completely. Nonetheless, CP can be also considered as 'living' or 'controlled' when conditions are adjusted accordingly. Meeting these conditions however requires highly purified solvents, monomers and an inert atmosphere. Besides the mentioned excessive purification steps, low or moderate temperatures are usually used to suppress undesired termination or transfer reactions. Consequently, CP is usually tedious and not very practical in comparison to other polymerizations methods.[38]

As the term already specifies, CP describes a chain-growth polymerization bearing a carbon centered cation as the reactive species. To form this species, the choice of monomers is crucial, since only a few are able to stabilize a carbon centered cation and can thus be polymerized by this technique. Therefore, vinyl monomers featuring electron-donating substituents attached to the C=C double bond, e.g. alkoxy, alkyl and alkenyl groups as well as aromatic substituents are among the polymerizable monomers (**Scheme 1a**).[38]

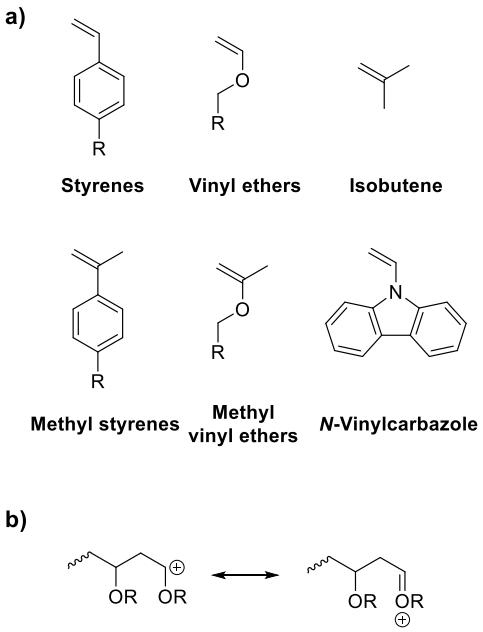

Scheme 1. a) Commonly employed monomers for CP.[38] **b)** Exemplary stabilization of the carbocation formed during the CP of a vinyl ether by delocalization of the positive charge over the carbon and the oxygen atom.

Similar to other chain growth polymerization techniques, CP of vinyl monomers can be subdivided into four different steps, *i.e.* initiation, propagation, termination and chain transfer reactions (**Scheme 2**).

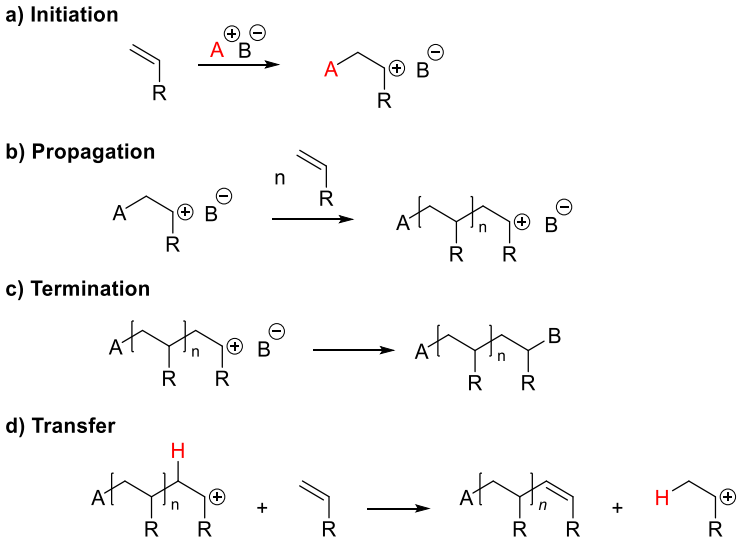

Scheme 2. General mechanism of a CP. **a)** Initiation through addition of a cation to the double bond. **b)** Propagation by addition of new monomers to the active center. **c)** Termination of the growing chain e.g., by interaction with the counter ion. **d)** Exemplary transfer reaction: β-proton transfer from the polymer chain to monomer.

Initiation of a CP can be induced by different methods, all of them eventually resulting in the formation of a carbon-centered cation (**Scheme 3**). Often strong protic acids or Lewis acids are used as initiators.[39,40] While the proton of protic acids is directly added to the C=C double bond and thus initiates the CP, Lewis acids react with impurities such as water or other molecules (e.g. alkyl halides) forming *in-situ* a cation being able to start the polymerization.[38,40] Further, carbenium salts display an elaborated method for initiation due to their easy handling as well as characteristic structure which facilitates subsequent analyses.[41]

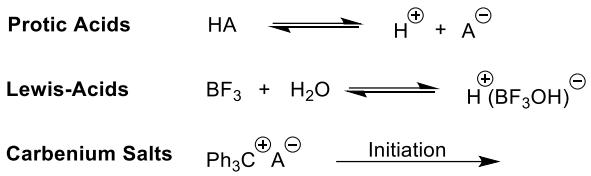

Scheme 3. Different initiators for CP by addition of a cation to the monomer.

Due to the cationic propagating species, termination/transfer processes are different from the ones observed with other polymerization techniques. While radical polymerization (RP) suffers from recombination due to the radical nature of the propagating species, the latter is not possible in CP due to the repulsion of equally charged cations. However, other termination reactions have been observed: Impurities like water for instance are able to create anions that can interact with the cationic propagating species, consequently resulting in the termination of the polymer chain. Further, β-proton elimination or the combination of the cationic active center with the counter ion or fragments of it are additional common termination reactions typical for CP (**Scheme 2c** and **2d**).[42]

2.1.1 Controlled Cationic Polymerization

As already mentioned above, CP can be considered as ‘controlled’ or ‘living’ when certain conditions are met. This means, transfer or termination reactions need to be absent or suppressed and the initiation needs to be faster than the propagation assuring simultaneous growth of all chains. Even more, the number-average molar mass (M_n) of the polymerization should increase linearly with the conversion. The absence of termination reactions ensures active chain ends, even after completed monomer consumption. Thus, further addition of monomer leads to the continuation of the polymerization and allows for the preparation of block copolymers and other architectures.[38,42] Noteworthy, e.g. the previously described, simple BF_3 initiated CP does not result in a controlled polymerization, therefore more elaborated systems were developed.

Herein, the key to achieve a controlled polymerization is the establishment of an equilibrium between an active ionic and dormant covalent species (**Scheme 4**), while the latter is predominant, therefore suppressing termination/transfer.

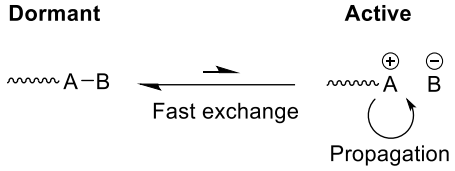

Scheme 4. The equilibrium between a dormant, covalent species and an active, ionic species enables a controlled CP.

Generally, three commonly employed methods are available to establish an equilibrium and consequently achieve a controlled CP: **a)** The combination with nucleophilic counter anions, **b)** added bases (nucleophiles) and **c)** added salts.[38] However, a fast and efficient initiation is at least of equal importance in order to ensure a controlled CP. Thus, so-called cationogens are often used as initiator, releasing carbocations which resemble the structure similar to that of the monomer upon reaction with the Lewis acid.[43]

The historical first description of a controlled CP was reported by Higashimura and Sawamoto in 1984.[44,45] They achieved a successful living polymerization of isobutyl vinyl ether (IBVE) by using a hydrogen iodide/iodine system to synthesize homo and block copolymers with controlled molar masses and low dispersities. As shown in **Scheme 5a**, hydrogen iodide as strong acid adds to the double bond of the vinyl ether forming a dormant adduct. Then, upon

reaction with I_2 a carbocation is released (which is able to propagate) and I_3^- is formed, which can reversibly react with the active center forming the dormant species once again. Thus, the targeted equilibrium is established enabling the synthesis of poly(vinyl ether)s in a controlled manner. This general procedure can be found in numerous systems, as also shown in **Scheme 5b**. Here, HCl is responsible for the initiation while $ZnCl_2$ as Lewis acid acts as activator.[46] In contrast to this, the 'base-assisting system' usually employs a beforehand synthesized cationogen as initiator. As mentioned above, this cationogen displays a stable adduct of the monomer that is targeted to be polymerized and an acid such as HCl or acetic acid. Then, upon reaction with a strong Lewis base such as $EtAlCl_2$ or other metal chlorides (e.g. $FeCl_3$, $SnCl_4$, $TiCl_4$ etc.) the cation able to propagate is formed (**Scheme 5c**). Additionally, a Lewis base (usually ethers or esters) is required in order to adjust the Lewis acidity of the metal complex as well as stabilize the carbocation.[47] Generally, all these systems are able to produce well-defined polymers, however, they need to be adjusted to the specific demands of a certain monomer. As already mentioned before, these techniques require even more reactants to be perfectly dried and thus result in a huge effort to conduct a controlled CP.

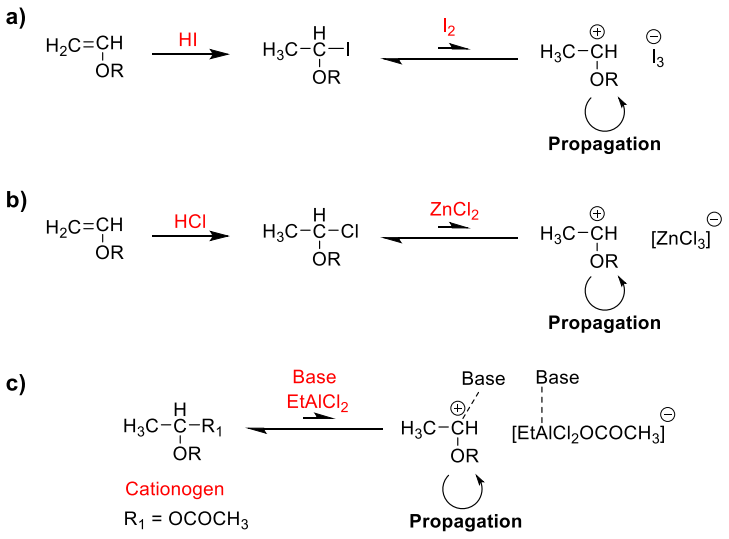

Scheme 5. Different initiation/control systems that are suitable to yield a controlled CP. **a)** After addition of HI to the double bond an adduct is formed, which can reversibly react with iodine to form an active species which is able to propagate. **b)** Analogous to the HI/I_2 system, HCl adds to the double bond forming an adduct which can be activated by $ZnCl_2$. **c)** The base-assisting system uses a beforehand synthesized cationogen (e.g. adduct of vinyl ether and acetic acid) which is activated by a Lewis acid to form an active species. Further, a Lewis base is required, helping to stabilize the cationic species as well as adjusting the Lewis acidity of the metal complex.

In 2019, Kottisch *et al.*[48] reported on a remarkable advancement in the controlled CP of vinyl ethers. They showed that pentakis(methoxycarbonyl)cyclopentadiene (PMCCP) (**Scheme 6**) as a strong organic acid[49] enables the single-component initiation and control over the CP of a series of alkyl vinyl ethers in bulk under ambient atmosphere (mechanism shown in **Scheme 6**). The conducted polymerizations resulted in polymers with low $Đ$ ranging from 1.06 to 1.33 with predictable experimental molar masses. They recently expanded their studies, showing that an additional hydrogen bond donor molecule stabilizes the formed complex during polymerization and thus enables the synthesis of high molar mass alkyl-based poly(vinyl ether)s.[50] However, they did not investigate the polymerizations of vinyl ethers bearing any functional group, which would be of high interest for subsequent modification reactions.

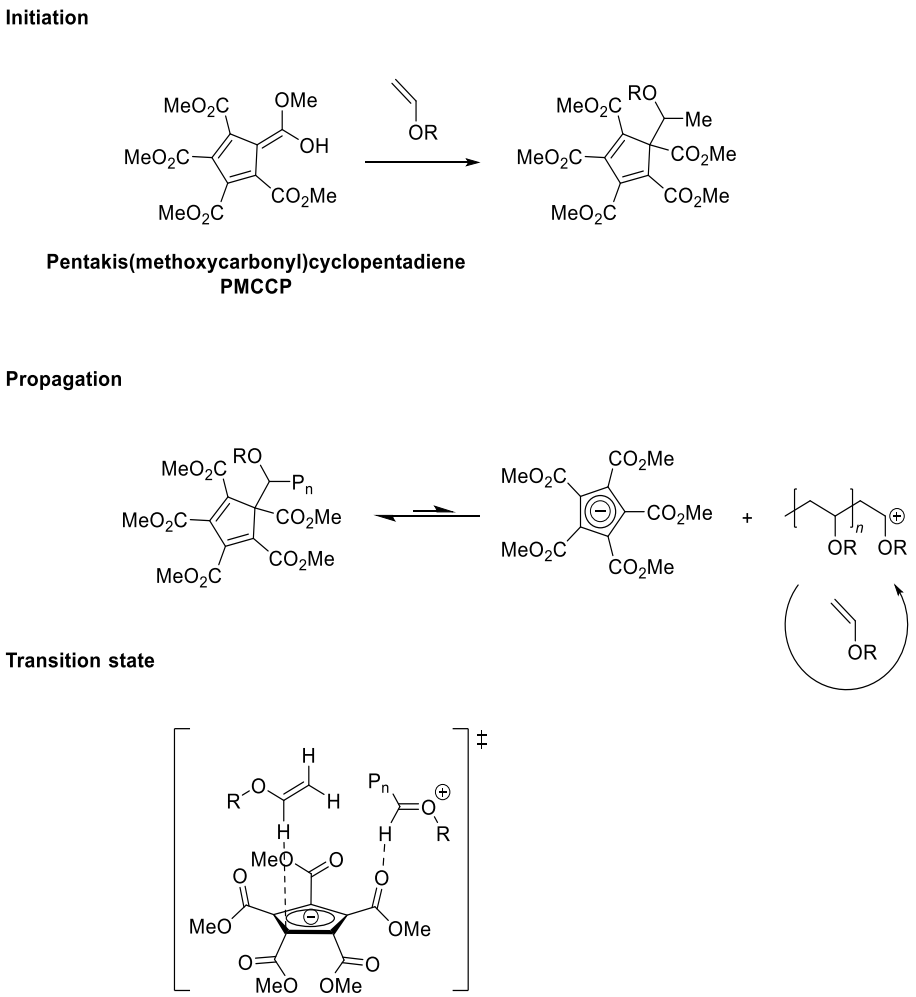

Scheme 6. Initiation and propagation of the polymerization of vinyl ethers using PMCCP as single-component initiation and control agent as well as the proposed transition state. The polymerization is initiated by the addition of PMCCP to the monomer. Afterwards, an equilibrium between a predominant, dormant (covalently bound) and an active species (cyclopentadienyloxocarbenium salt) is formed. Further addition of monomer to the active species (salt) leads to the propagation of the polymerization.[48]

2.2 Reversible-Deactivation Radical Polymerization

Among all the polymerization techniques, *radical polymerization* (RP) processes are used to produce around 50% of all synthetic polymers.[51] There are various reasons for this huge success, such as the straightforward polymerization conditions, and the low demand for high purities of solvents or reagents. In contrast to the before mentioned CP, RP is tolerant to protic impurities such as water and the high tolerance of radicals to many functional groups leads to a wide range of monomer structures. In conventional *free radical polymerization* (FRP) high molar masses are reached at early stages of the polymerization, so neither high conversions nor resulting long reaction times are necessarily required as opposed to step-growth polymerization.[52]

However, there is one major disadvantage of conventional RP especially in comparison with AP processes. As described before, AP can yield so-called 'living polymers' with a perfect control over molar mass, dispersity and architecture, due to the absence of chain breaking reactions *i.e.*, termination or transfer. While transfer is not a big issue in RP (in comparison to CP), termination is simply not avoidable due to the nature of radicals. Two ions with the same charge cannot combine and terminate because of charge repulsion, but two radicals will terminate eventually. Thus, it is only possible to minimize termination reactions in RP, but not to eliminate them completely.[52]

To solve the problems of conventional FRP new polymerization techniques were developed. They have been summarized under the initial term CRP (*controlled/living radical polymerization*). Due to the fact that 'living' is *per se* wrong, because termination reactions can never be eliminated in radical processes, the term RDRP (*reversible-deactivation radical polymerization*) is nowadays used in most cases and also recommended by the IUPAC, since it describes the actual situation more accurately.[53]

In general, there are two main mechanisms in RDRP minimizing termination. On the one hand, an equilibrium between a dormant species and an active species, the propagating radical chains, is established. When the equilibrium is on the side of the dormant species, the number of free radicals able to undergo termination is drastically decreased. Thus, this principle resembles living cationic polymerization. On the other hand, however, the second general mechanism is based on a continuous radical transfer between all chains. This means that radical chain transfer to other chains, by usage of a *chain-transfer agent* (CTA), is favored over termination.[54]

The RDRP protocols allow to reach low $Đ$ with a linear increase of the molar mass with conversion. The achieved control allows to synthesize polymers with many different

architectures, e.g. (block) copolymers[55], different topologies such as brush shaped polymers,[56] stars,[57] or dendrimers[58] and side or end group functionalization.

Based on the RDRP methods mentioned above there are mainly three techniques which are commonly used: *reversible addition-fragmentation chain-transfer* (RAFT) polymerization, *atom transfer radical polymerization* (ATRP) and *nitroxide-mediated polymerization* (NMP).

2.2.1 Atom Transfer Radical Polymerization

The principle of atom transfer radical polymerization (ATRP) is based on a dynamic equilibrium between a dormant species (P_n-X) and a propagating radical chain ($P_n^{\bullet}$) (**Scheme 7**). The dormant species, at the beginning an alkyl halide and later during the polymerization a macromolecular halide species, is activated through a reaction with a transition metal complex in a lower oxidation state (M^m/L). Therefore, a radical species able to propagate is formed and the metal species is oxidized to the oxidation state *m+1*. The reverse reaction of the activation forms the dormant species again. It is crucial that the rate of deactivation is order of magnitudes higher than the rate of activation, meaning that the equilibrium is primary on the side of the dormant species. This ensures a low termination rate since the termination is proportional to the concentration of radical species squared (~ $[P_n^{\bullet}]^2$).[59]

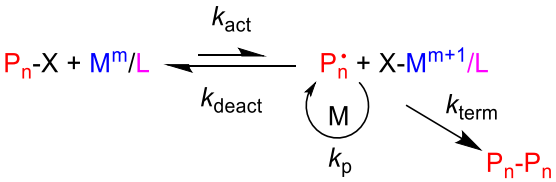

Scheme 7. General mechanism of an ATRP with the reversible catalytic redox equilibrium between an alkyl halide (dormant species, left) and a radical (active species, right) which can undergo chain extension with present monomer.[59]

The commonly used metal system for ATRP is Cu^I/Cu^{II}, but other metals like Ru, Fe, Mo, or Os are also possible.[60] However, the usage of a redox metal system generally leads to a high sensitivity against oxygen and additionally requires the removal of the metal after the polymerization in most cases due to toxicity reasons.

2.2.2 Nitroxide-Mediated Polymerization

Nitroxide-mediated polymerization (NMP) is based on nitroxides, which are *N*,*N*-disubstituted radicals of the NO type. In general, they are designed to be stable at room temperature, enabled by delocalization of the single electron between the nitrogen and the oxygen atom.[61] Due to the persistent radical effect, nitroxides cannot initiate a radical polymerization by themselves.[62] In opposite, they react with carbon radicals to form thermolabile alkoxyamines as dormant species, which again can dissociate into a carbon centered radical (active species) and nitroxide radical at a certain temperature depending on the exact structure.[63]

Scheme 8 shows the mechanism of NMP. The left side of the equilibrium represents the dormant species while the right side represents the active species, which is able to propagate.

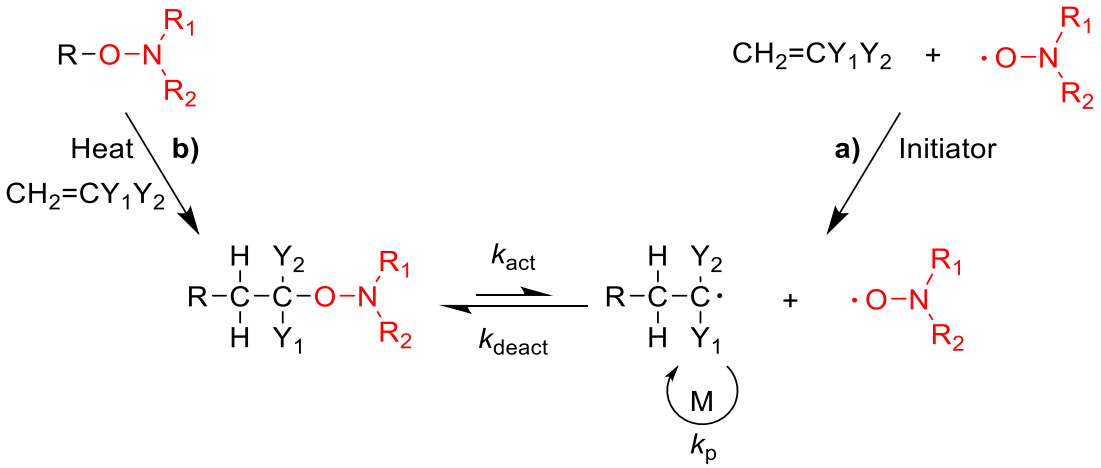

Scheme 8. Activation-deactivation equilibrium in NMP with the predominant dormant alkoxyamine species on the left and the nitroxide as well as the active radical species on the right side. Bicomponent initiating system **a)** and monocomponent initiating system **b)**.[64]

As shown in **Scheme 8** there are two possible pathways to initiate NMP. For pathway **a)**, a nitroxide and a conventional initiator like AIBN can be used. Thus, such a system is called a two-component initiating system. Pathway **b)** on the other hand only employs an alkoxyamine, representing a monocomponent system. Here, upon heating of the reaction mixture the dissociation temperature of the alkoxyamine is reached, causing a homolytic bond cleavage to form a carbon-centered radical and a nitroxide radical. Since the ratio of radical:nitroxide should be 1:1 in order to gain control over the polymerization, pathway **b)** (monocomponent initiating system) is more commonly used, because it inherently fulfills this requirement.[64]

Caused by the highly stable alkoxyamine bond, NMP features rather slow reaction rates and requires high reaction temperatures. However, this ensures well-defined polymers with low dispersities. Nonetheless, there is no need for an additional component like a metal ion as in ATRP, which would need to be removed again afterwards.

2.2.3 Reversible Addition-Fragmentation Chain-Transfer Polymerization

As mentioned before, there are two general categories of RDRP techniques. In opposite to NMP and ATRP, which are both based on a reversible termination mechanism, reversible addition-fragmentation chain-transfer (RAFT) polymerization relies on a continuous degenerative radical transfer between chains enabled by so-called RAFT agents. This results in a constant radical concentration, which leads to higher polymerization rates in comparison to both other techniques.[65]

Those RAFT agents are particularly designed molecules with a reactive C=S double bond, while the most frequently used ones are based on a dithioester or trithiocarbonate structural motif, as depicted in **Scheme 9**. The selection of a proper stabilizing Z group is essential, since it has to ensure a sufficient reactivity of the C=S bond towards radicals on the one hand and an adequate stabilization of the formed intermediate radical on the other hand. Further, the R group displays the so-called leaving group, which is released from the RAFT agent as a radical species, after the first radical (chain) was added to the latter. Thus, it must be able to efficiently initiate the propagation of new chains in order to continue the polymerization. In general, there is a wide range of different chain-transfer agents suitable for a broad field of monomers.[66]

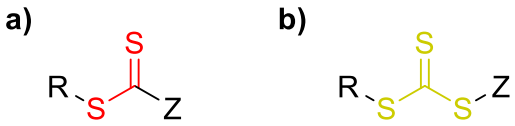

Scheme 9. General structure of RAFT agents. **a)** Represents a dithioester while **b)** is a trithiocarbonate. R = leaving group; Z = stabilizing group.

Analogous to FRP, conventional initiators are necessary in common RAFT polymerizations. However, initiation can occur by all thinkable ways (thermally, photoinitiation, etc.) as long as radical species are formed, which are able to start a polymerization (**Scheme 10a**). In the next step the propagating radical chains react with the RAFT agent **b)**, releasing the leaving group R *via* a stable radical intermediate. As mentioned before, the formed radical R$^{\bullet}$ must be able to initiate polymerization of the monomer **c)**, in order to create new growing chains. Afterwards,

a continuous radical transfer among all growing chains through reaction with the RAFT agent **d)** is established. Termination **e)** occurs, as in every RP, *via* radical-radical recombination or disproportion of two growing chains.[67]

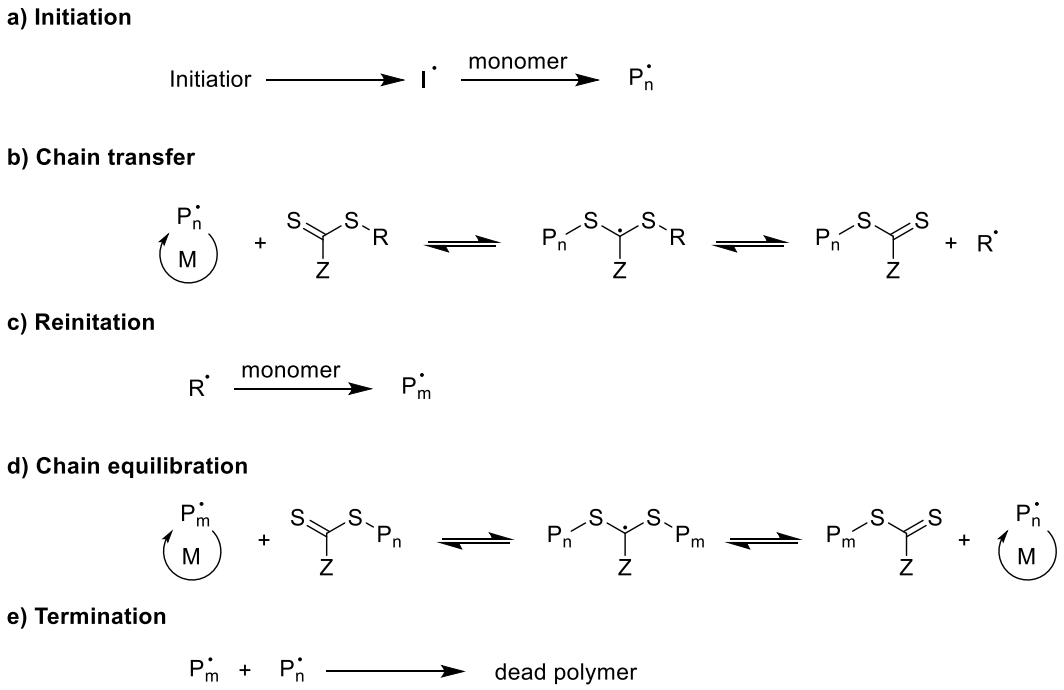

Scheme 10. General mechanism of the RAFT process including two equilibria that are responsible for the continuous degenerative radical transfer which is responsible for the control over the reaction. Since the reaction of radicals with the RAFT agent is favored over the reaction of two active chains, termination is minimized.[67]

The advantages of RAFT are the possibility to control nearly all monomers with a suitable agent, the high tolerance towards functional groups, a high compatibility to different reaction conditions (bulk, (mini-)emulsion, organic or aqueous medium etc.), and the higher reaction rates in comparison to ATRP and NMP.[68]

2.3 Post-Polymerization Modification

Modification of polymers is known since the early days of polymer science. The vulcanization of natural rubber using elemental sulfur in 1840[69] or the nitration of cellulose for the production of nitrocellulose in 1847[70] are two commonly known examples. Generally, post-polymerization modification (PPM) enables to obtain a broad variety of functional polymers from numerous precursor polymers, the former being, in some cases, not even accessible by direct polymerization of the respective monomers.[71] While PPMs had been around ever since, they received particular attention when combined with the previously addressed RDRP techniques, which allowed for the synthesis of well-defined polymers with numerous elaborated structural motifs.[72,73] However, to fully benefit from the controlled character of RDRP techniques, the reaction employed as PPM method should be efficient and ideally feature quantitative conversion without the formation of side products. The development of so-called *click* reactions[74–76] such as *thiol-ene* reactions[77] or *copper(I)-catalyzed alkyne-azide cycloaddition* (CuAAC)[78] as *chemo-selective* and highly efficient reactions was therefore essential for the huge success of PPM methods. Moreover, transesterifications or amidations of poly(active ester)s[79] or ring-opening reactions of epoxides such as poly(glycidyl methacrylate)[80] have proven their viability as efficient techniques to modify polymers after polymerization.

In general, the *thiol-ene* reaction describes a hydrothiolation of a C=C double bond and proceeds *via* a radical or a nucleophilic mechanism.[81] The actual nature of the mechanism depends on the electron density of the C=C double bond: Electron-deficient C=C double bonds react under the catalyzed *Michael addition*, while the radical addition constitutes a possible pathway for any C=C double bond.[81] Concerning the latter, the reaction can be started for instance by a thermal radical initiator or by a photoinitiator[82] and is followed by propagating chain reaction and termination as shown in **Scheme 11**.[83] Due to its numerous advantages over other PPM contenders, such as the simple synthetic procedure, high atom economy, easy purification and the high yield under mild reaction conditions, *thiol-ene* click reactions are in many cases the first choice to modify polymers in an efficient and straightforward fashion.[83]

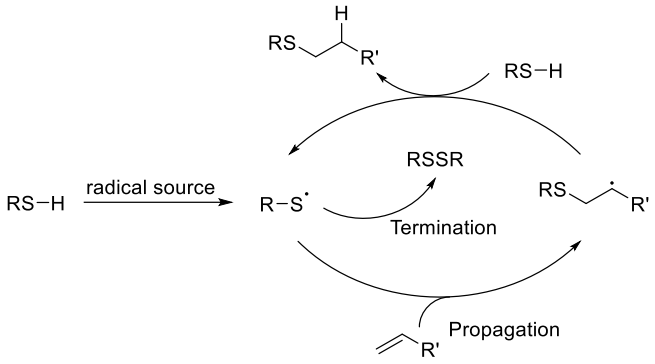

Scheme 11. Mechanistic pathway of the radical *thiol-ene* reaction with initiation, propagation and termination.[83]

The frequently used *copper(I)-catalyzed alkyne-azide cycloaddition* (CuAAC) represents a variation of the Huisgen 1,3-dipolar cycloaddition[84] which was independently reported by Tornøe *et al.*[85] and by Fokin and Sharpless[86] in 2002. In contrast to the non-catalyzed cycloaddition, *i.e.* the Huisgen cycloaddition, which produces a mixture of 1,4 and 1,5-disubstituted products, CuAAC yields selectively 1,4-disubstituted triazoles (**Scheme 12**).[78] Besides this selectivity, the reaction rate of the catalyst-assisted reaction is found to be 7 to 8 orders of magnitude higher than the reaction without catalyst[87] with quantitative yields in most cases.[88] It is compatible with different organic solvents as well as water/alcohol (e.g. methanol, ethanol or butanol) mixtures[89] and features a high tolerance towards functional groups.[78] Thus, CuAAC reactions have a broad field of application, ranging from PPM in polymer chemistry to drug development and biochemistry.[89]

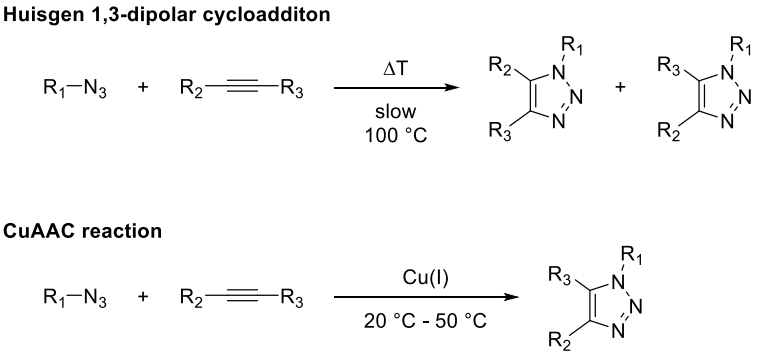

Scheme 12. Comparison of the uncatalyzed 1,3-dipolar cycloaddition and the catalyzed CuAAC reaction. Huisgen's 1,3-dipolar cycloaddition leads to a mixture of 1,4 and 1,5-disubstituted products, while the CuAAC reaction is selectively forming the 1,4-cycloadduct.

2.4 Graft Polymers

In general, the toolbox of the previously described controlled polymerization techniques as well as PPM methods allows for the synthesis of macromolecules with well-defined structures and topologies such as cyclic polymers,[90] star polymers,[91] dendrimers,[92] hyperbranched polymers[93] and graft polymers.[94] These sophisticated macromolecular architectures often come along with unique properties, thus making them highly interesting for both academia as well as industry.

In the scope of the present dissertation, especially graft polymers are of interest: They are a class of branched polymers with one end of the polymer chains attached to a linear polymer backbone (1D), to a planar surface (2D) or to a particle (3D) (**Figure 1**).[95,96] Their architecture and properties can be adjusted by changing different parameters such as the grafting density, the nature and thus e.g. the flexibility of the backbone and side chains as well as the choice of monomers. Depending on the grafting density, 1D graft polymers are often differentiated between comb polymers, which have a lower grafting density, and brush polymers with a higher density of grafted side chains.[97] Especially the latter are of high interest, as the high grafting density and thus the steric hindrance of the side chains forces the backbone from the normal gaussian random coil conformation into an elongated chain formation resulting e.g. in wormlike conformations, compact molecular dimensions or remarkable chain end effects.[98] In 2D and 3D graft polymers, the side chains are densely attached to a matrix and can therefore provide materials with remarkable properties making them promising candidates for application purposes such as lubricants,[99] anti-fouling coatings,[100] micelles which function as drug carriers,[101] or in the field of tissue engineering.[102]

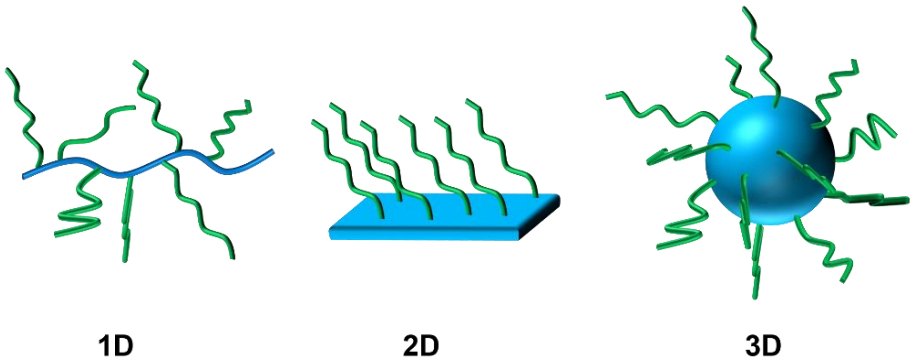

Figure 1. Depiction of different kinds of graft polymers which can be distinguished between one-dimensional (1D), two-dimensional (2D) and three-dimensional (3D) graft polymers.

However, the present dissertation will focus solely on 1D graft polymers. As mentioned before, these advanced structures can be synthesized by the already explained controlled polymerization techniques such as CP, RAFT, ATRP or NMP, while several techniques can be distinguished: *grafting onto*, *grafting through* and *grafting from* (**Scheme 13**).

The *grafting onto* approach can be realized by tethering the polymer side chains to a linear polymer backbone e.g. *via* nucleophilic substitution or coupling reactions such as '*click chemistry*'.[103] In this case, the linear backbone as well as the side chains are prepared (and characterized) separately and the polymerization method can thus be customized in accordance to the used monomers. This allows for a high degree of control over the graft architecture and straightforward characterization prior to the grafting process. However, high grafting densities can be hard to realize, especially when long side chains need to be attached due to steric hindrance. Hence, in most cases an excess of side chains is used which makes in turn the removal of excess side chains necessary.[104]

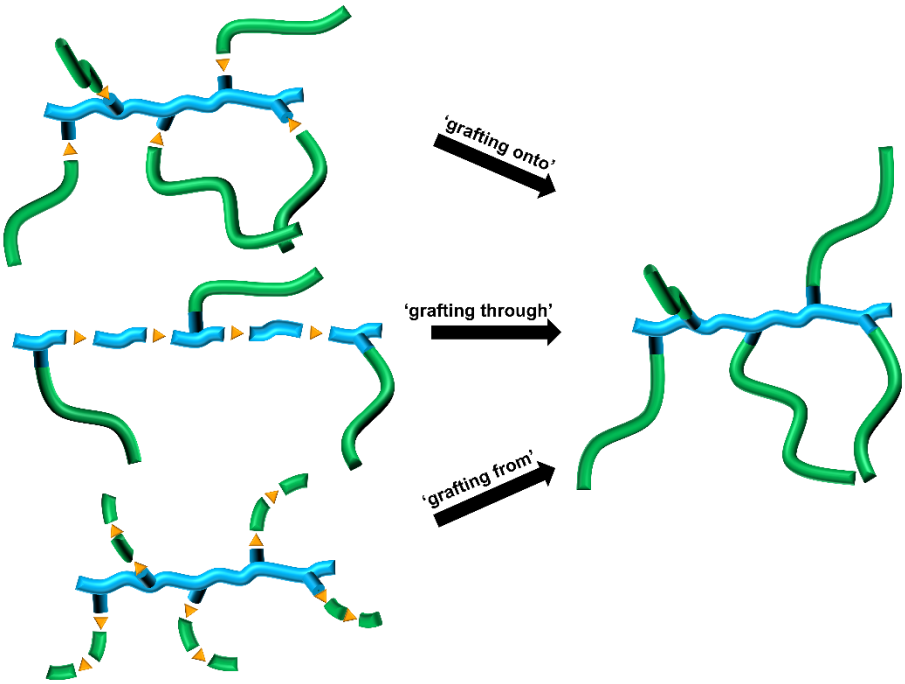

Scheme 13. Depiction of different approaches to obtain graft polymers *via* '*grafting onto'*, where polymer side chains can be attached to a linear backbone with functional groups, '*grafting through'* by employing monomers and macromonomers that contain both side chain polymer and a polymerizable functionality and '*grafting from'* by adding monomers to the polymer backbone macroinitiator. The orange arrows denote the reactive sides, respectively.

The *grafting through* approach represents another technique to obtain graft polymers. For this, a polymer backbone featuring polymerizable side groups is utilized in the polymerization of monomer, which allows the growing polymer chain to insert a polymerizable side group and

thereby attaching a polymer chain onto the polymer backbone. Further, polymerization of solely macromonomers (as special case of the *grafting through* approach) can be used to graft polymers.[105] Generally, one advantage is the independent synthesis of the macromonomer which can be purified and characterized prior to the polymerization. Further, the grafting density and the length of the side chains can be easily tuned beforehand. At the same time however, the practically achievable grafting density of the polymer is dependent on the reactivity of the polymerizable group and the steric hindrance of the side chain. Even more, if full conversion is not reached, it can be difficult to remove the unreacted macro monomers from the final graft polymer.

The *grafting from* method is based on a polymerization process from a linear polymer backbone comprising suitable functionalities.[106] Therefore, the steric hindrance during the grafting process is significantly reduced, because the smaller monomers can easily access the active polymer sites to promote chain growth. In this case e.g., ATRP and NMP offer the best conditions since the concentration of free radicals is kept very low in order to prevent termination *via* intramolecular macrocyclization of the side chains or intermolecular crosslinking between different macromolecules. Furthermore, in contrast to the other above-mentioned methods, the removal of unreacted side chains/macromonomers is not necessary.

2.5 Lithium-Ion Batteries

As result of the continuously growing demand of fossil resources which are fairly limited, the necessity for alternative energy resources and their storage is getting more and more urgent.[2] Among these energy storage technologies that are highly sought after, especially lithium-ion batteries (LIBs) are from great interest because of various advantages such as light weight, high voltage, high energy density, small self-discharge, no memory effect, excellent cycle life and a longer lifespan compared to other battery technologies.[107] Thus, the introduction of the first rechargeable lithium-ion battery by the Sony Corporation in 1991 enabled their commercialization and exploitation in numerous technical applications such as portable electronic devices and electric vehicles.[108] In 2019, the enormous importance of these findings were appreciated by awarding John B. Goodenough, M. Stanley Whittingham and Akira Yoshino for their contributions to the development of LIBs with the Noble Prize in chemistry. Nonetheless, the battery sector is still constantly growing due to an massively expanding demand in rechargeable batteries and extensive research in this area.[2]

In general, a conventional LIB consists of an anode, a cathode, and an electrolyte (**Figure 2**). In state-of-the-art cells, the employed electrolytes are organic liquids, thus making the use of a separator, which physically separates the anode from the cathode to prevent them from a short-circuit, essential. Further, commercialized LIBs are usually operated based on lithiated graphite as anode and cathode materials such as $LiCoO_2$ (LCO), $LiFePO_4$ (LFP), $LiMn_2O_4$ (LMO) or $Li(Ni_xMn_yCo_{1-x-y})O_2$ ($0 \leq x \leq 1$, $0 \leq y \leq 1$, and $0 \leq x + y \leq 1$) (NMC).[107]

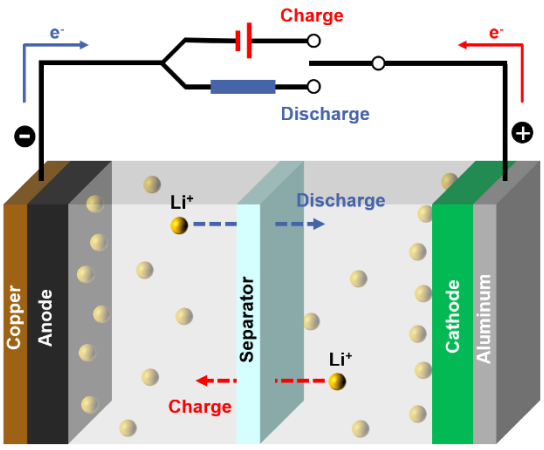

Figure 2. General depiction of a lithium-ion battery with a liquid electrolyte and a separator which separates the anode and cathode from each other. The charging process occurs through lithium-ion transport from the cathode to the anode and discharging through the opposite direction.[30]

However, the use of organic liquid electrolytes (OLEs) in LIBs has significant drawbacks since they are in most cases toxic, volatile and flammable,[109,110] potentially resulting in fire or explosion in case of mechanical, thermal or electrical impact.[111] Moreover, fulfilling the growing requirements to batteries due to the expanding market, new active materials which provide higher energy densities than state-of-the-art LIBs need to be commercialized.[108] Thus, higher specific capacities as well as higher anode/cathode potential differences are to be targeted.[112] In comparison to lithiated graphite, lithium-metal offers a significantly higher specific capacity (372 vs. 3860 mAh g^{-1})[113,114] and a slightly lower redox potential , its use however is limited due to safety concerns in particular when paired with usual OLEs. This mainly originates from an instable solid electrolyte interphase (SEI) and lithium dendrite growth during cycling, eventually leading to short-circuits.[115] To solve this problem solid-state electrolytes (SSEs) could provide sufficient mechanical strength to suppress lithium dendrite penetration.[8] Moreover, they are generally beneficial in terms of toxicity, electrochemical stability and thermal tolerance, thus potentially overcoming the safety issues of OLE-based batteries.[7] These SSE materials can in principle be divided into inorganic solid electrolytes and polymer electrolytes (PEs), with the latter being further discussed in the following chapter.

2.6 Polymer Electrolytes

As stated before, PEs represent a promising alternative to commonly employed OLEs, with the potential to overcome the drawbacks of the latter. Generally, they can be further categorized into solid polymer electrolytes (SPE) and gel polymer electrolytes (GPE).[8]

SPEs are defined as lithium salt dissolved in a polymer host, where the ions can move in the free volume of the polymer matrix and thus enable ionic conductivity mainly above the T_g.[21,116] SPEs are therefore also known as 'dry systems', since there is no liquid component involved. Generally, they feature numerous advantages such as their mechanical properties, flexibility, low cost and safety, *i.e.*, low flammability and no leakage. However, the reason why SPEs have not been widely commercialized so far is mainly due to their low ionic conductivity in comparison to OLEs, problems regarding the interfacial interactions between the electrode and electrolyte as well as the provided electrochemical stability window especially with respect to high-voltage cathode materials.[1]

In this regard, GPEs combine the advantages, but also to some extent the disadvantages of liquid electrolytes and SPEs, by featuring better ionic conductivities than SPEs and higher mechanical stability than OLEs. They are usually obtained by the addition of solvents or other liquid plasticizers into the polymer-salt system, thus enhancing the polymer mobility and consequently creating more mobility for the lithium ions as well as enabling transport solely by the solvent. Further, an improved contact between the electrode/electrolyte interface can usually be found because of a good wetting. However, due to the integration of liquids into the system, safety concerns regarding flammability and rapid decomposition are still valid and the mechanical stability is generally not as high as in SPE systems.[117,118]

A brief summary of the different properties of OLEs, SPEs and GPEs is given in **Table 1**. Although there might be some exceptions, it can generally be stated that SPEs and OLEs behave complementary to each other, while GPEs feature properties in between.

Table 1. Comparison of the properties for OLEs, SPEs and GPEs.[119]

Electrolyte properties	OLE	SPE	GPE
Ionic conductivity	+	-	o
range at RT	> 1 mS cm^{-1}	< 0.1 mS cm^{-1}	> 0.1 mS cm^{-1}
Contact/interfacial properties	+	-	o
Electrochemical stability	-	+	-
Thermal stability	-	+	-
Dimensional Stability	-	+	o
Safety	-	+	o

Concerning the actual application of PEs in LIBs, several properties are required to achieve an optimal performance: As such, high ionic conductivity at ambient temperature is of essential interest. Generally, OLEs with lithium salts can achieve an ionic conductivity of 1 mS cm^{-1} to 10 mS cm^{-1}, whereas PEs should reach at least an ionic conductivity of 0.1 mS cm^{-1}, which is already a challenge in most cases.[35] Furthermore, a large Li^+ transference number (t_{Li^+}), describing the fraction of Li^+ movement *vs.* the movement of all ions and thus corresponding to a high Li^+ mobility in comparison to the anion, is preferable. Generally, the t_{Li^+} value for salt-in-polymer PEs is below 0.5, meaning the anions are more mobile than the lithium ions.[120] During the discharge process those anions will accumulate on the anode resulting in polarization due to concentration gradients.[121] A high transference number close to 1 (equally to almost no anion mobility) however will lower the concentration polarization of electrolytes during the charge/discharge process, thus resulting in higher achievable energy densities.[122] Smart approaches to achieve a limited anion mobility are based on chemically tethering them to the polymer backbone creating so-called single-ion conducting polymer electrolytes.[123] Moreover, the introduction of anion receptors that can selectively complex anions in the electrolyte and therefore reduce their movement have successfully shown to increase t_{Li^+}.[30] Additionally, the polymer electrolytes should provide good mechanical strength in order to suppress lithium dendrite growth and be suitable for large scale production.[124] A good flexibility in opposite to brittleness is preferred, in order to resist stress during the manufacturing process, cell assembly, storage and usage. Further, a sufficient electrochemical stability window (ESW) denoting the difference between the oxidation and reduction potential of the electrolyte needs

to be provided. Hence, the oxidation potential must be higher than the Li^+ potential in the cathode and the reduction potential should be lower than the Li metal potential in the anode, usually resulting in required ESWs around $4 - 5$ V depending on the used anode/cathode materials.[125] Lastly, excellent chemical inertness towards other battery components and thermal stability to ensure the safe handling of batteries are important factors for the use of PEs.

2.7 Poly(ethylene oxide) as Polymer Electrolyte

Although poly(ethylene oxide) (PEO) as ion conducting matrix for alkali ions (**Scheme 14**) was already discovered nearly 50 years ago[16] and numerous other PEs were advertised to replace it, it is still among the most studied candidates.[12–15] For good reasons: PEO features a good chain flexibility, a low glass transition temperature (T_g), good electrochemical stability against lithium-metal, great solubility for conductive lithium salts, great film-forming ability and is comparably affordable. However, it still suffers from low ionic conductivities of 10^{-5} to 10^{-1} mS cm^{-1} at temperatures below its melting point (~ 65°C).[17] Nevertheless, its potential for solid state battery application in electric vehicles was successfully demonstrated by Bolloré,[126] introducing the Lithium Metal Polymer (LMP) battery technology in 2011, and to date, more than 8000 vehicles are operated based on the LMP technology, illustrating that PEO and variants thereof are not only of contemporary interest but also practically extremely relevant.[127,128]

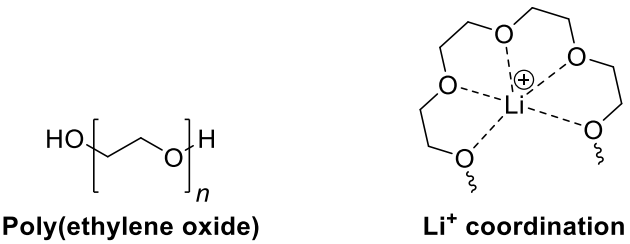

Scheme 14. Chemical structure of poly(ethylene oxide) and the schematic depiction of Li^+ coordination by several oxygen atoms.

The different ion transport mechanisms in PEO-based PEs are displayed in **Figure 3**. Transport can occur through continuous breakage and formation of lithium-oxygen bonds either along the polymer chain (intrachain hopping, **Figure 3b**) or between the polymer chains (interchain hopping, **Figure 3a**). These processes are mainly dominant at low temperatures or within crystalline phases.[17,129] At temperatures above the melting temperature or in completely amorphous PEs however, the chain segmental motion is mainly responsible for the ionic conduction by assisting both before mentioned processes significantly and further enabling movement of the ion with the chain (**Figure 3c**).[130] Furthermore, the Li^+ ions can form ion clusters with their corresponding anions depending on the salt concentration, but still relying on the same types of transport.

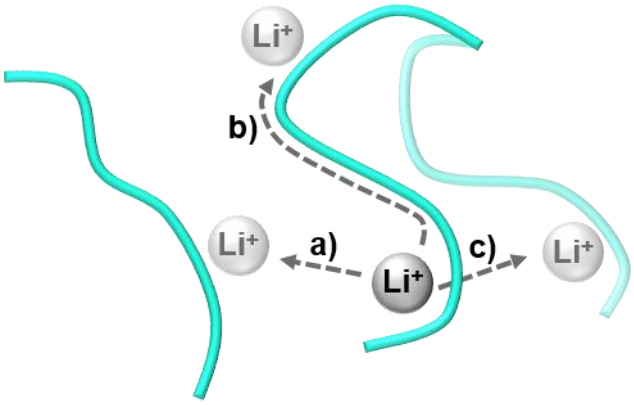

Figure 3. Ion transport mechanism in PEO-based PEs through either interchain hopping **a)**, intrachain hopping **b)** or segmental motion **c)**. All mechanisms can also appear in the case of ion clusters.

Moreover, the employed lithium salt constitutes a crucial factor for PEO-based PEs, because not all lithium salts show a strong dissociation and thus high ion mobility (e.g. LiCl features a low degree of dissociation and consequently really low ionic conductivities[131]). Therefore, a delocalized negative charge and low basicity are important criteria for the selection of a suitable salt. Traditionally, compounds such as $LiClO_4$,[132] $LiAsF_6$,[133] $LiPF_6$[134] and $LiBF_4$[135] have been used as salts in PEO. However, alternative lithium salts have been explored due to various safety concerns such as the explosive potential of $LiClO_4$ in organics,[136] the arsenic in $LiAsF_6$ that can form poisonous compounds, as well as the formation of toxic and corrosive HF under moist conditions of $LiPF_6$ and $LiBF_4$.[137] Perfluoro alkyl sulfonic-type conducting salts like lithium trifluoromethanesulfonate (LiTF),[138] lithium bis(fluorosulfonyl)imide (LiFSI),[139] lithium bis(trifluoromethanesulfonyl)imide (LiTFSI)[140] (**Scheme 15**) exhibit high solubility, ionic conductivity and electrochemical stability. These lithium salts have large anions that can easily dissociate in the PEO matrix and release free lithium cations, thus increasing the ionic conductivity. Further, the fluorinated moieties display a strong electron-withdrawing effect which enhances the acidity of the corresponding proton which stabilizes their conjugated base as a result of the delocalization of the negative charge. Even more, a big steric hindrance of the anion such as the $TFSI^-$ anion suppresses crystallization within the PEO matrix, thus indirectly enhancing the ionic conductivity due to an increased amorphous phase.

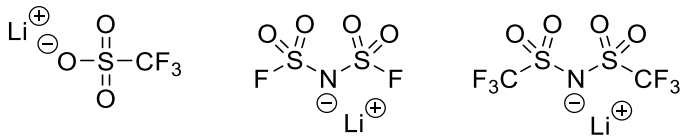

Scheme 15. Structures of lithium trifluoromethanesulfonate (LiTF), lithium bis(fluorosulfonyl)imide (LiFSI) and lithium bis(trifluoromethanesulfonyl)imide (LiTFSI).

As described in the beginning of this subchapter, the partial crystalline nature of PEO and the resulting low ionic conductivities display one of the biggest challenges within this class of materials. Therefore, increasing the amorphous phase and thus improving the ionic conductivity of PEO, its inherent crystallization can be reduced by different approaches such as the addition of plasticizer,[141,142] nanofillers,[143] blending with other polymers[144] or by crosslinking.[145,146] All these approaches interrupt chain alignment by the introduction of disturbing molecules/particles and consequently reduce crystallization. One additional approach consists of the synthesis of polymers bearing grafted PEO side chains, in which the crystallization of the latter is reduced due to being anchored to the backbone chain, eventually resulting in superior ionic conductivity at lower temperatures.[28,147] Here, Itoh *et al.* for instance studied a series of vinyl ether-*alt*-vinylene carbonate-[148] and pure vinyl ether[29]-based PEO side chain PEs with different side chain lengths ranging from two to 23.5 EO units in 2013 and 2017, respectively (**Scheme 16**). Despite the vinylene carbonate moiety incorporated in the former, the authors observed the ionic conductivity to be the highest (e.g. 0.12 mS cm^{-1} at 30 °C) with the longest side chain length of 23.5 units above a temperature of 20 °C. Further, Rosenbach *et al.*[28] synthesized PEO side chain copolymers with two different side chain lengths (23 and 45 EO units) and two different backbone structures in 2019 (poly(methacrylate) and poly(norbornene), **Scheme 16**). In general, they observed higher ionic conductivities for the PEO side chain copolymer based on a poly(methacrylate) backbone (~ 0.13 mS cm^{-1} at 30 °C) in comparison to poly(norbornene)-based ones (~ 0.07 mS cm^{-1} at 30 °C) as a result of the higher relative PEO content in those polymers due to the lower molecular weight of the methacrylate structural motif in comparison to norbornene. Furthermore, PEs with longer side chains (45 EO units) featured higher ionic conductivities (~ 0.13 mS cm^{-1} at 30 °C) than their counterparts with shorter side chains (23 EO units, ~ 0.07 mS cm^{-1} at 30 °C) independent of the employed backbone chemistry, which is in accordance with the results of Itoh *et al*.

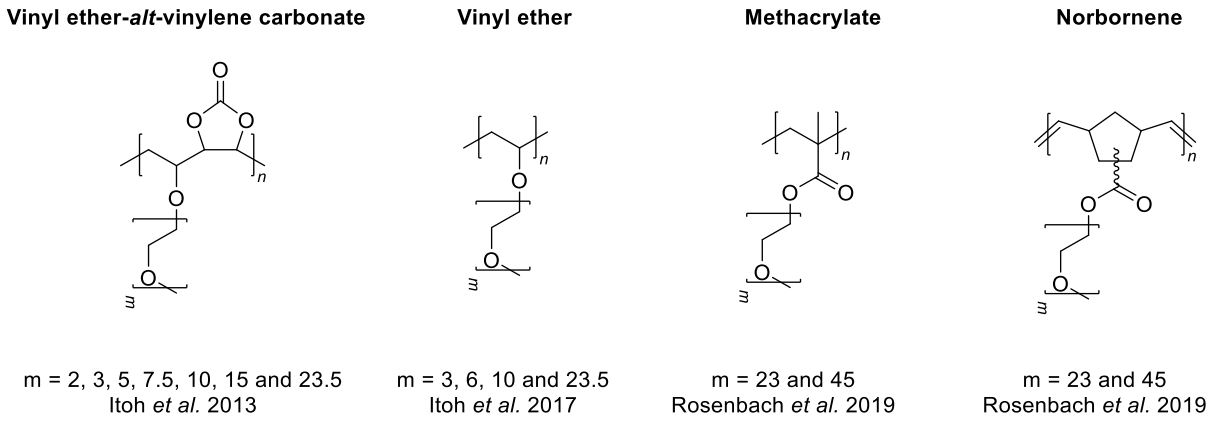

Scheme 16. PEO side chain copolymers bearing different side chain lengths and backbone chemistries as published by Itoh *et al*. 2013,[148] Itoh *et al*. 2017[29] and Rosenbach *et al*.[28]

Unfortunately, completely amorphous PEO results in a loss of dimensional stability at room temperature due to the low T_g at around -65 °C.[17,149] Consequently, the before mentioned PEO side chain copolymers are all highly viscous fluids. High molar mass polymers are able to solve this problem partially by providing substantial chain entanglement and therefore a macroscopically stable material. Though, the soft matrix characterized by the low T_g does not provide sufficient resistance against lithium dendrite penetration. A compromise can be found when a limited amount of plasticizer is implemented and the polymer matrix is cross-linked simultaneously for instance, providing both decent ion transport due to the plasticizer and decent mechanical stability due to the cross-linking.[22] However, the adjustable range of the ratio of polymer and plasticizer is limited around a narrow 'sweet spot' and still remains only a tradeoff. In addition, it was just recently shown that lithium dendrite penetration as a consequence of insufficient mechanical stability and not as commonly assumed insufficient oxidative stability might also be the reason why PEO-based SPEs cannot be used in combination with high voltage cathode materials such as NMC622, which is essential in order to achieve high energy densities.[14,15,150,151]

In this regard, a tradeoff is established where a low T_g and therefore a high chain mobility provides better ionic conductivity but insufficient mechanical stability for PEO-based SPEs whereas a high T_g affords better mechanical stability, but at the expense of a reduced ionic conductivity. To solve this dilemma, it is necessary to tune both properties independently from each other. For this purpose, block copolymers have demonstrated to be a valuable candidate to overcome this issue by introduction of one PEO-based polar block, as well as a high T_g non-

polar block, such as polystyrene (PS).[32] By self-assembly of these block copolymers, e.g. *via* slow solvent evaporation, phase separated polar and non-polar micro domains are formed, where one domain (usually the polar PEO domain) contributes to the ion transport whereas the other domain (usually the non-polar high T_g domain) provides mechanical stability, hence, when properly balanced, yielding macroscopically solid block copolymer films.[152,153] Here, one of the most studied examples is PS-*b*-PEO (**Scheme 17**) which is synthesized by sequential AP. In 2007 Singh *et al.*[154] for instance reported ionic conductivities of 0.36 mS cm^{-1} at 90 °C and high storage moduli of 10^6 to 10^7 Pa in comparison to 100 Pa for pure PEO. Further, Wang *et al.*[155] in 2003 studied a PS-*b*-(PS-*graft*-PEO)-*b*-PS triblock copolymer (**Scheme 17**) which featured an ionic conductivity of 0.1 mS cm^{-1} at 60 °C, however no rheological or other mechanical data were provided. Zhang *et al.*[156] also studied a PS-*b*-PEO-*b*-PS triblock copolymer (**Scheme 17**) with different polystyrene block lengths. They reported an ionic conductivity of 0.23 mS cm^{-1} at 70 °C for a composition with a decent film forming ability, but no data proving the mechanical stability were provided. Even more, those type of block copolymers were paired with the previously described commercially available methacrylate-based PEO side chain copolymers giving PS-*b*-POEGMA. Here, Rolland *et al.*[147] observed ionic conductivites up to 0.1 mS cm^{-1} at 60 °C and storage moduli up to 10^4 Pa whereas pure POEGMA showed the properties of a free-flowing newtonian fluid.

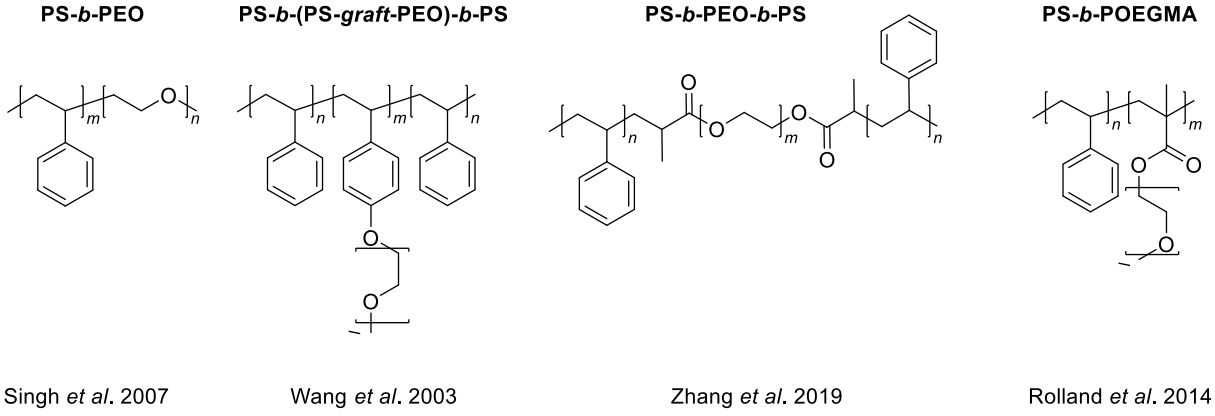

Scheme 17. Structure of selected PEO-based block copolymers as published by Singh *et al.*,[154] Wang *et al.*,[155] Zhang *et al.*[156] and Rolland *et al.*[147]

However, all of the before-mentioned systems suffer from different drawbacks: The synthesis of PS-*b*-PEO, which is prepared by AP, is both tedious and highly dangerous since ethylene oxide gas is used as monomer.[154,157,158] Further, crystallization is still an issue in such linear

PEO block copolymers. Here PS-*b*-POEGMA for instance features a reduced crystallinity due to the side chain approach, however the ester moieties of the methacrylate represents a chemical weak point in terms of thermal and electrochemical stability as well as against nucleophilic impurities.[159,160] All in all, while numerous (block) copolymers of PEO have been studied as PEs for LIBs, all still suffer from at least one particular deficit.

3 Motivation and Goal

As stated before, PEO-based PEs are of great interest due to their typical advantages such as a low T_g, chain flexibility, electrochemical stability against lithium-metal and great solubility for conductive lithium salts. Further, it is readily available and straightforward to use due to its great film forming ability. However, the provided ionic conductivity (especially at room temperature) does not meet the high demands due to its tendency to crystallize. Herein, polymer chemists are able to address this challenge by architectural approaches, inherently reducing the crystallinity within the PEO-based materials by changing its molecular structure; e.g. polymers bearing grafted PEO side chains represent a facile method of overcoming crystallinity issues. Because of being anchored to the polymer backbone, the PEO side chains feature a less pronounced crystallization tendency (**Figure 4a**) resulting in superior ionic conductivity at lower temperatures. Thus, in the frame of the present dissertation such architectural approaches should be explored: Side chain PEO copolymers should be synthesized and subsequently thoroughly analyzed to determine optimal parameters such as side chain length, lithium salt content or grafting density. Furthermore, other architectural approaches should be taken into account, providing a view of the great toolbox of synthetic polymer chemistry.

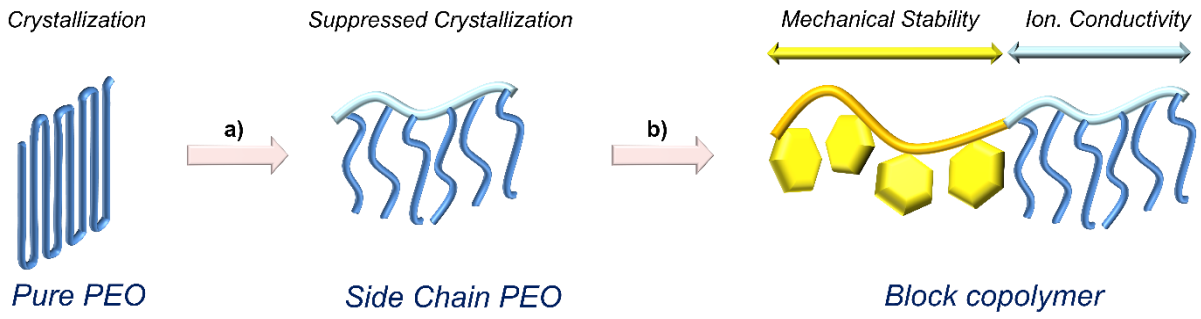

Figure 4. Schematic depiction of the intended concept of the present thesis. **a)** Architectural approaches such as the synthesis of side chain PEO should be followed to reduce the inherent crystallinity. **b)** Further, block copolymers bearing the previously explored PEO side chain polymers and a second block possessing mechanical stability should be introduced, thus providing a possible solution for the mechanical stability/ionic conductivity dilemma.

Moreover, block copolymers have demonstrated their versatility as PEs from a practical point of view. Their inherent property to form a microphase separated morphology on the nanometer scale ensures the decoupling of domains providing mechanical stability from domains guaranteeing ionic conductivity. Thus, they represent one possibility of solving the mechanical stability/ionic conductivity dilemma, as explained in **Chapter 2.7** of this thesis. Combining the

advantage of previously addressed PEO side chain copolymers and block copolymers, respective block copolymers should be synthesized and their corresponding PEs should be characterized by thermal, morphological and electrochemical properties, providing a comprehensive view onto the underlying structure-properties relationships.

4 Results and Discussion

The current chapter provides an insight into the work and achievements of this dissertation. To do so, subchapters each discuss a specific issue in a rounded manner providing the reader with a comprehensive view onto the specific topic. Nonetheless, the different chapters are structured chronologically as well as logically, giving a continuous deeper understanding of PEO-based architectures.

In the first part, vinyl ether-based PEO side chain copolymers were synthesized and thoroughly characterized by thermal and electrochemical means elucidating the influence of side chain length, LiTFSI content and grafting density on the T_g, the crystallinity and the resulting ionic conductivity.

The second chapter arose from the first project and deals with the first report of the PPM of defined functional vinyl ethers that were synthesized by controlled cationic polymerization using a novel single-component initiation and control agent.

The third chapter describes the use of a novel four-arm *cage*-shaped PEO polymer as PE and its thermal and electrochemical characterization, a study that had been conducted jointly with Dr. Martin Gauthier-Jaques, who was responsible for the *cage* polymer synthesis.

The fourth chapter deals with styrene-based PEO side chain block copolymers as PEs. Here, a comprehensive view regarding the synthesis, a brief look onto the ideal side chain length and LiTSFI content, thermal, morphological and electrochemical properties, is provided. Ultimately, it was shown that the provided mechanical stability of this SPEs enables operation in high voltage lithium-metal batteries.

The fifth chapter extends the previous one by elucidating a strategy, that enables to plasticize microphase separated block copolymers without loss of mechanical stability, thus giving an advanced solution for the mechanical stability/ionic conductivity dilemma.

All projects were previously published in peer-reviewed journals by the author (Andreas J. Butzelaar) as disclosed in the beginning of each subchapter.

4.1 A Systematic Study of Vinyl ether-based Poly(ethylene oxide) Side Chain Polymer Electrolytes

As described in **Chapter 2.7**, Itoh et al.[29] described the ionic conductivity of pure vinyl ether-based ethylene oxide side chain homopolymers with $(O\text{-}CH_2\text{-}CH_2)_n$ side chain lengths of n = 3, 6, 10 and 23.5 units, corresponding to a side chain molecular weight of ~ 160, 300, 470 and 1000 g mol^{-1} respectively. They found the highest ionic conductivity when using LiTFSI with a ratio of [Li^+]:[EO] 1:20 and the longest side chain (23.5 units/1000 g mol^{-1}) at temperatures above 20 °C. However, the majority of their employed side chains were relatively short (10 units or less), and they did not use a PEO side chain longer than 23.5 units (1000 g mol^{-1}), although their findings show a clear trend that longer side chains might be beneficial above room temperature.

Therefore, the area of vinyl ether-based PEO side chain structures was expanded in this study in order to draw a comprehensive picture of how different parameters such as PEO side chain length, LiTFSI content and grafting density influence the thermal properties as well as the ionic conductivity of those PEs (**Figure 5**). This provided an important and fundamental understanding of the structure-property relationship that is valuable for various PEO side chain PEs, independent of the nature of their polymer main chain backbone.

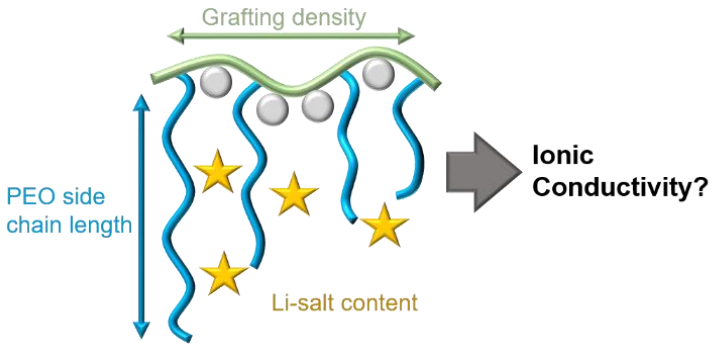

Figure 5. Intended concept: Examination of the influence of PEO side chain length, LiTFSI content and grafting density on the thermal properties as well as the ionic conductivity.

Parts of this chapter and the corresponding parts in the experimental section were adapted with permission from a publication written by the author (Andreas J. Butzelaar).[27]

4.1.1 Synthesis Strategy

Motivated by the previously referenced results of Itoh *et al.*[29] different vinyl ether-based PEO side chain copolymers with different grafting densities were synthesized. In doing so, the focus was laid on side chain lengths above 10 EO repeating units (up to 54 units) since longer side chains showed promising ionic conductivities according to the as-mentioned study. Simultaneously, a relatively low grafting density of 20% ([comonomer]:[PEO side chain] 4:1) was targeted to ensure a significant spatial distance between each PEO side chain, thus possibly suppressing crystallization.

To fulfill this goal, poly(ethylene oxide) methyl ethers (mPEOz; z is hereby defined as the corresponding average molar mass as indicated by the supplier) were used for the synthesis of a series of five different vinyl ether-based copolymers (**polymer** series **Az**; **z** is defined as the molar mass of the corresponding mPEOz) bearing PEO side chains *via* the 'grafting-to' approach described by Gao and Matyjaszewski.[161] For this, a precursor polymer **3** was synthesized by cationic copolymerization of cyclohexyl vinyl ether **1** and diethylene glycol vinyl ether tosylate **2**. Herein, **1** was chosen to ensure a spatial separation of the PEO chains by its bulky cyclohexyl motif while featuring comparable oxidative stability to PEO[17] (**Figure 88**). Afterwards, post-polymerization modification (*PPM*) based on a nucleophilic attack of *in-situ* generated mPEOz-alkoxides was conducted in order to obtain the desired PEO side chain copolymers **4** (see **Scheme 18**).

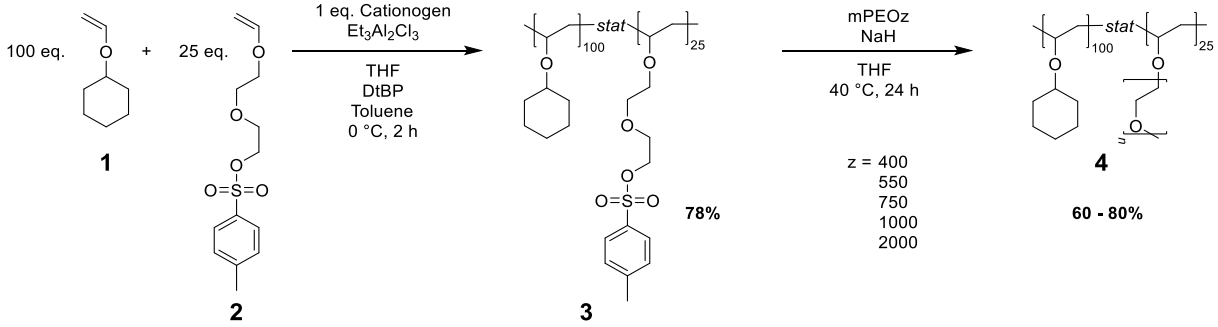

Scheme 18. Route for the synthesis of vinyl ether-based PEO side chain copolymers. Starting from cyclohexyl vinyl ether (**1**) and diethylene glycol vinyl ether tosylate (**2**), a precursor polymer (**3**) was synthesized *via* cationic polymerization using the base-assisted initiating system[162]. Afterwards, this precursor polymer was functionalized using post-polymerization modification *via* nucleophilic substitution with *in-situ* generated mPEO alkoxides yielding the final polymers (**4**). All PPMs featured quantitative conversions.

The successful and quantitative PPM was proven by SEC (exemplary **Figure 6a**, **Table 15**) and ^{1}H-NMR spectroscopy (**Figure 6b**). Here a significant shift of the polymers' molar mass as well as the disappearance of the tosyl (δ = 7.75, 7.32 and 2.45 ppm) and the appearance of the PEO side chains signals (δ = 3.55 and 3.37 ppm) were visible. Further, the thermal properties, as discussed in the following, also supported the successful PPM.

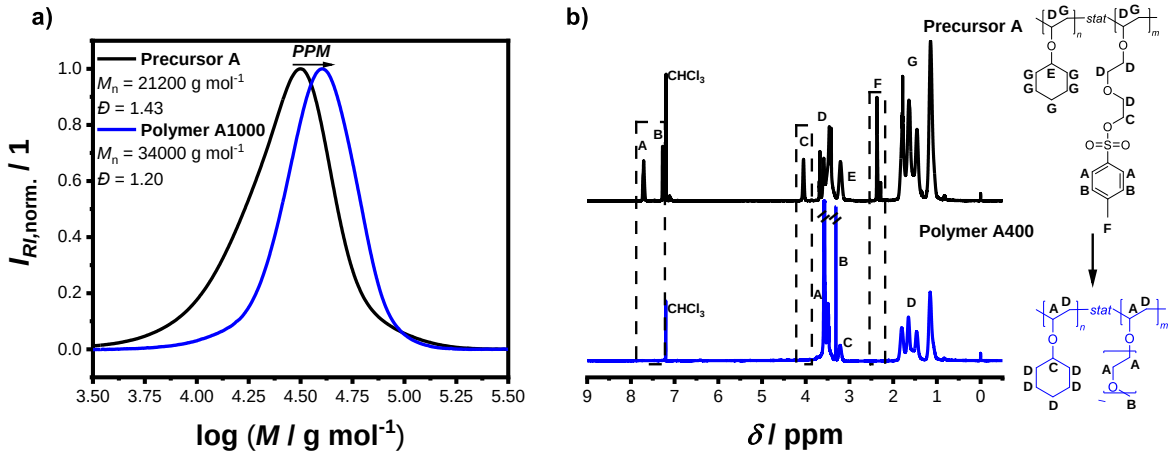

Figure 6. Successful and quantitative post-polymerization modification shown by **a)** SEC (exemplary **polymer A1000**) and **b)** ^{1}H-NMR spectroscopy (exemplary **polymer A400**).

4.1.2 Thermal Characterization

After the successful synthesis of the targeted PEO side chain copolymers, their thermal properties of the PEO side chain vinyl ethers were analyzed *via* DSC and TGA (summary given in **Table 2**). While **precursor A** showed 5% weight loss (T_{d5}) at 190 °C, the functionalized PEO side chain **polymers A400 – A2000** were stable up to T_{d5} ~ 340 °C showing a good thermal stability as wells as proving once more the clean post-polymerization modification (**Figure 7**). Furthermore, the thermal stability after the addition of LiTFSI ([Li^+]:[EO] 1:10) was examined, since this is more representative for the real application of these polymers. Only a negligible shift towards lower decomposition temperatures was observed, most probable due to the decreased T_d of pure LiTFSI (333 °C[163]) as compared to pure **polymers A400 – A2000**.

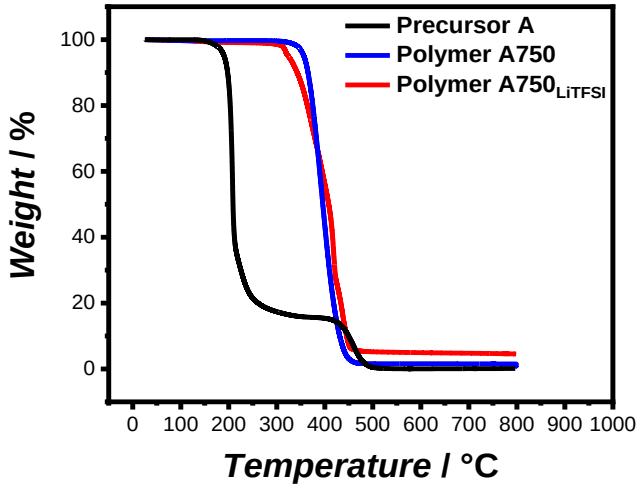

Figure 7. TGA thermograms of the **precursor A** (T_{d5} = 190 °C, black line), **polymer A750** (T_{d5} = 356 °C, blue line) as an example of the PEO side chain copolymers and the polymer electrolyte obtained after blending of **polymer A750** and LiTFSI ([Li^+]:[EO] 1:10; T_{d5} = 328 °C, red line).

Generally, DSC measurements of PEO-based polymer electrolytes are of particular interest since the results are closely related to the ionic conductivity.[164,165] While the precursor **polymer A** had a T_g of around 5 °C, the series of modified **polymers A400 – A2000** showed the usual characteristics of PEO-based materials owing to their semi-crystalline structure (**Table 2**, exemplary **Figure 8**).[166,167] Therefore, regarding their side chain length, a T_g and/or a melting point T_m of the PEO side chains was observed. For polymers bearing shorter PEO side chains (**polymers A400 – A750**) a T_g at around -65 °C was detected, which is in accordance with the typical temperature reported in the literature[168]. However, for longer side chain lengths

(**polymers A1000** and **A2000** corresponding to around 24 & 54 EO repeating units, respectively) a T_g could not be observed under the measuring conditions used, owing to their higher degree of crystallinity. Instead, prominent melting points were detected. It has to be mentioned that although **polymers A400 – A750** featured a T_g, they still featured melting points due to the as-mentioned semi-crystalline structure.

Table 2. Summary of the glass transition temperature T_g, the melting temperature T_m, and the temperature at 5% weight loss T_{d5} with and without added LiTFSI ([Li^+]:[EO] 1:10) for **polymer A400 – 2000** as well as the **precursor A**.

Entry	Polymer	EO units*	T_g [°C]	T_m [°C]	$T_{g\ +\ LiTFSI}$ [°C]	$T_{m\ +\ LiTFSI}$ [°C]	T_{d5} [°C]	$T_{d5\ +\ LiTFSI}$ [°C]
1	**Precursor A**	-	5	n.d.	-	-	190	-
2	**Polymer A400**	11.3	-66	-1	-35	n.d.	350	320
3	**Polymer A550**	15.8	-67	14	-41	n.d.	336	306
4	**Polymer A750**	19.8	-65	27	-40	n.d.	356	328
5	**Polymer A1000**	24.3	n.d.	34	-41	n.d.	346	286
6	**Polymer A2000**	54.0	n.d.	50	-43	n.d.	351	306

n.d. = not detectable, *Calculated by ^{1}H-NMR integration.

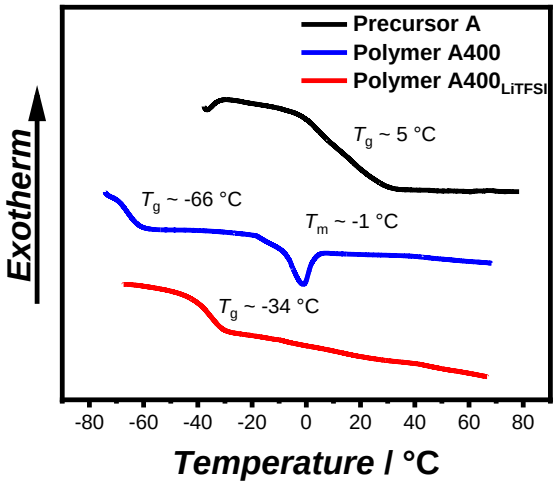

Figure 8. Exemplary depiction of the difference in the thermal behavior before the attachment of PEO side chains (black), after the attachment (blue) and after blending with LiTFSI ([Li^+]:[EO] 1:10, red).

One key point is the fact that EO side chain length, melting point T_m and required energy per mass to melt the crystalline phases ΔH_{melt} (equals to the integral of T_m) are directly correlated. **Polymer A400** with a side chain length of around 11 EO repeating units only showed a barely detectable melting point at around -1 °C. However, with increasing side chain length, the melting point shifted towards higher values while also the peak integral (ΔH_{melt}) increased (**Figure 9a** and **b**). Since ΔH_{melt} is directly correlated to the degree of crystallinity, the reduction of the latter in comparison to pure PEO (196.4 J g^{-1})[169] could be calculated (**Figure 9b**). It is remarkable that **polymer A400** showed a reduction in crystallinity of around 98%, while a reduction of around 81% was found for **polymer A550**. Interestingly, even **polymer A2000**, which contained around 54 EO repeating units, still featured a remarkable reduction in crystallinity of 48%. Overall, these results showed the successful approach of side chain architectures in order to reduce the crystallinity of such PEO-based materials by a significant degree.

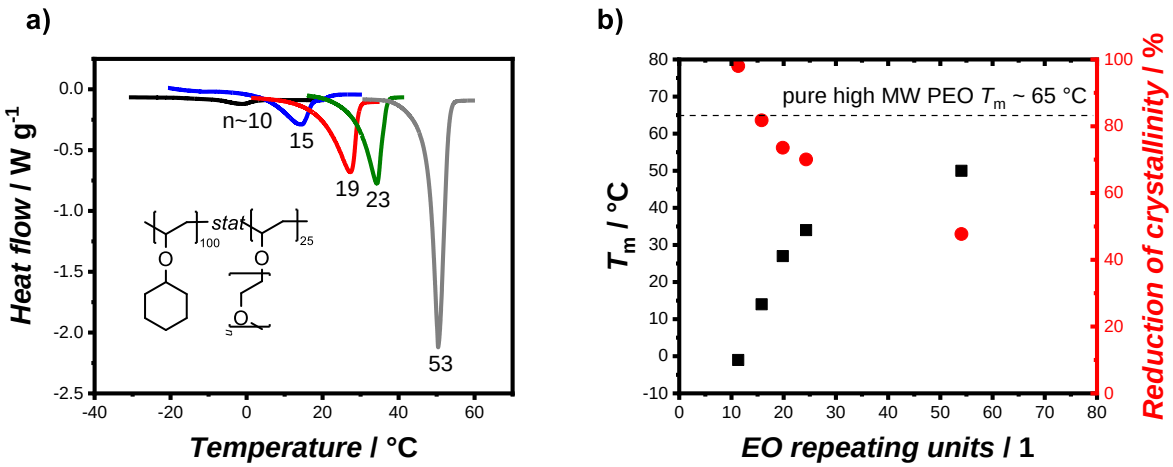

Figure 9. a) Depiction of the increasing value as well as the area of the melting points T_m of the polymers bearing different PEO side chain lengths. **b)** Development of the melting points with increasing side chain length and corresponding percental reduction of crystallinity in comparison to pure PEO (see also **Table 22**).

Additionally, the thermal behavior of the polymer materials after mixing with LiTFSI was examined. As shown in **Table 2**, the polymer electrolytes did not show any melting point after mixing with LiTFSI in a ratio of [Li^+]:[EO] of 1:10. Instead, they featured a glass transition temperature that was shifted to higher temperatures in comparison to the pure materials. Both effects, the reduction in crystallinity as well as the shift of the T_g, are typical for blends of PEO-based materials with LiTFSI.[170] On the one hand, this is caused by the so-called *quasi-ionic*

cross-linking, which describes the physical linking of different PEO chains by polar interaction originating from the coordination of lithium ions, thus decreasing mobility and therefore increasing the T_g. On the other hand, the *quasi-ionic cross-linking* and the bulky $TFSI^-$ anion are suppressing crystallization of PEO chains by hindering their alignment. Generally, as reported in literature,[29,148] especially short PEO side chains suffer from a huge increase in the glass transition temperature after mixing with lithium salts, probably due to the higher number of *inter chain* cross-links in comparison to *intra chain* cross-links. Since the shortest side chain used in this work already consists of around 11 EO repeating units, this effect was not very prominent, but yet **polymer A400** showed a noticeable higher T_g than the longer polymer derivatives **A550 – A2000** (**Table 2**).

Furthermore, **polymer A1000** (average PEO side chain length within **polymer** series **A**) was chosen to be candidate to present the influence of LiTFSI concentration onto the glass transition temperature (**Figure 10**). Four different blends employing $[Li^+]$:[EO] ratios of 1:5, 1:10, 1:15 and 1:20 were prepared and DSC measurements were conducted. All four ratios were sufficient in completely suppressing the crystallization of PEO side chains, while the corresponding T_g increased nearly linearly with increasing LiTFSI concentration from -51 °C ($[Li^+]$:[EO] = 1:20) up to -33 °C ($[Li^+]$:[EO] = 1:5). This can be explained by the fact that the number of *quasi-ionic cross-linking* points increases with each added lithium ion up to a saturation limit where each oxygen atom already coordinates to one Li^+ ion.

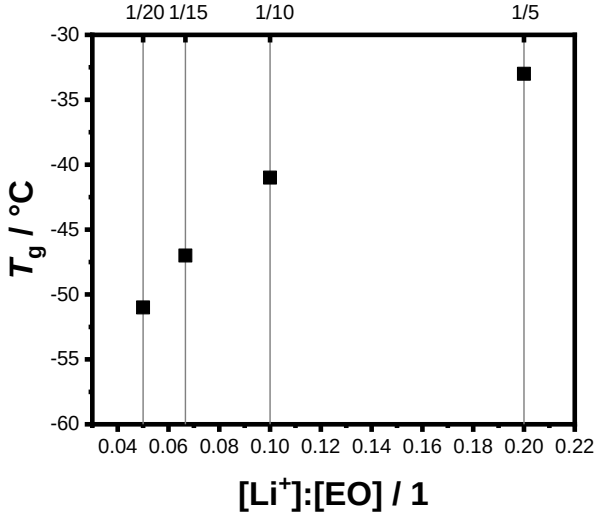

Figure 10. Dependency of the glass transition temperature T_g of **polymer A1000** on different $[Li^+]$:[EO] ratios. The nearly linear trend can be explained by the direct correlation of lithium ions and *quasi-ionic cross-linking* points.

4.1.3 Ionic Conductivity

After thoroughly examining the thermal properties, the ionic conductivity was studied and the relationship between both properties was elaborated in great detail. Thus, temperature-dependent electrochemical impedance spectroscopy (EIS) was conducted to elucidate the impact of the PEO side chain length and the LiTFSI salt content on the ionic conductivity. In this regard each **polymer A400 – A2000** was used to obtain four different polymer electrolytes featuring [Li^+]:[EO] ratios of 1:5, 1:10, 1:15 and 1:20, respectively. All ionic conductivity plots comprising the different LiTFSI ratios are shown in **Figure 11**.

As generally known for PEO-based polymer electrolytes, a strong dependency of the LiTFSI content on the ionic conductivity was observed, reflecting trends that were already discussed for the evaluation of the DSC data. As shown in **Figure 9d**, high contents of Li^+ ions lead to a high number of *quasi-ionic cross-linking* points, thus reduce the side chains mobility resulting in a high T_g. However, low T_g values are generally preferred, since segmental motion of PEO chains significantly assist ion transport in such materials and consequently the value of T_g can be used as an indication of the (side) chain mobility.[171,172] In addition, very high amounts of Li^+ ions hinder ion transport *via inter*/*intra-chain hopping*[17,173] since most oxygen atoms are already occupied limiting the free volume. As a result, the highest LiTFSI content of [Li^+]:[EO] of 1:5 lead to the lowest ionic conductivity (~ 10^{-3} mS cm^{-1} and lower at 20 °C) among all polymers studied being one order of magnitude lower in comparison to lower contents (~ 10^{-2} mS cm^{-1} at 20 °C), respectively (**Figure 11a – 11e**).

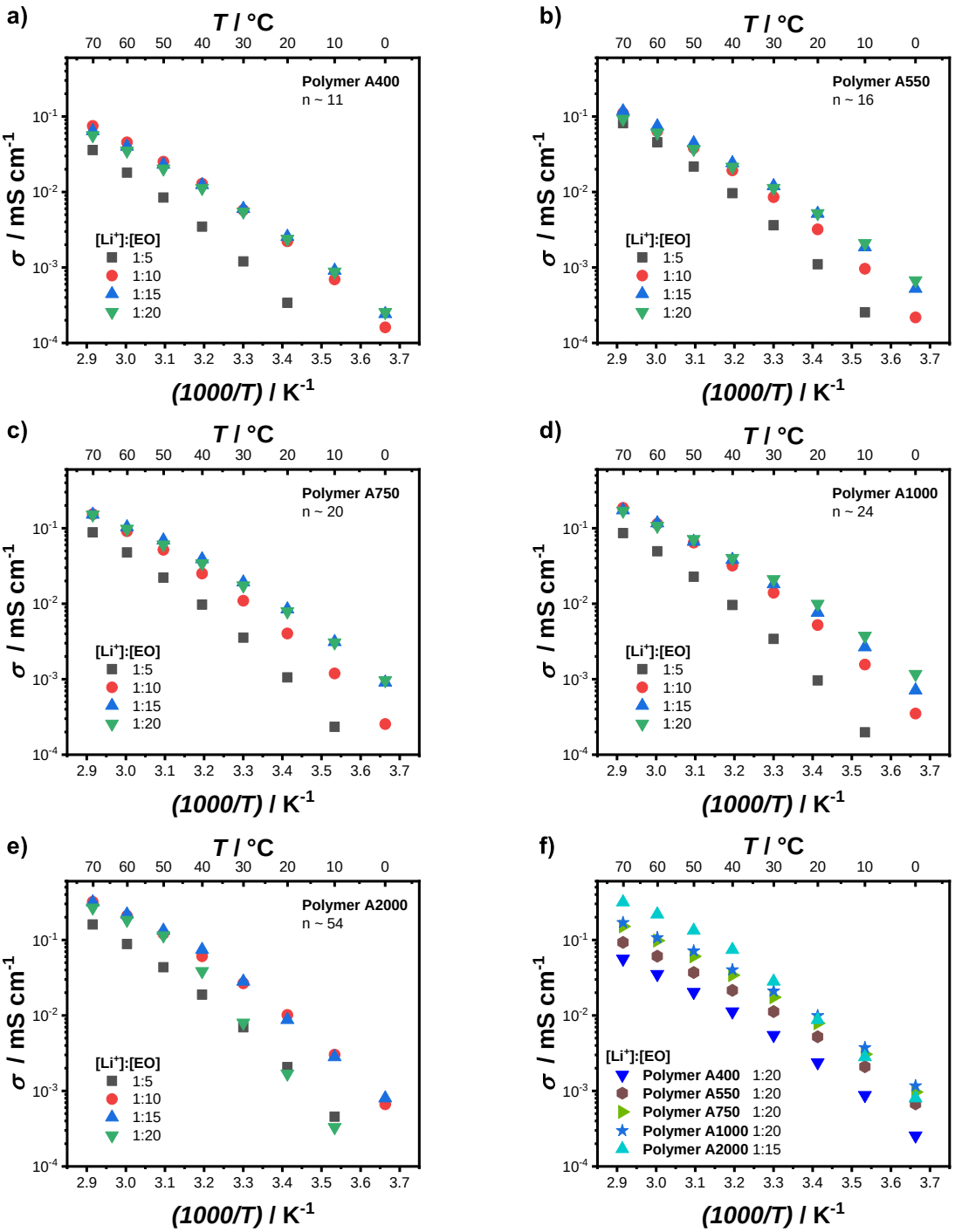

Figure 11. a) – e) Temperature-dependent ionic conductivity derived from EIS measurements of the copolymer systems bearing different PEO side chain lengths. The LiTFSI content was varied with respect to EO units. **f)** Depiction of the best performing polymer:LiTFSI combinations (1:20 for **polymers A400 – A1000** and 1:15 for **polymer A2000**).

It has to be further considered that there are several parameters which influence the ionic conductivity of PEs in different ways analogous to the impact on the thermal properties. It is well known that the $TFSI^-$ anion decreases the crystallinity as well as the T_g due to its bulky structure, thus acting as plasticizer and therefore having a positive impact on the ionic

conductivity.[174] However, since LiTFSI is introduced as a salt, the number of Li^+ ions is equivalent to the number of $TFSI^-$ anions and since the Li^+ ions drastically increase the T_g (*quasi-ionic cross-linking*), the total amount of LiTFSI has to be adjusted carefully. Furthermore, longer PEO side chain lengths increase the crystallinity as result of chain alignment in the pure polymer, but also decrease the T_g showing higher side chain mobility as discussed previously for the DSC data (**Table 2** and **Figure 9**). The combined effects of these different parameters are reflected in the ionic conductivity behavior. **Polymers A400 – A1000** (*i.e.* polymers with a side chain length of up to 24 EO repeating units) exhibited the highest ionic conductivity with a low content of LiTFSI of 1:20 in comparison to higher amounts, since the crystallinity was already drastically reduced by the side chain architecture and the drawback of using more Li^+ ions outweighed the positive influence of the $TFSI^-$ anion (**Figure 11a-d**). On the contrary, **polymer A2000** bearing the longest PEO side chain showed that the ionic conductivity at $[Li^+]$:[EO] of 1:20 suffered from a significant drop below 40 °C due to a beginning partial crystallization (**Figure 11e**). Since the increasing side chain length also increased the chain alignment and therefore the crystallinity, a higher LiTFSI content of 1:15 was beneficial due to the absent of crystallinity caused by the additional $TFSI^-$ anions. This general trend is summarized in **Table 3**.

Table 3. Influence of the PEO side chain length, Li^+ and $TFSI^-$ ions onto the crystallinity/chain alignment tendency, the T_g as well as the ionic condcuctivity.

Entry	Influence	Effect	Crystallinity/Chain alignment	T_g	Ion. conductivity
1	**Increasing side chain length**		↑	↓	Temperature-dependent
2	**$TFSI^-$**	Plasticizer	↓	↓	↑
3	**Li^+**	Quasi-ionic cross-linking	(↓)	↑↑	↓

When comparing the highest obtained ionic conductivity for **polymers A400 – A1000**, longer side chains perform better (24 > 20 > 16 > 11 units, corresponding to a factor of 3-5 between 24 and 11 units) at all measured temperatures as shown in **Figure 11f** and more precisely in **Figure 12**. However, when comparing **polymer A1000** (24 units) with **polymer A2000** (54 units), it is noticeable that a tradeoff between the ionic conductivity at higher and lower temperatures is established. While the longer side chain (54 units) showed a higher ionic conductivity at higher temperatures (30 °C and above; e.g. 7.4×10^{-2} mS cm^{-1} *vs.*

4.0×10^{-2} mS cm^{-1} at 40 °C), the shorter side chain (24 units) resulted in superior ionic conductivity at lower temperatures (20 °C and below; e.g. 1.2×10^{-3} mS cm^{-1} *vs.* 0.8×10^{-3} mS cm^{-1} at 0 °C). This effect can be explained by the previously described circumstances that the suppression of crystallization and the influence on the T_g cannot be addressed individually. Therefore, polymers with shorter side chains show a well-suppressed chain alignment enabling superior ionic conductivity at lower temperatures, but the disadvantage regarding their T_g and thus their low side chain mobility results in lower ionic conductivities at higher temperatures, where suppression of chain alignment does not play any role. Further, polymers with longer side chains show a lower T_g (higher side chain mobility) and thus featuring higher ionic conductivity at higher temperatures, but their lack in suppression of chain alignment results in comparable lower ionic conductivities at lower temperatures.

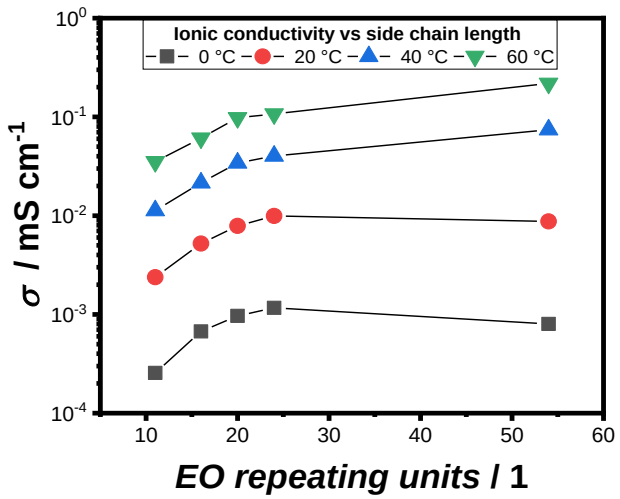

Figure 12. Depiction of the ionic conductivity with respect to EO side chain length for the different **polymers A400 – A2000**. The best performing [LiTFSI]:[EO] ratio taken from **Figure 11f** is displayed. For polymers with side chains of 24 repeating units and less, a longer side chain is preferable at each measured temperature. This changes in the transition from 24 to 54 repeating units. At 30 °C and higher the longer side chain shows a higher ionic conductivity, while at temperatures below 30 °C shorter side chains show higher ionic conductivity.

4.1.4 Influence of the Grafting Density

In the next step, the view onto the relationship between different side chain lengths, lithium salt content, thermal properties and ionic conductivity was expanded with respect to the grafing density. Therefore, statistical copolymers with a grafting density of 50% (**polymer** series **B**; **Scheme 19**, **Table 16**) were synthesized for comparability with **polymers A400 – A2000**, which featured a grafting density of 20%. While doing so, the focus was set on the shortest (~ 11 EO units) and the longest side chains (24 and 54 EO units) as wells as $[Li^+]$:[EO] ratios of 1:15 and 1:20 for the EIS measurements as a consequence of the previously discussed results.

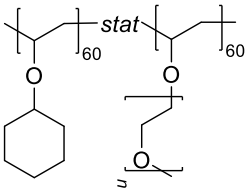

Polymer B400 n ~ 11
Polymer B1000 n ~ 24
Polymer B2000 n ~ 54

Scheme 19. Three statistical copolymers **(polymers B400 – B2000**) were synthesized featuring a higher grafting density (monomer ratio 1:1; grafting density 50%) in comparison to **polymers A400 – A2000** (monomer ratio 4:1; grafting density 20%).

Table 4. Overview of the three different synthesized copolymers featuring a grafting density of 50%. T_g and T_m were obtained by DSC measurements. Samples with added LiTFSI featured a $[Li^+]$:[EO] ratio of 1:10.

Entry	Polymer	EO units*	T_g [°C]	T_m [°C]	$T_{g\ +\ LiTFSI}$ [°C]	$T_{m\ +\ LiTFSI}$ [°C]
1	**Polymer B400**	11.7	n.d.	9	-42	n.d.
2	**Polymer B1000**	25.2	n.d.	39	-42	n.d.
3	**Polymer B2000**	52.2	n.d.	53	-44	n.d.

*Calculated by ^{1}H-NMR integrals (difference to **polymer** series **A** within the error), n.d. = not detectable.

When comparing the DSC results of **polymer** series **B** (**Table 4**) with series **A** (**Table 2**), it became obvious that a higher grafting density resulted in a higher melting point (10, 5 and 3 °C increase for **polymers B400**, **B1000** and **B2000**, respectively) going hand in hand with a higher degree of crystallinity (**Table 22**). Still, **polymers B400**, **B1000** and **B2000** featured remarkable reductions in crystallinity of 75, 51 and 39% in comparison to pure PEO, respectively (**Figure**

13a). However, at the same time, the T_g of **polymers B400**, **B1000** and **B2000** after mixing with LiTFSI was noticeable lower for each polymer (**Table 4**) in comparison to their counterparts featuring lower grafting densities (**Table 2**; also summarized in **Table 5**). Furthermore, different amounts of LiTFSI were mixed with **polymer B1000** analogously to its counterpart **polymer A1000** revealing a lower T_g for each composition (**Figure 13b**). All these phenomena are direct results of the higher grafting density. Since there are more chains present and the distance between the chains is decreased in polymers with higher grafting densities, crystallization occurs more readily. Moreover, there are also more side chains per main chain, resulting in smaller number of chains taking part in the *inter chain quasi-ionic cross-linking* by Li^+ ions and thus lowering the T_g.

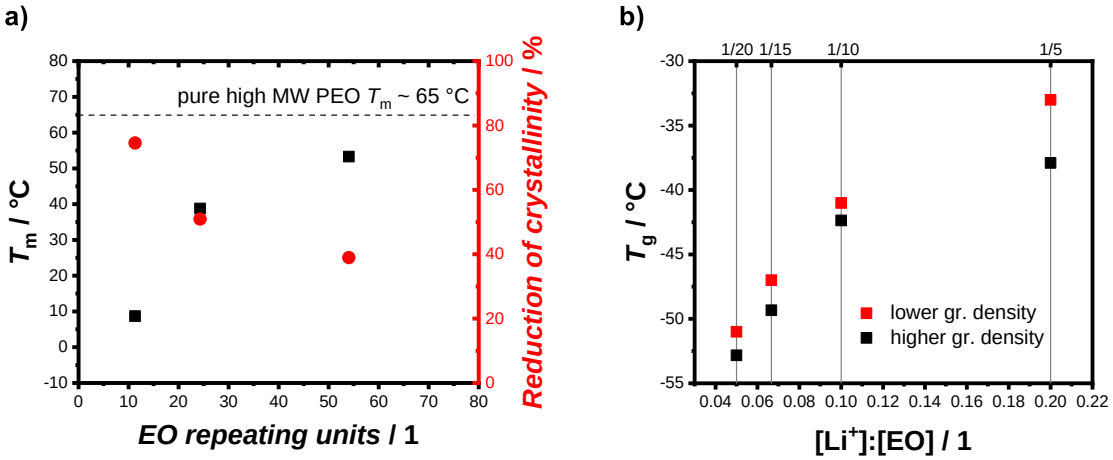

Figure 13. a) Development of the melting points of **polymer B400** – **B2000** with increasing side chain length and corresponding percental reduction of crystallinity in comparison to pure PEO. **b)** Dependency of the T_g of **polymer B1000** in regard to different [Li^+]:[EO] ratios. As comparison the T_g of **polymer A1000** (see also **Figure 10**), which features the same side chain length but a lower grafting density, is shown.

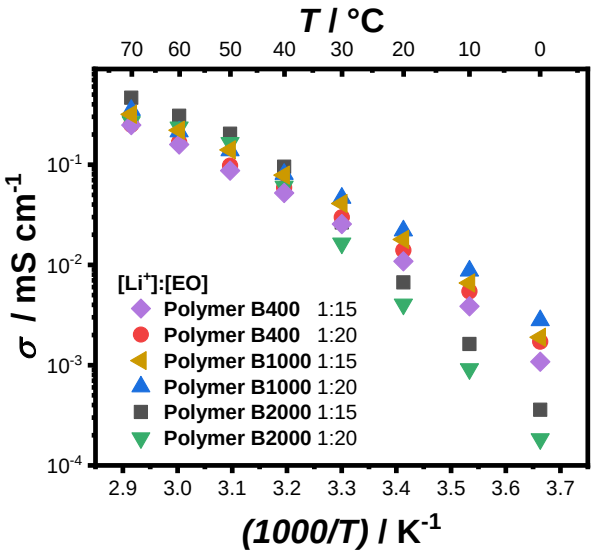

Figure 14. Temperature-dependent ionic conductivity derived from EIS measurements of **polymer B400 – B2000** comprising [Li^+]:[EO] ratios of 1:15 and 1:20.

As already stated for the discussion of the ionic conductivities of **polymers A400 – A2000**, the DSC results of **polymers B400 – B2000** are in line with the results of the EIS measurements (**Figure 14**, **Figure 15** and **Table 5**). Although, the initial suppression of crystallization by the side chain architecture was lower for copolymers featuring a higher grafting density in comparison to the copolymers featuring a lower grafting density (**Table 5**), it was still sufficient to suppress crystallization in combination with added LiTFSI for **polymers B400** and **B1000** (11 and 24 EO repeating units). At the same time, a lower T_g was observed resulting in higher chain mobility and thus in higher ionic conductivities at all measured temperatures in comparison to **polymers A400** and **A1000**, respectively (**Figure 15** and **Table 5**). For **polymer B2000** the trend of a temperature-dependent tradeoff, which was already observed for its counterpart **polymer A2000,** continued. Here, the higher grafting density resulted once more in a reduced suppression of chain alignment but a slightly lower T_g, which consequently led to an even greater tradeoff between high and low temperatures (**Figure 15** and **Table 5**). When summarizing these findings, it can be stated that an increasing grafting density results in the same effect as increasing side chain length.

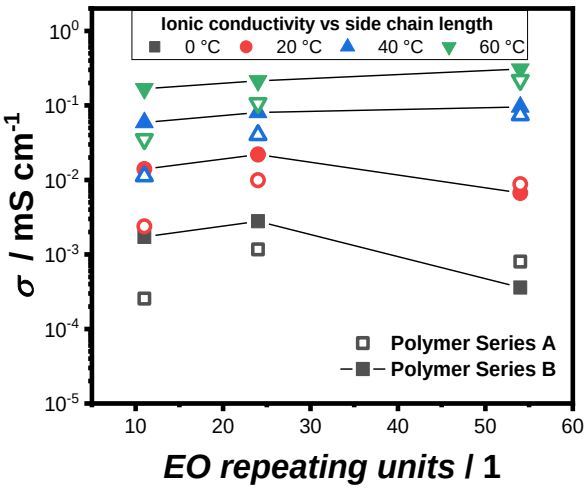

Figure 15. Depiction of the ionic conductivity with respect to EO side chain length for the different **polymers B400 – B2000** (—■—). The best performing [LiTFSI]:[EO] ratio taken from **Figure 14** is displayed (**B400** & **B1000**: [Li]:[EO] 1:20; **B2000**: [Li]:[EO] 1:15) . As comparison the ionic conductivity of **polymers A400**, **A1000** and **A2000** (□) comprising the same lithium salt contents (taken from **Figure 12**) is shown.

Table 5. Summarizing comparison of the reduction of the crystallinity (RC) of the copolymers relative to pure PEO, the T_g ([Li^+]:[EO] ratio 1:10) of the polymer electrolyte and the ionic conductivity at 0 as wells as 60 °C.

Entry	Polymer	RC [%]	$T_{g\ +\ LiTFSI}$ [°C]	$\sigma_{0°C}$* [mS cm^{-1}]	$\sigma_{60°C}$* [mS cm^{-1}]
1	**Polymer A400**	98	-35	0.26×10^{-3}	0.35×10^{-2}
2	**Polymer B400**	75	-42	1.72×10^{-3}	1.67×10^{-1}
3	**Polymer A1000**	70	-41	1.17×10^{-3}	1.07×10^{-1}
4	**Polymer B1000**	50	-42	2.79×10^{-3}	2.14×10^{-1}
5	**Polymer A2000**	48	-43	0.80×10^{-3}	2.19×10^{-1}
6	**Polymer B2000**	39	-44	0.36×10^{-3}	3.07×10^{-1}

*Taken from **Figure 15**

4.1.5 Recapitulation

A series of different vinyl ether-based PEO side chain copolymers was synthesized and the corresponding polymer electrolytes featuring different PEO side chain lengths, different grafting densities and varying LiTFSI salt contents were studied. Consequently, a detailed picture of the influence of these different parameters on the thermal behavior and the ionic conductivity was drawn. Herein, it was shown that the PEO side chain approach is capable of reducing the degree of crystallinity of PEO phases dramatically, ranging from a reduction by 98% (**polymer A400**) to 39% (**polymer B2000**) in comparison to pure PEO. Furthermore, it was precisely described that copolymers bearing longer PEO side chains and higher grafting densities showed higher crystallization tendencies but lower T_gs. Also, the addition of LiTFSI reduced the crystallization due to the $TFSI^-$ anion acting as plasticizer, while the Li^+ cations increased the T_g as a result of *quasi-ionic cross-linking* of PEO chains. When summing up all these effects, it is obvious that each parameter has positive and negative influences on the thermal behavior. Since this is directly reflected in the ionic conductivity, a 'sweet spot' has to be found in order to minimize chain alignment, while at the same time maintaining a low T_g. However, this seems to be only partially possible, because at one point a tradeoff between high and low temperature ionic conductivity is established. Consequently, the best achieved ionic conductivity at room temperature (20 °C) was 2.19×10^{-2} mS cm^{-1} using **polymer B1000** (50% grafting density, 24 units side chain) and a [LiTFSI]:[EO] ratio of 1:20, while at 60 °C **polymer B2000 (**50% grafting density, 54 units side chain) showed the best results (3.07×10^{-1} mS cm^{-1}) when employing a [LiTFSI]:[EO] ratio of 1:15. Overall, a fundamental and detailed view of the strong relationship between structure and ionic conductivity was provided, thus acting as guidance for future studies on PEO-based side chain architectures for application as solid polymer electrolytes within this dissertation.

4.2 Synthesis and Post-Polymerization Modification of Defined Functional Poly(vinyl ether)s

This project originated as a side project of the first one. Since the vinyl ethers used in **Chapter 4.1** were polymerized by CP, different systems to do so were evaluated. In this regard, the novel single-component initiation and control system[48] described in **Chapter 2.1.1** was examined, but it was not possible to control the vinyl ether systems employed in **Chapter 4.1**. Nonetheless, the system generally displayed a facile method for the synthesis of poly(vinyl ether)s. Because the latter as electron rich monomers are typically polymerized by CP (as explained in **Chapter 2.1**) pendant side groups featuring isolated C=C double or C≡C triple bonds do not interfere with the CP itself in comparison to radical side reactions in RP.[38] Yet, it is surprising to note that until now not many studies of PPM of poly(vinyl ether)s bearing functional groups consisting of C=C double or C≡C triple bonds have been reported. This might be due to the general requirements of CCPs such as highly purified and dried reactants and solvents, the demand for a perfectly inert atmosphere and usually low reaction temperatures, as previously described.[175–177] Additionally, the limited scope of commercially available vinyl ethers is possibly also a consequence of their rare use in PPMs and vice versa. Therefore, the straightforward CP using PMCCP displayed an intriguing method as it allows for unprecedented PPMs of poly(vinyl ether)s. Thus, a series of four different functionalized vinyl ethers was synthesized and their polymerization and subsequent modification was investigated in order to provide a fundamental insight into the synthesis of functional poly(vinyl ether)s to broaden potential application areas of this polymer class (**Figure 16**)

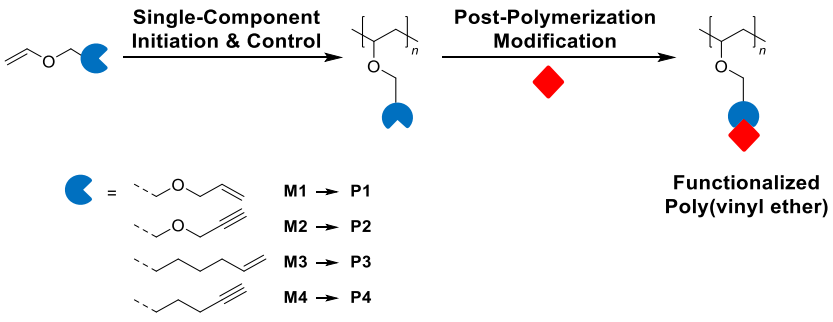

Figure 16. Strategy for the synthesis of functional poly(vinyl ether)s **P1** – **P4** bearing C=C double- or C≡C triple-bonds and their subsequent post-polymerization modification *via click* chemistry.

Parts of this chapter and the corresponding parts in the experimental section were adapted with permission from a publication written by the author (Andreas J. Butzelaar).[178]

4.2.1 Monomer Synthesis

In order to combine the novel single-component initiation system by Kottisch *et al.*[48] using PMCCP with the prominent and highly efficient *thiol-ene/-yne* and CuAAC reactions for PPMs, two types of monomer classes bearing pendant C=C double or C≡C triple bonds, respectively, were investigated. Both functional groups were linked either by an alkyl spacer or an ethyleneglycol spacer to the vinyl ether monomer to investigate the potential influence of the spacer on the polymerization and subsequent PPM.

Monomer **M1** and **M2** were synthesized by nucleophilic substitution employing deprotonated ethylene glycol vinyl ether and allyl bromide or propargyl bromide, respectively (**Scheme 20**). Monomer **M3** and **M4** were synthesized from tosylated tetramethylene glycol vinyl ether using either an *in-situ* generated organocuprate (monomer **M3**) derived from allyl magnesium bromide and copper(I) bromide or with lithium acetylide (monomer **M4**) (see **Chapter 6.4** for synthesis details).

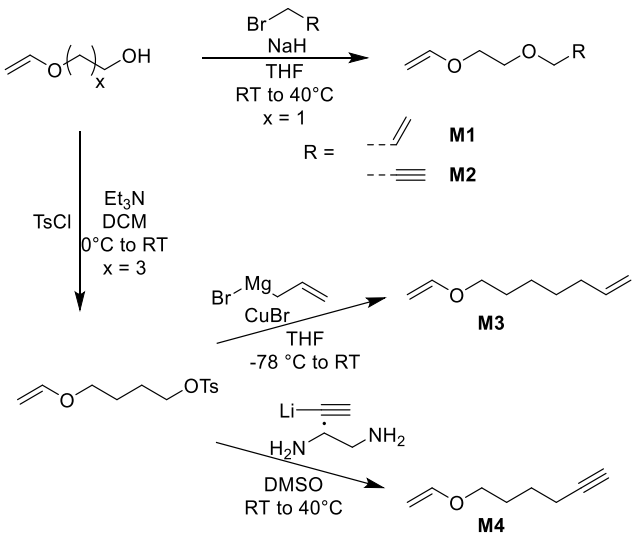

Scheme 20. Synthesis of functional vinyl ether monomers **M1 – M4** bearing either C=C double or C≡C triple bonds starting from ethylene glycol vinyl ether (x = 1) or tetramethylene (x = 3) glycol vinyl ether.

4.2.2 Controlled Cationic Polymerization

After the successful synthesis of the functional monomers, their cationic polymerization using PMCCP as single-component initiator and control agent was studied. Herein, for each monomer three polymerizations yielding polymers with targeted degrees of polymerization (DP) of 25, 50 and 100 were conducted in order to show the controlled character of the polymerization. In general, the targeted molar masses were reached in most cases within the tolerance of the molar mass determination by SEC while maintaining low dispersities (**Table 6,** exemplary **Figure 17a**). Further, all functional groups remained untouched as proven by ^{1}H-NMR spectroscopy (exemplary **Figure 17b**; **Figure 69 – Figure 72**).

Table 6. Overview of the polymerizations of the different **monomers 1 – 4** using PMCCP as single-component initiator and control agent.

Entry	Monomer	Eq.	Atmosphere	Time [h]	$M_{n,theo}$[§] [g mol^{-1}]	$M_{n,exp}$[*] [g mol^{-1}]	$Đ$[*] [1]
1	**M1**	25	Air	2	3200	3400	1.25
2	**M1**	50	Air	2	6400	5700	1.14
3	**M1**	100	Air	3	12800	3700	1.56
4	**M1**	100	N_2	3	12800	7500[#]	1.33
5	**M2**	25	Air	1	3150	4000	1.16
6	**M2**	50	Air	2	6300	7100	1.19
7	**M2**	100	Air	3	12600	5100	1.45
8	**M2**	100	N_2	3	12600	11000	1.36
9	**M3**	25	Air	3	3500	3000	1.07
10	**M3**	50	Air	3	7000	5200	1.06
11	**M3**	100	Air	6	14000	10500	1.11
12	**M4**	25	Air	3	3100	3000	1.07
13	**M4**	50	Air	4	6200	6000	1.05
14	**M4**	100	Air	8	12400	9800	1.10

*Determined by SEC with PMMA standards. [#]M_p = 11700 g mol^{-1} (Showing that in principle the targeted molar mass is reached, but the broad dispersity results in a comparably low M_n) [§]$M_{n,theo}$ = M(monomer) × eq.

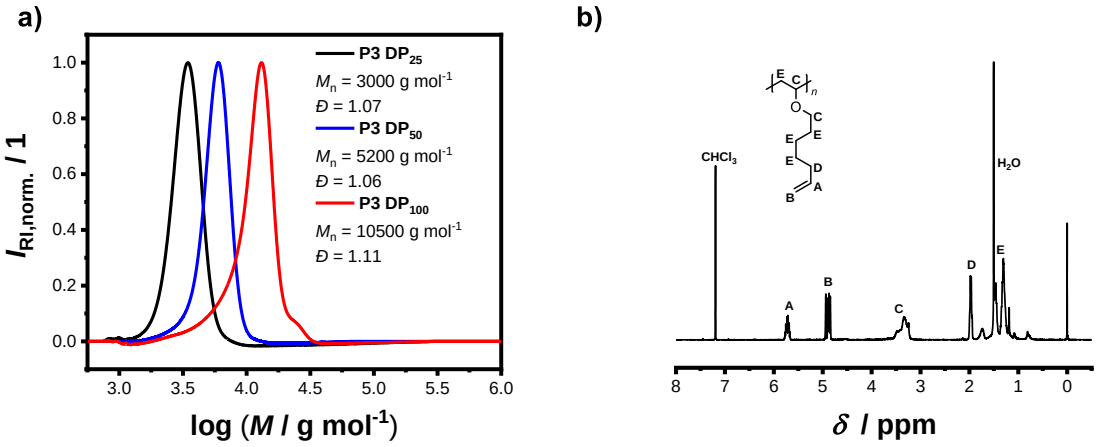

Figure 17. a) SEC traces of the polymerization of monomer **M3** targeting DPs of 25, 50 and 100 using PMCCP as single-component initiator and control agent. **b)** ^{1}H-NMR of polymer **P3** (DP_{50}) proving the intact vinyl group after polymerization.

However, several trends were observed: Within each polymer series, polymers with the largest DP = 100 exhibited the highest dispersity. This is most probably due to the prolonged reaction time and less PMCCP present, which increased the chance for side reactions. Nevertheless, it appeared that the monomers without an additional oxygen atom in the spacer (*i.e.* monomer **M3** and **M4**) allowed for a better control over the polymerization in comparison to the ones with an additional oxygen atom in the spacer (*i.e.* monomer **M1** and **M2**). This becomes obvious when comparing the dispersities of the respective polymers **P3** and **P4** ($Đ$ = 1.05 – 1.11) with polymers **P1** and **P2** ($Đ$ = 1.14 – 1.36) and is further supported by the fact that it was not possible to synthesize polymers **P1** and **P2** with a DP of 100 in a controlled manner without changing the atmosphere to nitrogen (**Figure 18a**; **Table 6 entry 3/4** and **7/8**), while the polymerization of monomers **M3** and **M4** did not suffer from this issue under ambient conditions. Furthermore, it was noticed that polymerizations conducted under air atmosphere resulted in polymers with broader distributions when the atmosphere was frequently changed, for example by removing the lid of the reaction vessel during polymerization (**Figure 18b**). It therefore seems on the one hand that the PMCCP system can handle a certain amount of air, but not an unlimited exposure to ambient air. On the other hand, the control over the polymerization is apparently suffering if additional oxygen atoms are present in the monomer structure, probably due to an interaction of the second oxygen with the transition state complex,[48] thus weakening the interaction with the vinyl ether oxygen, or an overall higher polarity of the monomer. Both effects result in more possibilities for side reactions to take place therefore eventually increasing the dispersity. This outcome is also in accordance with the

observation that PEO-based vinyl ethers of **Chapter 4.1** could not be polymerized with this system. Nonetheless, a straightforward polymerization of functional vinyl ethers could be successfully realized under air atmosphere in most cases.

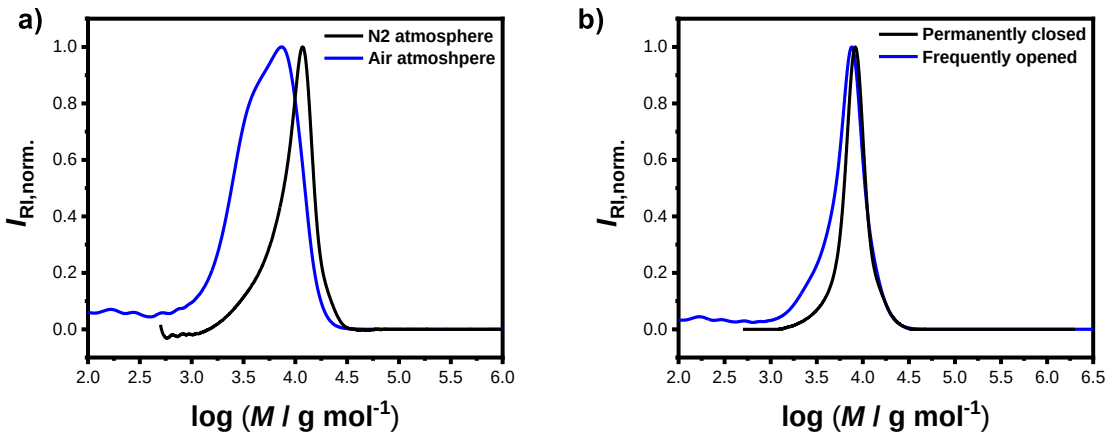

Figure 18. a) Comparison of the polymerization results of **M1** targeting a DP of 100 under air (blue) and nitrogen (black) atmosphere. **b)** SEC results of the polymerization of **M2** targeting a DP of 50 where the vial was opened frequently (blue) or kept closed (black).

In addition, an exemplary kinetic study of the polymerization was conducted using monomer **M2** in order to further investigate its controlled character. For a controlled or 'living' polymerization a linear increase of ln([M]$_0$/[M]) with time as well as a linear correlation of the molar mass M_n and the conversion is characteristic.[177,179,180] As shown in **Figure 19a** and **b** both characteristics were fulfilled proving the first order kinetics of the polymerization as well as the linear increase of M_n with conversion, in accordance with the theoretically expected values of M_n. Therefore, it can be stated that side reactions are well suppressed and that a living character of the polymerization can be assumed for the functional vinyl ethers **M1** – **M4** in analogy to the alkyl vinyl ethers described by Kottisch *et al.*[48]

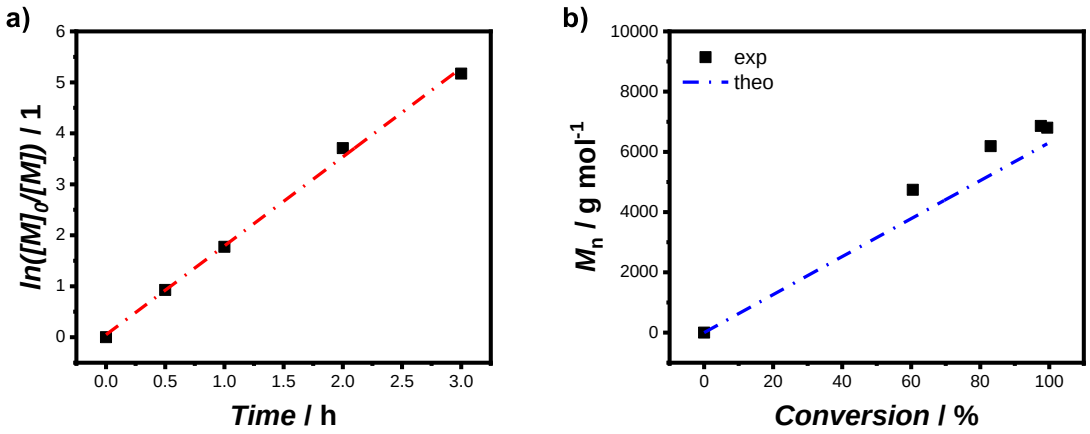

Figure 19. a) Kinetic study of monomer **M2** (DP = 50) proving the controlled character of the reaction by the linear development of ln([M]$_0$/[M]) vs time as well as **b)** the linear development of the molar mass M_n with conversion, which is in good agreement with the theoretically calculated development.

4.2.3 Post-Polymerization Modification

Next, the synthesized polymers **P1** – **P4** with a DP of 50 were used for a subsequent post-polymerization modification *via thiol-ene* reaction of **P1** and **P3**, or *thiol-yne* and CuAAC reaction of **P2** and **P4**. Herein, *thiol-ene* reactions of the vinyl groups in **P1** and **P3** were conducted using three different substrates, *i.e.* 1-dodecanethiol (DDT), 4-*tert*-butylbenzylthiol (TBBT) and mercaptoethanol (ME). The alkyne group containing polymers **P2** and **P4** were functionalized using DDT and TBBT for *thiol-yne* reactions as well as benzyl azide (BzN_3) for the CuAAC reaction (**Table 7**).

Table 7. Overview of the post-polymerization modification reactions of polymers **P1** – **P4**.

Entry	Polymer	PPM	Reactant	$M_{n,before}$* [g mol^{-1}]	$Đ_{before}$* [1]	$M_{n,after}$* [g mol^{-1}]	$Đ_{after}$* [1]
1	**P1**	Thiol-ene	DDT	5700	1.14	14600	1.13
2	**P1**	Thiol-ene	TBBT	5700	1.14	10100	1.14
3	**P1**	Thiol-ene	ME	5700	1.14	7400	1.12
4	**P2**	Thiol-yne	DDT	7100	1.19	19200	1.22
5	**P2**	Thiol-yne	TBBT	7100	1.19	15500	1.33
6	**P2**	CuAAC	BzN_3	7100	1.19	9900	1.11
7	**P3**	Thiol-ene	DDT	5200	1.06	10500	1.07
8	**P3**	Thiol-ene	TBBT	5200	1.06	8700	1.07
9	**P3**	Thiol-ene	ME	5200	1.06	6500	1.08
10	**P4**	Thiol-yne	DDT	6000	1.05	15000	1.06
11	**P4**	Thiol-yne	TBBT	6000	1.05	12200	1.10
12	**P4**	CuAAC	BzN_3	6000	1.05	7400	1.05

*Determined by SEC with PMMA standards. All PPMs featured quantitative conversion of the respective functional group as determined by ^{1}H-NMR spectroscopy.

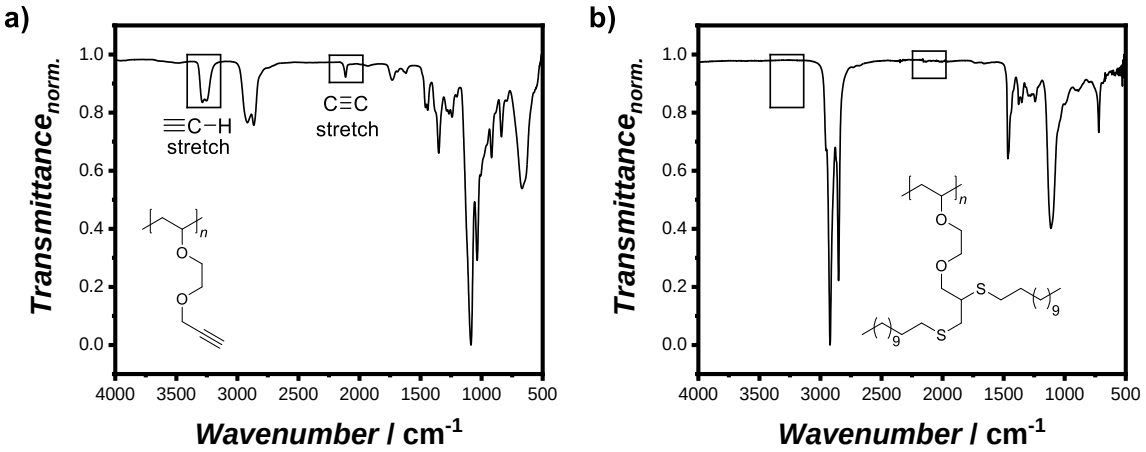

Figure 20. Exemplary FT-IR spectrum before **a)** and after **b)** the PPM of polymer **P2** with DDT showing the disappearance of the C≡C triple-bond.

Generally, all PPM reactions proceeded quantitatively in both the consumption of their functional group as well as the attachment of the substrate (**Table 7**), with the disappearance and appearance of the corresponding signals in the ^{1}H-NMR spectra of the successfully formed products (see **Chapter 6.4**). Moreover, FT-IR as well as ESI-MS measurements were used to further prove the successful reaction and quantitative conversion of the functional groups (**Figure 20** and additionally **Figure 90** – **Figure 100**). Further, a shift of the polymers' molar masses M_n as indicated by SEC confirmed the efficient PPM using the employed *click* reactions (exemplarily shown in **Figure 21** for the *thiol-ene* reaction of polymer **P1** with TBBT).

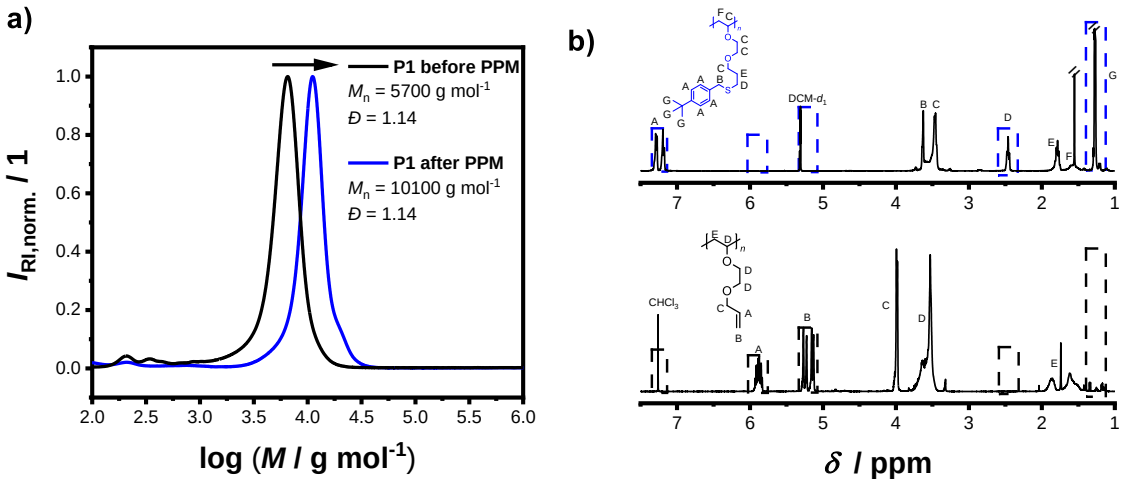

Figure 21. PPM of polymer **P1** using TBBT as shown by **a)** the clear shift of the SEC elugram while maintaining a low dispersity and a symmetrical signal and by **b)** the conversion of the double bond as well as the appearance of the corresponding signal of the *tert*-butylbenzylthio ether as determined by ^{1}H-NMR spectroscopy (**bottom**: before, **top**: after).

Also, the dispersity of the post-modified poly(vinyl ether)s remained mostly constant with some minor exceptions showing a slight increase in dispersity after functionalization (e.g. **Table 7 entry 5**). Probably, this is a result of an excessive radical concentration causing minor radical coupling reactions of carbons next to the formed thioether moieties. The influence of the amount of AIBN and thiol moiety on the outcome of the *thiol-yne* reaction was exemplarily demonstrated using **P2** with TBBT in order to prove that the broadening can be minimized by optimization of the reaction parameters (**Figure 22**). A lower amount of AIBN resulted in a less pronounced shoulder, but using 0.125 equivalents of AIBN was not sufficient in reaching full functionalization. Furthermore, the equivalents of TBBT were increased, both with and without a reduction of the overall concentration. The former did not reach full conversion, but by using 0.25 equivalents of AIBN, 8.00 equivalents of TBBT per alkyne group and the standard concentration a satisfying peak shape (shoulder barely visible) as well as full functionalization was reached. Therefore, successful optimization of the reaction conditions could be eventually demonstrated.

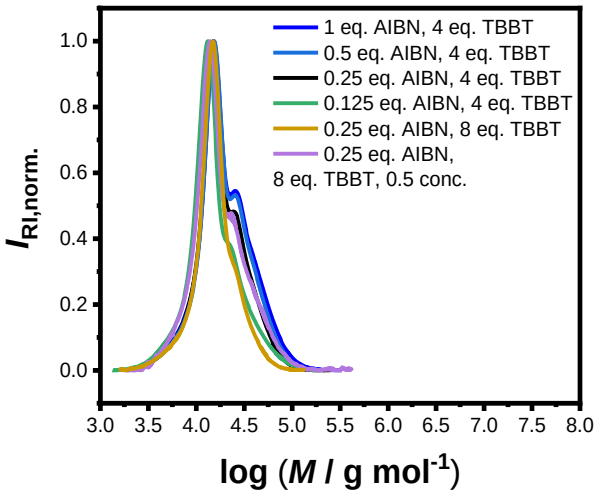

Figure 22. SEC results of the optimization of the *thiol-yne* reaction of **P2** and TBBT.

4.2.4 Recapitulation

In summary, a series of four different vinyl ether monomers **M1** – **M4** bearing pendant C=C double or C≡C triple bonds as functional groups were successfully employed in the controlled cationic polymerization *via* the PMCCP single-component initiation system under air atmosphere. It was found that the PMCCP only tolerates certain disturbing factors, such as variations in the chemical monomer structure and targeted molar mass. Yet, a nitrogen atmosphere is beneficial for the outcome of the controlled polymerization, especially with respect to high targeted molar masses of the functional poly(vinyl ether)s. Subsequently, the successful and quantitative PPM of the poly(vinyl ether)s **P1 – P4** *via thiol-ene/yne* or CuAAC reactions using different substrates was demonstrated. Overall, the synthesis of diversely functionalized poly(vinyl ether)s was advanced by successfully combining the PMCCP-controlled cationic polymerization of poly(vinyl ether)s with the efficient PPM *via* different click reactions, hence minimizing the synthetic complexity.

4.3 The Power of Architecture – *Cage*-shaped PEO and its Application as a Polymer Electrolyte

In this chapter, the gram scale synthesis of a four-arm *cage*-shaped PEO and its application as PE is discussed. The well suppressed crystallization by the *cage* architecture significantly improved the ionic conductivity at lower temperature in comparison to control samples with other architectures, thus proving the great toolbox of polymer chemists to overcome crystallization issues in PEO-based PEs.

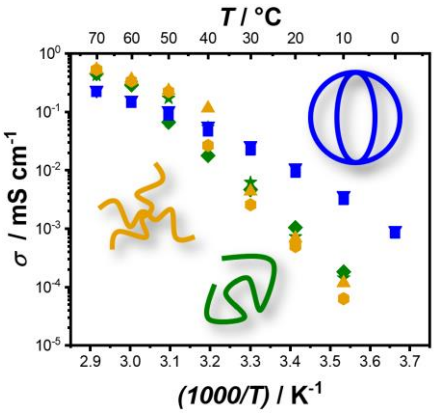

Figure 23. Ionic conductivity as function of PEO molecular architecture. The *cage* architecture shows an increased ionic conductivity at temperatures below 40 °C due to the well suppressed crystallization.

Parts of this chapter and the corresponding parts in the experimental section were adapted with permission from a publication written by the author (Andreas J. Butzelaar).[181]

The synthesis of the *cage*-shaped PEO was developed and conducted by Dr. Martin Gauthier-Jaques and is covered in detail in his dissertation,[182] while the thermal characterization as well as all PE-related parts were done by the author (Andreas J. Butzelaar).

4.3.1 Synthesis

As stated above, the synthesis was developed and conducted by M. Gauthier-Jaques, thus only a brief overview will be given. For more details, the reader is referred to the corresponding publication and dissertation.[181,182]

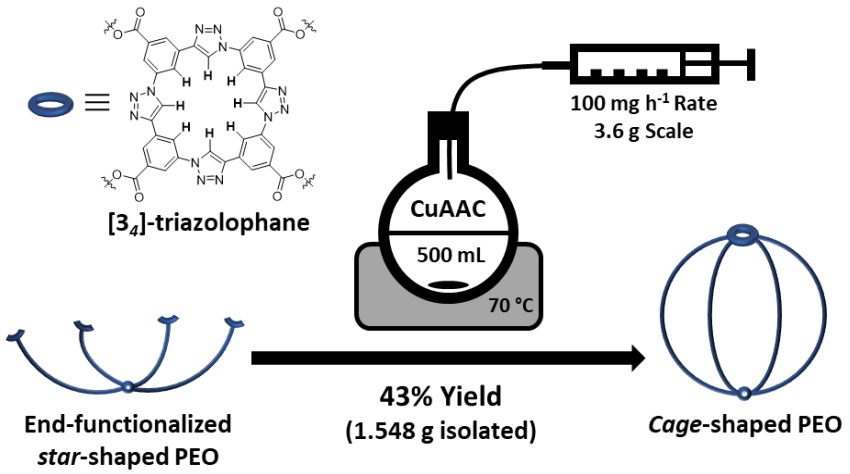

Scheme 21. Schematic summary of the gram scale synthesis of **PEO$_{cage}$** by semi-batch CuAAC reaction.

As starting material, a commercially available four-arm *star*-shaped PEO polymer (**PEO$_{star}$**), with a M_n of 5.0 kg mol^{-1} and a dispersity below 1.05 was used. The functional end-group 3-azido-5-ethynylbenzoic acid (AEBA) was synthetized beforehand in accordance with the previous study of M. Gauthier-Jaques.[183] Subsequently, esterification of **PEO$_{star}$** with AEBA was successfully conducted under mild conditions by EDC coupling, yielding end-functionalized *star*-shaped PEO (**PEO$_{end\text{-}func}$**). Then, a topological conversion of the end-functionalized *star*-shaped polymer into the *cage*-shaped PEO was performed by adapting conditions from a previous report[183] and expanded to the gram-scale in order to obtain a sufficient quantity of material for the intended application as PE. To do so, the synthetic closing step was performed in a semi-batch process guaranteeing a steady-state concentration of the reactive species throughout the reaction (**Scheme 21**), thereby efficiently suppressing undesired intermolecular reactions that would yield a cross-linked material. In detail, the topological conversion of the *star*-shaped **PEO$_{end\text{-}func}$** into its *cage*-shaped counterpart (**PEO$_{cage}$**) was achieved by CuAAC and resulted in an isolated yied of 43% (*i.e.* 1.55 g) after subsequent chromatography column purification (**Table 8**). The structure was confirmed by in-depth analysis as covered in the dissertation of M. Gauthier-Jaques.[182]

Table 8. Overview of the main characteristics PEO polymers by SEC and ^{1}H-NMR analysis.

Entry	Polymer	M_n^* [g mol^{-1}]	$M_n^{\#}$ [g mol^{-1}]	$Đ$ [1]	Yield [%]
1	**PEO$_{star}$**	5700	7200	1.04	-
2	**PEO$_{end\text{-}func}$**	6400	8000	1.05	94
3	**PEO$_{cage}$**	6400	4700	1.14	43

*Obtained by ^{1}H-NMR. $^{\#}$Obtained by SEC.

4.3.2 Polymer Electrolytes

The thermal properties of the *cage*-shaped PEO were characterized by DSC and compared to the unfunctionalized *star*-shaped PEO. As discussed beforehand, PEO-based materials are commonly comprised of both crystalline and amorphous domains in variable ratios. Thus, their semi-crystalline nature can be characterized by their T_m and T_g as well as the related enthalpies.[184] As mentioned before, within this thesis PEO-based PEs are of primary interest, which should preferably exhibit a completely amorphous phase, i.e a non-existing crystallization, in order to enable ionic conductivity in the created free volume.[185] Additionally, a low T_g ensures a maximal chain mobility and an optimal ion transport by segmental motion.[23,186]

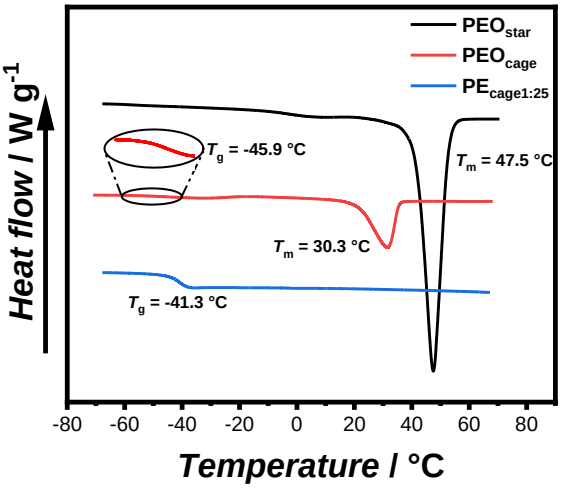

Figure 24. Comparison of DSC thermograms of **PEO$_{star}$**, **PEO$_{cage}$** and **PE$_{cage1:25}$** samples, showing the reduced/suppressed crystallization as consequence of architecture change and lithium salt addition. Subscripted numbers correspond to the [LiTFSI]:[EO] ratio.

The predominant crystalline nature of **PEO$_{star}$** was confirmed by the prominent T_m located at 47.5 °C, the high fusion enthalpy ΔH_{melt} of 121.0 J g^{-1} and the absence of a noticeable T_g (**Figure 25a**, **Table 9**). In comparison, literature values for high molar mass linear PEO are reported as T_m ~ 65 °C[187–189], ΔH_{melt} = 196.4 J g^{-1} [169], indicating an influence of the PEO architecture on the crystallization, yet not suppressing it completely. A further suppression of the crystallization was observed after the topological conversion into **PEO$_{cage}$**, with T_m and ΔH_{melt} reduced to 30.3 °C and 51.6 J g^{-1}, respectively, and a clearly detectable T_g of -45.9 °C (**Figure 25a**, **Table 9**). These values correspond to a reduction of crystalline domains by 58%

or 74% in comparison to **PEO$_{star}$** or pure PEO,[190] respectively, and represent an impressive reduction of crystallinity induced *via* a topological conversion into a *cage*-shaped architecture. In comparison, the reduction of crystallinity observed in the *comb*-shaped polymer architecture (**Chapter 4.1**), consisting of comparable 24 and 54 ethylene oxide (EO) repeating units per side chain, was only 51% and 39% (**Table 5**), respectively, relative to pure PEO. Furthermore, the thermal properties of different PEs prepared from **PEO$_{cage}$** (thus denoted as **PE$_{cage}$**) as well as **PEO$_{star}$** by addition of Li^+-salt (**PE$_{star}$**) for comparison were examined considering that the addition of LiTFSI salt impacts the crystallinity substantially due to its plasticizing character. While lithium salt loadings of [Li^+]:[EO] of 1:20 and 1:25 completely suppressed crystallization of the **PEO$_{cage}$**, these loading values were not sufficient to suppress the crystallization for the comparable **PE$_{star}$** samples with ΔH_{melt} = 38.6 J g^{-1} and 61.6 J g^{-1} for [Li^+]:[EO] of 1:20 and 1:25, respectively, as shown in **Table 9**. Notably, significantly higher LiTFSI loadings comprised of [Li^+]:[EO] between 1:6 – 1:12 are usually necessary to ensure a completely amorphous PEO.[190] Moreover, in both **PE$_{star}$** and **PE$_{cage}$** samples, the T_g values decreased when the [Li^+]:[EO] ratio was reduced from 1:20 to 1:25, due to a lower amount of *quasi-ionic cross-linking* between the PEO chain segments.[191] On the contrary, higher T_g values were systematically observed for **PE$_{cage}$** in comparison with **PE$_{star}$** arising from the architecture-induced restriction of the polymers' segmental motion. Nonetheless, the thermal characterization showed quite impressively that the topological conversion into a *cage*-based architecture not only reduces crystallinity, but also allows for lower LiTFSI loadings than usual.

Table 9. Overview of the thermal properties obtained by DSC analysis for **PEO$_{star}$** and **PEO$_{cage}$** and their related PEs.

Entry	Polymer / PE	[Li^+]:[EO]	T_m [°C]	ΔH_{melt} [J g^{-1}]	T_g [°C]
1	**PEO$_{star}$**	-	47.5	121.0	n.d.
2	**PE$_{star1:20}$**	1:20	35.0	38.6	-42.5
3	**PE$_{star1:25}$**	1:25	39.0	61.6	-44.2
4	**PEO$_{cage}$**	-	30.3	51.6	-45.9
5	**PE$_{cage1:20}$**	1:20	n.d.	n.d.	-40.8
6	**PE$_{cage1:25}$**	1:25	n.d.	n.d.	-41.3

n.d. = not detectable.

In addition, the thermal stabilities of **PEO$_{star}$**, **PEO$_{cage}$** and **PE$_{cage1:25}$** were examined by TGA measurements. All materials showed a good thermal stability up to over 280 °C with a decomposition temperature at 5% weight loss T_{d5} of around 334 °C for **PEO$_{star}$**, 299 °C for **PEO$_{cage}$** and 288 °C for **PE$_{cage1:25}$** (**Figure 25b**). Here, the presence of thermally more labile ester moieties might induce a small reduction in thermal stability when comparing **PEO$_{star}$** with both other samples. Further, the remaining char above 500 °C of ~12% (for **PEO$_{cage}$**) and ~15% (for **PE$_{cage1:25}$**), could be correlated to the theoretical content of [3$_4$]-triazolophane within **PEO$_{cage}$** (11.8%) and the remaining lithium species within **PE$_{cage1:25}$**.

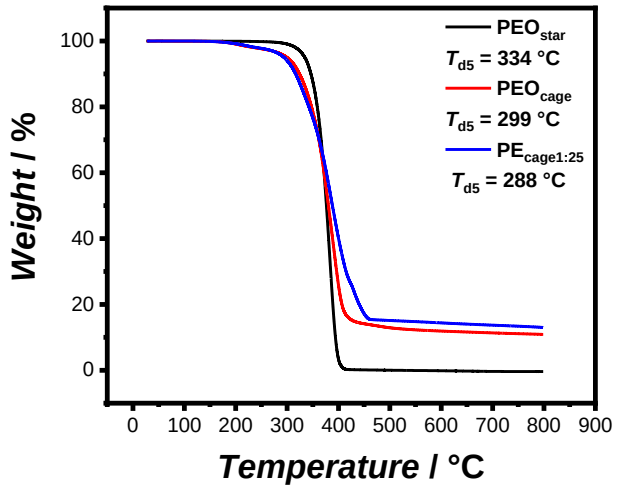

Figure 25. Comparison of TGA thermograms displaying the degradation profile of **PEO$_{star}$**, **PEO$_{cage}$** and **PE$_{cage1:25}$**. Subscripted numbers correspond to the [LiTFSI]:[EO] ratio.

Finally, the ionic conductivities of both **PE$_{cage}$** samples were measured within a temperature range of 70 °C to 0 °C by EIS and compared to the values obtained from **PE$_{star}$** and a linear PEO-based electrolyte (**PE$_{linear}$** with 5 Mg mol^{-1}) (**Figure 26**). In accordance with the DSC results, the complete crystallization suppression of the **PE$_{cage}$** samples led to a typical Vogel-Tammann-Fulcher behavior regarding their ionic conductivity. In addition, **PE$_{cage1:25}$** performed slightly better than **PE$_{cage1:20}$** over the whole temperature range, as predicted by the difference in T_g of 0.5 °C noticed between their respective DSC thermograms resulting from the lower LiTFSI salt loading, which reduced the *quasi-ionic cross-linking* and thus increased the segmental motion. Instead, EIS analyses of **PE$_{star}$** and **PE$_{linear}$** showed the known and eminent drop in ionic conductivity as soon as PEO crystallization occurred in the range from 50 °C to 30 °C depending on the respective topology and the LiTFSI content. However, the

higher chain mobility of **PE$_{star}$** and **PE$_{linear}$** above their melting points resulted in a slightly enhanced ionic conductivity compared to **PE$_{cage}$**. Yet, **PE$_{cage}$** exhibited a superior ionic conductivity below 40 °C, leading to ionic conductivity values of 1×10^{-2} mS cm^{-1} at 20 °C, therefore outperforming the **PE$_{star}$** and **PE$_{linear}$** by a factor of 10. Nonetheless, it has to be stated that these obtained ionic conductivities are still relatively low in a practical point of view (compared to the usually targeted 1×10^{-1} mS cm^{-1} at 20 °C), though showing what architectural approaches taken by polymer chemists are capable of.

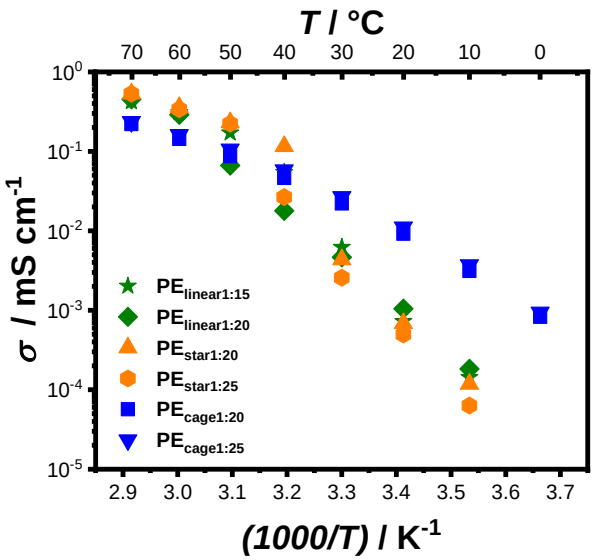

Figure 26. Temperature-dependent ionic conductivity of **PE$_{cage}$** compared to **PE$_{star}$** and **PE$_{linear}$** samples with different LiTFSI loading ratios. Subscripted numbers correspond to the [LiTFSI]:[EO] ratio.

4.3.3 Recapitulation

In conclusion, the gram scale synthesis of a four-arm *cage*-shaped PEO was successfully accomplished, opening the possibility for applicational studies. For this, **PEO_{cage}** was investigated as a potential PE for LIBs. In this regard, addition of a low amount of lithium salt to the PE resulted in purely amorphous samples with superior ionic conductivity below 40 °C. Notably, the ionic conductivity gap recorded at 20 °C exceeded the values of the PE control samples by 10 times. Besides being a significant step ahead in the research of applications for *cage*-shaped polymers, the present study clearly underlines the importance of topology and architecture when designing polymer materials for specific applications. Lastly, the exciting opportunities offered by architectural approaches might contribute to the conception of next generation PEs to advance electric energy storage.

4.4 Styrene-Based Poly(ethylene oxide) Side Chain Block Copolymers as Solid Polymer Electrolytes for High-Voltage Lithium-Metal Batteries

This chapter covers styrene-based PEO side chain block copolymers as SPE. Based on **Chapter 4.1** which already dealt with PEO side chain architectures, the impact of different PEO side chain lengths and the LiTFSI content onto the thermal properties as well as the ionic conductivity of the derived microphase separated SPEs was briefly examined. The block copolymer composition providing the highest ionic conductivity was selected to proceed with further detailed thermal, mechanical and electrochemical characterization, eventually illustrating a successful long-term cycling in lithium-metal||NMC622 full cells.

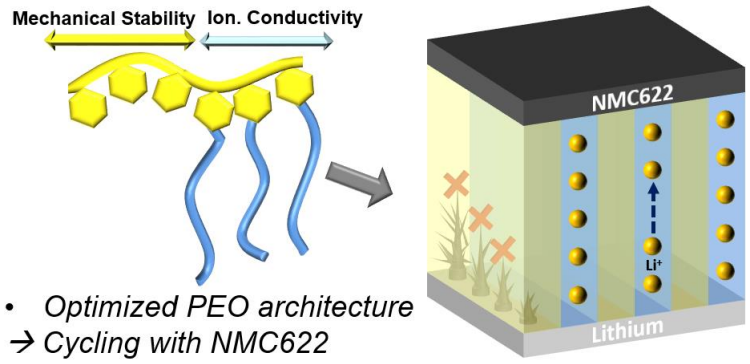

Figure 27. The optimized PEO-based block copolymer structure suppressed lithium-dendrite growth and thus enabled cycling with NMC622 without commonly observed rapid cell failure.

Parts of this chapter and the corresponding parts in the experimental section were adapted with permission from a publication written by the author (Andreas J. Butzelaar).[192]

The electrochemical experiments were conducted in close cooperation by Philipp Röring from Helmholtz Institute Münster.

4.4.1 Strategy

As described in **Chapter 2.7**, block copolymers have demonstrated to be capable of solving the mechanical stability/ionic conductivity dilemma through introduction of one PEO-based polar block, as well as a high T_g non-polar block, such as PS.[32] However, the synthesis of frequently used PS-*b*-PEO, prepared by AP, has the drawback of being both tedious and highly dangerous due to the employed ethylene oxide gas.[154,157,158] Moreover, in other systems such as PS-*b*-POEGMA, the ester moieties of the methacrylate represent a chemical weak point in terms of thermal and electrochemical stability as well as against nucleophilic impurities.[159,160] Thus, a synthetic approach toward block copolymers was developed overcoming both before mentioned drawbacks by exploiting styrene and styrene monomers featuring PEO side chains, resulting in block copolymers with a thermally and (electro)chemically stable backbone. PS was chosen as the non-conducting block to provide a good mechanical stability due to its T_g of around 100 °C,[193] affordable price and exceptional compatibility with common polymerization techniques such as RAFT, thus avoiding AP. Furthermore, the side chain approach reduces the inherent crystallinity as already shown in **Chapter 4.1**. In comparison to the previously described study however, the PEO side chains were attached to styrene in order to keep perfect compatibility with the unfunctionalized styrene during the polymerization. Finally, the microphase separation of the block copolymers allows for the preparation of a macroscopically self-standing, truly ‘dry’ SPE having both good flexibility as well as intrinsic mechanical stability.

4.4.2 Synthesis

Block copolymers were prepared affording flexible, self-standing films of dry PEO-based polymer electrolytes, which feature sufficient mechanical stability to prevent lithium dendrite growth and reasonable ionic conductivity. A key point is the ability of both blocks to form so-called microphase separated domains on a nanoscale level driven by their polarity difference, *i.e.* difference in their mixing parameter χ.[194–196] Thus, block copolymers were synthesized by firstly polymerizing the macromonomers vinyl benzyl mPEOz ether (**VBmPEOz)**, which feature a styrene functionalized mPEOz chain, using 2-(dodecylthiocarbonothioylthio)-2-methylpropionic acid (DDMAT) as RAFT agent to achieve perfect control over the radical polymerization (**Scheme 22**). Consequently, a macro-RAFT agent[197] based on styrene repeating units with grafted PEO side chains was obtained (**PVBmPEOz**). Subsequently, **PVBmPEOz** was used for the chain extension with styrene as exemplarily shown in **Figure 28** to eventually obtain the block copolymer **PVBmPEOz-*b*-PS** (hereinafter denoted as **BPz**).

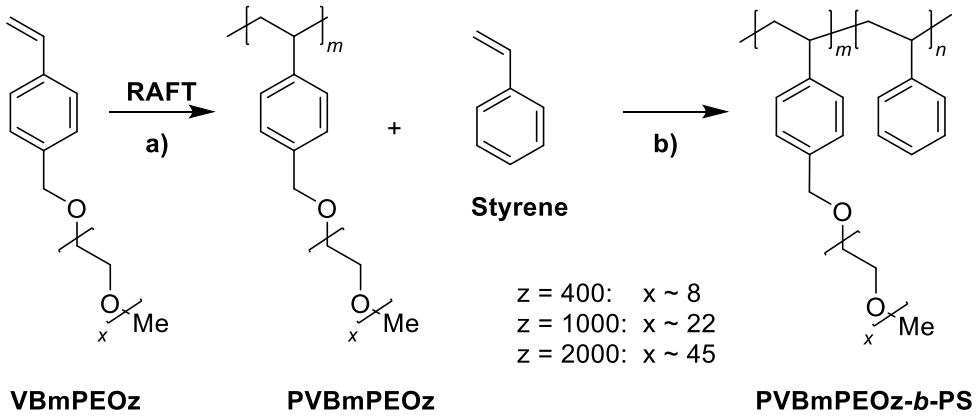

Scheme 22. Sequential block copolymerization by **a)** RAFT polymerization of VBmPEOz giving a so-called macro-RAFT agent (**PVBmPEOz**) followed by **b)** chain extension with styrene eventually yielding **PVBmPEOz-*b*-PS** (**BPz**).

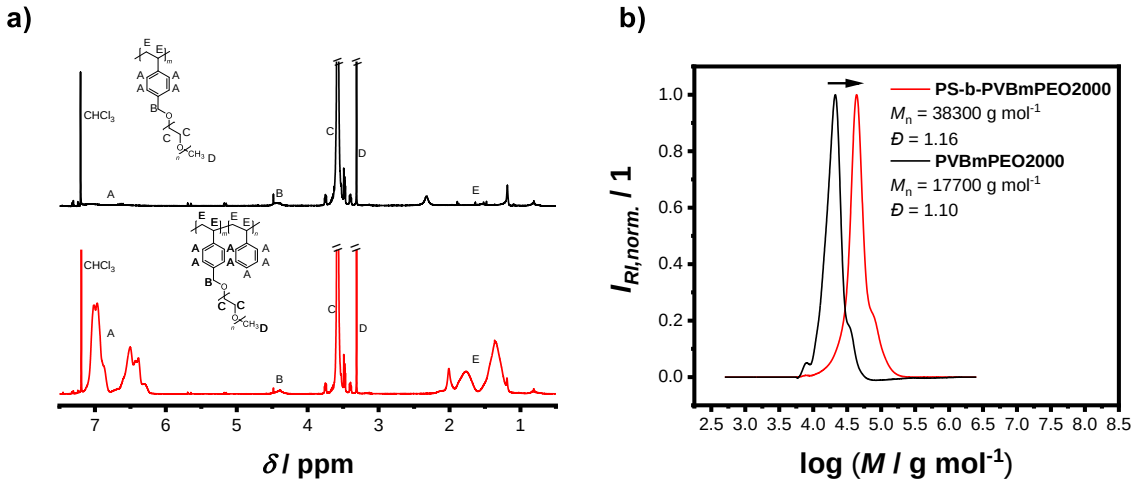

Figure 28. Exemplary **a)** ^{1}H-NMR and **b)** SEC spectrum of the chain extension of **PVBmPEO2000** with styrene forming **PS-*b*-PVBmPEO2000** (**BP2000**). The shift of the polymers' molar mass as well as the appearance of the PS proton signals confirm the successful formation of a block copolymer.

Three different PEO side chain lengths were employed featuring 8, 22 and 45 EO units corresponding to a mPEOz side chain molar mass of z = 400, 1000 and 2000 g mol^{-1}, respectively. Thus, the *degree of polymerization* (DP) of **PVBmPEOz** was predefined to be 30 (z = 400), 15 (z = 1000), and 9 (z = 2000) with respect to their different molar mass and their different reactivity. Furthermore, the length of the second block, *i.e.* the PS block, was adjusted to feature a mass fraction of 50% of the final block copolymer, to obtain flexible, self-standing films. This is of particular interest due to the facilitated processing as well as the fact that a dimensionally stable film in principle yields more robust electrode interfaces.[10,147] Consequently block copolymers with total molar masses M_n of ~ 25, 29 and 38 kg mol^{-1} (as determined by SEC with PS standards, see **Table 10**) for **BP400**, **BP1000** and **BP2000** were obtained, respectively.

Table 10. Overview of the different block copolymers.

Entry	Polymer	EO units*	$M_{n,\,PVBmPEOz}$§ [g mol^{-1}]	$Đ_{PVBmPEOz}$§	$M_{n,\,BPz}$§ [g mol^{-1}]	$Đ_{BPz}$§	$w_{VBmPEOz}$#	$\phi_{VBmPEOz}$$
1	**BP400**	9.4	10100	1.11	24900	1.22	0.56	0.53
2	**BP1000**	25.5	10400	1.08	28600	1.25	0.52	0.49
3	**BP2000**	48.4	17600	1.10	38300	1.16	0.49	0.46

*Average per PEO side chain. Calculated by ^{1}H-NMR integrals. §Measured by SEC with PS standards. #Calculated by ^{1}H-NMR integrals $Calculated using the densities of PS (1.07 g cm^{-3}) and PEO (1.21 g cm^{-3}). Note that this calculation is not 100% correct, since PEO is attached as side chain.

4.4.3 Polymer Electrolytes

The previously synthesized block copolymers **BPz** were used to prepare SPEs with self-standing film properties in order to study the impact of different side chain lengths as well as the LiTFSI content onto the thermal properties and ionic conductivity. Although a detailed description of all the relationships has been elaborated in previous works,[27,28] the influence of different parameters was briefly explored since it was not clear whether block copolymers would behave in analogy to the previously examined homopolymers.

To begin with, **BP1000** with a side chain length of around 22 EO units was chosen to examine the influence of different LiTFSI concentrations, since this side chain length showed promising ionic conductivities in previous studies and features a medium length among the three different side chains.[27–29] SPEs with [Li^+]:[EO] ratios of 1:5, 1:10, 1:15 and 1:20 were produced and investigated using EIS as well as DSC. The latter showed that all LiTFSI concentrations in combination with the side chain approach were sufficient in rendering the PEO-based domain completely amorphous (**Table 11**), which is of particular importance, since ion transport is suspected to be mainly possible within amorphous domains.[198,199] Furthermore, the T_g increased with increasing LiTFSI content due to a higher number of *quasi-ionic cross-links*, lowering the overall segmental motion of the side chain (**Table 11**, **Figure 29c**).[190]

Table 11. Overview of the thermal properties of the PEO domains of the different SPEs.

Entry	Polymer	[LiTFSI]:[EO]	$T_{g\ PEO\ domain}$ [°C]	$T_{m\ PEO\ domain}$ [°C]
1	**BP400**	1:15	-42.2	n.d.
2	**BP1000**	1:5	-32.8	n.d.
3	**BP1000**	1:10	-43.2	n.d.
4	**BP1000**	1:15	-47.2	n.d.
5	**BP1000**	1:20	-49.5	n.d.
6	**BP2000**	1:15	-47.6	n.d.

n.d. = not detectable.

Upon inspection of the corresponding ionic conductivities (**Figure 29a**), it became obvious that the [Li^+]:[EO] ratio of 1:5 showed by far the worst ionic conductivity among the different LiTFSI contents over the whole temperature range. However, all other employed ratios resulted

in higher but very similar conductivities over the whole temperature range. A ratio of 1:10 was beneficial at higher temperatures, while ratios of 1:15 and 1:20 were better at lower temperatures. Overall, it was decided to continue the characterization of the SPEs with a [Li^+]:[EO] ratio of 1:15 in the following, since it exhibited the best overall performance over the whole measured temperature range.

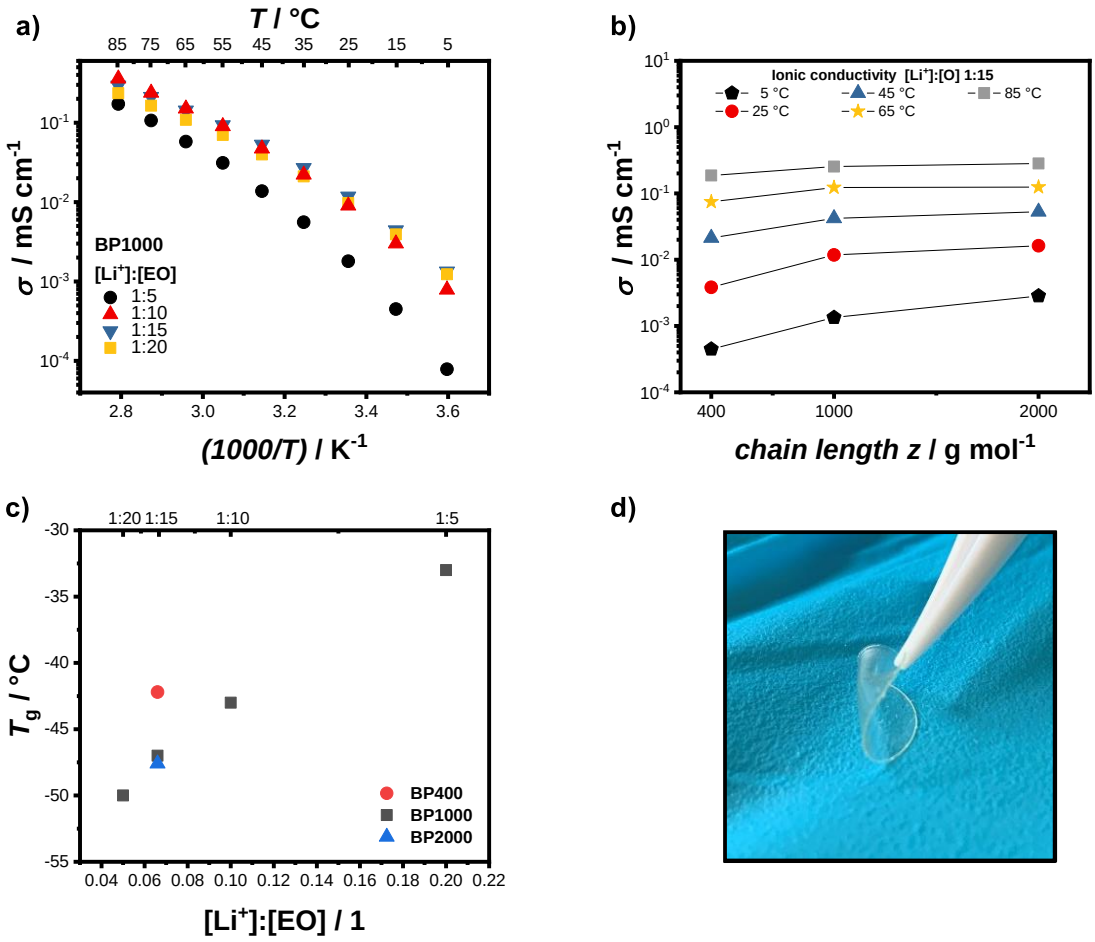

Figure 29. **a)** Ionic conductivities of SPEs derived from **BP1000** and different LiTFSI concentrations and **b)** comparison of the ionic conductivities of **BP400**, **BP1000** and **BP2000** featuring a LiTFSI ratio of [Li]:[EO] of 1:15. **c)** Corresponding T_gs to **a)** and **b). d)** Exemplary depiction of the flexible character of the SPE derived from **BP2000** with LiTSFI forming a self-standing film.

Next, the ionic conductivities of **BP400**, **BP1000** and **BP2000** with a [Li^+]:[EO] ratio of 1:15 were compared. An increasing ionic conductivity with increasing number of EO units from **BP400** to **BP2000** was observed (**Figure 29b**). Taking **BP400** as an example, around 20 wt% of the PEO-based domain consists of styrene from the backbone due to the fact that each side

chain with around 400 g mol^{-1} features one styrene functionality with around 100 g mol^{-1}. This results on the one hand in a lower fraction of the PEO-based domain being actually able to conduct ions and on the other hand an increase in T_g due to the significantly higher T_g of styrene in comparison to PEO (**Table 11**, **Figure 29c**). These relationships become quite visible, when **BP1000** and **BP2000** are included in this consideration. They exhibited a styrene content of 9 and around 5 wt%, respectively, and therefore the percental fraction of styrene content as well as the T_g of the PEO-based domain is decreasing within this series (**Table 11**, **entry 1**, **4** and **6, Figure 29c**). Furthermore, longer PEO side chains statistically lead to less inter molecular *quasi-ionic cross-linking* in comparison to short side chains, which also affects the T_g.[27,28] Comparing consistent LiTFSI ratios, a lower T_g results in higher segmental motion at the same temperature and thus in higher ionic conductivity, as can be seen in **Figure 29b**. Another further explanation for this behavior might be a better phase separation of PS and PEO-based domains due to a higher difference in polarity when less 'backbone PS' contributes to the PEO-based domain. However, this aspect is difficult to quantify and beyond the scope of this project. Furthermore, it was noticed that in contrast to **Chapter 4.1** there was no tradeoff established between PEO side chain lengths of 1000 and 2000 g mol^{-1}, where the former showed higher ionic conductivity at higher temperatures and the latter at lower temperatures.[27] This might be attributed to the formation of domains on a nanoscale level caused by the block copolymer architecture, hence potentially hindering chain alignment within these domains (thus boosting ionic conductivity for longer chains at lower temperatures). Therefore, this contrasts with the previously considered homopolymers, where the whole bulk material forms a single macroscopic domain.

Still, it has to be noted that the measured ionic conductivities of 1.6×10^{-2} mS cm^{-1} at 25 °C and 1.8×10^{-1} mS cm^{-1} at 65 °C are relatively low from a practical point of view, but very competitive considering that a truly 'dry' PEO-based microphase separated block copolymer having about 50 wt% PS incorporated was used.[155,156,159] In addition, it has to be mentioned that ionic conductivity is only one important feature of a SPE. Other properties such as flexibility (**Figure 29d**) and wettability and thus better interfacial contact to the electrodes, a sufficient electrochemical stability towards the electrodes as well as sufficient high limiting currents are also highly important for a stable battery performance. Moreover, a high mechanical stability of the SPE and a high limiting current density influence the dendritic growth and thus the cell safety.[200–202] Overall, based on the conductivity results, the SPE prepared from **BP2000** and LiTFSI with a ratio of [Li$^+$]:[EO] = 1:15 (in the following denoted as **BPE2000**) was further characterized.

4.4.4 In-depth Characterization of BPE2000

One reason for choosing PS as the backbone as well as the block providing the mechanical solidity was due to its high thermal stability.[203] To verify this, a TGA measurement of **BPE2000** was conducted, showing a highly stable SPE with a 5% weight loss at a temperature of 331 °C (T_{d5}) (**Figure 30**). The single degradation suggests a simultaneous decomposition of PS, PEO as well as LiTFSI, which are all known to degrade around this temperature.[163,203,204]

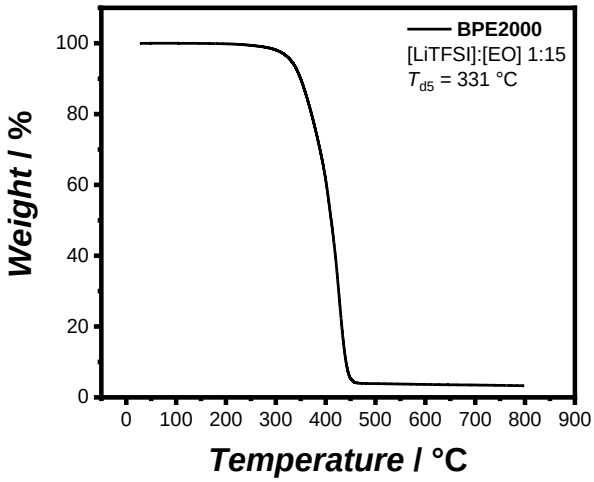

Figure 30. TGA thermogram of **BPE2000** showing a single degradation step.

Furthermore, the morphology of **BPE2000** was investigated in more detail. DSC measurements confirmed the microphase separation by showing two distinct T_gs for both PS- and PEO-based domains at 100°C and -47°C, respectively (**Figure 31a**). Furthermore, the ionic conductivities as shown in **Figure 29** can only be achieved if phase separation occurred, since a non-separated structure would decrease the ionic conductivity significantly because the conductive domain would contain a substantial amount of a non-conducting polymer (*i.e.* PS), which would increase the T_g and thus decrease the mobility. To further elucidate the morphology, small-angle x-ray scattering (SAXS) measurements were conducted (**Figure 31b**). Herein, the presence of a primary maximum at a scattering vector (q) of $q^* = 0.23\ nm^{-1}$ confirmed the microphase separation, whereas the presence of additional maxima at $2q^*$ and barely visible at $3q^*$ revealed a high degree of ordering, since non-ordered microphase separated polymers only show the main maximum.[205] In addition, it is indicative for a lamellar, long-range ordered morphology,[206] as anticipated for a block copolymer with a block ratio in the range of 50/50.[158]

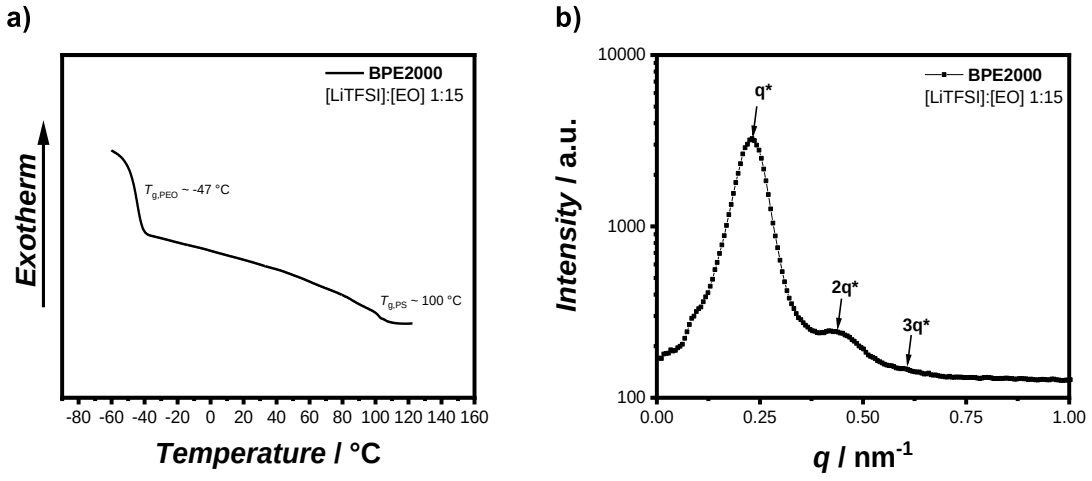

Figure 31. a) DSC thermogram of **BPE2000** revealing the phase separation by simultaneously showing the T_g of the PEO-based and the PS domain and **b)** SAXS spectrum suggesting a long-range ordered, lamellar morphology.

Moreover, the average domain spacing (*d*) of around 27 nm was calculated by **Equation 1**, which is in agreement with comparable PS-*b*-PEO or PS-*b*-POEGMA structures featuring a similar molar mass of the blocks (~ 19 kg mol^{-1} per block).[196,207] However, these values are not straightforward to compare, because the LiTFSI content and the macromolecular architecture (linear vs. grafted) influence the domain size.[158,208–210]

$$d = \frac{2\pi}{q^*} \qquad \textbf{(Equation 1)}$$

In addition, rheological measurements of **BPE2000** and the corresponding homopolymer electrolyte (*i.e.* without the PS block) were conducted (**Figure 32**). While the homopolymer electrolyte was a viscous liquid as shown by the low storage modulus *G'* and loss modulus *G''*, **BPE2000** was a self-standing film with *G'* of around 1 MPa and *G''* of around 0.1 MPa. However, it has to be noted that these measured values describe the rheological behavior for the bulk material comprising both PS and PEO domains. Thus, due to the phase separation of the block copolymer it can be expected that PS domains with their T_g at 100°C are predominantly contributing to the mechanical stiffness, which is characterized by a G modulus of around 1 GPa.[211] This high mechanical stiffness is even in the range of metallic lithium (G modulus of 3.4 GPa) and essential for the use of **BPE2000** as SPE in lithium-metal batteries in order to suppress lithium dendrite growth.[124,200,202] Srinivasan *et al.* proposed that in PEO-based polymer electrolytes a G modulus higher than 3.4 MPa ($G_{SPE} > 10^{-3}\, G_{Li}$) leads to plastic

deformation of the lithium-metal dendrite, thus decreasing the height of the dendrite protrusion and therefore additionally decreasing the concentration/overpotential contribution to dendrite growth.[200] Further, PEO-based domains are characterized by a low T_g and also a high flexibility and wettability, which is shown for the homopolymer, therefore providing an optimal contact towards the electrodes.

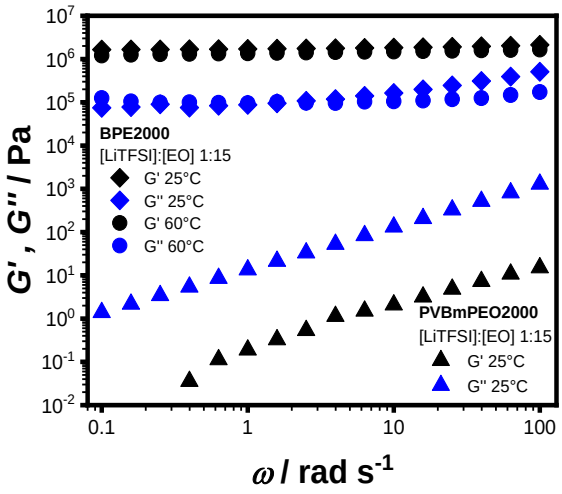

Figure 32. Oscillatory rheology of **BPE2000** and the corresponding homopolymer electrolyte (**PVBmPEO2000**) showing the improved bulk mechanical stability of the former.

4.4.5 Electrochemical Characterization

Since the ionic conductivity of a dual-ion conducting SPE is a combination of anion ($TFSI^-$) and cation (Li^+) mobility and thus only points out the overall ion movement, it is necessary to determine the transference number of such a SPE to obtain an insight in the actual lithium ion mobility. For this, the combined potentiostatic polarization and complex impedance measurement proposed by Evans *et al.*[212] was used to determine the transference number of **BPE2000** (**Figure 33**). As explained in **Chapter 6.1.11**, the transference number of **BPE2000** was calculated to 0.13, which is in the typical range of PEO-based SPEs[28,156,213,214] and thus underlines the assumption of a successful microphase separation and the ion conduction within the PEO-based domain.

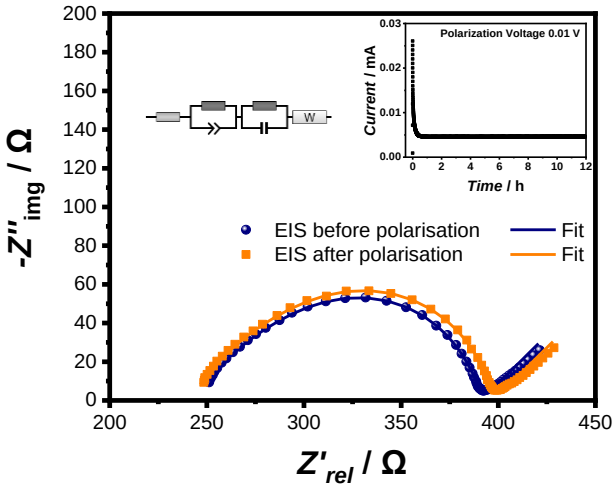

Figure 33. Chronoamperometry and EIS for the measurement of the transference number for **BPE2000**.

In the next step, the electrochemical stability of **BPE2000**, which is an essential information for the practical application as SPE, was evaluated. The intrinsic reductive stability was tested using linear sweep voltammetry (LSV) with copper as working electrode in a range from 3.0 – -0.5 V *vs.* $Li|Li^+$. As shown in **Figure 34a**, a small peak at ~ 1.5 V as well as a tiny, broad peak at ~ 0.3 – 0.5 V was observed, followed by lithium plating below 0 V. Especially, the peak at ~ 1.5 V is a known phenomenon, yet its origin is not fully understood, but reported to be a one-time event.[215,216] In fact, cyclic voltammetry (CV) from 3.0 V – -1 V *vs.* $Li|Li^+$confirmed the presence of this peak during the first cycle only (**Figure 34b**). In addition, the peak at 0.3 V seemed to decrease during cycles.

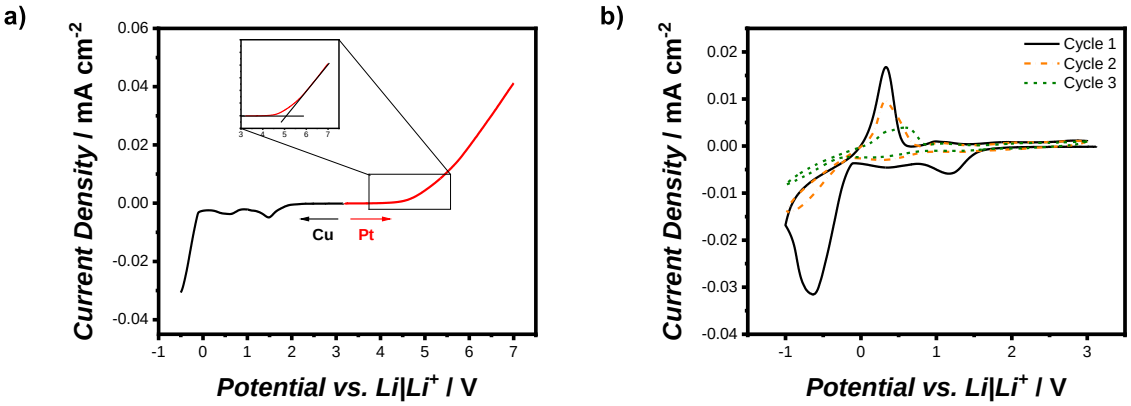

Figure 34. Determination of the electrochemical stability of **BPE2000** by **a)** LSV in a range from -0.5 – 7.0 V *vs.* Li|Li$^+$ (0.1 mV s^{-1}) and **b)** CV in a range from -1.0 – 3.0 V V *vs.* Li|Li$^+$ (0.1 mV s^{-1})

Moreover, the intrinsic oxidative stability of the SPE using an anodic sweep from 3.0 – 7.0 V was determined as 5.1 V *vs.* Li|Li$^+$ with platinum serving as working electrode (**Figure 34b**). However, these values are highly dependent on the set limits. Often, 0.01 or 0.015 mA cm^{-2} are chosen[217], corresponding to even higher values. Still, the electrochemical stability window measured on inert materials such as platinum or copper does not reflect a realistic behavior in a lithium-metal battery. High surface area cathodes and chemical reactive lithium-metal often support electrochemical degradation during cycling.[150,215] Therefore, to further investigate the compatibility with high voltage cathode materials, galvanostatic overcharging of the positive electrode was performed to determine limiting potentials in a more realistic way (**Figure 35**). Commonly employed LNMO as well as NMC622 were used as high voltage cathode materials to determine the onset of oxidation. Independent of the different mechanisms of lithium de-/intercalation a characteristic voltage plateau at 4.75 V *vs.* Li|Li$^+$ was observed for both LNMO and NMC622 cathodes. This voltage plateau reflects parasitic reactions originating from oxidative decomposition of either the SPE itself, the present poly(vinylidene fluoride) PVdF in the composite cathode or both.[218] As mentioned above, the onset of oxidative decomposition of the SPE against active materials can differ from the decomposition against inert materials such as platinum or copper. Nonetheless, there is no apparent current (< 0.01 mA cm^{-2} for potentiodynamic and no obvious voltage plateau for galvanostatic measurement) evolving from electrolyte oxidation below 4.3 V *vs.* Li|Li$^+$ for both potentiodynamic and galvanostatic measurements and therefore an application of this SPE using high voltage cathode materials such as NMC622 appears very likely.

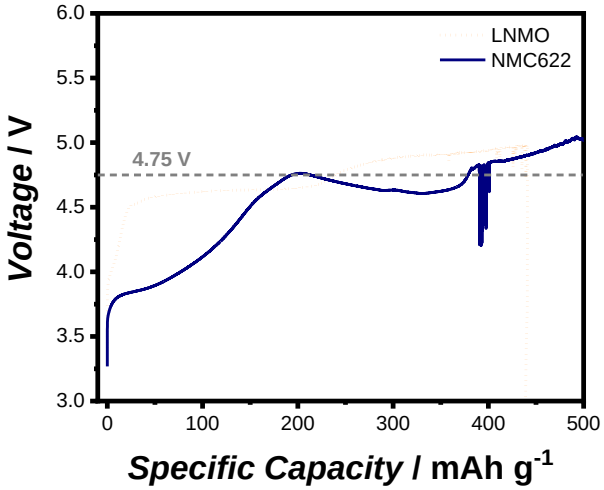

Figure 35. Determination of the electrochemical stability of **BPE2000** by galvanostatic overcharging (0.1 C) using LNMO and NMC622 as high voltage cathode materials.

Since one of the major advantages of SSBs is the use of lithium-metal resulting in an increased energy density, it is essential that the solid state electrolyte is suitable for use against lithium-metal electrodes.[115,219] Moreover, the increased mechanical stability attributed to the PS block (*vide supra*) is beneficial for the inhibition of lithium dendritic growth. Therefore, lithium plating stripping experiments were conducted at a current density of 0.1 mA cm^{-2} to examine the interfacial long-term stability on lithium-metal and the ability to reduce lithium dendrite growth. As shown in **Figure 36**, the overvoltage (initial overvoltage ~ 0.075 V) increased within the first cycles reflecting an increase of the resistance, presumably originating from the formation of an additional SEI by insignificant electrolyte decomposition. Once the SEI layer was formed completely, the overvoltage remained nearly stable at ~ 0.15 V over thousand hours. In general, this long-term overvoltage of ~ 0.15 V is a common value for similar PEO-based SPEs, whereas the initial overvoltage of ~ 0.075 V is rather low[156,220] However, overvoltages in Li|SPE|Li cells are strongly related to several polymer properties such as film dimensions, interface resistances or mechanical properties and are thus of a complex nature, making it difficult to compare. Moreover, the shape of the voltage profiles (see inset of **Figure 36**) rapidly reached a plateau implying a reduced cell polarization due to ionic concentration gradients.[215] These findings indicated a stable and homogeneous lithium deposition behavior and consequently no short-circuit by dendrite penetration was observed over thousand hours,

whereas comparable PS-PEO block copolymers already underwent a short-circuit after 240 h[156] and pure PEO even within < 40 h[220] under the same current density.

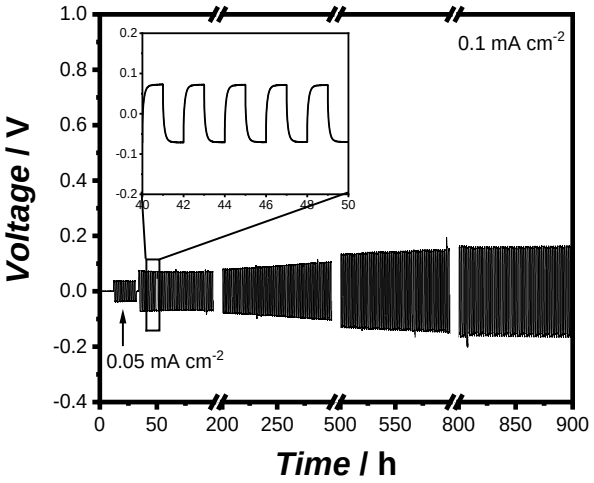

Figure 36. Lithium plating stripping experiments. Conditioning using 0.05 mA cm^{-2} for 10 cycles. Afterwards, lithium was constantly plated and stripped with a current density of 0.1 mA cm^{-2} for one hour over a total of 1000 hours.

To further investigate the lithium dendrite growth, plating and stripping experiments were performed with a longer plating and stripping time as well as alternating current densities.

As shown in **Figure 37** the plating and stripping time with a current density of 0.1 mA cm^{-2} was extended to four hours to evaluate the influence of a longer plating/stripping time. Similar to **Figure 36** the voltage plateau at ~ 0.1 V was rapidly reached and remained nearly constant for around three hours and thus no cell polarization could be found implying a stable lithium deposition behavior. Afterwards, a small increase in overvoltage was observed (see inset of **Figure 37**) which probably resulted from kinetic limitations, possibly leading to a slow growth of lithium dendrites. However, this polarization seems to be reversible and does not result in a rapid cell failure or short circuit as can be seen from the stable long-term overvoltage, which showed only a small increase over ~ 300 hours (see also the corresponding EIS data **Figure 103**).

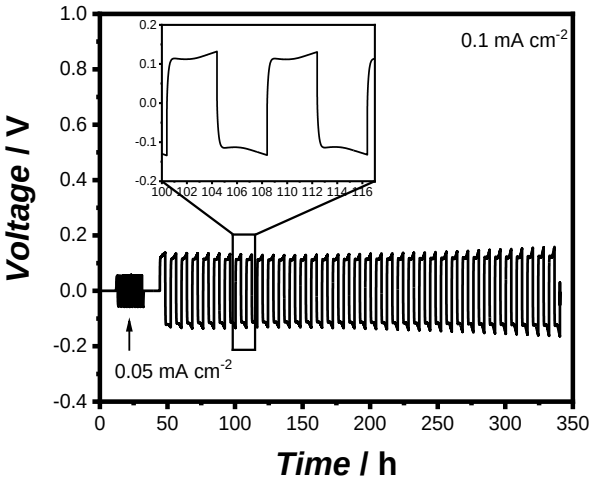

Figure 37. Conditioning using 0.05 mA cm^{-2} for 10 cycles. Afterwards, lithium was constantly plated and stripped with a current density of 0.1 mA cm^{-2} for four hours over a total of 296 hours.

Moreover, the influence of different current densities (**Figure 38**) was evaluated by gradually increasing the latter from 0.1 to 0.3 mA cm^{-2} in intervals of 10 cycles. In addition, the cell was allowed to cycle for 10 cycles at 0.1 mA cm^{-2} between two intervals. As summarized in **Figure 38**, it was found that the application of a current density of 0.3 mA cm^{-2}, led to a swift increase of the overall overvoltage and to a severe polarization during one cycle (see inset of **Figure 38**), whereas a stable voltage plateau at 0.1 V and 0.25 V was reached for current densities of 0.1 and 0.2 mA cm^{-2}, respectively. This polarization originated from concentration gradients within the electrolyte as a result of an insufficient Li^+ transport and resulted in a considerable dendrite growth that cannot be suppressed by the morphology, hence, leading to a cell failure for current densities higher than 0.3 mA cm^{-2}. However, compared to a pure PEO-based SPE, for which a short circuit is quickly observed at 0.2 mA cm^{-2}, the limiting current density shown here is significantly increased with an even lower ionic conductivity.[221]

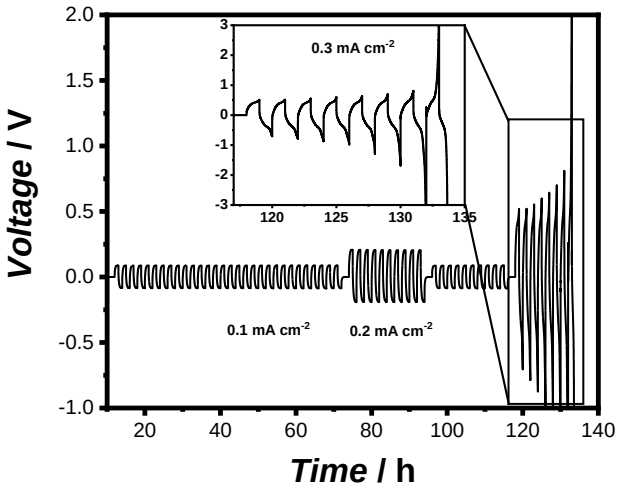

Figure 38. Lithium plating stripping with alternating current densities with 10 cycles at 0.1 mA cm^{-2} in between.

To corroborate the current density limitations derived from plating and stripping experiments, LSV was conducted with symmetrical Li|SPE|Li cells (**Figure 39**). The plateau at a current density of ~ 0.3 mA cm^{-2} is assumed to be the limiting current density and is in good agreement with the current density limitations previously identified in plating and stripping experiments. As indicated before, the limiting current density is higher compared to literature-known PEO-based SPEs comprising comparable or even significant higher ionic conductivities, thus underlining the beneficial interplay between mechanical stability provided by the PS domain, resulting in suppression of dendritic growth, and the ion conduction derived from the PEO-based domain once more.[221–223]

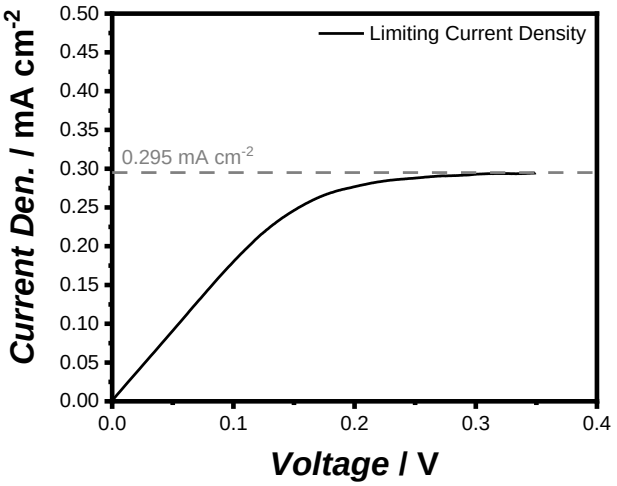

Figure 39. LSV measurement in a Li||Li cell with a sweep rate of 0.02 mV s^{-1} to identify the limiting current density derived from the plateau.

4.4.6 Galvanostatic Cycling and Rate Capability

After the promising results regarding the electrochemical stability against high voltage cathodes as well as stable Li|SPE interfaces, long-term constant current cycling and rate capability tests were conducted in Li||NMC622 full cells. Constant current cycling was performed at 60 °C and a rate of 0.1 C (**Figure 40a**, corresponding EIS data **Figure 104**). Remarkably, neither a rapid cell failure nor a commonly described voltage noise, both usually associated with the combination of PEO-based PEs and NMC622[14,15,150] was observed over the course of 100 cycles (**Figure 40b**). These results strongly support the recent findings regarding the compatibility of the use of PEO-based electrolytes in combination with NMC cathodes. Homann *et al.* showed that the voltage noise/rapid cell failure might not be caused by an insufficient oxidative stability, but rather reflect an insufficient mechanical stability and eventually Li-dendrite penetration.[14] However, if sufficient mechanical stability[15,150] or electrolyte thickness (e.g. 800 µm)[14] is provided, dendrite penetration (and thus voltage noise and rapid cell failure) are suppressed or prolonged, respectively. Although, the employed **BPE2000** films featured a thickness of only ~ 100 µm, the provided mechanical stability (G' = 1 MPa for the bulk material, up to G' = 1 GPa within the PS domain) due to the PS domain allowed for the successful cycling in Li||NMC622 full cells, which supports the statement that PEO-based SPEs can be used with NMC622 as long as a sufficient mechanical stability is guaranteed. Nonetheless, the cells did still show a noticeable capacity fading in comparison to other reports on non-PEO-based SPE classes in combination with NMC.[217] However, each SPE class features their own advantages and disadvantages in terms of performance, but also availability and affordability, thus complicating a direct comparison. Still, the origin of the capacity fading needs to be evaluated in more detail in upcoming studies in order to target an efficient cycling of PEO-based SPEs in Li||NMC622 cells.

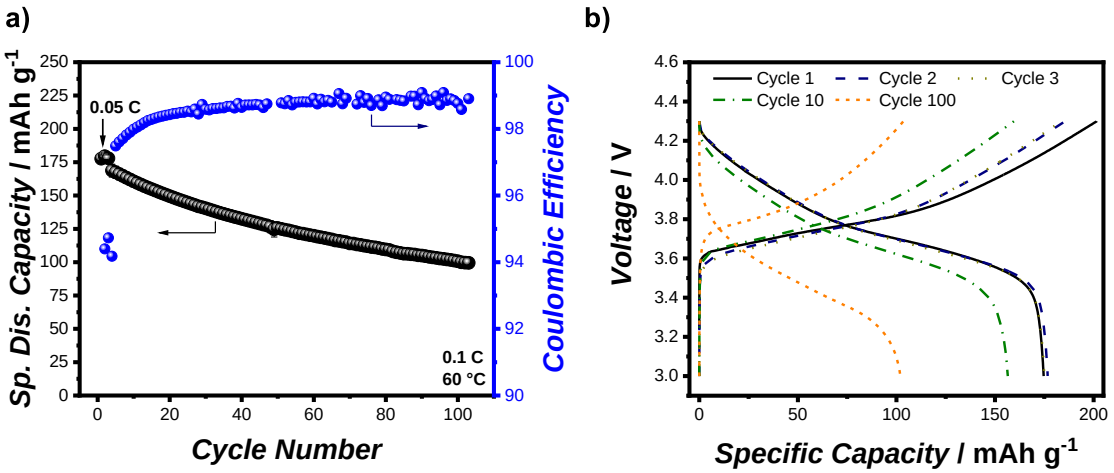

Figure 40. a) Constant current cycling at 0.1 C of Li|BPE2000|NMC622 cells at 60 °C. **b)** Selected charge and discharge profiles of different cycles. Notably no voltage noise or rapid cell failure was observed.

In addition, the rate capability was evaluated by variation of the charge rate, while the discharge rate was kept constant at 0.1 C. At 0.5 C, the cells retain 80% of the initial specific capacity and a severe decrease of the capacity retention merely occurred at C-rates higher than 0.66 C (**Figure 41a** and **41b**), which is in good agreement with the measured limiting current density, resulting in sufficient capacity retention until a current density of ~ 164 mA g^{-1} (180 mA g^{-1} = 1 C). The provided ionic conductivity of the PEO-based electrolytes was too low to enable a sufficient Li^+ transport at higher C-rates. Here, probably kinetic limitations resulted in a blocking type polarization and thus a massive decrease in available capacity.[223] This behavior can be seen in **Figure 41b** where a steep voltage increase is visible for 1, 2 and 5 C without a noticeable gain in capacity. Nevertheless, even at those high C-rates neither voltage noise nor rapid cell failure were observed as shown in **Figure 41b**, which is another proof for the enormous potential of **BPE2000**.

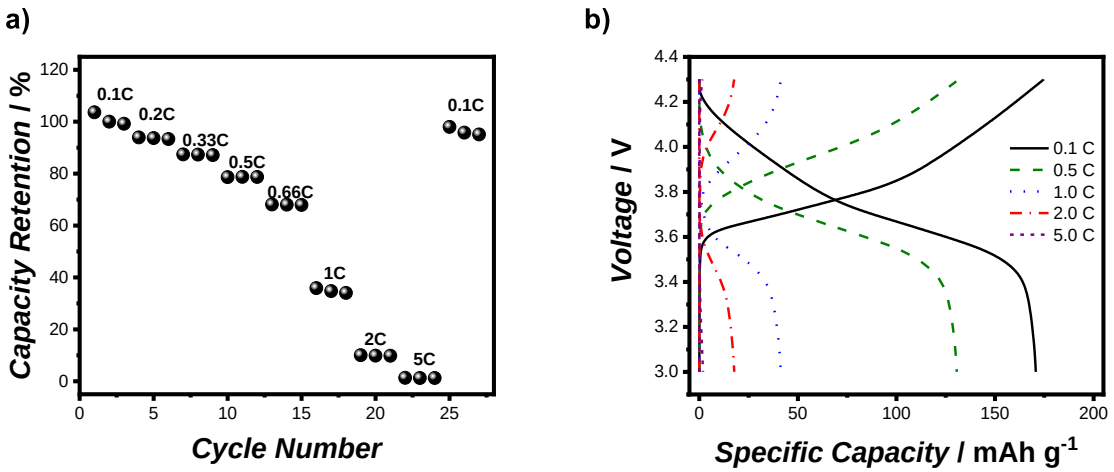

Figure 41. a) Rate capability tests (varying charge rate; 100% corresponds to ~ 172 mAh g^{-1}) of Li|BPE2000|NMC622 cells at 60 °C. **b)** Selected charge and discharge profiles of different C-rates. Notably no voltage noise or rapid cell failure was observed.

To overcome the capacity fading as well as the limited C-rate capability in a first instance, it is necessary to enhance the ionic conductivity of **BPE2000**. For this, the implementation of additives such as plasticizers is one of the most commonly applied approaches.[17,23,24,215] However, for bulk materials, plasticizers do not only increase the mobility of chains (and thus decrease the T_g), but also decrease the mechanical stability as a consequence, resulting again in issues with accelerated lithium dendrite growth. In this regard, block copolymers such as **BP2000** can be designed in a sophisticated way to allow for the selective implementation of plasticizers into the PEO domain, while maintaining an untouched PS domain, thus – when properly balanced – resulting in an increased ionic conductivity without a decreased mechanical stability. This possibility in combination with the straightforward synthesis of the styrene-based PEO side chain block copolymers shows once more the huge potential of this type of material, since it allows for a simple decoupling of the implementation of additives and mechanical stability, which is hard to achieve by other methods. Thus, further studies will focus on optimizing the here presented SPE using non-volatile additives in order to enhance the ionic conductivity while still featuring a ‘dry’ SPE.

4.4.7 Recapitulation

Herein, the straightforward synthesis of an inexpensive and fully ‘dry’ polymer electrolyte based on styrene featuring PEO side chains was introduced, overcoming both common drawbacks of comparable systems, namely on the one hand the tedious synthesis of PS-*b*-PEO as well as on the other hand the insufficient stability of PS-*b*-POEGMA block copolymers. The sophisticated architecture allowed to a) reduce crystallization, b) enable a microphase separation with long-range order, resulting in c) a good mechanical stability (G’ = 1 MPa for the bulk material, up to G’ = 1 GPa within the PS domain) and d) a good ionic conductivity decoupled from the mechanical stability. First, the impact of different LiTFSI ratios as well as different side chain lengths on the ionic conductivity and the thermal properties were briefly examined, showing that a [LiTFSI]:[EO] ratio of 1:15 and a relatively long side chain with around 45 EO repeating units exhibited a reasonably high ionic conductivity of 1.6×10^{-2} mS cm^{-1} at 25 °C. Subsequently, the SPE comprising the highest ionic conductivity was further analyzed in detail. It was shown that the PS and PEO-based domains are separated on a microscopic level forming a long-range ordered, most probably lamellar block copolymer morphology as suggested by SAXS data, allowing for the preparation of an overall flexible, self-standing film featuring a good mechanical stability provided by the high modulus PS domains as well as a good wettability provided by the low modulus PEO domains (**Figure 42**).

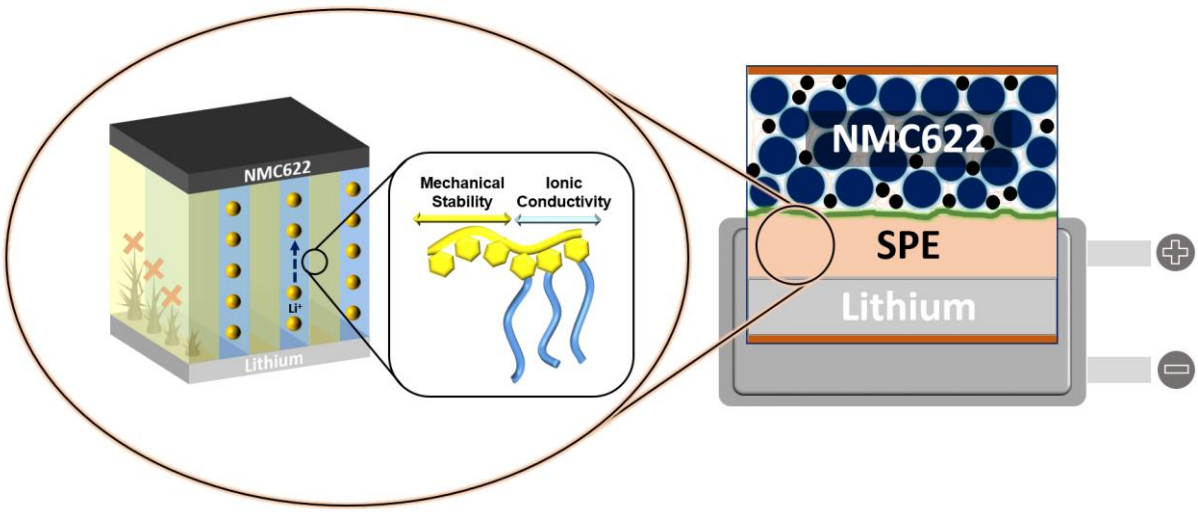

Figure 42. Schematics of dendrite suppression by microphase separation of block copolymers. As soon as a dendrite is in contact with the mechanically rigid block, its growth is stopped or significantly slowed down, depending on mechanical or local electric field effects.

A sufficient oxidative stability at voltages beyond 4.75 V was found using both potentiostatic and galvanostatic techniques as well as different electrodes and active materials, which demonstrated relevant compatibility with high voltage cathode materials such as NMC622. A stable Li|SPE interface was proven from LSV/CV as well as lithium stripping/plating tests over 1000 hours and a comparable high limiting current density of 0.3 mA cm^{-2} was derived with respect to the provided ionic conductivity as consequence of improved mechanical stability. Full cell cycling in Li||NMC622 cells did not show any indication of rapid cell failure or the presence of voltage noise, unlike previously associated with the combination of PEO-based SPEs and NMC622, thus supporting the recently proposed opinion that sufficient mechanical stability is necessary for PEO-based SPEs to be applicable in combination with high voltage cathodes, such as NMC622 (**Figure 42**). Moreover, it was shown that such microphase separated PEO-based SPEs are of high interest for the next generation of high voltage lithium-metal batteries, providing a straightforward and inexpensive approach for polymer-based energy storage solutions. In contrast to Bolloré's state-of-the-art LMP® technology, the replacement of LFP with high voltage cathodes such as NMC622 increases the SSBs performance in terms of energy density and costs and thus might promote the applicability of SPEs in SSB.[18] Nonetheless, the present SPE is still limited by its ionic conductivity in a practical point of view and noticeable capacity fading in combination with NMC622. To overcome this issue, further studies focusing on enhancement of the ionic conductivity, while maintaining all the other beneficial properties, are covered in the following chapter. This will not only allow for higher C-rates but also enable long-term cycling at lower temperatures, thereby circumventing parasitic processes. Moreover, the origin of capacity fading should be examined to drive forward the application of inexpensive PEO-based SPEs in high voltage lithium-metal batteries.

4.5 Advanced Block Copolymer Design for Polymer Electrolytes: Prospects of Microphase Separation

This chapter deals with the improvement of the PEs established in **Chapter 4.4**. To do so, a strategy was developed based on the inclusion of plasticizers into the conducting phase of the PE without affecting the mechanical stability, thus offering a potential solution to the mechanical stability/ionic conductivity dilemma. This was achieved by selectively plasticizing only the conducting domain of the previously synthesized block copolymers with ionic liquids (ILs) while synthetically adjusting the PS domain accordingly to provide mechanical stability. The prepared PE films and membranes were characterized by thermal and electrochemical methods, corroborating microphase separation, the selective implementation of ILs, the enhanced ionic conductivity and thus the intended concept.

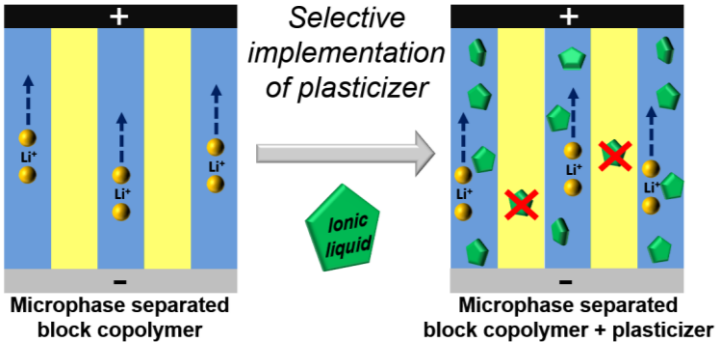

Figure 43. The selective implementation of ILs as plasticizer allows for an enhanced mechanical stability of PEs in contrast to common plasticized PEs.

Parts of this chapter and the corresponding parts in the experimental section were adapted with permission from a publication written by the author (Andreas J. Butzelaar).[224]

4.5.1 Strategy

Herein, the microphase separation of block copolymers was utilized to selectively plasticize the conductive domain, thus maintaining the mechanical stability provided by the other domain. Taking advantage of this principle, the PS-based PEO side chain block copolymers (**PVBmPEO2000-*b*-PS**)[192] introduced in **Chapter 4.4** were employed and block copolymers with four different PS:PVBmPEO2000 ratios were synthesized. To do so, **PVBmPEO2000-*b*-PS** was chosen as starting point and the length of the PS block was simply increased, while the degree of polymerization of the PEO side chain block (*i.e.*, PVBmPEO2000) was retained constant. Afterwards, a defined amount of plasticizer was implemented into the PVBmPEO2000 phase (creating the 'conducting phase') in order to reach a final ratio of PS to conducting phase that enabled the formation of self-standing films (**Figure 44**).

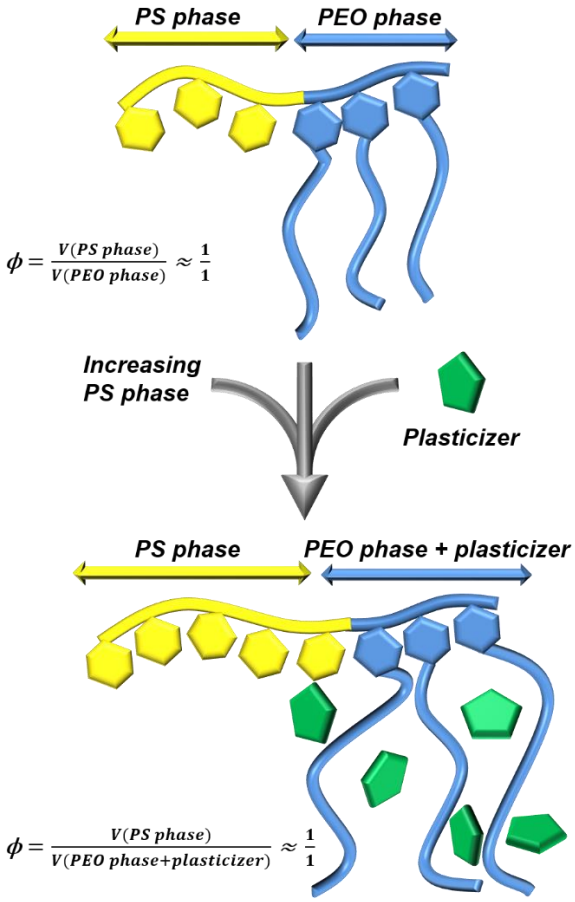

Figure 44. Schematics of the selective implementation of plasticizer into the conducting PEO side chain phase, while adjusting the PS phase synthetically. The retained block volume ratio (ϕ) of around 1:1 ensures great self-standing film properties, while the microphase separation guarantees enhanced ionic conductivity and good mechanical stability due to the unaffected PS phase.

As model compounds for the implemented plasticizer, two ionic liquids (ILs), namely $Pyr_{14}TFSI$ and $Pyr_{O7}TFSI$ (structures shown in **Scheme 23**), were employed because of their high ionic conductivity, high thermal stability, large electrochemical window, their negligible vapor pressure and their known non-miscibility with PS.[127]

Pyr_{14} TFSI **Pyr_{O7} TFSI**

Scheme 23. Chemical structures of 1-butyl-1-methylpyrrolidinium bis(trifluoromethylsulfonyl)imide ($Pyr_{14}TFSI$) and 1-oligo(ethylene oxide)-1-methylpyrrolidinium bis(trifluoromethylsulfonyl)imide ($Pyr_{O7}TFSI$).

4.5.2 Synthesis

Block copolymers with different block ratios were synthesized to obtain a series of polymers featuring the inherent property to show microphase separation due to the difference in their mixing parameter χ.[225] To do so, **PVBmPEO2000-*b*-PS** with a block ratio of around 20 kg mol^{-1}: 20 kg mol^{-1} was taken as starting point and the PS domain was incrementally increased. Thus, using the same macro-RAFT agent approach as in **Chapter 4.4** a simple increase of the amount of styrene for the chain extension was sufficient (**Scheme 24**).

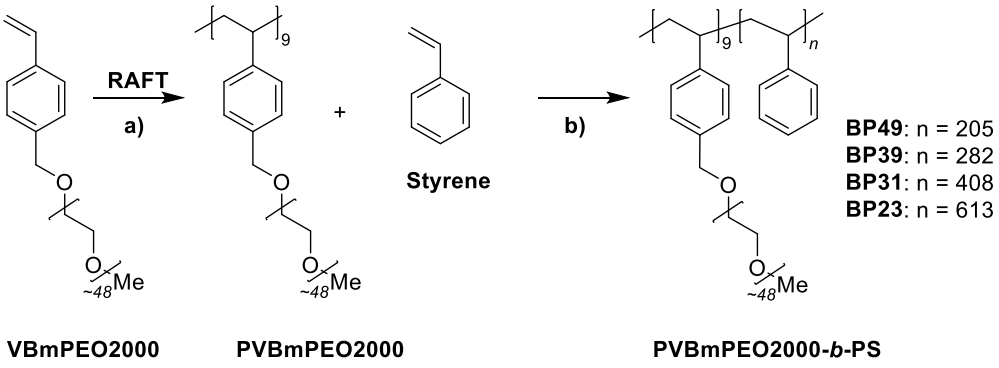

Scheme 24. Block copolymer synthesis by **a)** polymerization of **VBmPEO2000** giving **PVBmPEO2000** as macro-RAFT agent. Subsequently, an increasing amount of styrene was used for the chain extension **b)** yielding **PVBmPEO2000-*b*-PS** comprising different block ratios (denoted as **BP*w*** where '*w*' refers to *w*(PVBmPEO2000); see **Table 12**). Molar ratios were calculated by comparison of the integrals in ^{1}H-NMR spectroscopy.

Hence, the application of straightforward RAFT polymerization allows for a fast and efficient synthesis of all these different compositions in a controlled manner with low dispersities ($Đ$ ~ 1.1 – 1.2) (**Figure 45**, **Table 12**), showing once more the synthetic advantage of this approach in comparison to e.g. PS-*b*-PEO synthesized by AP.

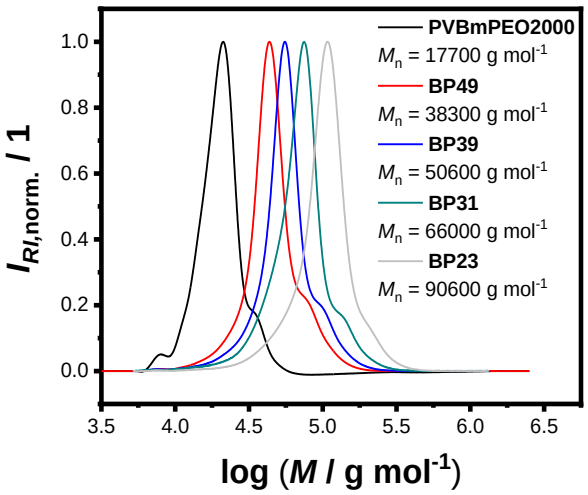

Figure 45. SEC traces of the macro-RAFT agent **PVBmPEO2000** as well as the respective block copolymers **BP49**, **BP39**, **BP31** and **BP23** after chain extension with styrene. SECs were measured in THF, using PS as calibration standard.

^{1}H-NMR spectroscopy was employed to determine the block ratios with respect to its composition and, as a result, its molar mass as depicted in **Scheme 24** and **Table 12**. Block copolymers with a block weight ratio of PVBmPEO2000:PS of 0.49 (being identical to BP2000 in **Chapter 4.4**), 0.39, 0.31 and 0.23 were obtained, respectively. These specific ratios were chosen to ensure a sufficient difference between all compositions, thus emphasizing the change in properties for subsequent analyses. The lowest ratio was 0.23 (*i.e.*, the block copolymer with the longest PS chain) because reaching even higher molar masses is challenging using RAFT polymerization on the one hand, while a ratio of 0.23 already enables the implementation of an enormous amount of plasticizer on the other hand. In order to calculate the volume ratio (ϕ) of both blocks, the densities for PS as well as PEO were used (**Table 12**). However, this calculation is not 100% correct because PEO is attached as side chains to PS and thus the density may differ slightly to that of pure PEO. Hence, it was decided to denote the block copolymers as **BP*w***, where '*w*' is referring to the respective weight ratio of PVBmPEO2000 in the block copolymer as shown in **Table 12**.

Table 12. Overview of the different **PVBmPEO2000-*b*-PS** block copolymers (denoted as **BP*w*** where '*w*' refers to *w*(PVBmPEO2000)).

Entry	Polymer	M_n[§] [g mol^{-1}]	$Đ$[§]	*w*(PVBmPEO2000)[*]	ϕ(PVBmPEO2000)[#]
1	**PVBmPEO2000**	17 700	1.10	1	1
2	**BP49**	38 300	1.16	0.49	0.46
3	**BP39**	50 600	1.17	0.39	0.36
4	**BP31**	66 000	1.15	0.31	0.28
5	**BP23**	90 600	1.20	0.23	0.21

[§]Determined by SEC in THF using PS standards. *Calculated by integration of the respective signals in ^{1}H-NMR spectroscopy. [#]Calculated using the densities of PS (1.07 g cm^{-3}) and PEO (1.21 g cm^{-3}). Noteworthy, this calculation is not 100% correct because PEO is attached as side chain.

4.5.3 Polymer Electrolytes

Next, the block copolymer series **BP*w*** was used to prepare PE films showing microphase separation by addition of LiTFSI as conductive salt. Moreover, the addition of plasticizer should increase the ionic conductivity, the weight and thus the volume of the conducting phase, while still guaranteeing self-standing films by targeting an appropriate volume ratio of the two phases. This ability to form self-standing films facilitates the manufacturing of battery cells, but is also necessary to create stable interfaces and a resistance against lithium dendrite growth.

Furthermore, the choice of the implemented plasticizer is of essential interest. Obviously, the plasticizer should decrease the T_g of the conducting PEO phase, thus enhancing segmental motion and consequently increasing the ionic conductivity.[118,226] However, in this particular case it also is essential that the plasticizer is selectively infiltrating the conductive phase only, since plasticization of the PS phase would be counterproductive. Additionally, the plasticizer should be non-volatile, since it is necessary to control the optimized ratio of all ingredients exactly to form self-standing films. Thus, ILs were chosen as the candidate of choice because they fulfill all required demands: high ionic conductivity, high ability to plasticize PEO, no volatility and no miscibility with PS.[227]

Subsequently, Pyr_{14}TFSI was selected as one of the ILs of choice, due to the before-mentioned properties, its frequent application and readily availability.[151,216] Recently however, it has been reported that the incorporation of Pyr_{14}TFSI drastically decreases the lithium-ion transference number (t_{Li^+}) of a pure cross-linked PEO-based PE. To overcome this drawback, the butyl chain attached to the pyrrolidinium cation was replaced by a PEO chain bearing around 7 EO repeating units, thus giving Pyr_{O7}TFSI. Using this IL, not such a drastic drop in t_{Li^+} was detected, therefore providing an overall superior electrochemical performance.[215] Nevertheless, both Pyr_{O7}TFSI and Pyr_{14}TFSI were investigated as potential IL candidates, since it was possible to incorporate much higher amounts of Pyr_{14}TFSI in the PEO graft block copolymers in comparison to linear PEO reported in the literature.[215,216,228] It was therefore hypothesized that t_{Li^+} would rise again once a certain threshold concentration of IL is exceeded due to the formation of IL-dominated channels inside the PEO phase.[127]

First, the series of block copolymers **BP*w*** was investigated semi-empirically to determine the maximum amount of IL that can be incorporated while retaining the ability to form flexible but self-standing films (**Figure 46**). To do so, the [LiTFSI]:[EO] ratio was fixed to 1:10, which was a slightly higher LiTFSI content than in **Chapter 4.4** (1:15), because a slight increase was expected to be necessary to compensate for the addition of IL, which would lower the overall

concentration again. Additionally, this allows for a better comparison to other literature studies, in which a ratio of 1:10 is frequently used. Consequently the obtained PEs of polymer series **BP*w*** are denoted as **BPE*w*$_{\mathbf{IL,[LiTFSI]:[EO]}}$**, where '*w*' corresponds to the weight ratio of PVBmPEO2000, 'IL' to the type of IL used (either '$_{14}$' = Pyr$_{14}$TFSI or '$_{O7}$' = Pyr$_{O7}$TFSI) and '[LiTFSI]:[EO]' to the ratio between lithium ion and the EO repeating units.

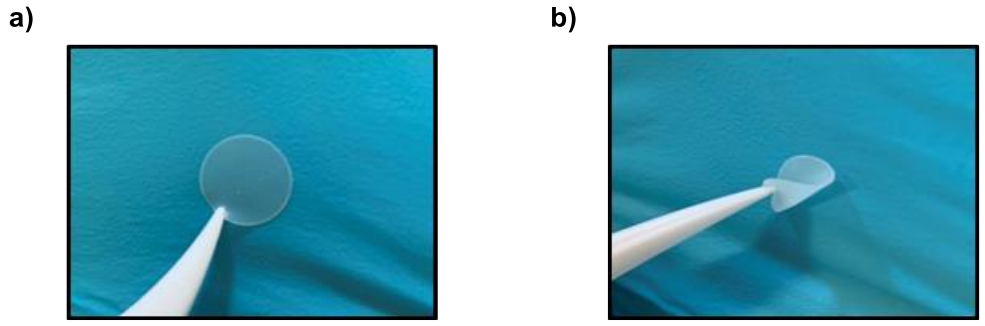

Figure 46. Exemplary pictures of the self-standing films (10 mm diameter, 100 µm thickness) derived from block copolymer electrolyte **BPE$_{O7,1:7.5}$** showing its great flexibility.

As shown in **Table 13**, different amounts of 50, 150 and 288 wt% of both ILs were incorporated with respect to the weight of the PVBmPEO2000 phase for **BPE39$_{IL,1:10}$**, **BPE31$_{IL,1:10}$** and **BPE23$_{IL,1:10}$**, respectively. Interestingly, the weight ratio of the resulting conductive phase featured a value of around 0.58 for all different compositions. Having in mind that the density of PS is slightly lower (1.07 g cm^{-3}), than the density of PEO, LiTFSI and the ILs (all with densities ~ 1.2 – 1.4 g cm^{-3}) it seems that the volume ratio of both phases must be still in the range of 0.5, providing a good ratio of volume and mechanical stability of each domain in order to form overall flexible self-standing films as exemplary shown in **Figure 46**. Furthermore, the molar contents of LiTFSI were increased for the highest amount of Pyr$_{O7}$TFSI introduced (**BPE23$_{O7}$**), since here each ion pair of IL already adds seven more EO units into the conductive phase, thus decreasing the overall [LiTFSI]:[EO] ratio.

Table 13. Overview of the incorporated amount of LiTFSI, the added amount of IL and the resulting conductive phase of the different polymer electrolytes **BPE*w*$_{IL,[LiTFSI]:[EO]}$.**

Entry	PE	[LiTFSI]:[EO]*	IL	*w*(added IL)[#]	*w*(resulting cond. phase)[§]
1	**BPE49$_{1:15}$**	1:15	-	0	0.58
2	**BPE39$_{14,1:10}$**	1:10	$Pyr_{14}TFSI$	0.50	0.58
3	**BPE39$_{O7,1:10}$**	1:10	$Pyr_{O7}TFSI$	0.50	0.58
4	**BPE31$_{14,1:10}$**	1:10	$Pyr_{14}TFSI$	1.50	0.58
5	**BPE31$_{O7,1:10}$**	1:10	$Pyr_{O7}TFSI$	1.50	0.58
6	**BPE23$_{14,1:10}$**	1:10	$Pyr_{14}TFSI$	2.88	0.57
7	**BPE23$_{O7,1:10}$**	1:10	$Pyr_{O7}TFSI$	2.88	0.57
8	**BPE23$_{O7,1:7.5}$**	1:7.5	$Pyr_{O7}TFSI$	2.88	0.58
9	**BPE23$_{O7,1:5}$**	1:5	$Pyr_{O7}TFSI$	2.88	0.60

*With respect to EO units in the polymer. [#]With respect to the weight of the PVBmPEO2000 phase. [§]Calculated by $w = \frac{m(PVBmPEO2000) + m(LiTFSI) + m(IL)}{m(PVBmPEO2000) + m(LiTFSI) + m(IL) + m(PS)}$

4.5.4 Thermal and Morphological Characterization

In the next step, DSC measurements of all PE films were conducted (**Figure 47**). Although this technique is often only used to report thermal phase transitions for a polymer, it represents in this case an essential and powerful tool to reveal multiple essential properties with just one measurement. First, fully amorphous PEs were obtained for all studied combinations as observed by the absence of any melting point. Next, the microphase separation itself was also proven for all PE films by detection of a T_g for the PEO-based conductive phase in the range of -50 to -75 °C as well as a T_g for the PS phase at around 105 °C. The high and constant T_g of the PS phases, which was equal to the T_g of pure PS in all cases,[193] evidenced substantial phase separation and the selective mixing of the IL only within the conductive phase. Moreover, an increase of the IL content was found to significantly decrease the T_g of the PEO-based phase, starting from a T_g of around -47 °C for the non-plasticized **BPE49$_{1:15}$** (see **Figure 32b**), over ~ -53 °C for both **BPE39** and ~ -62 °C for both **BPE31** IL combinations (**Figure 47a** and **b**). The T_g of the Pyr$_{14}$TFSI-based PEs were observed to be generally slightly lower than its Pyr$_{O7}$TFSI-based counterparts. This behavior was in particular visible when comparing both ILs using **BPE23**. Here, an significant increase of Pyr$_{14}$TFSI (~ 2 times) when comparing **BPE31$_{14,1:10}$** and **BPE23$_{14,1:10}$** lowered the T_g from -62 °C to -74 °C (**Figure 47a)**, whereas for Pyr$_{O7}$TFSI only a decrease from ~ -61 °C to ~ -65 °C was observed (**Figure 47b**). This can be explained by incrementally reaching the inherent T_g of pure Pyr$_{O7}$TFSI itself which was reported to be at around -69 °C.[215] Due to the lower molar mass and thus higher number of equivalents of Pyr$_{14}$TFSI compared to Pyr$_{O7}$TFSI, when the same weight ratios are employed, a higher 'plasticizing effect' and thus lower T_gs were observed for Pyr$_{14}$TFSI. Further, the two compositions of **BPE23$_{O7}$** with higher LiTFSI contents (**BPE23$_{O7,1:7.5}$** and **BPE23$_{O7,1:5}$**) featured higher T_gs in comparison to their counterpart **BPE23$_{O7,1:10}$** as a result of a higher number of *quasi-ionic cross-links* among PEO chains due to coordination of additional lithium ions and thus a slight immobilization.[27,29]

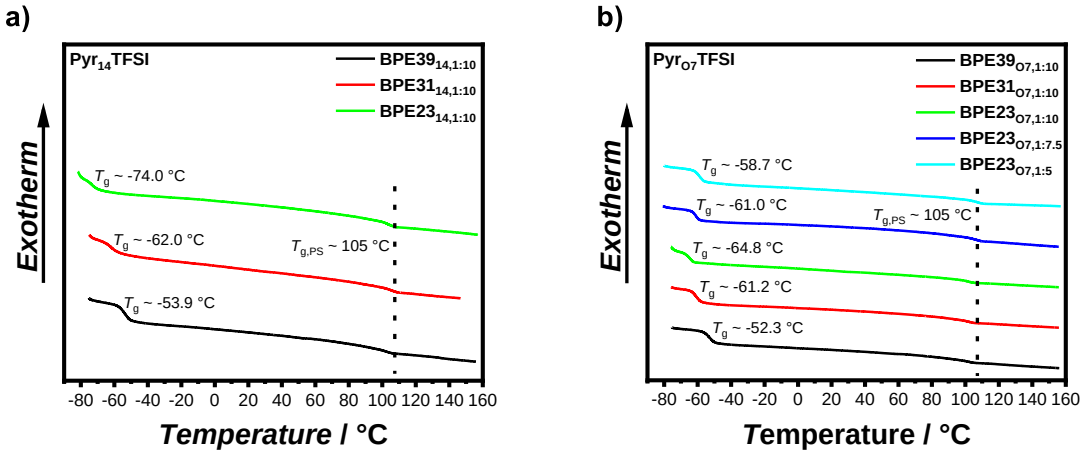

Figure 47. DSC analyses of all manufactured polymer electrolytes using either **a)** $Pyr_{14}TFSI$ or **b)** $Pyr_{O7}TFSI$ as IL. All polymer electrolytes show a microphase separated morphology by showing a T_g for the conductive, PEO-based phase as well as the T_g of the PS phase.

Additionally, exemplary TGA measurements were conducted to verify the solid character and non-volatility of the films and their ingredients. For this, **$BPE23_{14,1:10}$** and **$BPE23_{O7,1:10}$** were investigated, both comprising the highest relative amount of IL and thus possibly showing the biggest difference in comparison to the non-plasticized reference **$BPE49_{1:15}$**. As displayed in **Figure 48**, the reference PE **$BPE49_{1:15}$** showed a decomposition temperature at 5% weight loss (T_{d5}) of 331 °C. Both plasticized PEs featured decomposition temperatures in the same range: **$BPE23_{14,1:10}$** had a slightly higher T_{d5} of around 353 °C whereas **$BPE23_{O7,1:10}$** featured a slightly lower T_{d5} of around 317 °C, yet both PEs showed a high thermal stability and are in accordance with the literature.[215]

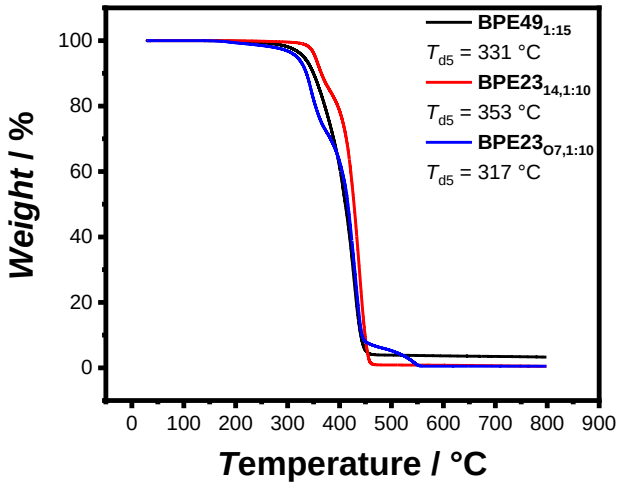

Figure 48. a) Exemplary TGA thermograms of **BPE49$_{1:15}$** (T_{d5} = 331 °C), **BPE23$_{14,1:10}$** (T_{d5} = 353 °C) and **BPE23$_{O7,1:10}$** (T_{d5} = 317 °C).

Next, the microphase separated structure was further corroborated by SAXS measurements of all films. **Figure 49a** displays an exemplary spectrum of **BPE23$_{14,1:10}$**. The detection of a primary peak at a scattering vector (q) of q^* = 0.101 nm^{-1} confirmed the microphase separation. Moreover, the presence of additional maxima at 2q^* 3q^* and 4q^* revealed a long-range ordering, which is indicative for a lamellar morphology.[229] As seen in **Figure 105 - Figure 109**, all films featured these characteristic scattering peaks of a microphase separated, lamellar morphology. Thus, all films behaved exactly as intended, taking into account that the volume ratio of both domains was fixed at around 1:1 over the course of the series of polymers in order to guarantee the formation of self-standing films.

Furthermore, the average domain spacing (d) was calculated for all films using **Equation 1** (see **Chapter 4.4.4**). Since the domain spacing of **BPE49$_{1:15}$** was found to be ~ 28 nm, all other films were expected to feature larger domain spacings due to the higher molar mass and thus volume of the domains.[154] As shown in **Figure 49b**, the measured domain spacing increased as a function of IL content, which corresponds to an increase in domain size for both the PS domains as well as the conducting domains. Further, PEs with Pyr$_{O7}$TFSI seemed to feature a slightly larger domain spacing in comparison to their Pyr$_{14}$TFSI-based counterparts, probably as a result of the slightly different density.

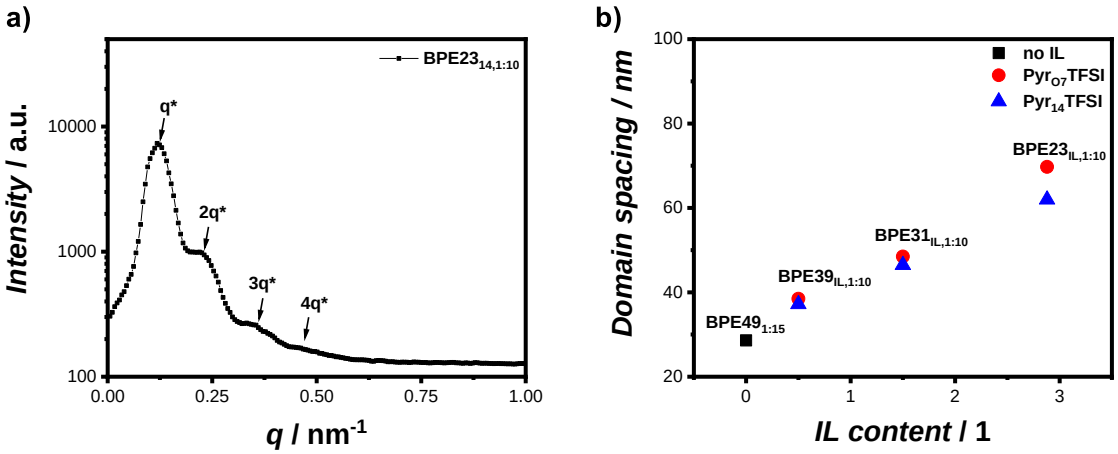

Figure 49. a) Exemplary SAXS spectrum of **BPE23$_{14,1:10}$** revealing the microphase separation as well as indicating a lamellar long-range order. **b)** Domain spacing of all **BPE$_{IL,1:10}$** samples as obtained by SAXS measurements.

Moreover, exemplary rheological measurements of **BPE23$_{O7,1:7.5}$** were conducted (**Figure 50**). For the non-plasticized **BPE49$_{1:15}$** values of G' of around 1 MPa and G'' of around 0.1 MPa were already reported in **Chapter 4.4**. However, the measurement of **BPE23$_{O7,1:7.5}$** revealed a G' of around 0.5 MPa and G'' of around 0.06 MPa, indicating that the PE films were slightly more flexible in comparison to the non-plasticized one. Nonetheless, these results were in line with the expectations since the volume ratio of both domains and the T_g of the PS domain remained constant, whereas the T_g of the conducting domain was slightly lower corresponding to a 'softer' behavior, consequently resulting in a slightly more flexible film. Nonetheless, it shall be noted that these findings do only show the bulk material properties and not the properties of each domain itself. As for **BPE49$_{1:15}$**, a rigid PS domain characterized by the high T_g of ~ 105 °C with a G modulus of around 1 GPa[211] can be expected, which is typical for amorphous, non-oriented polymers below their T_g, providing the required resistance towards lithium dendrite growth.[124,202]

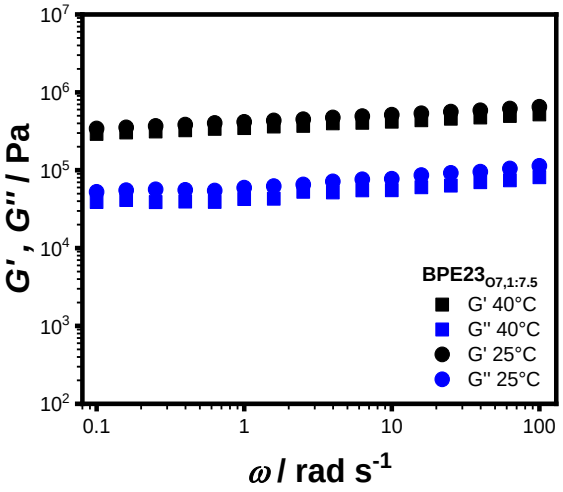

Figure 50. Exemplary oscillatory rheology measurement of **BPE23$_{O7,1:7.5}$** showing the bulk rheological behavior.

4.5.5 Ion Transport

After successfully demonstrating the concept of selective mixing of plasticizers into microphase separated block copolymers by thermal and morphological analyses, in-depth analyses of the ion transport in the above-described PEs were conducted. Thus, EIS measurements were performed for all PEs in a temperature range from 0 to 70 °C using blocking-type stainless steel electrodes to determine the IC. **Figure 51a** and **b** show the results of the series of block copolymer electrolytes with [LiTFSI]:[EO] ratios of 1:10 comprising either Pyr_{14}TFSI or Pyr_{O7}TFSI. The introduction of ILs significantly increased the IC over the whole temperature range even at low IL loadings, reflecting the lowered T_g in comparison to the non-plasticized sample on the one hand, as well as the increased amount of charge carriers on the other hand.[228,230,231] Secondly, higher IL loadings led to higher ICs, but the additional benefit decreased with higher IL contents: While the increase of ICs between 0 wt%, 50 wt% and 150 wt% was significant, it was not as pronounced between 150 wt% and 288 wt%, although the amount of IL was nearly twice as high (compare **Figure 51a** and **b**). This could be observed especially for Pyr_{O7}TFSI, where the difference between **BPE31$_{O7,1:10}$** and **BPE23$_{O7,1:10}$** was small. Such a trend was anticipated as the IC is approaching a 'limit' given by the inherent IC of the pure IL. Further, especially for Pyr_{O7}TFSI the difference in T_g was small, because the inherent T_g of the IL itself was approached at such high contents, meaning that no additional mobility is gained by the introduction of even higher amounts of IL.

Moreover, the ICs of the samples comprising Pyr_{14}TFSI as plasticizer were significantly higher than the ICs of PEs at 40 °C with Pyr_{O7}TFSI, e.g. 0.18 mS cm^{-1} for **BPE39$_{14,1:10}$** *vs.* 0.10 mS cm^{-1} for **BPE39$_{O7,1:10}$** or 0.90 mS cm^{-1} for **BPE23$_{14,1:10}$** *vs.* 0.28 mS cm^{-1} for **BPE23$_{O7,1:10}$**, respectively. Again, this was one the one hand attributed to the lower T_g and thus higher chain mobility of samples with Pyr_{14}TFSI and on the other hand to the fact that Pyr_{14}TFSI exhibited more charge carriers in the same mass due to the lower molecular weight. Even more, the implementation of those IL was found to improve the IC especially at lower temperatures. For Pyr_{14}TFSI a maximum improvement (**BPE49$_{1:15}$** *vs*. **BPE23$_{14,1:10}$**) of a factor of ~ 13 was reached at 70 °C while a factor of ~ 120 was reached at 0 °C. Pyr_{O7}TFSI showed the same trend, but resulted only in a factor of ~ 4.5 at 70 °C and a factor of ~ 20 at 0 °C.

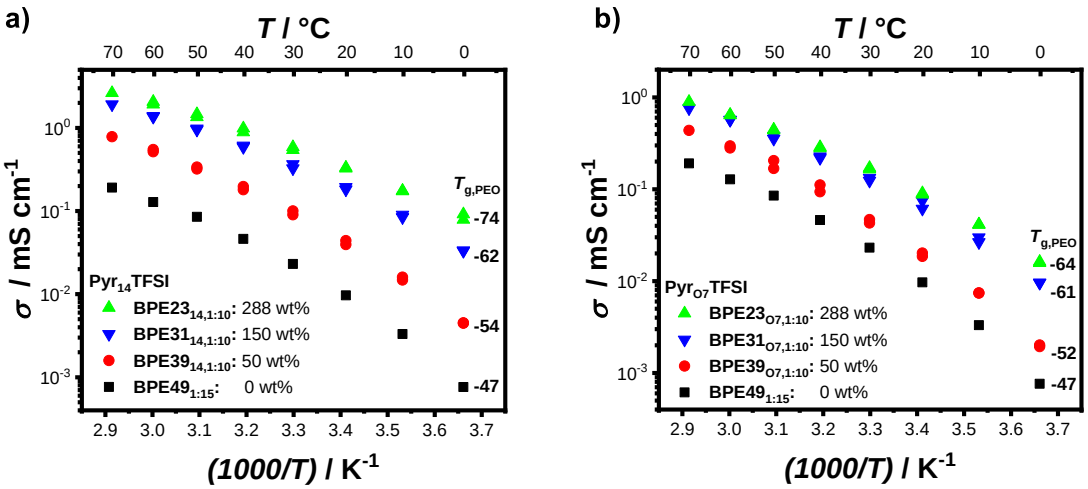

Figure 51. Ionic conductivity plots derived from EIS measurements of the series of polymer electrolytes using **a)** $Pyr_{14}TFSI$ and **b)** $Pyr_{O7}TFSI$ as plasticizers. Multiple visible data points show the slight difference between measurements during heating and cooling.

Furthermore, the ICs for **BPE23** with $Pyr_{O7}TFSI$ comprising different [LiTFSI]:[EO] ratios were compared. Since the initial [LiTFSI]:[EO] ratio was fixed at 1:10 corresponding to the EO units in the polymer, the overall concentration of LiTFSI decreased during the introduction of additional $Pyr_{O7}TFSI$ since each ion pair of IL adds seven more EO units to the conducting domain. As shown in **Figure 52**, **BPE23$_{O7,1:10}$** and **BPE23$_{O7,1:5}$** showed either higher IC at high or at lower temperatures, respectively, whereas **BPE23$_{O7,1:7.5}$** exhibited a higher IC than both other samples at all measured temperatures. Although **BPE23$_{O7,1:7.5}$** featured a higher T_g (~ -61 °C) in comparison to the T_g of **BPE23$_{O7,1:10}$** (~ -65 °C), the increased amount of charge carriers seemed to lead to an overall improved IC due to an optimized overall [LiTFSI]:[EO] ratio.

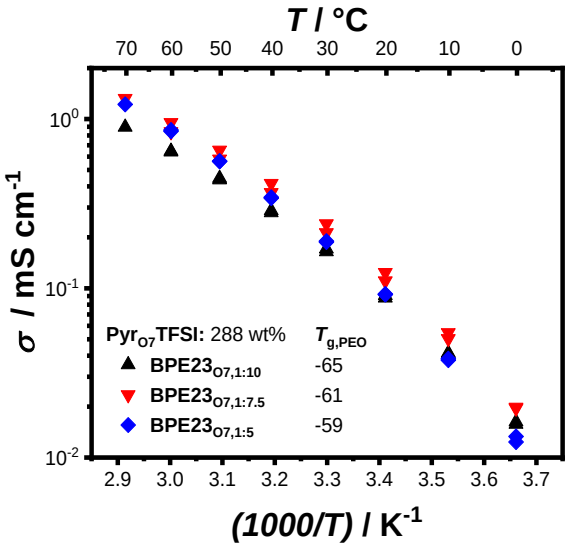

Figure 52. Comparison of the ionic conductivity of **BPE23$_{O7,1:10}$**, **BPE23$_{O7,1:7.5}$** and **BPE23$_{O7,1:5}$**. Multiple visible data points show the slight difference between measurements during heating and cooling.

Next, the impact of different compositions on the Li^+ transference number (t_{Li^+}) was evaluated. This is of particular interest since the implementation of ILs into PEO often not only drastically increases the IC but also decreases the t_{Li^+}.[215,232] Thus, a lot of 'unproductive' ion movement of all charge carrying ions is detected, while only a small fraction actually contributes to the overall battery performance. By determining the t_{Li^+} and subsequently calculating the overall Li^+-IC (σ_{Li^+}) an overall picture can be drawn, revealing the actual benefit of the implementation of ILs. It should be mentioned that the literature concerning ternary PEs comprising PEO, LiTFSI and ILs often do not report transference numbers rendering unambiguous comparison of the results difficult. Nonetheless, recently Atik *et al.* highlighted the importance of t_{Li^+} by revealing a superior performance of Pyr_{O7}TFSI in comparison to Pyr_{14}TFSI, mainly attributed to the higher transference number despite the lower overall IC.[215]

The method of Evans *et al.*[212] was employed to determine the t_{Li^+} of all PEs at a temperature of 40 °C. As shown in **Figure 53**, the non-plasticized **BPE49$_{1:15}$** showed a t_{Li^+} of ~ 0.127, which is in the typical range for PEO-LiTFSI-based PEs.[28,156,215] However, an introduction of 50 wt% of IL (sample **BPE39$_{IL,1:10}$**) resulted in a decrease of t_{Li^+} to 0.035 and 0.081 for Pyr_{14}TFSI and Pyr_{O7}TFSI, respectively. Already at this low content, a large difference between both ILs in terms of their impact on the t_{Li^+} became evident. For PEs bearing even higher amounts of IL, this remarkable gap became even more pronounced, *i.e.* t_{Li^+} = 0.015 *vs.* 0.060 for **BPE31$_{14,1:10}$**

vs. **BPE31$_{O7,1:10}$** and finally t_{Li^+} = 0.009 *vs.* 0.059 for **BPE23$_{14,1:10}$** *vs.* **BPE23$_{O7,1:10}$**, respectively. Similar observations were reported previously, but not for compositions featuring that high IL contents compared to PEO.[215] Thus, it was assumed that once a certain threshold would be reached, t_{Li^+} would rise again for $Pyr_{14}TFSI$ likely due to formation of 'IL-dominated channels' where a higher transference number similar to the reported transference number of pure $Pyr_{14}TFSI$[127,233–235] could possibly be achieved. This, however, was not the case. Instead, t_{Li^+} was reduced by a factor of ~ 14 when comparing **BPE23$_{14,1:10}$** with the initial non-plasticized **BPE49$_{1:15}$**. Interestingly, t_{Li^+} of **BPE31$_{O7,1:10}$** and **BPE23$_{O7,1:10}$** remained nearly constant (0.060 *vs.* 0.059) although the amount of IL was nearly doubled, suggesting that t_{Li^+} of $Pyr_{O7}TFSI$ was approached and became a dominating factor at such high IL contents. Furthermore, the t_{Li^+} for both PEs with higher LiTFSI contents (**BPE23$_{O7,1:7.5}$** and **BPE23$_{O7,1:5}$**) were examined. A higher [LiTFSI]:[EO] ratio reduced the t_{Li^+} from 0.059 at 1:10 over 0.057 at 1:7.5 to 0.046 at 1:5, probably as a result of different coordination and ion-pairing effects.

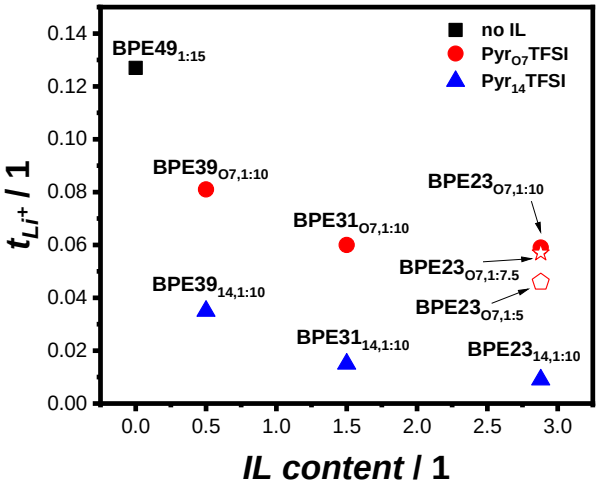

Figure 53. Results of the t_{Li^+} measurements for all PEs at 40 °C.

Next, the effective Li^+-IC (σ_{Li^+}) at 40 °C using the measured IC as well as the measured t_{Li^+} were calculated (**Figure 54**, **Table 14**). As reference the σ_{Li^+} of the non-plasticized PE (**BPE49$_{1:15}$**) was determined at 40 °C as well as 60 °C, whereas all other data were collected at 40 °C. Generally, the σ_{Li^+} of all PEs with IL surpassed the non-plasticized reference PE at the same temperature. Thus, the benefit of the increased IC overcompensates the reduction of t_{Li^+} regarding σ_{Li^+}. Though, there are significant differences visible when comparing PEs

comprising $Pyr_{14}TFSI$ and $Pyr_{O7}TFSI$: The former did only show slight improvements in σ_{Li^+} and a maximum σ_{Li^+} for **BPE31$_{14,1:10}$**, only almost twice as high as the reference (**9.2 × 10^{-3} mS cm^{-1} *vs.* 5.8 × 10^{-3} mS cm^{-1}**). Moreover, **BPE23$_{14,1:10}$** featuring an even higher amount of incorporated $Pyr_{14}TFSI$ showed a lower σ_{Li^+} in comparison to **BPE31$_{14,1:10}$**, meaning that the benefit of the even higher IC was vanished because of the lower t_{Li^+}.

A different picture is drawn upon inspection of PEs bearing $Pyr_{O7}TFSI$ as plasticizer. Here, a constant increase of σ_{Li^+} was obtained for all combinations. Further, the difference in σ_{Li^+} between $Pyr_{14}TFSI$ and $Pyr_{O7}TFSI$ became even more prominent with higher IL contents, resulting in a difference of 22% for 50 wt% IL content up to a difference of 110% for 288 wt% IL content and a constant [LiTFS]:[EO] ratio of 1:10. Although PEs featuring $Pyr_{14}TFSI$ as IL showed much higher ICs, the higher t_{Li^+} of $Pyr_{O7}TFSI$-based PEs made up for the lower IC, resulting in a substantially higher σ_{Li^+}. Furthermore, **BPE23$_{O7,1:7.5}$** even surpassed **BPE23$_{O7,1:10}$** due to the higher IC and a comparable t_{Li^+}. Eventually, this combination outperformed the reference at 40 °C by a factor of 3.8 and even the reference at 60 °C by a factor of 1.4 despite being determined at 20 °C lower temperature.

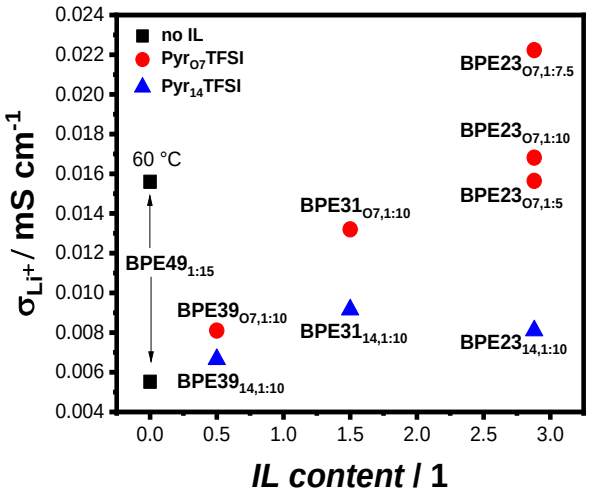

Figure 54. Li^+ ion conductivity (σ_{Li^+}) of all PEs derived from the overall IC and the t_{Li^+} values. All data were collected at 40 °C except for the additional, marked data point of **BPE49$_{1:15}$** at 60 °C being added as comparison.

Further, the area specific Li|PE interfacial resistance of the charge-transfer as well as the SEI (ASR_{CT+SEI}) for all PEs as derived from the measurements of the transference number at 40 °C was compared (**Table 14**). Here, **BPE49$_{1:15}$** showed by far the highest *ASR* of 464 Ω *cm*^{2} while

all PEs containing ILs showed significant reduced values by a factor between two and four probably due to a better surface wetting and an improved SEI formation. Moreover, PEs containing $Pyr_{14}TFSI$ showed higher *ASR*s than their counterparts with $Pyr_{O7}TFSI$ (210 *vs*. 156 Ω cm^2, 206 *vs*. 99 Ω cm^2 and 259 *vs*. 134 Ω cm^2), again probably due to an improved SEI formation or charge-transfer taking place when using the functionalized IL. Noteworthy, PEs containing 150 wt% of ILs showed a slightly lower $ASR_{CT + SEI}$ than their counterparts featuring 288 wt% of IL. Therefore, it seems that the ratios of polymer, IL and LiTFSI has a major impact on the nature of the SEI. Concluding these findings, **BPE31$_{O7,1:10}$** featured a lower *ASR* but also lower σ_{Li^+}, while **BPE23$_{O7,1:10}$** featured a higher *ASR* but a higher σ_{Li^+}, thus quite impressively demonstrating that different parameters need to be balanced accordingly and always seen in the bigger context of improving the final performance. Therefore, a closer look at the composition as well as the long-term development of the SEI needs to be taken into account for future studies in order to gain a deeper insight into the processes taking place.

Table 14. Overview of the T_g of the conductive phase, ionic conductivity (σ), transference number (t_{Li^+}), resulting calculated Li^+ conductivity (σ_{Li^+}) and the area specific resistance ($ASR_{CT + SEI}$), all at 40 °C.

Entry	PE	$T_{g,cond}$ [°C]	σ(40 °C) [mS cm^{-1}]	t_{Li^+}(40 °C)	σ_{Li^+}(40 °C) [mS cm^{-1}]	$ASR_{CT + SEI}$ (40°C) [Ω cm^2]
1	**BPE49$_{1:15}$**	-47	4.6×10^{-2}	0.127	5.8×10^{-3}	464
2	**BPE39$_{14,1:10}$**	-53.9	1.9×10^{-1}	0.035	6.6×10^{-3}	210
3	**BPE39$_{O7,1:10}$**	-52.3	1.0×10^{-1}	0.081	8.1×10^{-3}	156
4	**BPE31$_{14,1:10}$**	-62.0	6.1×10^{-1}	0.015	9.2×10^{-3}	206
5	**BPE31$_{O7,1:10}$**	-61.2	2.2×10^{-1}	0.060	1.3×10^{-2}	99
6	**BPE23$_{14,1:10}$**	-74.0	9.0×10^{-1}	0.009	8.1×10^{-3}	259
7	**BPE23$_{O7,1:10}$**	-64.8	2.9×10^{-1}	0.059	1.7×10^{-2}	134
8	**BPE23$_{O7,1:7.5}$**	-61.0	3.9×10^{-1}	0.057	2.2×10^{-2}	161
9	**BPE23$_{O7,1:5}$**	-58.7	3.4×10^{-1}	0.046	1.6×10^{-2}	145

Overall, these results confirm the intended concept quite impressively by significantly increasing the IC of microphase separated block copolymer-based PEs, demonstrating the presence of sophisticated approaches to overcome the dilemma regarding the mechanical stability/IC correlation. Moreover, the importance of a detailed analysis regarding the

implementation of ILs, evaluating the ‘true’ benefit of the described strategic avenue, was shown. Consequently, a substantial increase of σ_{Li^+} was achieved even surpassing the reference at 20 °C higher temperature.

4.5.6 Constant Current Cycling

Ultimately, these advanced block copolymer electrolytes did not only show improved IC and σ_{Li^+} and thus appear highly promising from a theoretical point of view, but should also be practically usable in full cells. Therefore, **BPE23$_{O7,1:7.5}$** was exemplary chosen due to its highest σ_{Li^+} among all studied PEs and was accordingly employed in Li||LFP full cells. As seen in **Figure 55** cycling at 40 °C as well as 60 °C was performed. Within the measured 50 cycles, a marginal capacity fading was observed, though a successful operation over 50 cycles could be achieved without any special adjustments or optimizations using standard LFP cathodes. In summary, the successful implementation of ILs as plasticizers in block copolymer PEs in its intended area of application was shown, opening the door for follow-up performance-oriented studies. These include the investigation of other plasticizers, possibly revealing even better ICs and full cell cycling stabilities as well as in-depth electrochemical characterization, thus making an application more viable.

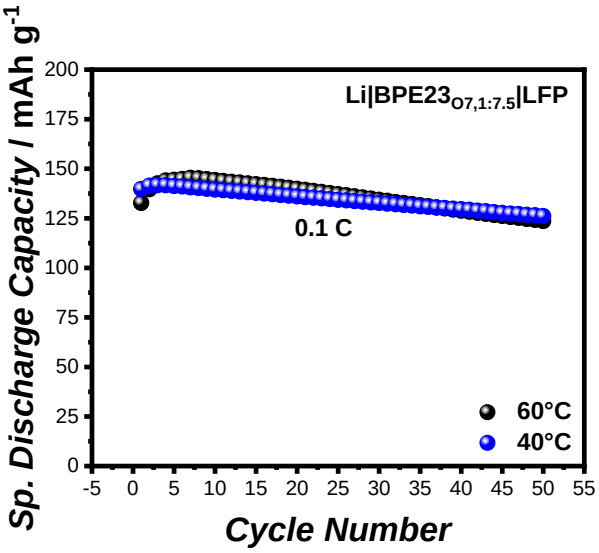

Figure 55. Constant current cycling at 0.1 C of Li|BPE23$_{O7,1:7.5}$|LFP cells at 40 °C (blue dots) and 60 °C (black dots).

4.5.7 Recapitulation

Although block copolymers have proven their successful application in lithium-metal batteries, their practical exploitation at lower temperatures was quite limited due to their low IC. Herein, a principle for the selective implementation of plasticizer into microphase separated block copolymers was utilized, thereby increasing the IC without affecting the domain which is responsible for the mechanical stability. To do so, a series of four block copolymers with a constant DP of the styrene-based PEO side chain block was synthesized as well as a varying DP of the PS block, thus resulting in different weight/volume ratios for both blocks. Then, roughly maintaining a volume ratio of PS:conducting phase of 1:1, plasticizer and LiTFSI were added to the different block copolymers leading to flexible, self-standing PE films. Here, two ILs ($Pyr_{14}TFSI$ or $Pyr_{O7}TFSI$) were selected as plasticizer due to their high IC, good thermal stability, good electrochemical windows and their negligible vapor pressure. Further, the thermal and morphological properties of the resulting films were examined by DSC, TGA, SAXS and rheological measurements, not only revealing the microphase separation with a lamellar long-range order and the successful incorporation of the ILs selectively into the conductive phase, but also a good thermal and mechanical stability.

Moreover, all derived films were thoroughly characterized by measurements of their ICs as well as transference numbers. Here, it was generally shown that the addition the ILs significantly increased the IC in comparison to a non-plasticized reference sample by up to two orders of magnitude (e.g. up to 1 mS cm^{-1} at 40 °C). In this regard, PEs employing $Pyr_{14}TFSI$ showed a higher IC, but a lower t_{Li^+} than PEs comprising $Pyr_{O7}TFSI$, which showed a comparably lower IC, but a higher t_{Li^+}. Consequently, the effective σ_{Li^+} was calculated showing a significant increase from 5.8×10^{-3} mS cm^{-1} for the non-plasticized block copolymer (**BPE49$_{1:15}$**) up to 2.2×10^{-2} mS cm^{-1} for **BPE$_{O7,1:7.5}$** at 40 °C, which even surpassed the σ_{Li^+} of **BPE49$_{1:15}$** at 60 °C (1.5×10^{-2} mS cm^{-1}). An exemplary full cell cycling in Li|PE|LFP cells was also conducted, which ultimately evidenced the practical applicability of these advanced block copolymer electrolytes. Consequently, the stage was set for further research not only transferring the gained knowledge onto the implementation of other types of plasticizers into block copolymer electrolytes, but also conducting performance-oriented studies that will focus in more detail on the actual electrochemical properties, the cell optimization as well as the application.

5 Conclusion and Outlook

The present dissertation dealt with PEO-based polymer architectures, their synthesis in general and their application as polymer electrolytes in LMBs. An insight should be given, demonstrating synthetic challenges polymer chemists face to overcome common challenges within the field of polymer electrolytes such as crystallization issues or the dilemma regarding mechanical stability *vs*. ionic conductivity.

Firstly, the synthesis of a systematic library of vinyl ether-based PEO side chain copolymers to reduce the crystallization tendency of PEO was covered. Herein, the influence of different PEO side chain lengths, the grafting density and the [Li^+]:[EO] ratio after mixing with LiTFSI on the T_g, the crystallinity and the resulting ionic conductivity was thoroughly examined. In this regard, copolymers bearing longer PEO side chains and higher grafting densities showed higher crystallization tendencies and a lower T_g at the same time. Furthermore, the addition of LiTFSI reduced the crystallization, but increased the T_g. Since these effects are directly affecting the ionic conductivity, it was demonstrated that the different parameters need to be carefully adjusted in order to balance their influence appropriately. Overall, a fundamental view enlightening PEO side chain copolymers for their application as polymer electrolytes was provided, thus laying the baseline for following projects of this thesis.

The second topic was developed as a side project from the first one being based on controlled cationic polymerization of vinyl ethers. This technique is known for a good control over chain growth, thus yielding polymers with well-defined molar mass distributions and low dispersities. However, the practical challenges involved in the synthesis of poly(vinyl ether)s by cationic polymerization techniques so far limited suitable post-polymerization modifications (PPM) *via* chemoselective *click* reactions. Within this project, the successful controlled cationic polymerization of vinyl ethers bearing pendant C=C double and C≡C triple bonds using a single-component initiation and control agent (PMCCP) under ambient conditions was reported. Subsequently, the PPM *via thiol-ene*/*-yne* and CuAAC reaction of the obtained polymers was successfully realized laying the foundation for the straightforward synthesis of unprecedented functional poly(vinyl ether)s.

In a third project, the gram-scale synthesis of a four-arm *cage*-shaped PEO and its pioneering application as PE is described for the first time. The obtained PEs comprising low LiTFSI loading ([Li^+]:[EO] 1:25) showed good ionic conductivities at low temperatures due to their well suppressed crystallization by the *cage* architecture, thus overcoming the necessity to add any further plasticizer or structural solvent. Therefore, this project expanded the findings of the

first project and further prove the great toolbox of synthetic polymer chemistry to overcome crystallization issues in PEO-based PEs.

The fourth approach dealt with the design of styrene-based PEO side chain block copolymers (based on the results of the first project) featuring a microphase separation and their application as solid polymer electrolyte in high voltage lithium-metal batteries. A straightforward synthesis route was established overcoming typical drawbacks of PEO block copolymers prepared by anionic polymerization or ester-based PEO side chain copolymers. Both, the PEO side chain length as well as the LiTFSI content were varied and the underlying relationships were elucidated in view of polymer compositions with high ionic conductivity. Subsequently, a selected composition was subjected to further analyses including the prove of the phase separated morphology, providing not only excellent self-standing films with intrinsic mechanical stability but also the ability to suppress lithium dendrite growth as well as good flexibility, wettability and good contacts with the electrodes. Additionally, the good thermal and electrochemical stability was demonstrated. To do so, linear sweep and cyclic voltammetry, lithium plating/stripping tests and galvanostatic overcharging using high voltage cathodes were conducted demonstrating stable lithium-metal interfaces and a high oxidative stability of around 4.75 V. Consequently, cycling of Li||NMC622 cells did not exhibit commonly observed rapid cell failure or voltage noise associated with PEO-based electrolytes in Li||NMC622 cells, due to the high mechanical stability. Thus, a comprehensive view is provided highlighting that the combination of PEO and high voltage cathodes is not impossible *per se*.

The fifth project enhances the system established in the fourth project. Here, an advanced design for PEs built on the previously investigated microphase separated styrene-based PEO side chain block copolymers was introduced. Usually, such block copolymers are characterized by a high mechanical stability provided by the PS domain, while the PEO-based domain features decent ionic conductivities, however, mostly only at elevated temperatures as shown in project four. To enable suitable conductivities at lower temperatures, two ILs as model plasticizers for the PEO domain were selectively implemented. Since those ILs are non-miscible with PS, the latter domain is unaffected, thus still providing a great mechanical stability. To maintain the necessary self-standing film forming ability, the size of the PS domain was adjusted to match with the size of the conducting PEO-based domain. For this, a series of four block copolymers with different block ratios was synthesized, enabling the study of the influence of different amounts of IL on the thermal and electrochemical properties. Further, all derived polymer electrolytes were thoroughly characterized by thermal, morphological and electrochemical analyses. The microphase separated morphology with long-range order and a good thermal and

mechanical stability as well as the selective mixing of the ILs within the conducting domain was proven. Consequently, EIS revealed a significant increase in ionic conductivity up to two orders of magnitude in comparison to the non-plasticized control sample of project four. Further, exhaustive studies of the lithium-ion transference number not only showed the importance of such detailed analysis for IL containing PEs, but also the actual increase of the raw lithium-ion conductivity. Finally, full cycling in Li||LFP cells was conducted which clearly demonstrated the applicability of the present approach.

In summary, the results impressively demonstrated the importance of sophisticated approaches towards smart polymer designs as solutions to commonly observed crystallization issues of PEO-based PEs and the dilemma of mechanical stability and ionic conductivity. Here, structure-property relationships were clearly identified and thoroughly described. Beyond this, advanced approaches for the enhancement of ionic conductivity in block copolymer electrolytes without losing their mechanical stability were elaborated and further, it was shown that molecular architectures could be used to overcome common issues regarding the compatibility of PEO-based PEs with high voltage cathodes. Thus, in times of ever-growing demands of energy storage, a comprehensive view both from a theoretical and practical viewpoint on the symbiosis of battery and polymer chemistry was provided, laying the foundation for further advanced studies and a potential evolution or even revolution of polymer-based battery materials.

6 Experimental Section

Herein, instrumentation details used for characterization, the materials employed in the frame of the present thesis, as well as experimental procedures and analytical results are given. The procedures of the previously discussed projects are addressed in the respective subchapter.

6.1 Instrumentation and General Procedures

All instruments as well as general procedures are listed below, while syntheses procedures and further information are given in the respective subchapter.

6.1.1 Nuclear Magnetic Resonance (NMR) Spectroscopy

^{1}H-NMR and ^{13}C-NMR spectra were recorded on a Bruker Ascend III 400 MHz spectrometer at a frequency of ν = 400 MHz and ν = 101 MHz, respectively. All samples were dissolved in deuterated solvents; chemical shifts are reported relative to the residual solvent signals.

6.1.2 Size Exclusion Chromatography (SEC)

6.1.2.1 SEC using THF as Eluent I

Size exclusion chromatography was carried out in THF on a Tosoh Bioscience HLC-8320GPC EcoSEC system equipped with an autosampler, 3 PSS SDV columns 5 µm (100 Å, 1000 Å, 100000 Å) (8 × 300 mm), a UV and a differential refractive index (RI) detector. The operation temperature was set to 35 °C with a flow rate of 1 mL min^{-1}. The system was calibrated using poly(styrene) or poly(methyl methacrylate) standards ranging from 800 to 2.2 × 10^{6} g mol^{-1}. Typically, 50 µL of a filtered 2.0 mg mL^{-1} sample solution was injected onto the columns.

6.1.2.2 SEC using THF as Eluent II

Size exclusion chromatography was carried out in THF on a PL-SEC 50 Plus Integrated System, comprising an autosampler, a differential refractive index (RI) detector, a PLgel 5 µm bead-size guard column (50 × 7.5 mm) followed by three PLgel 5 µm Mixed C columns (300 × 7.5 mm) and a PLgel 3 µm Mixed E column (300 × 7.5 mm). The operation temperature was set to 35 °C with a flow rate of 1 mL min^{-1}. The system was calibrated using linear poly(styrene) or poly(methyl methacrylate) standards ranging from 800 to 2.2 × 10^{6} g mol^{-1}. Typically, 100 µL of a filtered 2.0 mg mL^{-1} sample solution was injected onto the columns.

6.1.3 Attenuated Total Reflection (ATR) Fourier-Transform (FT) Infrared (IR) Spectroscopy (ATR FT-IR)

ATR FT-IR spectra were recorded on a Bruker Vertex 80 from 500 - 4000 cm^{-1} at 25 °C.

6.1.4 Differential Scanning Calorimetry (DSC)

Differential scanning calorimetry was conducted using a DSC Q200 (TA Instruments) in ranges from -85 – -75 °C to 130 – 160 °C with a scan rate of 5 or 10 K min^{-1}.

6.1.5 Thermal Gravimetric Analysis (TGA)

Thermal Gravimetric Analysis (TGA) was carried out using a TGA 5500 (TA Instruments) at a heating rate of 10 K min^{-1} under nitrogen or air atmosphere up to 800 °C.

6.1.6 Electrospray Ionization Mass Spectrometry (ESI-MS)

Electrospray ionization mass spectra were recorded on a Thermo Fisher Q-Exactive Orbitrap mass spectrometer. As sample preparation, a polymer concentration of 0.05 mg ml^{-1} was prepared in a mixture of DCM/MeOH 3:1 enriched with 100 μM sodium trifluoroacetate as cation source.

6.1.7 Small-Angle X-Ray Scattering (SAXS)

2D-SAXS measurements were performed on a Hecus S3-Micro X-ray system using a point microfocus source, 2DX-ray mirrors, and a two-dimensional CCD detector from Photonic Science. Low background scattering was ensured by the use of a block collimation system. 2D spectra were radially averaged using self-developed plugins for ImageJ, corrected for absorption and primary beam intensity. Normalization of the q-range was done using crystalline silver behenate as standard.

6.1.8 Oscillatory Rheology

Rheological measurements were performed on a strain-controlled ARES G2 (TA Instruments) rheometer by small amplitude oscillatory shear experiments from 0.1 to 100 rad s^{-1} at 25 °C and 40 °C under nitrogen atmosphere using an 8 mm parallel plate geometry and a strain of 0.1%. Samples were prepared from the films obtained by the PE preparation with 8 mm in diameter and 0.5 mm in thickness.

6.1.9 Polymer Electrolyte (PE) Preparation

Prior to the PE preparation, the respective polymer was dried at 80 °C under vacuum (10^{-3} mbar) overnight.

6.1.9.1 PE preparation I – Project 1 and 3

The polymer as well as the corresponding amount of LiTFSI with predefined ratios of [Li^+]:[EO] 1:5, 1:10, 1:15, 1:20 or 1:25 were both separately dissolved in acetone. Subsequently, both solutions were combined to yield a homogenous mixture. Acetone was removed slowly under reduced pressure at 50 °C, followed by drying the polymer electrolytes under reduced pressure (10^{-3} mbar) at 80 °C for 24 h.

6.1.9.2 PE preparation II – Project 4

The polymer as well as the corresponding amount of LiTFSI with predefined ratios of [Li^+]:[EO] 1:5, 1:10, 1:15 or 1:20 were dissolved in acetonitrile (MeCN). Subsequently, the solution was poured into a Teflon mold. The mold was covered with a bigger mold and MeCN was allowed to evaporate slowly at ambient conditions enabling microphase separation. Subsequently, the obtained PE film was dried and simultaneously annealed at 120 °C under vacuum (10^{-3} mbar) for 24 h. The derived films featured a thickness of around 100 µm and were used for all measurements.

6.1.9.3 PE preparation III – Project 5

The polymer, the corresponding amount of IL (either $Pyr_{14}TFSI$ or $Pyr_{O7}TFSI$) with respect to the weight of the PVBmPEO2000 block and LiTFSI with predefined ratios of [Li^+]:$[EO]_{polymer}$ of 1:5, 1:7.5 or 1:10 were dissolved in THF. Subsequently, the solution was poured into a Teflon mold. The mold was covered with a bigger mold and THF was allowed to evaporate slowly at ambient conditions enabling microphase separation (overnight). Subsequently, the obtained SPE film was dried and simultaneously annealed at 120 °C under vacuum (10^{-3} mbar) for 24 h. The derived films featured a thickness of around 100 µm and were used for all measurements.

6.1.10 Electrochemical Impedance Spectroscopy (EIS)

6.1.10.1 EIS I – Project 1 and 3

For EIS measurements, coin cell-type cells (CR2032) were assembled, where the previously prepared polymer electrolytes were sandwiched between two stainless steel electrodes using a Mylar foil spacer ring (thickness l = 100 µm, inner diameter = 8 mm). Subsequently, these cells were preconditioned in a temperature chamber (Binder MK53, controlled with the Autolab Software Nova 2.1.3) with a gradual increase of temperature from 20 °C – 70 °C in 10 °C steps

while maintaining each temperature for 2 h. 1 h after the preconditioning was finished, measurements were carried out by gradually increasing the temperature in 10 °C steps from 0 °C to 70 °C with each temperature being maintained for 2 h to attain a thermal equilibrium. The measurements were performed using a PGSTAT302N potentiostat/galvanostat (Autolab) over a frequency range of 1 MHz – 1 Hz with an amplitude of 10 mV. The ionic conductivity σ was calculated according to **Equation 2**. For each PE three coin cells were prepared and measured. Subsequently, the mean average ionic conductivity of these three measurements was derived and discussed.

$$\sigma = \frac{1}{R_b} \cdot \frac{l}{A} \qquad \textbf{(Equation 2)}$$

with R_b being the bulk electrolyte resistance that can be accessed from the Nyquist plot, l the film thickness and A the film area.

6.1.10.2 EIS II – Project 4

The samples were prepared by placing the polymer electrolyte film between two stainless steel electrodes (2 setups with cells of 8 mm and 10 mm diameter) in a Swagelok-type cell setup. All samples were preconditioned overnight, in a temperature chamber (testequity model 115A) at 65 °C, in order to improve the interfacial contact between electrodes and electrolyte. The measurements were carried out using a VSP, SP-200 and SP-300 potentiostat (BioLogic Science Instruments) in a temperature range between 5 °C to 85 °C. An impedance measurement was conducted over a frequency range from 1 MHz to 500 mHz (and reverse) with an amplitude of 20 mV. A heating cycle consisted of a gradual temperature increase in 10 °C steps from 5 °C to 85 °C. The temperature was increased with a heating/cooling rate of 60 °C/h over 10 min, after which the temperature was held constant for another 50 min to acquire impedance spectra. At a temperature of 85 °C, the heating profile was reversed and gradually cooled down to 5 °C in similar temperature steps. The ionic conductivity σ was calculated according to **Equation 2**.

6.1.10.3 EIS III – Project 5

For EIS measurements, coin cell-type cells (CR2032) were assembled, where the previously prepared PEs were sandwiched between two stainless steel electrodes. The measurements were carried out using a VMP-300 potentiostat (BioLogic Science Instruments) in a temperature range between 0 °C to 70 °C. An impedance measurement was conducted over a frequency range from 5 MHz to 1 Hz with an amplitude of 10 mV. The heating cycle was comprised of a

gradual temperature increase in 10 °C steps from 0 °C to 70 °C. At a temperature of 70 °C, the heating profile was reversed and gradually cooled down to 0 °C. The temperature was increased with a heating/cooling rate of 60 °C/h over 10 minutes, after which the temperature was held constant for another 60 minutes to guarantee a stable temperature for acquiring impedance spectra. The ionic conductivity σ was calculated according to **Equation 2**.

6.1.11 Measurement of the Li^+ Transference Number (t_{Li^+})

6.1.11.1 t_{Li^+} Measurement I – Project 4

The measurement of the transference number was performed on a VMP3 potentiostat (BioLogic Science Instruments) at 60 °C. For the measurements symmetrical Li|SPE|Li cells were assembled. After the cells were conditioned for one hour, impedance measurements were conducted every four hours for a total of 20 h to guarantee a stable interface between the SPE and lithium-metal (Honjo Metal, thickness of 300 µm). Impedance data were collected between a frequency of 1 MHz to 100 mHz with an amplitude of 10 mV. Direct current polarization was applied with a polarization voltage of ΔV = 10 mV while the impedance was measured directly before and after the polarization, respectively. The data were evaluated using an equivalent circuit model as depicted in **Figure 35a** consisting of one resistor corresponding to the electrolyte resistance, two RC elements reflecting the charge transfer as well as the SEI and the Warburg element showing diffusion processes from/to the electrodes. The transference number t_{Li^+} was calculated using **Equation 3** where I_s is the steady state current, ΔV is the polarization voltage and R_0 and R_s are the electrode resistance (R_{CT} and R_{SEI}) before and after the polarization, respectively.

$$t_{Li^+} = \frac{I_s (\Delta V - I_0 R_0)}{I_0 (\Delta V - I_s R_s)} \qquad \textbf{(Equation 3)}$$

$$I_0 = \frac{\Delta V}{R_b + R_0} \qquad \textbf{(Equation 4)}$$

The initial current I_0 is calculated using **Equation 4**. R_b is the resistance of the polymer electrolyte and is determined by the impedance spectrum before polarization. Note that the initial current I_0, which is calculated by **Equation 4**, is equal to the experimental value, which can be derived from the polarization plot.

6.1.11.2 t_{Li+} Measurement II – Project 5

The measurement of the transference number was performed on a VMP-300 potentiostat (BioLogic Science Instruments) at 40 °C. For the measurements symmetrical Li|PE|Li cells were assembled. After the cells were conditioned for one hour, impedance measurements were conducted every four hours for a total of 20 – 40 hours to follow the interface formation guaranteeing a stable SEI between the SPE and lithium-metal (Honjo Metal, thickness of 300 µm). Impedance data were collected between a frequency of 1 MHz to 100 mHz with an amplitude of 10 mV. Afterwards, direct current polarization was applied with a polarization voltage of $\Delta V = 10$ mV while the impedance was measured directly before and after the polarization, respectively. The transference number t_{Li+} was calculated using **Equation 3** where I_s is the steady state current, ΔV is the polarization voltage and R_0 and R_s are the initial and steady-state electrode resistance (R_{CT} and R_{SEI}), respectively. The initial current I_0 is calculated using **Equation 4**. R_b is the resistance of the polymer electrolyte and is determined by the impedance spectrum before polarization. Note that the initial current I_0, which is calculated by **Equation 4**, is equal to the experimental value, which can be derived from the polarization plot.

6.1.12 Potentiodynamic Experiments

The electrochemical stability was measured in a Swagelok-type three electrode setup by conducting linear LSV and CV on a VSP potentiostat (BioLogic Science Instruments) at room temperature. Lithium was used as counter and reference electrode and copper or platinum as working electrode for the measurement of reductive or oxidative stability, respectively. LSV was conducted within a potential range of -0.5 and 7.0 V *vs.* Li|Li^+ and a sweep rate of 0.1 mV s^{-1}. For CV measurements three cycles were measured on copper as working electrode between a potential range of -1.0 and 3.0 V *vs.* Li|Li^+ and a scan rate of 0.1 mV s^{-1}.

For the measurement of the limiting current density, LSV was conducted in symmetrical Li|SPE|Li coin cells with a sweep rate of 0.02 mV s^{-1} until a cut-off voltage of 0.35 V *vs.* Li|Li^+. The reached plateau indicated the limiting current density.

6.1.13 Cathode Preparation

For the preparation of the cathodes 0.9 g of NMC622 (BASF Toda, 90wt%) or 0.9 g of $Li[Ni_{0.5}Mn_{1.5}O_4]$ (LNMO) (kindly provided by J. Binder[236], 90 wt%) or 0.9 g of LFP (kindly provided by the Fraunhofer institute for silicon technology (ISIT), 90 wt%), 0.07 g conductive carbon (Super P, Imerys, 7 wt%) and 0.03 g binder (PVdF 1100, Kureha, 3 wt%) were weighed in a sample container and 2 mL of NMP was added. The container was transferred to a Thinky

centrifugal mixer and stirred twice for five minutes at 1700 rounds per minutes. Then, the resulting homogeneous slurry was casted onto an aluminum current collector using the doctor blade technique with a gap width of 50 µm. The coating was dried in an oven at 80 °C overnight. To obtain a homogeneous thickness and surface the cathode sheets were roll-pressed to a final total thickness of ~ 40 µm (20 µm aluminum current collector, 20 µm electrode coating) resulting in a mass loading of ~ 1.8 mg cm^{-2}. Round disks with a diameter of Ø = 12 mm were punched out and dried at 120 °C under vacuum (10^{-3} mbar) prior to use.

6.1.14 Constant Current Cycling Experiments

6.1.14.1 Constant Current Cycling Experiments I – Project 4

All constant current cycling experiments were performed in a coin cell-type two electrode setup using a Maccor series 4000 battery cell test system. The cells were conditioned at 60 °C in a climate chamber (Binder KB 400). Lithium plating and stripping experiments were performed in a symmetrical lithium cell. Prior to long-term plating/stripping the cells were conditioned with a current density of 0.05 mA cm^{-2} for 10 cycles. Afterwards, lithium was constantly plated and stripped with a current density of 0.1 mA cm^{-2} for one hour over 500 cycles (1000 h) or for four hours over 37 cycles (296 h), respectively.

For the plating and stripping experiments with alternating current densities 30 cycles with a current density of 0.1 mA cm^{-2} were conducted before the current density was increased stepwise for 10 cycles each with 10 cycles at 0.1 mA cm^{-2} in between until a short circuit was observed or the safety limits were reached.

Galvanostatic overcharging was conducted (upper voltage limit of 6 V) with a specific current of 14.7 mA g^{-1} or 18.0 mA g^{-1} (~ 0.1 C) for LNMO or NMC622 cathodes, respectively. The discovered voltage plateau was taken as indication for the onset of the oxidative decomposition of the polymer electrolyte against cathode active materials.

Full cell cycling experiments were performed between 3.0 V and 4.3 V *vs.* $Li|Li^+$ at a C-Rate of 0.1 C. For rate performance experiments alternating charge rates were used whereas the discharge rate was maintained at 0.1 C. Three cycles at 0.05 C were conducted as formation prior to cycling.

The corresponding impedance data of the symmetrical lithium cells or full cells were collected using an Autolab PGSTAT204 potentiostat in a frequency range of 1 MHz to 10 mHz with an amplitude of 10 mV. The EIS measurements were performed at a cell voltage of 0 V for

symmetrical lithium cells and in a discharged state (3 V) for full cells. Data were collected before and after the formation and after cycling of the corresponding cells.

6.1.14.2 Constant Current Cycling Experiments II – Project 5

Constant current cycling experiments were performed in a coin cell-type two electrode setup using an Arbin Laboratory Battery Testing system. The cells were conditioned at 40 or 60 °C in a climate chamber (Binder BF 56). Full cell cycling experiments were performed between 3.0 V and 3.8 V *vs.* Li|Li^+ at a C-rate of 0.1 C. A formation procedure consisting of two cycles at 0.05 C, two cycles at 0.1 C and two cycles at 0.05 C was performed prior to long-term cycling at 0.1 C.

6.2 Materials

Acetic acid (100%, Carl Roth), allyl bromide (97%, Sigma Aldrich), allyl magnesium bromide (1 M solution in diethyl ether, Acros Organics), ammonia solution ($NH_4OH_{(aq.)}$, 30% ACS, Carl Roth), 4-arm star-shaped poly(ethylene oxide) 5000 g mol^{-1} (PEO_{star}, >95%, Jenkem Technology), 1,1′-azobis(cyclohexanecarbonitrile) (ABCN, 98%, Sigma Aldrich), 2,2′-azobis(2-methylpropionitrile) (AIBN, 98%, Sigma Aldrich), benzyl bromide (98%, Sigma Aldrich), calcium carbonate ($CaCO_3$, ≥98.5%, Carl Roth), calcium hydride (CaH_2, 95%, Sigma Aldrich), copper(I) bromide (CuBr, 98%, Alfa Aesar), copper(I) iodide (CuI, 98%, Acros Organics), 1,8-diazabicyclo[5.4.0]undec-7-ene (DBU, ≥99%, Merck), diethylene glycol vinyl ether (98%, TCI), 4-dimethylaminopyridine (DMAP, 99%, Acros Organics), 2,6-di-*tert*-butylpyridine (DtBP, >97%, Sigma Aldrich), 1-dodecane thiol (DDT, ≥98%, Sigma Aldrich), 2-(dodecylthiocarbonothioylthio)-2-methylpropionic acid (DDMAT, 98%, Sigma Aldrich), ethylaluminum sesquichloride (0.4 M in hexane, Acros Organics), ethylene glycol monovinyl ether (>98%, TCI), hydrochloric acid ($HCl_{(aq)}$, 37%, Carl Roth), isobutyl vinyl ether (IBVE, 99%, Sigma Aldrich), 2-mercaptoethanol (ME, ≥99.0% Sigma Aldrich), lithium acetylide ethylenediamine complex (90%, Sigma Aldrich), magnesium sulfate ($MgSO_4$, ≥99%, Carl Roth), *N*-(3-dimethylaminopropyl)-*N*′-ethylcarbodiimide hydrochloride (EDC-HCl, ≥99%, Carl Roth), *N*,*N*,*N*′,*N*″,*N*″-pentamethyldiethylenetriamine (PMDTA, >99%, TCI), pentakis(methoxycarbonyl)cyclopentadiene (97%, Sigma Aldrich), poly(ethylene oxide) monomethyl ether (mPEOz, M_n ~ 400, 550, 1000, 2000 g mol^{-1}, TCI), poly(ethylene oxide) monomethyl ether (mPEOz, M_n ~ 750, Sigma Aldrich), propargyl bromide (80 wt% in toluene, Sigma Aldrich), *p*-toluenesulfonyl chloride (TsCl, 99%, Aldrich), sodium azide (NaN_3, ≥99.5%, Sigma Aldrich), sodium hydride (NaH, 60% dispersion in mineral oil, Sigma Aldrich), sodium hydroxide (NaOH, >98%, Carl Roth). 4-*tert*-butylbenzyl thiol (TBBT, ≥98%, Sigma Aldrich), tetramethylene glycol monovinyl ether (>97%, TCI), triethylamine (Et_3N, 99%, Sigma Aldrich), 4-vinylbenzyl chloride (90%, Sigma Aldrich), were used as received.

Cyclohexyl vinyl ether (>98%, TCI) and styrene (99%, Acros) were passed through basic alumina oxide prior to use.

Bis(trifluoromethane)sulfonimide lithium salt (LiTFSI, 99.95%, Sigma Aldrich) was dried at 80 °C under vacuum for 2 days and subsequently stored inside a glove box (MBraun Unilab, <0.1 ppm H_2O, <0.1 ppm O_2) under inert argon atmosphere.

All other solvents and reagents were of analytical grade or higher and were used without further purification.

6.3 Procedures for 'A Systematic Study of Vinyl ether-based Poly(ethylene oxide) Side Chain Polymer Electrolytes'

The adduct of IBVE and acetic acid (*i.e.* the cationogen) was synthesized as described in literature.[43]

6.3.1 Synthesis of Diethylene glycol vinyl ether tosylate

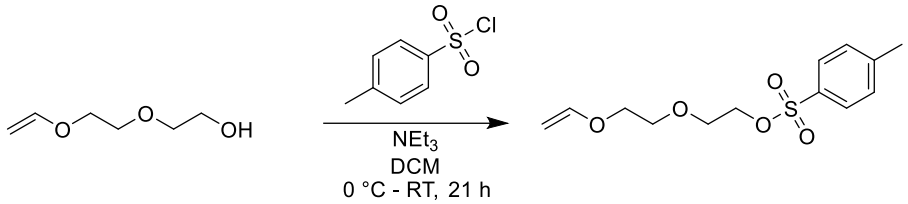

Diethylene glycol vinyl ether (4.84 g, 36.6 mmol, 1.00 eq.) and triethylamine (4.07 g, 40.3 mmol, 1.10 eq.) were given into a round-bottom flask and taken up with 50 mL of dichloromethane (DCM). The reaction mixture was cooled to 0 °C and tosyl chloride (7.33 g, 38.5 mmol, 1.05 eq.) was added under stirring. After 1 hour, the ice bath was removed, and the reaction mixture was stirred for additional 20 hours. The solution was washed twice with 1 M $HCl_{(aq.)}$, once with 1 M $NaOH_{(aq.)}$ and once with water. The combined aqueous phases were extracted twice with DCM. The combined organic phases were then dried over $CaCO_3/MgSO_4$, filtered, and the solvent was removed under reduced pressure yielding a slightly yellow oil. Subsequently, the crude product was purified by column chromatography using DCM:petrol ether in a ratio of 3:1. The obtained product was dried over CaH_2 and filtered through basic alumina to yield 4.51 g (81%) of a colorless oil.

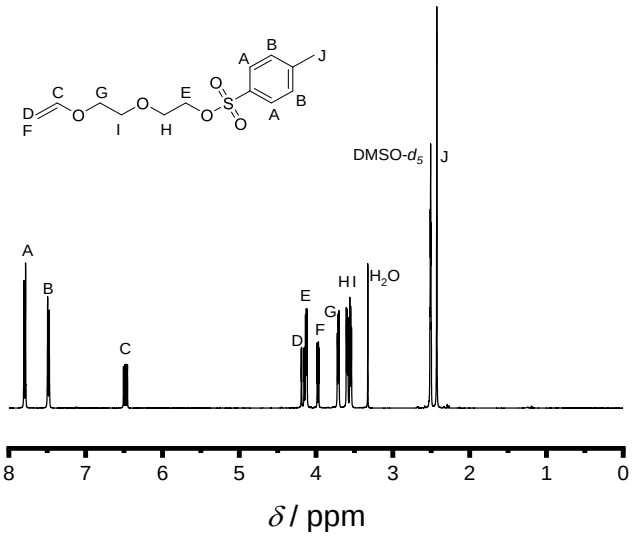

Figure 56. [1]H-NMR spectrum of diethylene glycol vinyl ether tosylate. Solvent: DMSO-d_6.

[1]H-NMR (400 MHz, DMSO-*d*6) δ / ppm = 7.78 (d, *J* = 8.4 Hz, 2H), 7.48 (d, *J* = 8.1 Hz, 2H), 6.47 (dd, *J* = 14.3, 6.8 Hz, 1H), 4.16 (dd, *J* = 14.3, 1.8 Hz, 1H), 4.12 (t, *J* = 4.4 Hz, 2H), 3.97 (dd, *J* = 6.8, 1.8 Hz, 1H), 3.70 (t, *J* = 5.0, 4.4 Hz, 2H), 3.59 (t, *J* = 4.2 Hz, 2H), 3.54 (t, *J* = 4.9, 4.4 Hz, 2H), 2.42 (s, 3H).

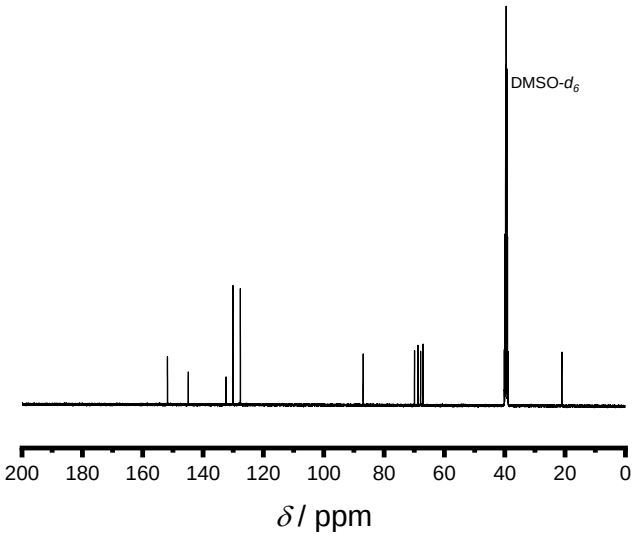

Figure 57. [13]C-NMR spectrum of diethylene glycol vinyl ether tosylate. Solvent: DMSO-d_6.

[13]C-NMR (101 MHz, DMSO-*d*6) δ / ppm = 151.79, 144.89, 132.38, 130.12, 127.62, 86.93, 69.92, 68.74, 67.90, 67.08, 21.09.

6.3.2 Synthesis of Precursor Polymer A/B

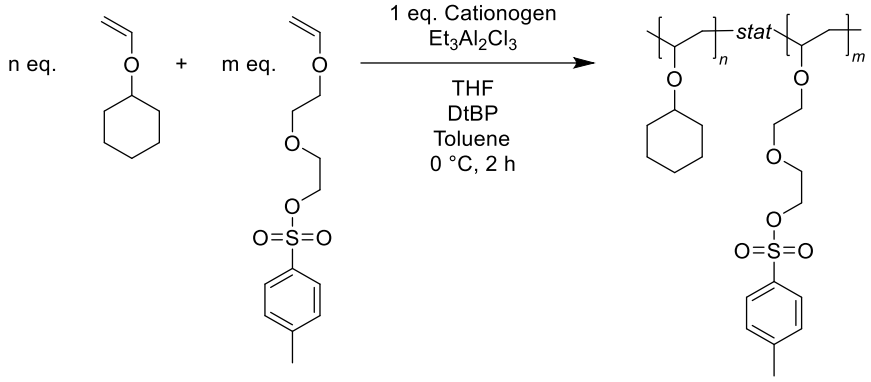

Cyclohexyl vinyl ether (**A**: 8.81 g, 69.84 mmol, 100.00 eq.; **B**: 1.76 g, 13.96 mmol, 60.00 eq.), diethylene glycol vinyl ether tosylate (5.00 g, 17.46 mmol, 25.00 eq.; **B**: 4.00 g, 13.96 mmol, 60.00 eq.), the cationogen (**A**: 0.112 g, 0.70 mmol, 1.00 eq.; **B**: 0.037 g, 0.23 mmol; 1.00 eq.), THF (**A**: 2.83 mL, 2.52 g, 34.92 mmol, 50.00 eq.; **B**: 0.944 mL, 0.839 g, 11.64 mmol, 50.00 eq.), DtBP (**A**: 0.668 g, 3.49 mmol, 5.00 eq.; **B**: 0.222 g, 3.49 mmol, 5.00 eq.) and **A**: 100 mL/**B**: 30 mL of dry toluene were mixed in a pre-dried round-bottom flask and closed air-tight. Subsequently, the flask was placed in an ice bath and the polymerization was started *via* addition of $Et_3Al_2Cl_3$ (**A**: 0.864 g, 3.49 mmol, 5.00 eq.; as 0.4 M solution in 8.73 mL of *n*-hexane; **B**: 0.288 g, 1.16 mmol, 5.00 eq.; as 0.4 M solution in 2.91 mL of *n*-hexane). After 2 hours the reaction was quenched by addition of 10 mL of a 1% NH_4OH in MeOH solution. Subsequently, most of the methanol was removed under reduced pressure and ethyl acetate (EtOAc) and brine were added to separate the phases. The organic phase was washed three times with 1 M $HCl_{(aq)}$ and the combined aqueous phase was extracted once with EtOAc. The combined organic phases were dried over $MgSO_4$, filtered and most of the solvent was removed. Then, the polymer was further purified by precipitating it three times from THF into MeOH. Subsequently, the resulting white solid was dried at 40 °C under vacuum overnight. Yield: **A**: 10.8 g (78%) / **B**: 4.3 g (79%).

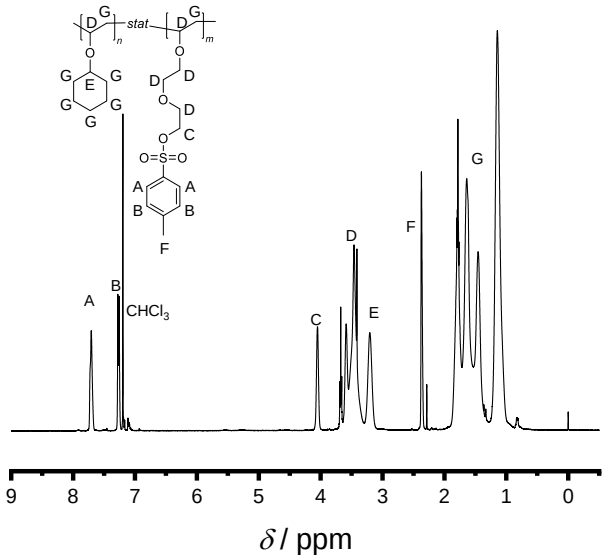

Figure 58. ^{1}H-NMR spectrum of **precursor A**. Solvent: $CDCl_3$.

^{1}H-NMR (400 MHz, Chloroform-*d*$_1$) δ / ppm = 7.87 – 7.69 (m, 2H), 7.38 – 7.28 (m, 2H), 4.25 – 3.98 (m, 2H), 3.70 – 3.37 (m, 11H), 3.37 – 3.18 (m, 4H), 2.52 – 2.37 (m, 3H), 2.01 – 0.94 (m, 50H).

SEC (THF): M_n = 21200 g mol^{-1}, $Đ$ = 1.43.

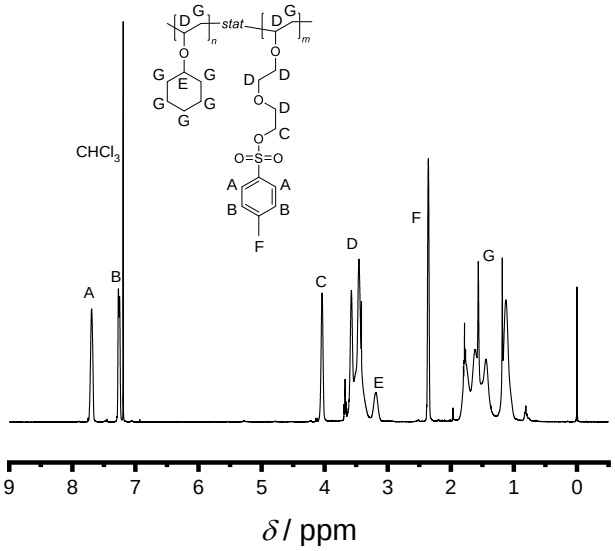

Figure 59. ^{1}H-NMR spectrum of **precursor B**. Solvent: $CDCl_3$.

^{1}H-NMR (400 MHz, Chloroform-d_1) δ / ppm = 7.87 – 7.69 (m, 2H), 7.38 – 7.28 (m, 2H), 4.25 – 3.98 (m, 2H), 3.70 – 3.37 (m, 8H), 3.37 – 3.18 (m, 1H), 2.52 – 2.37 (m, 3H), 2.01 – 0.94 (m, 14H).

SEC (THF): M_n = 17200 g mol^{-1}, $Đ$ = 1.52.

6.3.3 Synthesis of PEO Side Chain Copolymers A/B

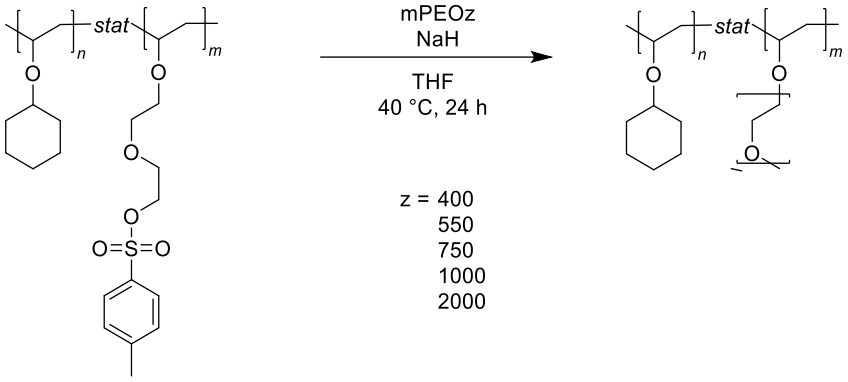

General procedure: Sodium hydride (60% dispersion in mineral oil, 3.20 eq. with respect to tosyl groups in the **precursor** copolymer **A**/**B**, final concentration = 0.134 mol L^{-1}) was placed into a round-bottom flask and the atmosphere was changed to N_2, before being suspended in dry THF. While stirring, poly(ethylene oxide) monomethyl ether (mPEOz); z = 400, 550, 750, 1000, 2000; 3.00 eq., final concentration: 0.126 mol L^{-1}) dissolved in dry THF was slowly added. After the H_2 formation stopped (~ 30 min), the **precursor** copolymer **A**/**B** (1.00 eq., final concentration: 0.042 mol L^{-1}) in THF was added and the reaction mixture was heated to 40 °C and stirred for 24 hours. The reaction was stopped by addition of H_2O and the solvent was removed under reduced pressure. Subsequently, the remaining crude mixture was taken up in a small amount of methanol and dialyzed against methanol to remove the excess of mPEOz. Spectra/Por^{TM} 6 dialysis tubing with a molecular weight cut-off (MWCO) of 2 kD was used for the removal of mPEOz = 400, 550 and 750, 3.5 kD for the removal of mPEO1000 and 8 kD for the removal of mPEO2000, respectively. After the completed dialysis, the solvent was removed under reduced pressure and the resulting polymer was dried at 40 °C under vacuum overnight. Yields are listed in **Table 15** and **Table 16**.

Table 15. Synthesis overview of **polymer** series **A**.

Entry	M_n (mPEOz) [g mol^{-1}]	EO units*	M_n[§] [g mol^{-1}]	$Đ$[§] [1]	MWCO for Dialysis[#] [kD]	Conversion* [%]	Yield
Precursor A	-	-	21200	1.43	-	-	-
Polymer A400	400	11.3	29700	1.36	2	100	3.7 g 61%
Polymer A550	550	15.8	31500	1.31	2	100	3.0 g 72%
Polymer A750	750	19.8	33800	1.27	2	100	2.8 g 69%
Polymer A1000	1000	24.3	34000	1.20	3.5	100	3.2 g 74%
Polymer A2000	2000	54.0	38800	1.11	8	100	3.5 g 79%

*Calculated by ^{1}H-NMR integrals. [§]Measured by SEC with PMMA standards. [#]Spectra/Por™ 6 dialysis tubing; MWCO: Molecular weight cut-off.

Table 16. Synthesis overview of **polymer** series **B**.

Entry	M_n (mPEOz) [g mol^{-1}]	EO units*	M_n[§] [g mol^{-1}]	$Đ$[§] [1]	MWCO for Dialysis[#] [kD]	Conversion* [%]	Yield
Precursor B	-	-	17200	1.52	-	-	-
Polymer B400	400	11.7	25700	1.27	4	100	2.5 g 74%
Polymer B1000	1000	25.2	31000	1.31	8	100	1.9 g 73%
Polymer B2000	2000	52.2	34800	1.12	8	100	1.8 g 62%

*Calculated by ^{1}H-NMR integrals. [§]Measured by SEC with PMMA standards. [#]Spectra/Por™ 6 dialysis tubing; MWCO: Molecular weight cut-off.

6.4 Procedures for 'Synthesis and Post-Polymerization Modification of Defined Functional Poly(Vinyl ether)s'

Benzyl azide (BzN_3) was synthesized as described in the literature.[237]

6.4.1 Allyl ethylene glycol vinyl ether (M1)

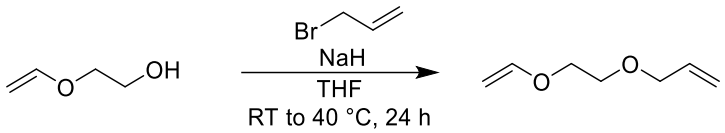

6.94 g of a 60% sodium hydride dispersion in mineral oil (equals to 4.17 g pure NaH, 0.174 mmol, 1.50 eq.) was given into a two-neck round-bottom flask and the atmosphere was immediately changed to nitrogen. Afterwards, it was taken up with 300 mL of dry THF. While stirring, ethylene glycol vinyl ether (15.3 g, 0.174 mmol, 1.50 eq.) was added. Then, allyl bromide (14.0 g, 0.116 mmol, 1.00 eq.) in 20.0 mL of dry THF was slowly added and the reaction was stirred for 24 hours at 40 °C. A sand colored precipitate was formed overnight. Water was carefully given into the reaction solution to quench unreacted NaH and THF was removed under reduced pressure. Afterwards, ethyl acetate and brine were added. Subsequently, the phases were separated, the organic phase was washed four times with water/brine and the aqueous phase was reextracted two times with ethyl acetate. The product was purified by column chromatography with DCM. After removal of the solvent under reduced pressure, 11.0 g (74%) of a yellowish liquid was obtained.

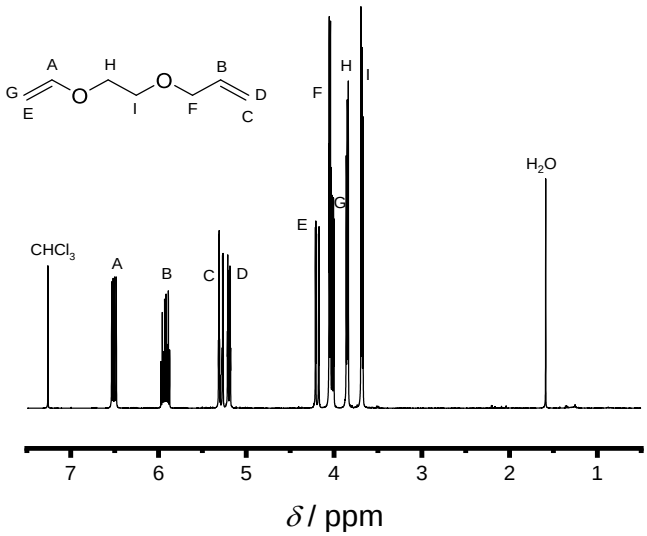

Figure 60. ^{1}H-NMR spectrum of allyl ethylene glycol vinyl ether. Solvent: $CDCl_3$.

^{1}H-NMR (400 MHz, Chloroform-*d*$_1$) δ / ppm = 6.50 (dd, *J* = 14.4, 6.8 Hz, 1H), 5.92 (ddt, *J* = 17.2, 10.4, 5.7 Hz, 1H), 5.29 (ddt, *J* = 17.3, 1.7, 1.7 Hz, 1H), 5.20 (ddt, *J* = 10.4, 1.8, 1.7 Hz, 1H), 4.19 (dd, *J* = 14.3, 2.2 Hz, 1H), 4.05 (dd *J* = 5.7, 1.5, 1.3 Hz, 2H), 4.01 (dd, *J* = 6.8, 2.1 Hz, 1H), 3.89 – 3.82 (m, 2H), 3.72 – 3.65 (m, 2H).

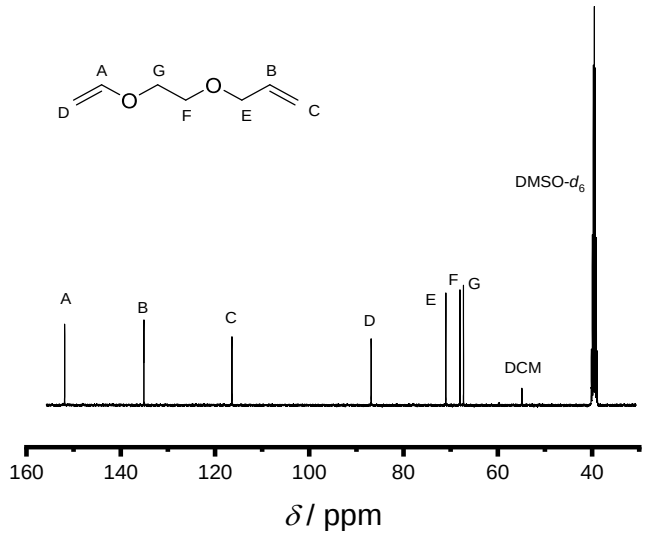

Figure 61. ^{13}C-NMR spectrum of allyl ethylene glycol vinyl ether. Solvent: DMSO-d_6.

^{13}C-NMR (101 MHz, DMSO-*d*$_6$) δ / ppm = 151.87, 135.09, 116.41, 86.87, 71.03, 68.03, 67.27.

6.4.2 Propargyl ethylene glycol vinyl ether (M2)

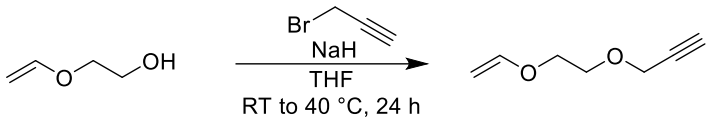

3.23 g of a 60% sodium hydride dispersion in mineral oil (equals to 1.94 g pure NaH, 80.7 mmol, 1.60 eq.) was given into a two-neck round-bottom flask and the atmosphere was immediately changed to nitrogen. Afterwards, it was taken up with 150 mL of dry THF. While stirring, 6.79 mL ethylene glycol vinyl ether (6.67 g, 75.7 mmol, 1.50 eq.) was added. Then, 7.02 mL of a propargyl bromide solution in toluene (equals to 6.00 g, 50.4 mmol, 1.00 eq.) was added slowly and the reaction was stirred for 24 hours at 40 °C. A sand colored precipitate was formed overnight. Water was carefully given into the reaction solution and THF was removed under reduced pressure. Afterwards, ethyl acetate and brine were added. Subsequently, the phases were separated, the organic phase was washed four times with brine and the aqueous phase was reextracted two times with ethyl acetate. The product was purified by column chromatography with DCM. After removal of the solvent under reduced pressure, 5.89 g (93%) of a yellowish liquid was obtained.

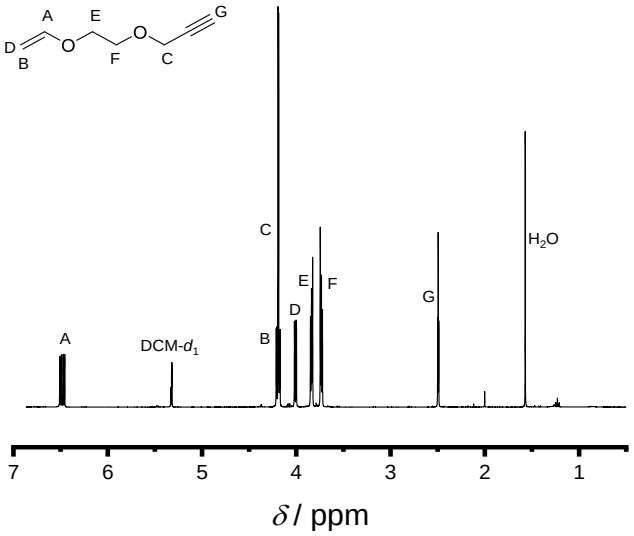

Figure 62. [1]H-NMR spectrum of propargyl ethylene glycol vinyl ether. Solvent: DCM-d_2.

[1]H-NMR (400 MHz, DCM-d_2) δ / ppm = 6.47 (dd, J = 14.3, 6.8 Hz 1H), 4.19 (dd, J = 14.3, 2.1 Hz, 1H), 4.19 (d, J = 2.4 Hz, 2H), 4.01 (dd, J = 6.8, 2.1 Hz, 1H), 3.86 – 3.82 (m, 2H), 3.75 – 3.72 (m, 2H), 2.49 (t, J = 2.4 Hz, 1H).

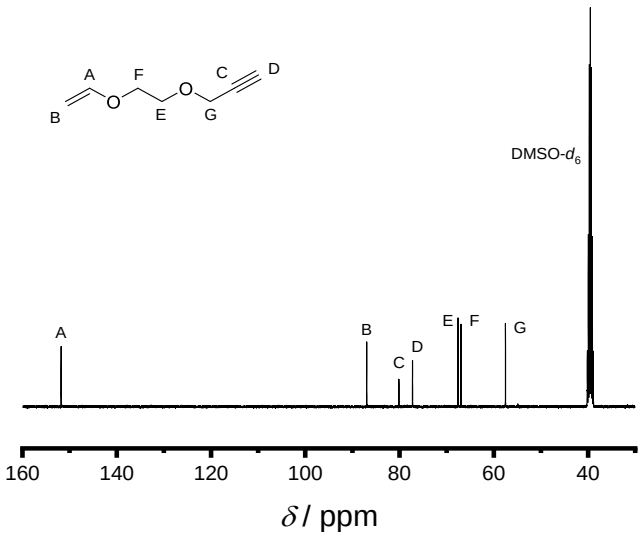

Figure 63. [13]C-NMR spectrum of propargyl ethylene glycol vinyl ether. Solvent: DMSO-d_6.

[13]C-NMR (101 MHz, DMSO-d_6) δ / ppm = 151.80, 86.97, 80.14, 77.3, 67.59, 66.97, 57.52.

6.4.3 4-(Vinyloxy) butyl 4-methylbenzenesulfonate

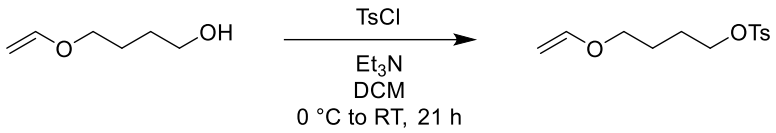

Tetramethylene glycol mono vinyl ether (9.50 g, 81.7 mmol, 1.00 eq.) and triethylamine (9.93 g, 98.2 mmol, 1.20 eq.) were given into a round-bottom flask and taken up with 100 mL of DCM. The reaction mixture was cooled to 0 °C and *p*-toluenesulfonyl chloride (17.15 g, 90.0 mmol, 1.10 eq.) was added while stirring. After 1 hour, the ice bath was removed, and the reaction mixture was stirred for additional 20 hours before it was stopped. The solution was washed twice with 1 M $HCl_{(aq.)}$, once with 1 M $NaOH_{(aq.)}$ and once with pure water. The combined aqueous phases were reextracted twice with DCM. The combined organic phases were then dried over $CaCO_3/MgSO_4$, filtered, and the solvent was removed under reduced pressure yielding 20.3 g (92%) of a slightly yellow oil.

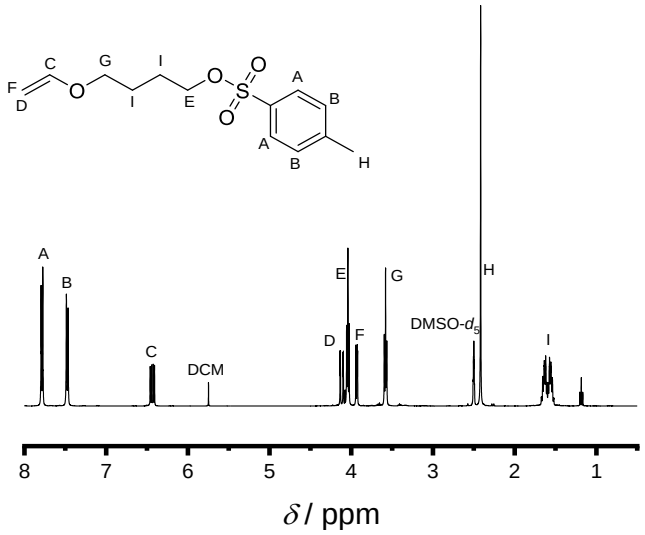

Figure 64. ^{1}H-NMR spectrum of 4-(vinyloxy) butyl 4-methylbenzenesulfonate. Solvent: DMSO-d_6.

^{1}H-NMR (400 MHz, DMSO-d_6) δ / ppm = 7.79 (d, J = 8.4 Hz, 1H), 7.49 (d, J = 8.0 Hz, 1H), 6.44 (dd, J = 14.3, 6.8 Hz, 1H), 4.12 (dd, J = 14.3, 1.7 Hz, 1H), 4.05 (t, J = 6.2 Hz, 1H), 3.94 (dd, J = 6.8, 1.7 Hz, 1H), 3.59 (t, J = 6.2 Hz, 1H), 2.42 (s, 2H), 1.73 – 1.46 (m, 2H).

6.4.4 7-(Vinyloxy)hept-1-ene (M3)

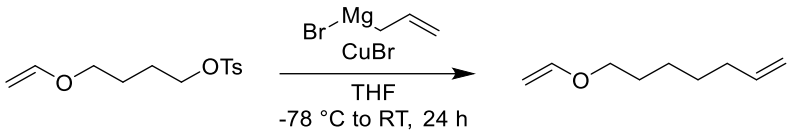

Copper(I) bromide (0.716 g, 4.99 mmol, 0.15 eq.) was filled into a round-bottom flask and the atmosphere was changed to nitrogen. Subsequently, 120 mL of dry diethyl ether were added and the mixture was cooled to -78 °C. Then, 39.9 mL of allyl magnesium bromide in diethyl ether solution (equals to 5.80 g, 39.9 mmol, 1.20 eq. pure allyl magnesium bromide) were added, followed by the slow addition of 4-(vinyloxy) butyl 4-methylbenzenesulfonate (9.00 g, 33.3 mmol, 1.00 eq.). The mixture was allowed to warm to room temperature and stirred for 24 hours before being quenched by the addition of 10 mL of water. The solution was washed three times with 1 M $HCl_{(aq.)}$, once with 1 M $NaOH_{(aq.)}$ and once with pure water. The combined aqueous phases were reextracted twice with diethyl ether. The combined organic phases were then dried over $CaCO_3/MgSO_4$, filtered, and the solvent was removed under reduced pressure yielding a slightly yellow liquid. The product was further purified by column chromatography with pure petrol ether. After removal of the solvent under reduced pressure, 1.96 g (42%) of a colorless liquid were obtained.

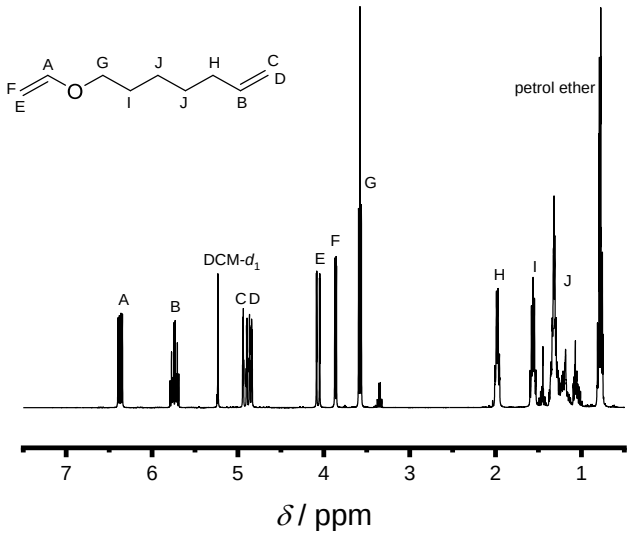

Figure 65. [1]H-NMR spectrum of 7-(vinyloxy)hept-1-ene. Solvent: DCM-d_2.

^{1}H-NMR (400 MHz, DCM-d_2) δ / ppm = 6.37 (dd, J = 14.4, 6.8 Hz, 1H), 5.74 (ddt, J = 16.9, 10.1, 6.7 Hz, 1H), 4.92 (ddt, J = 17.4, 3.0, 2.3 Hz, 1H), 4.85 (ddt, J = 10.2, 2.3, 1.2 Hz, 1H), 4.07 (dd, J = 14.3, 1.8 Hz, 1H), 3.86 (dd, J = 6.8, 1.8 Hz, 1H), 3.58 (t, J = 6.6 Hz, 2H), 2.05 – 1.89 (m, 2H), 1.68 – 1.51 (m, 2H), 1.43 – 1.26 (m, 4H).

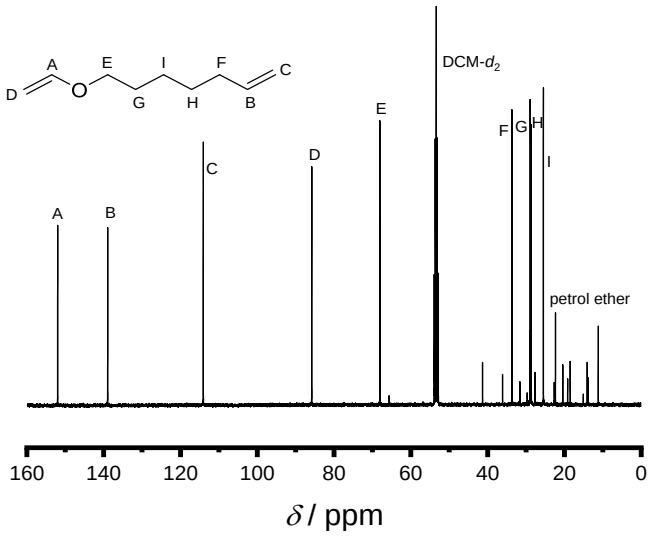

Figure 66. [13]C-NMR spectrum of 7-(vinyloxy)hept-1-ene. Solvent: DCM-d_2.

^{13}C-NMR (101 MHz, DCM-d_2) δ / ppm = 151.99, 138.96, 114.05, 85.81, 68.06, 33.66, 28.91, 28.65, 25.48.

6.4.5 6-(Vinyloxy)hex-1-yne (M4)

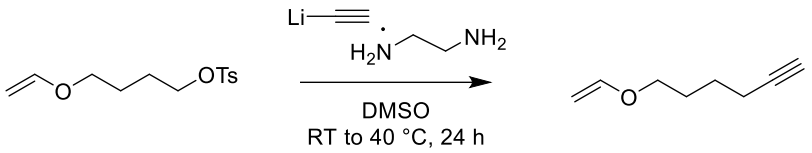

Lithium acetylide ethylenediamine complex (4.09 g, 4.43 mmol, 1.25 eq.) was given into a round-bottom flask and the atmosphere was changed to nitrogen. Subsequently, 40 mL of dry dimethyl sulfoxide (DMSO) were added followed by the slow addition of 4-(vinyloxy) butyl 4-methylbenzenesulfonate (9.60 g, 35.5 mmol, 1.00 eq.). The mixture was stirred for 24 hours before being quenched by the addition of 8 mL of water. 100 mL of brine and 100 mL of diethyl ether were added to separate the phases. The aqueous phase was extracted four times with diethyl ether and the combined organic phases were washed once with brine. Then, the organic phase was dried over $CaCO_3/MgSO_4$, filtered, and the solvent was removed under reduced pressure yielding a slightly yellow liquid. The product was further purified by column chromatography with pure petrol ether. After removal of the solvent under reduced pressure, 1.50 g (34%) of a colorless liquid were obtained.

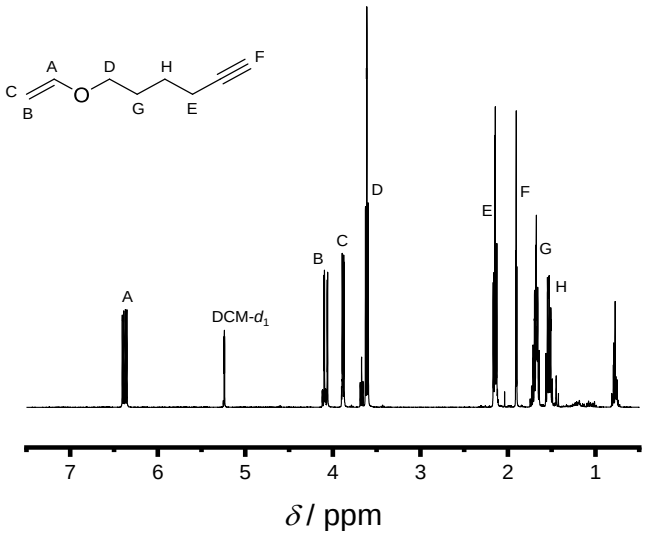

Figure 67. ^{1}H-NMR spectrum of 6-(vinyloxy)hex-1-yne. Solvent: DCM-d_2.

^{1}H-NMR (400 MHz, DCM-d_2) δ / ppm = 6.38 (dd, J = 14.3, 6.8 Hz, 1H), 4.08 (dd, J = 14.3, 1.9 Hz, 1H), 3.88 (dd, J = 6.8, 1.9 Hz, 1H), 3.61 (t, J = 6.3 Hz, 2H), 2.15 (td, J = 7.0, 2.7 Hz, 2H), 1.90 (t, J = 2.7 Hz, 1H), 1.77 – 1.62 (m, 2H), 1.59 – 1.51 (m, 2H).

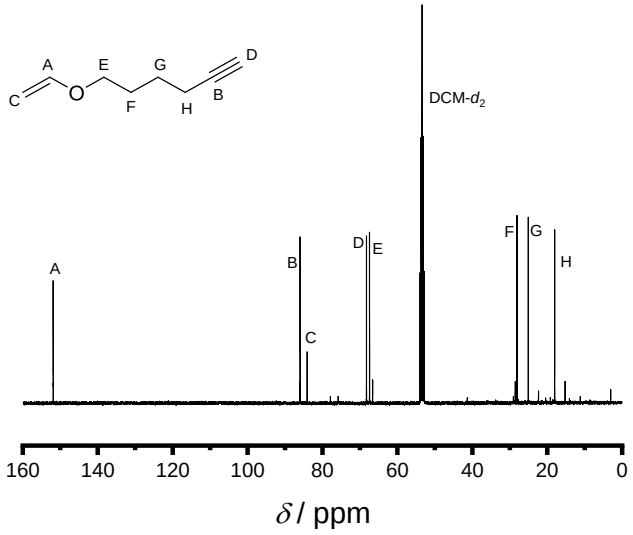

Figure 68. ^{13}C-NMR spectrum of 6-(vinyloxy)hex-1-yne. Solvent: DCM-d_2.

^{13}C-NMR (101 MHz, DCM-d_2) δ / ppm = 152.47, 86.56, 84.67, 68.84, 68.02, 28.67, 25.65, 18.61.

6.4.6 Polymerization Procedures

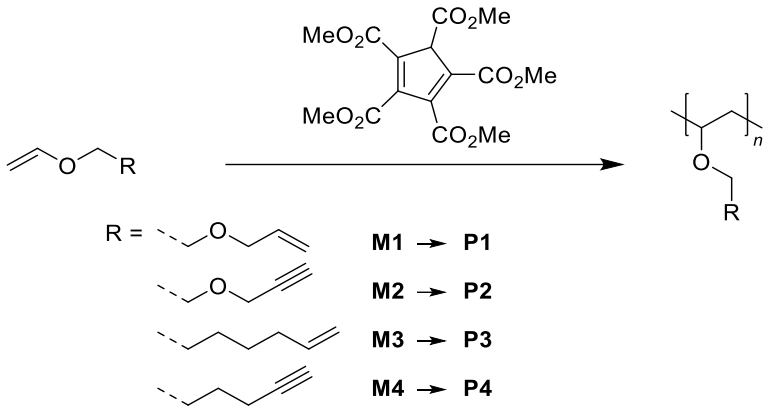

Pentakis(methoxycarbonyl)cyclopentadiene (PMCCP) (1.00 eq.) was given into a 10 mL crimp-cap vial under ambient conditions. Afterwards, the corresponding vinyl ether (25, 50 or 100 eq.) was added and the vial was closed. The polymerization was stopped after a specific time (see **Table 17**) by addition of MeOH/NH_4OH. The product was purified by dissolving the polymer in ethyl acetate, washing the organic phase with water/brine and reextracting the aqueous phase with ethyl acetate. In the end, the solvent was removed under reduced pressure at 50 °C (yields ~ 80%).

For polymerizations under nitrogen atmosphere the vials were closed prior to the vinyl ether addition, the atmosphere was purged with a nitrogen flow for 10 minutes and subsequently the corresponding vinyl ether was added with a syringe.

Samples were taken with a syringe if necessary and quenched with MeOH/NH_4OH.

Table 17. Overview of the polymerizations of the different **monomers 1** – **4** using PMCCP as single-component initiator and control agent.

Entry	Monomer	Eq.	Atmosphere	Time [h]	$M_{n,theo}$§ [g mol^{-1}]	$M_{n,exp}$* [g mol^{-1}]	$Đ$* [1]
1	**M1**	25	Air	2	3200	3400	1.25
2	**M1**	50	Air	2	6400	5700	1.14
3	**M1**	100	Air	3	12800	3700	1.56
4	**M1**	100	N_2	3	12800	7500	1.33
5	**M2**	25	Air	1	3150	4000	1.16
6	**M2**	50	Air	2	6300	7100	1.19
7	**M2**	100	Air	3	12600	5100	1.45
8	**M2**	100	N_2	3	12600	11000	1.36
9	**M3**	25	Air	3	3500	3000	1.07
10	**M3**	50	Air	3	7000	5200	1.06
11	**M3**	100	Air	6	14000	10500	1.11
12	**M4**	25	Air	3	3100	3000	1.07
13	**M4**	50	Air	4	6200	6000	1.05
14	**M4**	100	Air	8	12400	9800	1.10

*Determined by SEC with PMMA standards. §$M_{n,theo}$ = M(monomer) × eq.

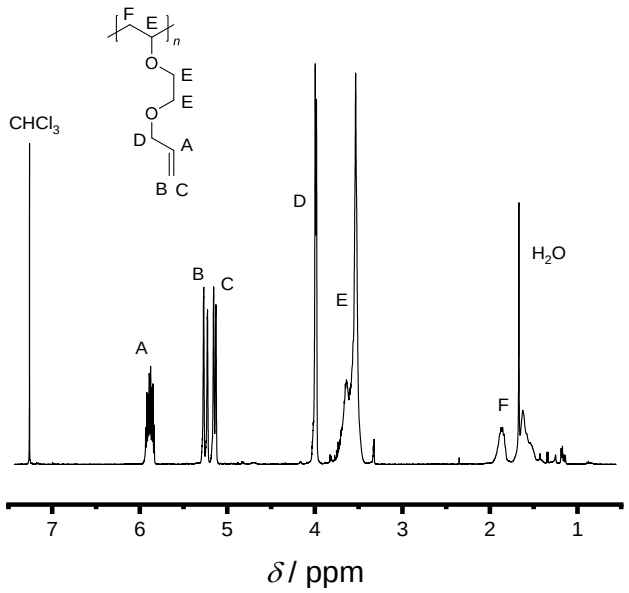

Figure 69. ^{1}H-NMR spectrum of poly(allyl ethylene glycol vinyl ether) (**P1**). Solvent: $CDCl_3$.

^{1}H-NMR (400 MHz, Chloroform-*d*$_1$) δ / ppm = 5.96 – 5.82 (m, 1H), 5.29 – 5.21 (m, 1H), 5.18 – 5.11 (m, 1H), 4.06 – 3.96 (m, 2H), 3.79 – 3.44 (m, 5H), 1.97 – 1.47 (m, 2H).

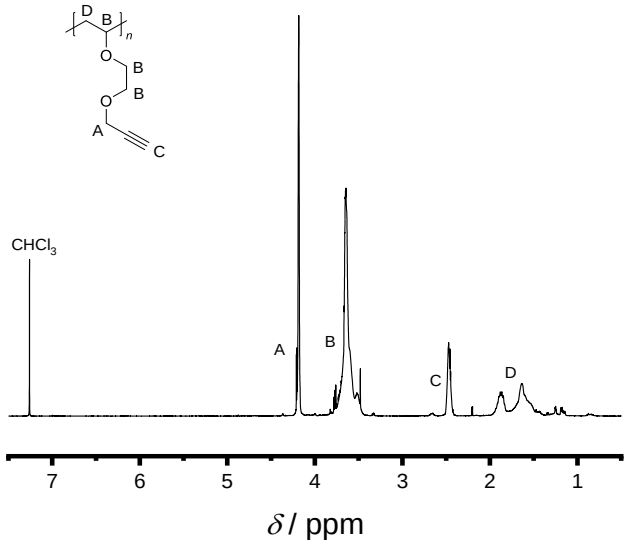

Figure 70. ^{1}H-NMR spectrum of poly(propargyl ethylene glycol vinyl ether) (**P2**). Solvent: $CDCl_3$.

^{1}H-NMR (400 MHz, Chloroform-*d*$_1$) δ / ppm = 4.23 – 4.15 (m, 2H), 3.80 – 3.46 (m, 5H), 2.53 – 2.42 (m, 1H), 1.95 – 1.48 (m, 2H).

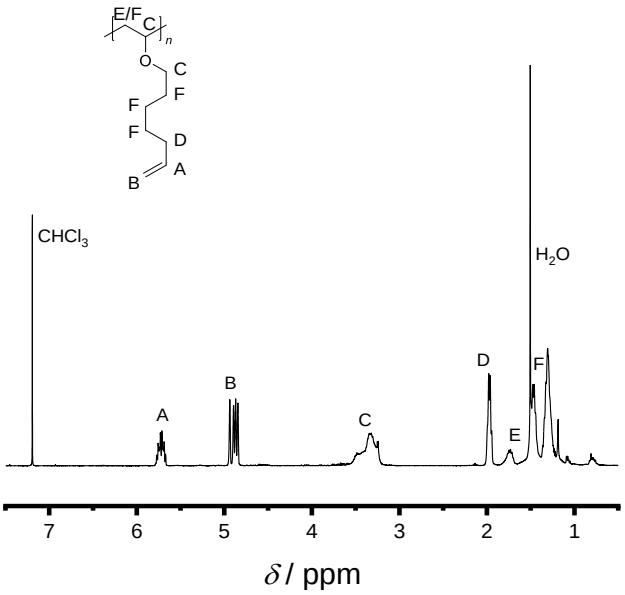

Figure 71. [1]H-NMR spectrum of poly(7-(vinyloxy)hept-1-ene) (**P3**). Solvent: $CDCl_3$.

^{1}H-NMR (400 MHz, Chloroform-*d*$_1$) δ / ppm = 5.78 – 5.66 (m, 1H), 4.95 – 4.83 (m, 2H), 3.53 – 3.21 (m, 3H), 2.02 – 1.93 (m, 2H), 1.88 – 1.68 (m, 1H), 1.59 – 1.16 (m, 7H).

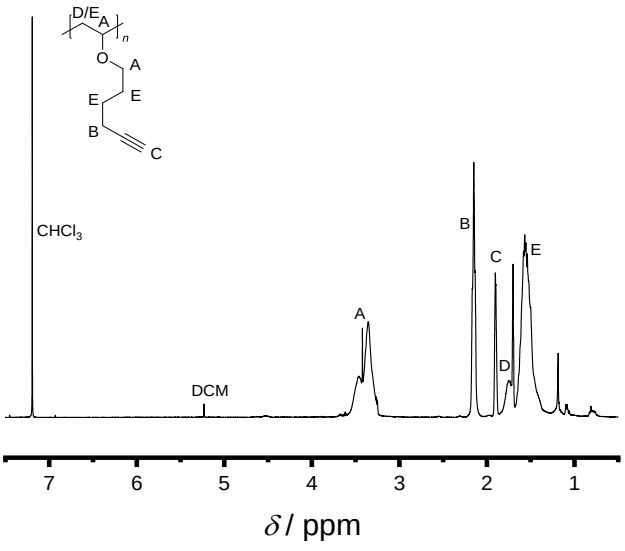

Figure 72. [1]H-NMR spectrum of poly(6-(vinyloxy)hex-1-yne) (**P4**). Solvent: $CDCl_3$.

^{1}H-NMR (400 MHz, Chloroform-*d*$_1$) δ / ppm = 3.56 – 3.24 (m, 3H), 2.20 – 2.09 (m, 2H), 1.92 – 1.87 (m, 1H), 1.81 – 1.68 (m, 1H), 1.68 – 1.33 (m, 5H).

6.4.7 Thiol-ene/yne Reaction Procedures

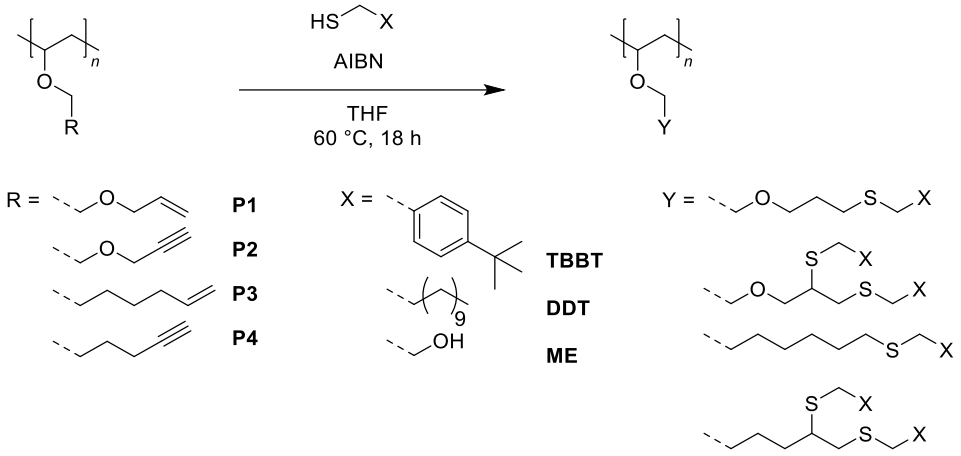

The respective poly(vinyl ether) (1.00 eq., 0.250 mol L^{-1}*) was given into a crimp-cap vial and dissolved in THF. Afterwards, the corresponding thiol (DDT, TBBT or ME, 4.00 eq. per repeating unit, 1.00 mol L^{-1}) followed by AIBN (1.00 eq. per repeating unit, 0.250 mol L^{-1}) were added to the reaction solution and the vial was sealed. The atmosphere was changed to nitrogen by purging for 10 minutes and the flask was placed into an oil bath at 60 °C. The solution was stirred overnight. Afterwards, the solution was precipitated into methanol (TBBT), ethanol (DDT) or diethyl ether (ME), centrifuged and washed three times with the respective precipitation liquid. Subsequently, the polymers were dried under vacuum at 40 °C overnight.

*equivalents and concentration with respect to each repeating unit

Table 18. Overview of the post-polymerization modification reactions of polymers **P1** – **P4**.

Entry	Polymer	PPM	Reactant	Conversion[#]	$M_{n,before}$* [g mol^{-1}]	$Đ_{before}$* [1]	$M_{n,after}$* [g mol^{-1}]	$Đ_{after}$* [1]
1	**P1**	Thiol-ene	DDT	Quant.	5700	1.14	14600	1.13
2	**P1**	Thiol-ene	TBBT	Quant.	5700	1.14	10100	1.14
3	**P1**	Thiol-ene	ME	Quant.	5700	1.14	7400	1.12
4	**P2**	Thiol-yne	DDT	Quant.	7100	1.19	19200	1.22
5	**P2**	Thiol-yne	TBBT	Quant.	7100	1.19	15500	1.33
6	**P3**	Thiol-ene	DDT	Quant.	5200	1.06	10500	1.07
7	**P3**	Thiol-ene	TBBT	Quant.	5200	1.06	8700	1.07
8	**P3**	Thiol-ene	ME	Quant.	5200	1.06	6500	1.08
9	**P4**	Thiol-yne	DDT	Quant.	6000	1.05	15000	1.06
10	**P4**	Thiol-yne	TBBT	Quant.	6000	1.05	12200	1.10

*Determined by SEC with PMMA standards. [#]Quantitative conversion of the respective functional group as determined by ^{1}H-NMR spectroscopy.

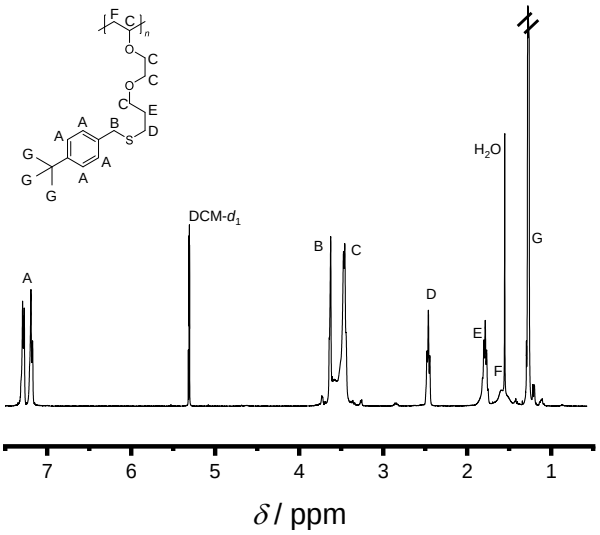

Figure 73. ^{1}H-NMR spectrum of **P1** after the *thiol-ene* reaction with TBBT. Solvent: DCM-d_2.

^{1}H-NMR (400 MHz, DCM-d_2) δ / ppm = 7.35 – 7.16 (m, 4H), 3.65 – 3.61 (m, 2H), 3.61 – 3.41 (m, 7H), 2.49 – 2.43 (m, 2H), 1.89 – 1.74 (m, 2H), 1.65 – 1.48 (m, 1H), 1.30 – 1.22 (m, 9H).

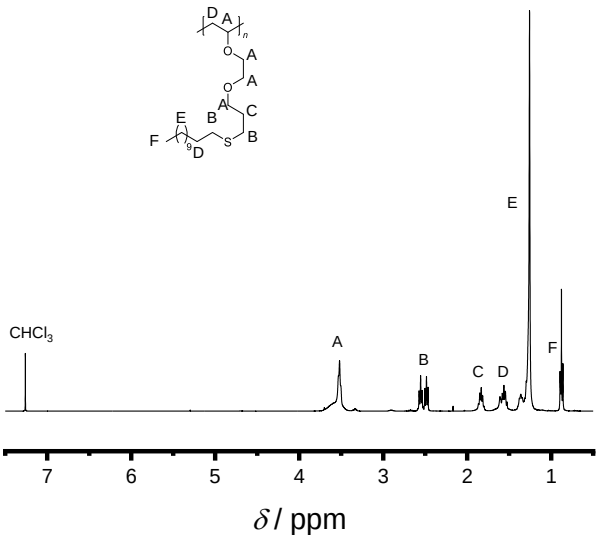

Figure 74. [1]H-NMR spectrum of **P1** after the *thiol-ene* reaction with DDT. Solvent: $CDCl_3$.

^{1}H-NMR (400 MHz, Chloroform-d_1) δ / ppm = 3.74 – 3.45 (m, 7H), 2.59 – 2.46 (m, 4H), 1.87 – 1.79 (m, 2H), 1.64 – 1.52 (m, 4H), 1.39 – 1.22 (m, 18H), 0.90 – 0.85 (m, 3H).

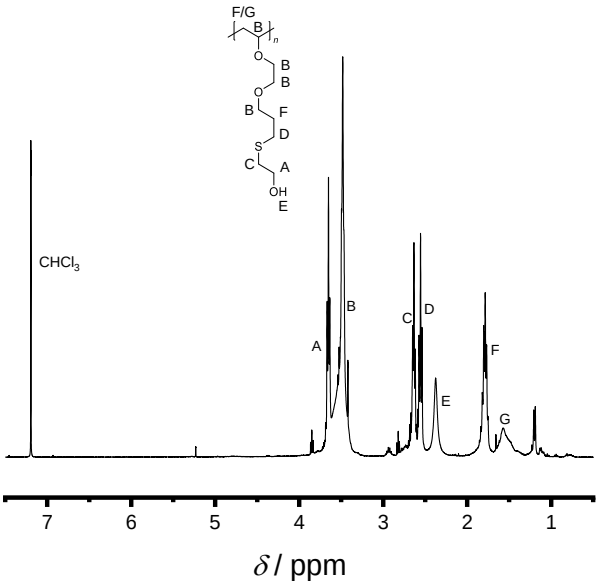

Figure 75. [1]H-NMR spectrum of **P1** after the *thiol-ene* reaction with ME. Solvent: $CDCl_3$.

^{1}H-NMR (400 MHz, Chloroform-d_1) δ / ppm = 3.68 – 3.62 (m, 2H), 3.62 – 3.37 (m, 7H), 2.68 – 2.61 (m, 2H), 2.60 – 2.52 (m, 2H), 2.44 – 2.31 (m, 1H), 1.88 – 1.72 (m, 3H), 1.69 – 1.39 (m, 1H).

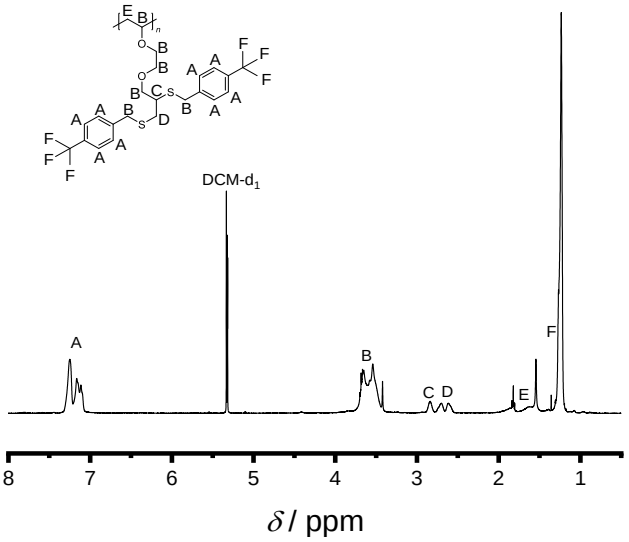

Figure 76. [1]H-NMR spectrum of **P2** after the *thiol-yne* reaction with TBBT. Solvent: DCM-d_2.

^{1}H-NMR (400 MHz, DCM-d_2) δ / ppm = 7.31 – 7.07 (m, 8H), 3.65 – 3.61 (m, 2H), 3.74 – 3.41 (m, 11H), 2.87 – 2.80 (m, 1H), 2.76 – 2.56 (m, 2H), 1.98 – 1.50 (m, 1H), 1.30 – 1.19 (m, 18H).

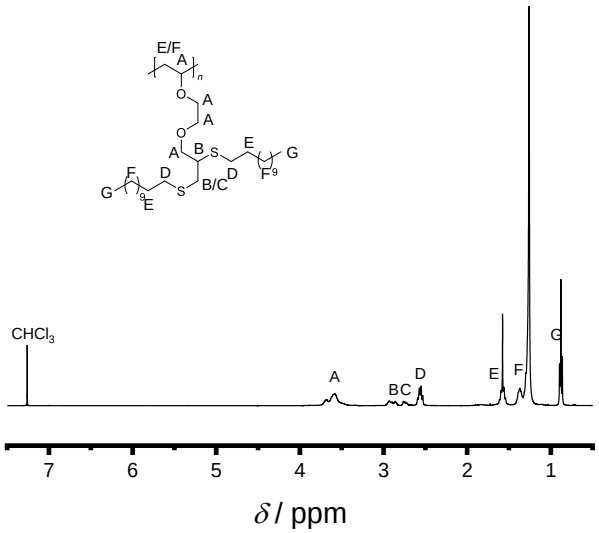

Figure 77. [1]H-NMR spectrum of **P2** after the *thiol-yne* reaction with DDT. Solvent: $CDCl_3$.

^{1}H-NMR (400 MHz, Chloroform-d_1) δ / ppm = 3.73 – 3.46 (m, 7H), 2.99 – 2.82 (m, 2H), 2.61 – 2.52 (m, 4H) 1.87 – 1.79 (m, 2H), 1.65 – 1.52 (m, 5H), 1.45 – 1.19 (m, 37H), 0.91 – 0.85 (m, 6H).

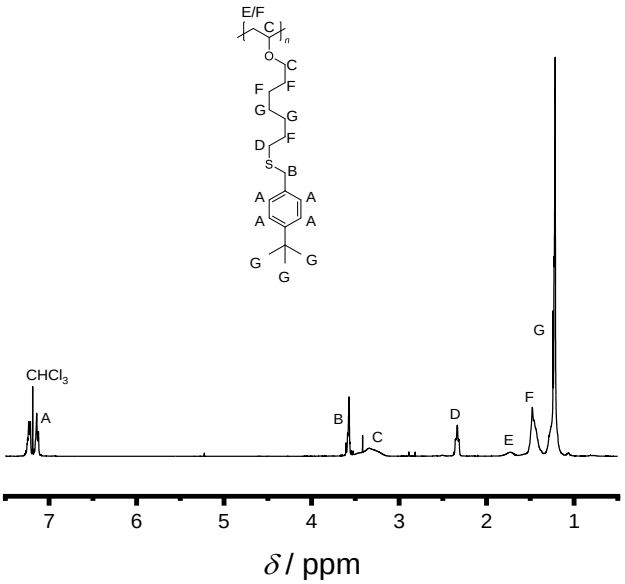

Figure 78. ^{1}H-NMR spectrum of **P3** after the *thiol-ene* reaction with TBBT. Solvent: $CDCl_3$.

^{1}H-NMR (400 MHz, Chloroform-*d*$_1$) δ / ppm = 7.28 – 7.09 (m, 4H), 3.62 – 3.54 (m, 2H), 3.48 – 3.13 (m, 3H), 2.37 – 2.30 (m, 2H), 1.80 – 1.65 (m, 1H), 1.55 – 1.35 (m, 5H), 1.32 – 1.13 (m, 9H).

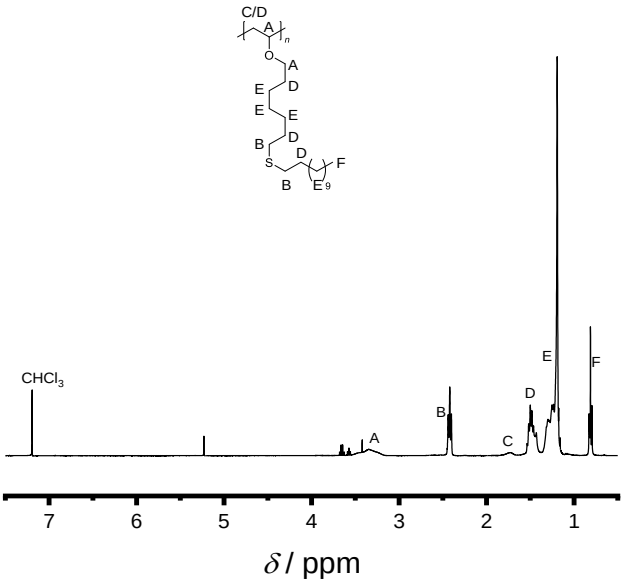

Figure 79. ^{1}H-NMR spectrum of **P3** after the *thiol-ene* reaction with DDT. Solvent: $CDCl_3$.

^{1}H-NMR (400 MHz, Chloroform-*d*$_1$) δ / ppm = 3.55 – 3.16 (m, 3H), 2.46 – 2.38 (m, 4H), 1.81 – 1.66 (m, 1H), 1.55 – 1.39 (m, 7H), 1.35 – 1.13 (m, 24H), 0.85 – 0.77 (m, 3H).

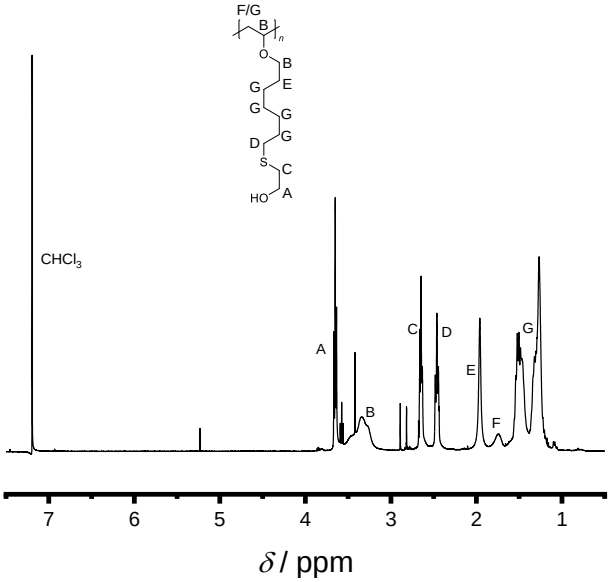

Figure 80. [1]H-NMR spectrum of **P3** after the *thiol-ene* reaction with ME. Solvent: $CDCl_3$.

^{1}H-NMR (400 MHz, Chloroform-d_1) δ / ppm = 3.69 – 3.60 (m, 2H), 3.55 – 3.15 (m, 3H), 2.68 – 2.57 (m, 2H), 2.50 – 2.38 (m, 2H), 2.02 – 1.89 (m, 2H), 1.86 – 1.68 (m, 1H), 1.62 – 1.16 (m, 9H).

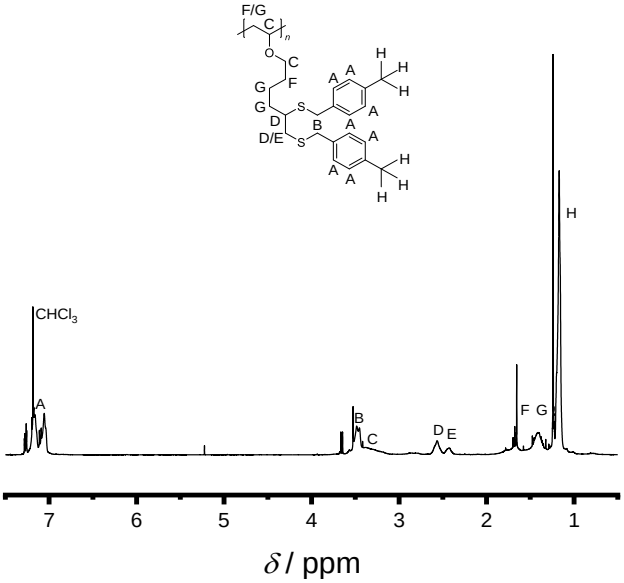

Figure 81. [1]H-NMR spectrum of **P4** after the *thiol-yne* reaction with TBBT. Solvent: $CDCl_3$.

^{1}H-NMR (400 MHz, Chloroform-d_1) δ / ppm = 7.28 – 7.02 (m, 8H), 3.53 – 3.42 (m, 4H), 3.58 – 3.15 (m, 3H), 2.62 – 2.50 (m, 2H), 2.49 – 2.37 (m, 1H), 1.84 – 1.57 (m, 3H), 1.54 – 1.30 (m, 5H), 1.25 – 1.12 (m, 18H).

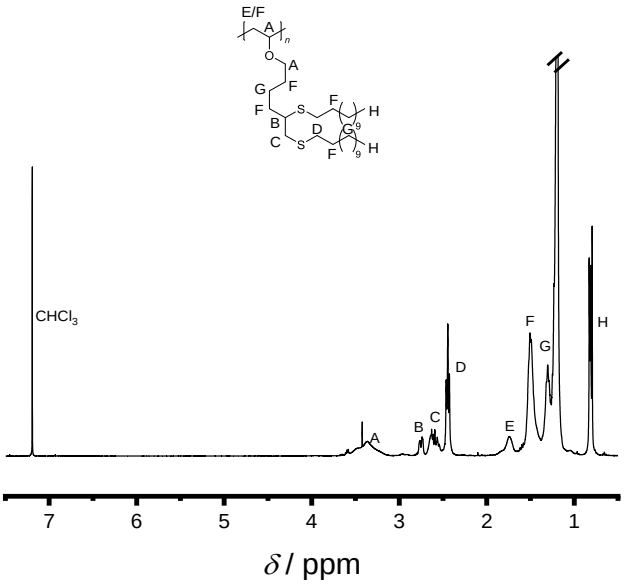

Figure 82. ^{1}H-NMR spectrum of **P4** after the *thiol-yne* reaction with DDT. Solvent: $CDCl_3$.

^{1}H-NMR (400 MHz, Chloroform-d_1) δ / ppm = 3.62 – 3.15 (m, 3H), 2.79 – 2.71 (m, 1H), 2.70 – 2.52 (m, 2H), 2.49 – 2.38 (m, 2H), 1.83 – 1.66 (m, 1H), 1.62 – 1.38 (m, 9H), 1.37 – 1.12 (m, 38H), 0.87 – 0.74 (m, 6H).

6.4.8 CuAAC Reaction Procedures

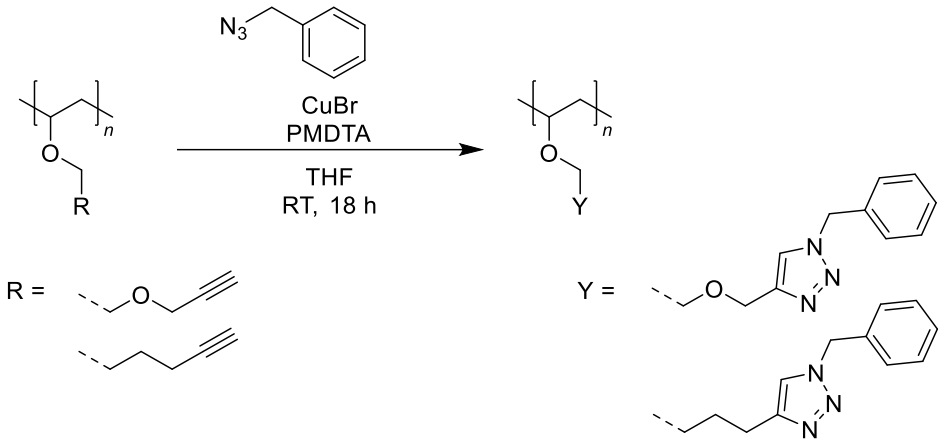

Copper(I) bromide (0.20 eq. per repeating unit, 0.037 mol L^{-1}) was given into a crimp-cap vial, the vial was closed and the atmosphere was changed to nitrogen. The respective poly(vinyl ether) (1.00 eq., 0.184 mol L^{-1}*), benzyl azide (3.00 eq per repeating unit, 0.553 mol L^{-1}) and PMDTA (0.4 eq. per repeating unit, 0.074 mol L^{-1}) were dissolved in THF and added into the crimp-cap vial with a syringe. The reaction was stirred at room temperature overnight. Afterwards, the solution was precipitated in methanol and washed three times with methanol. Subsequently, the resulting polymers were dried under vacuum at 40 °C overnight.

*equivalents and concentration with respect to each repeating unit

Table 19. Overview of the post-polymerization modification reactions of polymers **P2** and **P4**.

Entry	Polymer	PPM	Reactant	Conversion[#]	$M_{n,before}$* [g mol^{-1}]	$Đ_{before}$* [1]	$M_{n,after}$* [g mol^{-1}]	$Đ_{after}$* [1]
1	**P2**	CuAAC	BzN3	Quant.	7100	1.19	9900	1.11
2	**P4**	CuAAC	BzN3	Quant.	6000	1.05	7400	1.05

*Determined by SEC with PMMA standards. [#]Quantitative conversion of the respective functional group as determined by ^{1}H-NMR spectroscopy.

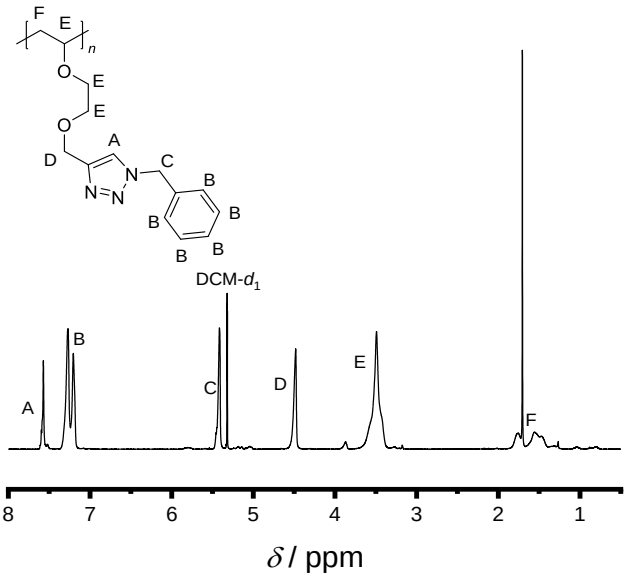

Figure 83. ^{1}H-NMR spectrum of **P2** after the CuAAC reaction with BzN_3. Solvent: DCM-d_2.

^{1}H-NMR (400 MHz, DCM-d_2) δ / ppm = 7.61 – 7.50 (m, 1H), 7.36 – 7.16 (m, 5H), 5.47 – 5.37 (m, 2H), 4.58 – 4.44 (m, 2H), 3.66 – 3.36 (m, 5H), 1.85 – 1.37 (m, 2H).

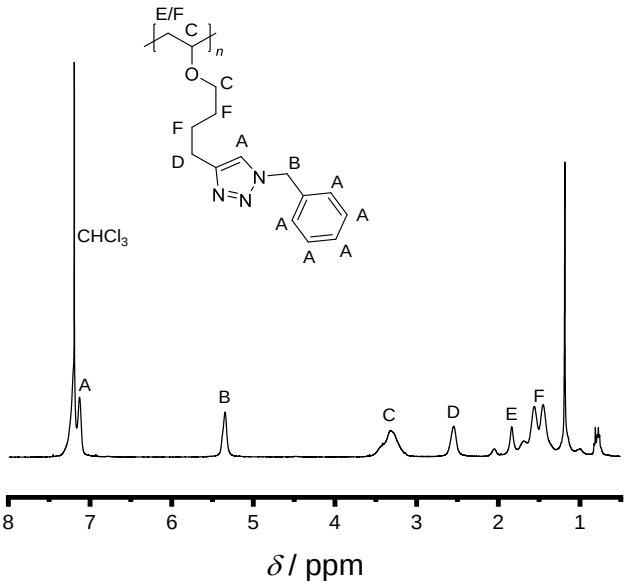

Figure 84. ^{1}H-NMR spectrum of **P4** after the CuAAC reaction with BzN_3. Solvent: $CDCl_3$.

^{1}H-NMR (400 MHz, DCM-d_2) δ / ppm = 7.37 – 7.06 (m, 6H), 5.43 – 5.24 (m, 2H), 3.57 – 3.10 (m, 3H), 2.65 – 2.42 (m, 2H), 1.94 – 1.76 (m, 1H), 1.74 – 1.30 (m, 5H).

6.5 Procedures for 'The Power of Architecture – *Cage*-shaped PEO and its Application as a Polymer Electrolyte'

The synthesis of the *cage*-shaped PEO was accomplished by Dr. M. Gauthier-Jaques and is therefore covered in his dissertation and/or the respective publication.[181,182]

The PE preparation and all other measurements were conducted accordingly to the general procedures.

6.6 Procedures for 'Styrene-Based Poly(ethylene oxide) Side Chain Block Copolymers as Solid Polymer Electrolyte for High-Voltage Lithium-Metal Batteries'

6.6.1 Macromonomer Synthesis (4-Vinylbenzyl mPEOz ether, VBmPEOz)

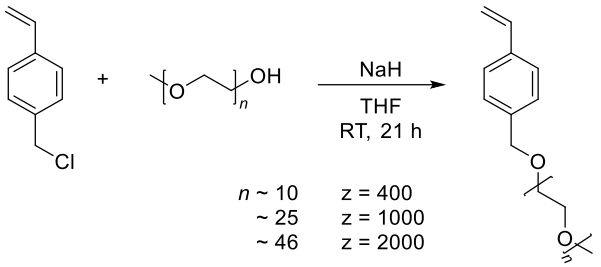

Sodium hydride (60% dispersion in mineral oil, 1.5 eq. pure NaH, 0.075 mol L^{-1}) was placed in a round-bottom flask with a corresponding amount of dry THF and purged with dry N_2 for 15 min while stirring. Afterwards, mPEOz (1.00 eq., 0.05 mol L^{-1}) was added dropwise (solid mPEOz was dissolved in dry THF prior addition) and the mixture was stirred until the H_2 formation stopped (~ 30 min). Then, 4-vinylbenzyl chloride (3.00 eq., 0.15 mol L^{-1}) was slowly added. The reaction was stirred overnight. Afterwards, the reaction was quenched with 10 mL of water and concentrated under reduced pressure. Water and DCM were added to separate the phases. The organic phase was washed with water four times and the aqueous phase was reextracted once with DCM. The combined organic phases were dried over $MgSO_4$, filtered and the solvent was concentrated under reduced pressure. Subsequently, the product was precipitated four times from THF into cold diethyl ether and centrifuged. The product was obtained as slightly yellow liquid (z = 400) or as slightly yellow/white solid (z = 1000/2000) and dried at 40 °C under vacuum overnight. Yields: 80 – 95%

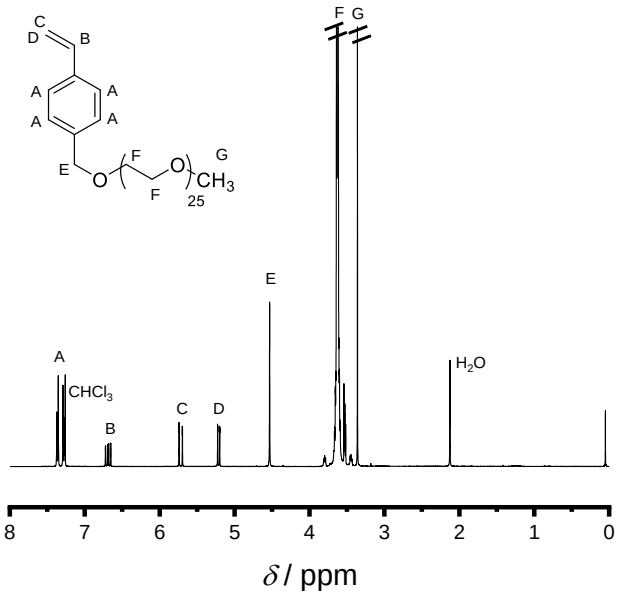

Figure 85. Exemplary ^{1}H-NMR spectrum of VBmPEO1000. Solvent: $CDCl_3$.

^{1}H-NMR (400 MHz, Chloroform-d_1) δ / ppm = 7.39 – 7.28 (m, 4H), 6.74 – 6.67 (dd, J = 17.6, 10.9 Hz, 1H), 5.75 – 5.71 (d, J = 17.6 Hz, 1H), 5.24 – 5.21 (d, J = 10.9 Hz, 1H), 4.54 (s, 2H), 3.68 – 3.52 (m, xH), 3.37 (s, 3H).

Integrals: z = 400: x = 38, z = 1000: x = 101, z = 2000: x= 194.

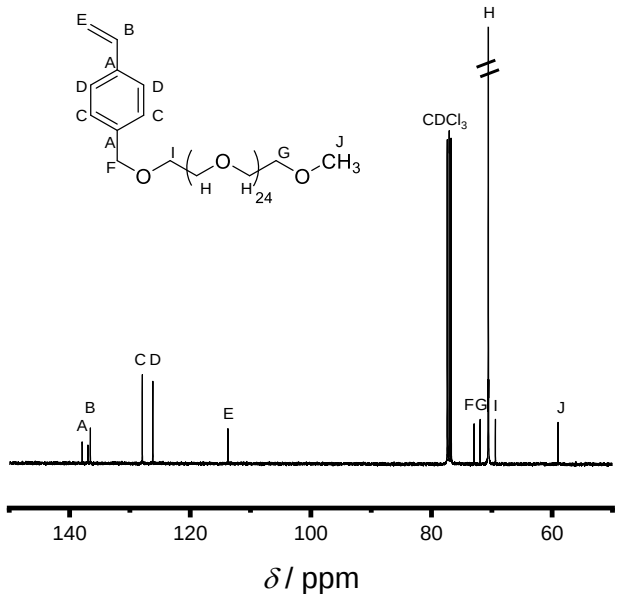

Figure 86. Exemplary ^{13}C-NMR spectrum of VBmPEO1000. Solvent: $CDCl_3$.

^{13}C-NMR (400 MHz, Chloroform-d_1) δ / ppm = 138.01, 137.04, 136.69, 128.03, 126.30, 113.82, 73.04, 72.04, 70.74, 69.49, 59.12.

6.6.2 Homopolymerization of VBmPEOz

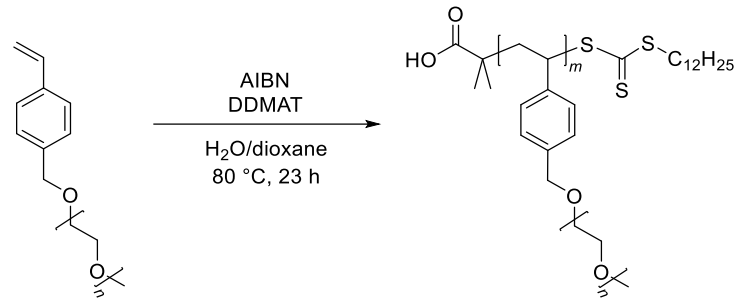

2-(Dodecylthiocarbonothioylthio)-2-methylpropionic acid (DDMAT, 1.00 eq.) was dissolved in a 1:1 mixture of water and dioxane in a round-bottom flask. VBmPEOz (z = 400: 30.0 eq, 0.65 mol L^{-1}, z = 1000: 15.0 eq., 0.45 mol L^{-1}, z = 2000: 9.00 eq., 0.35 mol L^{-1}) and AIBN (0.50 eq.) were added subsequently. The solution was purged with N_2 for 20 minutes and the polymerization was conducted at 80 °C for 23 hours. Subsequently, the polymerization was stopped by placing the flask in the freezer. Then, the solvent was removed under reduced pressure. Poly(VBmPEO400) was obtained as a highly viscous, yellow liquid, poly(VBmPEO1000) and poly(VBmPEO2000) were obtained as a solid product and used directly as macro RAFT-agents for the block copolymerization. Yields: 100%

6.6.3 Block Copolymerization

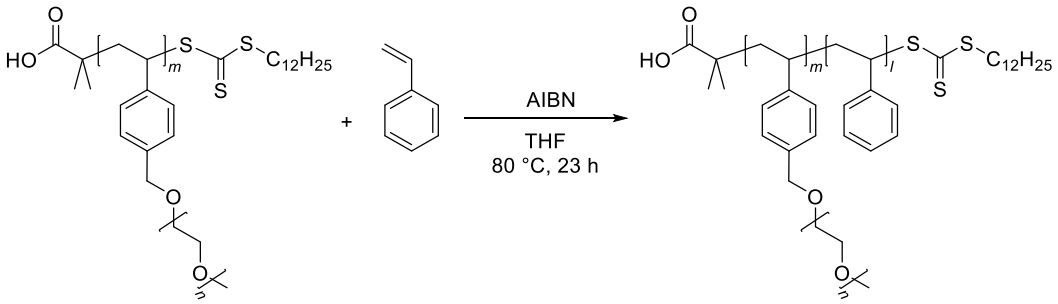

The previously obtained macroRAFT-agent (poly(VBmPEOz), 1.00 eq., z = 400: 0.014 mol L^{-1}, z = 1000: 0.013 mol L^{-1}, z = 2000: 0.009 mol L^{-1}) was dissolved in dioxane and styrene (z = 400: 200 eq, 2.88 mol L^{-1}, z = 1000: 200 eq., 2.54 mol L^{-1}, z = 2000: 500 eq. 4.37 mol L^{-1}) as well as AIBN (0.5 eq.) were added. The reaction was purged with N_2 for

10 min and polymerized at 80 °C for 23 hours. Subsequently, the product was precipitated into diethyl ether, redissolved in THF and reprecipitated in diethyl ether for three times. The resulting polymer was dried at 50 °C under vacuum overnight. Yields: 80 – 90%

Table 20. Overview of the different block copolymers.

Entry	$M_{n,mPEOz}$ [g mol^{-1}]	EO units*	$M_{n,\ PVBmPEOz}$§ [g mol^{-1}]	$Đ_{PVBmPEOz}$§	$M_{n,\ BPz}$§ [g mol^{-1}]	$Đ_{BPz}$§	$w_{VBmPEOz}$#	$\phi_{VBmPEOz}$$
BP400	400	9.4	10100	1.11	24900	1.22	0.56	0.53
BP1000	1000	25.5	10400	1.08	28600	1.25	0.52	0.49
BP2000	2000	48.4	17600	1.10	38300	1.16	0.49	0.46

*Average per PEO side chain. Calculated by ^{1}H-NMR integration. §Measured by SEC with PS standards. #Calculated by ^{1}H-NMR integration. $Calculated using the densities of PS (1.07 g cm^{-3}) and PEO (1.21 g cm^{-3}). Note that this calculation is not 100% correct, since PEO is attached as side chain.

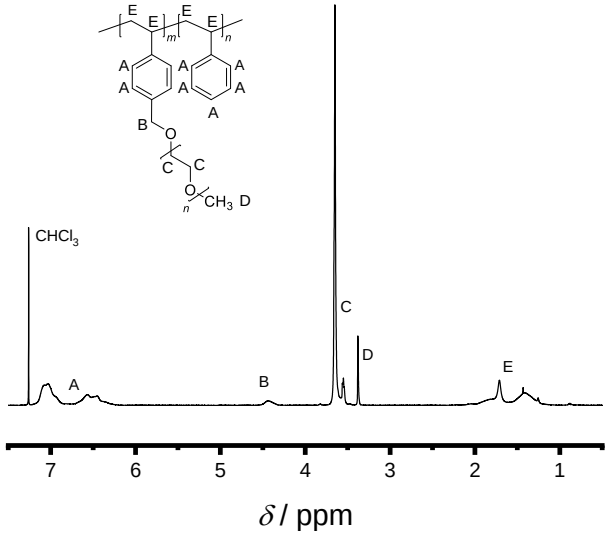

Figure 87. Exemplary ^{1}H-NMR spectrum of PS-*b*-VBmPEO400 (**BP400**). Solvent: $CDCl_3$.

^{1}H-NMR (400 MHz, Chloroform-d_1): δ / ppm = 7.22 – 6.18, 4.54 – 4.30, 3.71 – 3.49, 3.39 – 3.35, 2.00 – 1.16.

6.7 Procedures for 'Advanced Block Copolymer Design for Polymer Electrolytes: Prospects of Microphase Separation'

6.7.1 Block Copolymer Synthesis (PVBmPEO2000-*b*-PS)

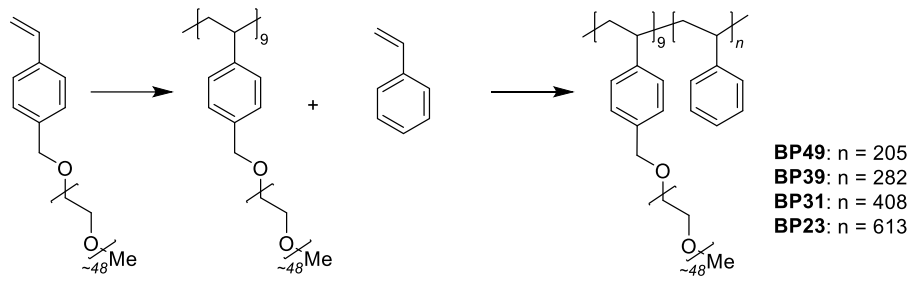

PVBmPEO2000

The poly(VBmPEO2000) (PVBmPEO2000) macro-RAFT agent was prepared as described in **Chapter 6.6.2**.

PVBmPEO2000 (1.00 eq., BP49: 0.0087 mol L^{-1}, BP39: 0.0073 mol L^{-1}, BP31: 0.0069 mol L^{-1}, BP23: 0.0039 mol L^{-1}) was dissolved in dioxane and styrene (BP49: 500 eq., BP39: 770 eq., BP31: 1050 eq., BP23: 2000 eq.) as well as AIBN (BP49/BP39: 0.5 eq., BP31/23: 0.6 eq.) and possibly 1,1′-azobis(cyclohexanecarbonitrile) (ABCN) (BP31: 0.1 eq., BP23: 0.2 eq.) were added. The reaction was purged with N_2 for 20 min and polymerized at 80 °C for 23 hours. Subsequently, the product was precipitated into diethyl ether, redissolved in THF and reprecipitated in diethyl ether for three times. The resulting polymer was dried at 60 °C under vacuum overnight. Yields: 80 – 90%

Table 21. Overview of the different block copolymers (denoted as **BP*w*** where '*w*' refers to *w*(PVBmPEO2000)).

Entry	M_n[§] [g mol^{-1}]	$Đ$[§]	*n*(PS)[*]	*w*(PVBmPEO2000)[*]	ϕ(PVBmPEO2000)[#]
PVBmPEO2000	17 700	1.10	-	1	1
BP49	38 300	1.16	205	0.49	0.46
BP39	50 600	1.17	282	0.39	0.36
BP31	66 000	1.15	408	0.31	0.28
BP23	90 600	1.20	613	0.23	0.21

[§]Determined by SEC in THF using PS standards. [*]Calculated by integration of the respective signals in ^{1}H-NMR spectroscopy. [#]Calculated using the densities of PS (1.07 g cm^{-3}) and PEO (1.21 g cm^{-3}). Noteworthy, this calculation is not 100% correct because PEO is attached as side chain.

7 Abbreviations

7.1 List of Abbreviations

%	Percentage
°C	Degree Celsius
ABCN	1,1′-Azobis(cyclohexanecarbonitrile)
AEBA	3-Azido-5-ethynylbenzoic acid
AIBN	2,2′-Azobis(2-methylpropionitrile)
AP	Anionic polymerization
Aq.	Aqueous
ASSB	All-solid-state battery
ATR FT-IR	Attenuated total reflection fourier-transform infrared spectroscopy
ATRP	Atom-transfer radical polymerization
a.u.	Atomic unit
b	*Block*
BPz	PS-*b*-PVBmPEOz, where ‘z’ refers to the employed mPEOz
BP*w*	PS-*b*-PVBmPEO2000, where ‘*w*’ refers to *w*(PVBmPEO2000)
BPE*w*	Polymer electrolytes derived from BP*w*
$BPEw_{IL,[LiTFSI]:[EO]}$	Polymer electrolyte derived from BP*w*, where ‘IL’ corresponds to the type of IL used and ‘[LiTFSI]:[EO]’ to the ratio between lithium ion and the EO repeating units
CCP	Controlled cationic polymerization
CH	Cyclohexane
CP	Cationic polymerization
CTA	Chain-transfer agent
CuAAC	Copper-catalyzed alkyne-azide cycloaddition
CV	Cyclic voltammetry
Đ	Dispersity

DCM	Dichloromethane
Δ	Delta
δ	Chemical shift in NMR spectroscopy
d	Day
DDMAT	2-(Dodecylthiocarbonothioylthio)-2-methylpropionic acid
DDT	1-Dodecanethiol
DMSO	Dimethyl sulfoxide
DP	Degree of polymerization
DSC	Differential scanning calorimetry
e.g.	Exempli gratia
EDC	1-Ethyl-3-(3-dimethylaminopropyl)carbodiimide
EIS	Electrochemical impedance spectroscopy
EO	Ethylene oxide
ESI-MS	Electrospray ionization mass spectrometry
et al.	Et alii
EtOAc	Ethyl acetate
Et_3N	Triethylamine
FRP	Free radical polymerization
g	Gram
GPE	Gel polymer electrolyte
h	Hour
HCl	Hydrochloric acid
Hz	Hertz
IBVE	Isobutyl vinyl ether
IC	Ionic conductivity
i.e.	*Id est*
IR	Infrared

Abbreviations

J	Joule
K	Kelvin
kg	Kilogram
LCO	$LiCoO_2$
LFP	$LiFePO_4$
LIB	Lithium-ion battery
LiFSI	Lithium bis(fluorosulfonyl)imide
LiTF	Lithium trifluoromethanesulfonate
LiTFSI	Lithium bis(trifluoromethanesulfonyl)imide
LNMO	$LiNi_{0.5}Mn_{1.5}O_4$
LMO	$LiMn_2O_4$
LSV	Linear sweep voltammetry
M	Molar
M1	Allyl ethylene glycol vinyl ether
M2	Propargyl ethylene glycol vinyl ether
M3	7-(Vinyloxy)hept-1-ene
M4	6-(Vinyloxy)hex-1-yne
M_n	Number-average molar mass
M_w	Weight-average molar mass
mA	Milliampere
ME	Mercaptoethanol
MeCN	Acetonitrile
MeOH	Methanol
mg	Milligram
MHz	Megahertz
mHz	Millihertz
mL	Milliliter

mm	Millimeter
mM	Millimolar
mmol	Millimole
mol	Mole
mol%	Mole percentage
mPEOz	Methoxy poly(ethylene oxide) with M_n = z
MWCO	Molecular weight cut-off
m/z	Mass divided by charge
NaOH	Sodium hydroxide
nm	Nanometer
NMCXYZ	$Li(Ni_xMn_yCo_z)O_2$
NMP	Nitroxide-mediated polymerization
NMP	*N*-methyl-2-pyrrolidone
NMR	Nuclear magnetic resonance
OEGMA	Oligo(ethylene glycol) methyl ether methacrylate
P1	Poly(allyl ethylene glycol vinyl ether)
P2	Poly(propargyl ethylene glycol vinyl ether)
P3	Poly(7-(vinyloxy)hept-1-ene)
P4	Poly(6-(vinyloxy)hex-1-yne)
PE	Polymer electrolyte
PE_x	Polymer electrolyte derived from PEO_x, 'x' can be linear, star or cage
PEO	Poly(ethylene oxide)
PEO_{cage}	*Cage*-shaped PEO
$PEO_{end\text{-}func}$	End-functionalized *star*-shaped PEO
PEO_{star}	Four-arm *star*-shaped PEO with M_n = 5.0 kg mol^{-1}
Polymer A/Bz	Poly(cyclohexyl vinyl ether-*co*-mPEOz vinyl ether), where 'z' refers to the employed mPEOz

Abbreviations

PPM	Post-polymerization modification
ppm	Parts per million
PS	Polystyrene
$Pyr_{14}TFSI$	1-Butyl-1-methylpyrrolidinium bis(trifluoromethylsulfonyl)imide
$Pyr_{O7}TFSI$	1-Oligo ethylene oxide-1-methylpyrrolidinium bis(trifluoromethylsulfonyl)imide
PVBmPEOz	Poly(vinyl benzyl methoxy PEOz ether), where 'z' refers to the employed mPEOz
PVdF	Poly(vinylidene fluoride)
q	Scattering vector
r.t.	Room temperature
RAFT	Reversible addition-fragmentation chain-transfer
RDRP	Reversible-deactivation radical polymerization
RI	Refractive index
ROP	Ring-opening polymerization
RP	Radical polymerization
σ	Ionic conductivity
σ_{Li^+}	Lithium-ion conductivity
SAXS	Small-angle x-ray scattering
SEC	Size exclusion chromatography
SEI	Solid electrolyte interphase
SPE	Solid polymer electrolyte
SSB	Solid-state battery
SSE	Solid-state electrolyte
T	Temperature
TBBT	4-*tert*-Butylbenzylthiol
T_{d5}	Decomposition temperature at 5% weight loss

T_g	Glass transition temperature
TGA	Thermogravimetric analysis
THF	Tetrahydrofuran
t_{Li^+}	Lithium-ion transference number
TLC	Thin-layer chromatography
Tosyl	Toluenesulfonyl
VBmPEOz	Vinyl benzyl mPEOz ether
vs.	Versus
$\tilde{\nu}$	Wavenumber

8 List of Schemes, Figures and Tables

8.1 List of Schemes

8.2 List of Figures

8.3 List of Tables

9 Danksagung

An dieser Stelle möchte ich allen danken, die mich während der Promotion begleitet haben. Darüber hinaus möchte ich den Zeitpunkt auch nutzen, um einmal allen zu danken, die mich auf meinem ganzen Weg bis hierhin unterstützt haben und dadurch auch indirekt zu dieser Arbeit beigetragen haben.

Zuerst gilt mein großer Dank PROF. DR. PATRICK THÉATO. Danke für die Möglichkeit die Promotion bei Dir durchzuführen. Danke auch, dass ich bei Dir die größte Freiheit genossen habe, meinen Ideen freien Lauf zu lassen.

Im Zuge dessen möchte ich mich auch herzlichst bei PROF. DR. MICHAEL MEIER für die bereitwillige Übernahme der Rolle des Korreferenten bedanken.

Ein großes Dankeschön möchte ich KATHARINA ELIES aussprechen. Danke für Deine liebe und lustige Art und deine unendliche Hilfsbereitschaft.

Des Weiteren gilt mein Dank DR. DOMINIK VOLL. Danke für unser gutes Verhältnis und all die organisatorische Unterstützung.

Auch möchte ich mich bei BÄRBEL SEUFERT-DAUSMANN und MARTINA RITTER für die bürokratische und organisatorische Unterstützung bedanken.

Ein großer Dank gilt PHILIPP RÖRING – ohne Dich wäre einiges hier nicht möglich gewesen. Danke für all die Erklärungen, Hilfe und Unterstützung. Ich denke wir waren ein sehr gutes und erfolgreiches Team.

Des Weiteren gilt mein großer Dank meinen Kollegen und Coautoren MARTIN GAUTHIER-JAQUES, KUN LIU (ROGER), ANNA KHUDYSKINA und MAXI HOFFMANN. Danke für die erfolgreiche Zusammenarbeit, all die fruchtvollen Diskussionen und die Unterstützung.

Zudem möchte ich mich bei meinen Studenten TIM MACH, SVEN SCHNEIDER und EDWARD KUSUMOWIDAGDU und bei KLARA URBSCHAT bedanken. Ihr habt alle zu meinen Erfolgen beigetragen – auch wenn ich immer nur am meckern war, wie langsam Ihr doch arbeitet. ;-)

Natürlich möchte ich mich auch bei allen Mitgliedern des AK Théato für die Zusammenarbeit bedanken. Namentlich möchte ich hier vor allem meine beiden besten Freunde STEFAN FRECH und EDGAR MOLLE erwähnen. Die Zeit mit Euch war grandios und ich bin sehr froh Euch zu kennen. Danke auch für die Korrektur dieser Arbeit. Des Weiteren gilt mein Dank MARTIN a.k.a GOETHE, SERGEJ, SVEN und NICO für die allzeit lustige Gemeinschaft.

Danksagung

Ein ganz spezieller Dank gilt auch dem ANATOLIA PIZZA & KEPABHAUS für die Bereitstellung der Nervennahrung für „Freigeist“ Stefan und mich.

Nicht in Vergessenheit geraten sollen die „Freunde der Chemie“: STEFAN, STEFAN, LEA, MAXI, MICHELLE, PETER, ANTOINE, STEPHANIE. Das Studium fühlt sich einfach schon ewig her an…

Nicht unerwähnt möchte ich auch DR. ANDREAS GNEKOW wissen, der zusammen mit meinem Vater meine Begeisterung für Chemie geweckt und geschürt hat.

Des Weiteren gilt ein großer Dank meinen langjährigen Freunden JULIUS SCHUSTER, PAUL HOFFMANN und MATTHIAS KRÄMER. Am Ende sind wir doch tatsächliche alle „Doktoren“ geworden bzw. auf dem Weg dahin. ;-) Insbesondere Matze: Der Ehrgeiz, der sich in unserem Grundschulalter entwickelt hat, bei wirklich allem so gut wie möglich zu sein, treibt mich heute noch an – egal ob beruflich oder sportlich (auch wenn letzteres mir vielleicht nicht ganz so gut getan hat…). Daher möchte ich auch ANITA KRÄMER danken.

Zu guter Letzt und damit an der wichtigsten Stelle möchte ich mich bei meinen Eltern, meinen Brüdern und meinen Großeltern bedanken. Danke für all die Unterstützung in all den Jahren. Danke Papa, dass Du uns in hunderttausend Museen geschleppt hast – manchmal weiß man Dinge erst später zu schätzen. Danke Mama für all Deine Fürsorge. In diesem Zuge möchte ich mich auch bei meinen Schwiegereltern für all die Unterstützung bedanken.

Zuallerletzt möchte ich der Person danken, der diese Arbeit gewidmet ist. Ohne Dich hätte ich das alles niemals geschafft. Danke, dass Du schon so unglaublich lange an meiner Seite stehst und mir den Rücken freihältst.

10 References

[1] Baskoro, F.; Wong, H. Q.; Yen, H.-J. Strategic Structural Design of a Gel Polymer Electrolyte toward a High Efficiency Lithium-Ion Battery. *ACS Appl. Energy Mater.*, **2019**, *2* (6), 3937–3971. DOI: 10.1021/acsaem.9b00295.

[2] Nitta, N.; Wu, F.; Lee, J. T.; Yushin, G. Li-ion battery materials: present and future. *Mater. Today*, **2015**, *18* (5), 252–264. DOI: 10.1016/j.mattod.2014.10.040.

[3] Zhou, J.; Qian, T.; Liu, J.; Wang, M.; Zhang, L.; Yan, C. High-Safety All-Solid-State Lithium-Metal Battery with High-Ionic-Conductivity Thermoresponsive Solid Polymer Electrolyte. *Nano letters*, **2019**, *19* (5), 3066–3073. DOI: 10.1021/acs.nanolett.9b00450.

[4] Chen, Y.; Kang, Y.; Zhao, Y.; Wang, L.; Liu, J.; Li, Y.; Liang, Z.; He, X.; Li, X.; Tavajohi, N.; Li, B. A review of lithium-ion battery safety concerns: The issues, strategies, and testing standards. *J. Energy Chem.*, **2021**, *59*, 83–99. DOI: 10.1016/j.jechem.2020.10.017.

[5] Cao, C.; Li, Y.; Feng, Y.; Peng, C.; Li, Z.; Feng, W. A solid-state single-ion polymer electrolyte with ultrahigh ionic conductivity for dendrite-free lithium metal batteries. *Energy Storage Mater.*, **2019**, *19*, 401–407. DOI: 10.1016/j.ensm.2019.03.004.

[6] Wang, R.; Cui, W.; Chu, F.; Wu, F. Lithium metal anodes: Present and future. *J. Energy Chem.*, **2020**, *48*, 145–159. DOI: 10.1016/j.jechem.2019.12.024.

[7] Zheng, F.; Kotobuki, M.; Song, S.; Lai, M. O.; Lu, L. Review on solid electrolytes for all-solid-state lithium-ion batteries. *J. Power Sources*, **2018**, *389*, 198–213. DOI: 10.1016/j.jpowsour.2018.04.022.

[8] Aziz, S. B.; Woo, T. J.; Kadir, M.F.Z.; Ahmed, H. M. A conceptual review on polymer electrolytes and ion transport models. *J. Sci.: Adv. Mater. Devices*, **2018**, *3* (1), 1–17. DOI: 10.1016/j.jsamd.2018.01.002.

[9] Mindemark, J.; Lacey, M. J.; Bowden, T.; Brandell, D. Beyond PEO—Alternative host materials for Li + -conducting solid polymer electrolytes. *Prog. Polym. Sci.*, **2018**, *81*, 114–143. DOI: 10.1016/j.progpolymsci.2017.12.004.

[10] Krause, C. H.; Butzelaar, A. J.; Diddens, D.; Dong, D.; Théato, P.; Bedrov, D.; Hwang, B.-J.; Winter, M.; Brunklaus, G. Quasi-solid single ion conducting polymer electrolyte membrane containing novel fluorinated poly(arylene ether sulfonimide) for lithium metal batteries. *J. Power Sources*, **2021**, *484*, 229267. DOI: 10.1016/j.jpowsour.2020.229267.

[11] Krause, C. H.; Röring, P.; Onishi, H.; Diddens, D.; Thienenkamp, J. H.; Brunklaus, G.; Winter, M.; Cekic-Laskovic, I. Propylene carbonate-nitrile solvent blends for thermally stable gel polymer lithium ion battery electrolytes. *J. Power Sources*, **2020**, *478*, 229047. DOI: 10.1016/j.jpowsour.2020.229047.

[12] Magistris, A.; Singh, K. PEO-based polymer electrolytes. *Polym. Int.*, **1992**, *28* (4), 277–280. DOI: 10.1002/pi.4990280406.

References

[13] Fenton, D. E.; Parker, J. M.; Wright, P. V. Complexes of alkali metal ions with poly(ethylene oxide). *Polymer*, **1973**, *14* (11), 589. DOI: 10.1016/0032-3861(73)90146-8.

[14] Homann, G.; Stolz, L.; Nair, J.; Laskovic, I. C.; Winter, M.; Kasnatscheew, J. Poly(Ethylene Oxide)-based Electrolyte for Solid-State-Lithium-Batteries with High Voltage Positive Electrodes: Evaluating the Role of Electrolyte Oxidation in Rapid Cell Failure. *Sci. Rep.*, **2020**, *10* (1), 4390. DOI: 10.1038/s41598-020-61373-9.

[15] Homann, G.; Stolz, L.; Winter, M.; Kasnatscheew, J. Elimination of "Voltage Noise" of Poly (Ethylene Oxide)-Based Solid Electrolytes in High-Voltage Lithium Batteries: Linear versus Network Polymers. *iScience*, **2020**, *23* (6), 101225. DOI: 10.1016/j.isci.2020.101225.

[16] Wright, P. V. Electrical conductivity in ionic complexes of poly(ethylene oxide). *Brit. Poly. J.*, **1975**, *7* (5), 319–327. DOI: 10.1002/pi.4980070505.

[17] Xue, Z.; He, D.; Xie, X. Poly(ethylene oxide)-based electrolytes for lithium-ion batteries. *J. Mater. Chem. A*, **2015**, *3* (38), 19218–19253. DOI: 10.1039/C5TA03471J.

[18] Varzi, A.; Thanner, K.; Scipioni, R.; Di Lecce, D.; Hassoun, J.; Dörfler, S.; Altheus, H.; Kaskel, S.; Prehal, C.; Freunberger, S. A. Current status and future perspectives of lithium metal batteries. *J. Power Sources*, **2020**, *480*, 228803. DOI: 10.1016/j.jpowsour.2020.228803.

[19] Zhang, H.; Eshetu, G. G.; Judez, X.; Li, C.; Rodriguez-Martínez, L. M.; Armand, M. Electrolyte Additives for Lithium Metal Anodes and Rechargeable Lithium Metal Batteries: Progress and Perspectives. *Angew. Chem. Int. Ed.*, **2018**, *57* (46), 15002–15027. DOI: 10.1002/anie.201712702.

[20] Zhu, L.; Li, J.; Jia, Y.; Zhu, P.; Jing, M.; Yao, S.; Shen, X.; Li, S.; Tu, F. Toward high performance solid‐state lithium‐ion battery with a promising PEO / PPC blend solid polymer electrolyte. *Int. J. Energy Res.*, **2020**, *44* (13), 10168–10178. DOI: 10.1002/er.5632.

[21] Devaux, D.; Bouchet, R.; Glé, D.; Denoyel, R. Mechanism of ion transport in PEO/LiTFSI complexes: Effect of temperature, molecular weight and end groups. *Solid State Ionics*, **2012**, *227*, 119–127. DOI: 10.1016/j.ssi.2012.09.020.

[22] Zhang, Y.; Lu, W.; Cong, L.; Liu, J.; Sun, L.; Mauger, A.; Julien, C. M.; Xie, H.; Liu, J. Cross-linking network based on Poly(ethylene oxide): Solid polymer electrolyte for room temperature lithium battery. *J. Power Sources*, **2019**, *420*, 63–72. DOI: 10.1016/j.jpowsour.2019.02.090.

[23] Das, S.; Ghosh, A. Ionic conductivity and dielectric permittivity of PEO-LiClO 4 solid polymer electrolyte plasticized with propylene carbonate. *AIP Advances*, **2015**, *5* (2), 27125. DOI: 10.1063/1.4913320.

[24] Banitaba, S. N.; Semnani, D.; Heydari-Soureshjani, E.; Rezaei, B.; Ensafi, A. A. The effect of concentration and ratio of ethylene carbonate and propylene carbonate plasticizers on characteristics of the electrospun PEO-based electrolytes applicable in lithium-ion batteries. *Solid State Ionics*, **2020**, *347*, 115252. DOI: 10.1016/j.ssi.2020.115252.

[25] Xu, L.; Li, J.; Deng, W.; Li, L.; Zou, G.; Hou, H.; Huang, L.; Ji, X. Boosting the ionic conductivity of PEO electrolytes by waste eggshell-derived fillers for high-performance solid lithium/sodium batteries. *Mater. Chem. Front.*, **2021**, *5* (3), 1315–1323. DOI: 10.1039/D0QM00541J.

[26] Patla, S. K.; Ray, R.; Asokan, K.; Karmakar, S. Investigation of ionic conduction in PEO–PVDF based blend polymer electrolytes. *J. Appl. Phys.*, **2018**, *123* (12), 125102. DOI: 10.1063/1.5022050.

[27] Butzelaar, A. J.; Liu, K. L.; Röring, P.; Brunklaus, G.; Winter, M.; Theato, P. A Systematic Study of Vinyl Ether-Based Poly(Ethylene Oxide) Side-Chain Polymer Electrolytes. *ACS Appl. Polym. Mater.*, **2021**, *3* (3), 1573–1582. DOI: 10.1021/acsapm.0c01398.

[28] Rosenbach, D.; Mödl, N.; Hahn, M.; Petry, J.; Danzer, M. A.; Thelakkat, M. Synthesis and Comparative Studies of Solvent-Free Brush Polymer Electrolytes for Lithium Batteries. *ACS Appl. Energy Mater.*, **2019**, *2* (5), 3373–3388. DOI: 10.1021/acsaem.9b00211.

[29] Itoh, T.; Fujita, K.; Uno, T.; Kubo, M. Polymer electrolytes based on vinyl ethers with various EO chain length and their polymer electrolytes cross-linked by electron beam irradiation. *Ionics*, **2017**, *23* (2), 257–264. DOI: 10.1007/s11581-016-1815-x.

[30] Long, L.; Wang, S.; Xiao, M.; Meng, Y. Polymer electrolytes for lithium polymer batteries. *J. Mater. Chem. A*, **2016**, *4* (26), 10038–10069. DOI: 10.1039/C6TA02621D.

[31] Pu, K.-C.; Zhang, X.; Qu, X.-L.; Hu, J.-J.; Li, H.-W.; Gao, M.-X.; Pan, H.-G.; Liu, Y.-F. Recently developed strategies to restrain dendrite growth of Li metal anodes for rechargeable batteries. *Rare Met.*, **2020**, *39* (6), 616–635. DOI: 10.1007/s12598-020-01432-2.

[32] Phan, T. N. T.; Issa, S.; Gigmes, D. Poly(ethylene oxide)-based block copolymer electrolytes for lithium metal batteries. *Polym. Int.*, **2019**, *68* (1), 7–13. DOI: 10.1002/pi.5677.

[33] Tang, X.; Thankappan, S. K.; Lee, P.; Fard, S. E.; Harmon, M. D.; Tran, K.; Yu, X. Polymeric Biomaterials in Tissue Engineering and Regenerative Medicine. In Natural and Synthetic Biomedical Polymers; Kumbar, S. G., Laurencin, C. T., Deng, M., Eds.; *Elsevier*, **2014**; pp 351–371. DOI: 10.1016/B978-0-12-396983-5.00022-3.

[34] Ishihara, K. Highly lubricated polymer interfaces for advanced artificial hip joints through biomimetic design. *Polym. J.*, **2015**, *47* (9), 585–597. DOI: 10.1038/pj.2015.45.

[35] Bocharova, V.; Sokolov, A. P. Perspectives for Polymer Electrolytes: A View from Fundamentals of Ionic Conductivity. *Macromolecules*, **2020**, *53* (11), 4141–4157. DOI: 10.1021/acs.macromol.9b02742.

[36] Szwarc, M. 'Living' Polymers. *Nature*, **1956**, *178* (4543), 1168–1169. DOI: 10.1038/1781168a0.

[37] Living polymerization. In The IUPAC Compendium of Chemical Terminology; Gold, V., Ed.; *International Union of Pure and Applied Chemistry (IUPAC)*, **2019**. DOI: 10.1351/goldbook.L03597.

[38] Aoshima, S.; Kanaoka, S. A renaissance in living cationic polymerization. *Chem. Rev.*, **2009**, *109* (11), 5245–5287. DOI: 10.1021/cr900225g.

[39] Chojnowski, J.; Cypryk, M.; Kaźmierski, K. Cationic Polymerization of a Model Cyclotrisiloxane with Mixed Siloxane Units Initiated by a Protic Acid. Mechanism of Polymer Chain Formation. *Macromolecules*, **2002**, *35* (27), 9904–9912. DOI: 10.1021/ma021060n.

[40] Kostjuk, S. V. Recent progress in the Lewis acid co-initiated cationic polymerization of isobutylene and 1,3-dienes. *RSC Adv.*, **2015**, *5* (17), 13125–13144. DOI: 10.1039/C4RA15313H.

[41] Matyjaszewski, K. Cationic Polymerizations: Mechanisms, Synthesis, and Applications; Plastics Engineering Ser, v.35; *Chapman and Hall/CRC*, **1996**.

[42] Kennedy, J. P. Living cationic polymerization of olefins. How did the discovery come about? *J. Polym. Sci. A Polym. Chem.*, **1999**, *37* (14), 2285–2293. DOI: 10.1002/(SICI)1099-0518(19990715)37:14<2285:AID-POLA1>3.0.CO;2-P.

[43] Aoshima, S.; Higashimura, T. Living cationic polymerization of vinyl monomers by organoaluminum halides. 3. Living polymerization of isobutyl vinyl ether by ethyldichloroaluminum in the presence of ester additives. *Macromolecules*, **1989**, *22* (3), 1009–1013. DOI: 10.1021/ma00193a001.

[44] Miyamoto, M.; Sawamoto, M.; Higashimura, T. Living polymerization of isobutyl vinyl ether with hydrogen iodide/iodine initiating system. *Macromolecules*, **1984**, *17* (3), 265–268. DOI: 10.1021/ma00133a001.

[45] Miyamoto, M.; Sawamoto, M.; Higashimura, T. Synthesis of monodisperse living poly(vinyl ethers) and block copolymers by the hydrogen iodide/iodine initiating system. *Macromolecules*, **1984**, *17* (11), 2228–2230. DOI: 10.1021/ma00141a005.

[46] Hashimoto, T.; Nakamura, T.; Tanahashi, S.; Kodaira, T. Gel formation in cationic polymerization of divinyl ethers. III. Effect of oligooxyethylene chain versus oligomethylene chain as central spacer units. *J. Polym. Sci., Part A*, **2004**, *42* (15), 3729–3738. DOI: 10.1002/pola.20229.

[47] Aoshima, S.; Yoshida, T.; Kanazawa, A.; Kanaoka, S. New stage in living cationic polymerization: An array of effective Lewis acid catalysts and fast living polymerization in seconds. *J. Polym. Sci. A Polym. Chem.*, **2007**, *45* (10), 1801–1813. DOI: 10.1002/pola.21995.

[48] Kottisch, V.; O'Leary, J.; Michaudel, Q.; Stache, E. E.; Lambert, T. H.; Fors, B. P. Controlled Cationic Polymerization: Single-Component Initiation under Ambient Conditions. *J. Am. Chem. Soc.*, **2019**, *141* (27), 10605–10609. DOI: 10.1021/jacs.9b04961.

[49] Bruce, M. I.; Walton, J. K.; Williams, M. L.; Skelton, B. W.; White, A. H. Pentakis(methoxycarbonyl)cyclopentadiene, a strong organic acid: Crystal and molecular structures of $HC_5(CO)_2Me)_5$ and $Li[C_5(CO_2Me)_5](H_2O)$. *J. Organomet. Chem.*, **1981**, *212* (3), C35-C38. DOI: 10.1016/S0022-328X(00)85671-5.

[50] Kottisch, V.; Jermaks, J.; Mak, J.-Y.; Woltornist, R. A.; Lambert, T. H.; Fors, B. P. Hydrogen Bond Donor Catalyzed Cationic Polymerization of Vinyl Ethers. *Angew. Chem. Int. Ed.*, **2021**, *60* (9), 4535–4539. DOI: 10.1002/anie.202013419.

[51] Nesvadba, P. Radical Polymerization in Industry. In Encyclopedia of radicals in chemistry, biology and materials; Chatgilialoglu, C., Studer, A., Eds.; *Wiley*, **2012**. DOI: 10.1002/9781119953678.rad080.

[52] Müller, A. H. E.; Matyjaszewski, K. Controlled and living polymerizations: Methods and materials; *Wiley-VCH*, **2009**. DOI: 10.1002/9783527629091.

[53] Jenkins, A. D.; Jones, R. G.; Moad, G. Terminology for reversible-deactivation radical polymerization previously called "controlled" radical or "living" radical polymerization (IUPAC Recommendations 2010). *Pure Appl. Chem.*, **2009**, *82* (2), 483–491. DOI: 10.1351/PAC-REP-08-04-03.

[54] Shipp, D. A. Reversible-Deactivation Radical Polymerizations. *Polym. Rev.*, **2011**, *51* (2), 99–103. DOI: 10.1080/15583724.2011.566406.

[55] Tsarevsky, N. V.; Pintauer, T.; Matyjaszewski, K. Deactivation Efficiency and Degree of Control over Polymerization in ATRP in Protic Solvents. *Macromolecules*, **2004**, *37* (26), 9768–9778. DOI: 10.1021/ma048438x.

[56] Pyun, J.; Kowalewski, T.; Matyjaszewski, K. Synthesis of Polymer Brushes Using Atom Transfer Radical Polymerization. *Macromol. Rapid Commun.*, **2003**, *24* (18), 1043–1059. DOI: 10.1002/marc.200300078.

[57] Matyjaszewski, K. The synthesis of functional star copolymers as an illustration of the importance of controlling polymer structures in the design of new materials. *Polym. Int.*, **2003**, *52* (10), 1559–1565. DOI: 10.1002/pi.1339.

[58] Matyjaszewski, K.; Qin, S.; Boyce, J. R.; Shirvanyants, D.; Sheiko, S. S. Effect of initiation conditions on the uniformity of three-arm star molecular brushes. *Macromolecules*, **2003**, *36* (6), 1843–1849. DOI: 10.1021/ma021633w.

[59] Matyjaszewski, K. Atom Transfer Radical Polymerization (ATRP): Current Status and Future Perspectives. *Macromolecules*, **2012**, *45* (10), 4015–4039. DOI: 10.1021/ma3001719.

[60] Krys, P.; Matyjaszewski, K. Kinetics of Atom Transfer Radical Polymerization. *Eur. Polym. J.*, **2017**, *89*, 482–523. DOI: 10.1016/j.eurpolymj.2017.02.034.

[61] Moad, G.; Rizzardo, E. Chapter 1. The History of Nitroxide-mediated Polymerization; *Royal Society of Chemistry*, **2015**. DOI: 10.1039/9781782622635-00001.

[62] Fischer, H. The persistent radical effect: a principle for selective radical reactions and living radical polymerizations. *Chem. Rev.*, **2001**, *101* (12), 3581–3610. DOI: 10.1021/cr990124y.

[63] Grubbs, R. B. Nitroxide-Mediated Radical Polymerization: Limitations and Versatility. *Polym. Rev.*, **2011**, *51* (2), 104–137. DOI: 10.1080/15583724.2011.566405.

[64] Nicolas, J.; Guillaneuf, Y.; Lefay, C.; Bertin, D.; Gigmes, D.; Charleux, B. Nitroxide-mediated polymerization. *Prog. Polym. Sci.*, **2013**, *38* (1), 63–235. DOI: 10.1016/j.progpolymsci.2012.06.002.

[65] Chiefari, J.; Chong, Y. K.; Ercole, F.; Krstina, J.; Jeffery, J.; Le, T. P. T.; Mayadunne, R. T. A.; Meijs, G. F.; Moad, C. L.; Moad, G.; Rizzardo, E.; Thang, S. H. Living Free-Radical Polymerization by Reversible Addition−Fragmentation Chain Transfer: The RAFT Process. *Macromolecules*, **1998**, *31* (16), 5559–5562. DOI: 10.1021/ma9804951.

[66] Moad, G.; Rizzardo, E.; Thang, S. H. RAFT polymerization and some of its applications. *Chem. Asian J.*, **2013**, *8* (8), 1634–1644. DOI: 10.1002/asia.201300262.

[67] Zhu, J.; Zhu, X.; Di Zhou; Chen, J.; Wang, X. Study on reversible addition-fragmentation chain transfer (RAFT) polymerization of MMA in the presence of 2-cyanoprop-2-yl 1-dithiophenanthrenate (CPDPA). *Eur. Polym. J.*, **2004**, *40* (4), 743–749. DOI: 10.1016/j.eurpolymj.2003.11.024.

[68] Moad, G.; Rizzardo, E.; Thang, S. H. Reversible Addition Fragmentation Chain Transfer (RAFT) Polymerization. *Mater. Matters*, **2010** (5), 1.

[69] Cunningham, W. A. Sulfur. III. *J. Chem. Educ.*, **1935**, *12* (3), 120. DOI: 10.1021/ed012p120.

[70] Oesper, R. E. Christian Friedrich Schonbein. Part II. Experimental labors. *J. Chem. Educ.*, **1929**, *6* (4), 677. DOI: 10.1021/ed006p677.

[71] Gauthier, M. A.; Gibson, M. I.; Klok, H.-A. Synthesis of functional polymers by post-polymerization modification. *Angew. Chem. Int. Ed.*, **2009**, *48* (1), 48–58. DOI: 10.1002/anie.200801951.

[72] Matyjaszewski, K. Advanced Materials by Atom Transfer Radical Polymerization. *Adv. Mater.*, **2018**, *30* (23), e1706441. DOI: 10.1002/adma.201706441.

[73] Hill, M. R.; Carmean, R. N.; Sumerlin, B. S. Expanding the Scope of RAFT Polymerization: Recent Advances and New Horizons. *Macromolecules*, **2015**, *48* (16), 5459–5469. DOI: 10.1021/acs.macromol.5b00342.

[74] Arslan, M.; Acik, G.; Tasdelen, M. A. The emerging applications of click chemistry reactions in the modification of industrial polymers. *Polym. Chem.*, **2019**, *10* (28), 3806–3821. DOI: 10.1039/C9PY00510B.

[75] Arslan, M.; Tasdelen, M. A. Click Chemistry in Macromolecular Design: Complex Architectures from Functional Polymers. *Chem. Afr.*, **2019**, *2* (2), 195–214. DOI: 10.1007/s42250-018-0030-8.

[76] Binder, W. H.; Sachsenhofer, R. 'Click' Chemistry in Polymer and Materials Science. *Macromol. Rapid Commun.*, **2007**, *28* (1), 15–54. DOI: 10.1002/marc.200600625.

[77] Lowe, A. B. Thiol–ene "click" reactions and recent applications in polymer and materials synthesis: a first update. *Polym. Chem.*, **2014**, *5* (17), 4820–4870. DOI: 10.1039/C4PY00339J.

[78] Liang, L.; Astruc, D. The copper(I)-catalyzed alkyne-azide cycloaddition (CuAAC) "click" reaction and its applications. An overview. *Coord. Chem. Rev.*, **2011**, *255* (23-24), 2933–2945. DOI: 10.1016/j.ccr.2011.06.028.

[79] Xue, W.; Mutlu, H.; Theato, P. Post-polymerization modification of polymeric active esters towards TEMPO containing polymers: A systematic study. *Eur. Polym. J.*, **2020**, *130*, 109660. DOI: 10.1016/j.eurpolymj.2020.109660.

[80] Benaglia, M.; Alberti, A.; Giorgini, L.; Magnoni, F.; Tozzi, S. Poly(glycidyl methacrylate): a highly versatile polymeric building block for post-polymerization modifications. *Polym. Chem.*, **2013**, *4* (1), 124–132. DOI: 10.1039/C2PY20646C.

[81] Hoyle, C. E.; Bowman, C. N. Thiol-ene click chemistry. *Angew. Chem. Int. Ed.*, **2010**, *49* (9), 1540–1573. DOI: 10.1002/anie.200903924.

[82] Griesbaum, K. Problems and Possibilities of the Free-Radical Addition of Thiols to Unsaturated Compounds. *Angew. Chem. Int. Ed.*, **1970**, *9* (4), 273–287. DOI: 10.1002/anie.197002731.

[83] Sinha, A. K.; Equbal, D. Thiol−Ene Reaction: Synthetic Aspects and Mechanistic Studies of an Anti-Markovnikov-Selective Hydrothiolation of Olefins. *Asian J. Org. Chem.*, **2019**, *8* (1), 32–47. DOI: 10.1002/ajoc.201800639.

[84] Berg, R.; Straub, B. F. Advancements in the mechanistic understanding of the copper-catalyzed azide-alkyne cycloaddition. *Beilstein J. Org. Chem.*, **2013**, *9*, 2715–2750. DOI: 10.3762/bjoc.9.308.

[85] Tornøe, C. W.; Christensen, C.; Meldal, M. Peptidotriazoles on solid phase: 1,2,3-triazoles by regiospecific copper(i)-catalyzed 1,3-dipolar cycloadditions of terminal alkynes to azides. *J. Org. Chem.*, **2002**, *67* (9), 3057–3064. DOI: 10.1021/jo011148j.

[86] Rostovtsev, V. V.; Green, L. G.; Fokin, V. V.; Sharpless, K. B. A Stepwise Huisgen Cycloaddition Process: Copper(I)-Catalyzed Regioselective "Ligation" of Azides and Terminal Alkynes. *Angew. Chem. Int. Ed.*, **2002**, *41* (14), 2596–2599. DOI: 10.1002/1521-3773(20020715)41:14<2596:AID-ANIE2596>3.0.CO;2-4.

[87] Himo, F.; Lovell, T.; Hilgraf, R.; Rostovtsev, V. V.; Noodleman, L.; Sharpless, K. B.; Fokin, V. V. Copper(I)-catalyzed synthesis of azoles. DFT study predicts unprecedented reactivity and intermediates. *J. Am. Chem. Soc.*, **2005**, *127* (1), 210–216. DOI: 10.1021/ja0471525.

[88] Theato, P.; Klok, H.-A. Functional polymers by post-polymerization modification: Concepts, guidelines, and applications; *Wiley-VCH*, **2013**.

[89] Haldón, E.; Nicasio, M. C.; Pérez, P. J. Copper-catalysed azide-alkyne cycloadditions (CuAAC): an update. *Org. Biomol. Chem.*, **2015**, *13* (37), 9528–9550. DOI: 10.1039/c5ob01457c.

[90] Liénard, R.; Winter, J. de; Coulembier, O. Cyclic polymers: Advances in their synthesis, properties, and biomedical applications. *J. Polym. Sci.*, **2020**, *58* (11), 1481–1502. DOI: 10.1002/pol.20200236.

[91] Ren, J. M.; McKenzie, T. G.; Fu, Q.; Wong, E. H. H.; Xu, J.; An, Z.; Shanmugam, S.; Davis, T. P.; Boyer, C.; Qiao, G. G. Star Polymers. *Chem. Rev.*, **2016**, *116* (12), 6743–6836. DOI: 10.1021/acs.chemrev.6b00008.

[92] Abbasi, E.; Aval, S. F.; Akbarzadeh, A.; Milani, M.; Nasrabadi, H. T.; Joo, S. W.; Hanifehpour, Y.; Nejati-Koshki, K.; Pashaei-Asl, R. Dendrimers: synthesis, applications, and properties. *Nanoscale Res. Lett.*, **2014**, *9* (1), 247. DOI: 10.1186/1556-276X-9-247.

[93] Zheng, Y.; Li, S.; Weng, Z.; Gao, C. Hyperbranched polymers: advances from synthesis to applications. *Chem. Soc. Rev.*, **2015**, *44* (12), 4091–4130. DOI: 10.1039/C4CS00528G.

[94] Alagi, P.; Zapsas, G.; Hadjichristidis, N.; Hong, S. C.; Gnanou, Y.; Feng, X. All-Polycarbonate Graft Copolymers with Tunable Morphologies by Metal-Free Copolymerization of CO_2 with Epoxides. *Macromolecules*, **2021**, *54* (13), 6144–6152. DOI: 10.1021/acs.macromol.1c00659.

[95] Wang, S.; Wang, Z.; Li, J.; Li, L.; Hu, W. Surface-grafting polymers: from chemistry to organic electronics. *Mater. Chem. Front.*, **2020**, *4* (3), 692–714. DOI: 10.1039/C9QM00450E.

[96] Zhang, H.; Wang, W.; Akinc, M.; Mallapragada, S.; Travesset, A.; Vaknin, D. Assembling and ordering polymer-grafted nanoparticles in three dimensions. *Nanoscale*, **2017**, *9* (25), 8710–8715. DOI: 10.1039/C7NR00787F.

[97] Abbasi, M.; Faust, L.; Wilhelm, M. Comb and Bottlebrush Polymers with Superior Rheological and Mechanical Properties. *Adv. Mater.*, **2019**, *31* (26), e1806484. DOI: 10.1002/adma.201806484.

[98] Rathgeber, S.; Pakula, T.; Wilk, A.; Matyjaszewski, K.; Beers, K. L. On the shape of bottle-brush macromolecules: systematic variation of architectural parameters. *J. Chem. Phys.*, **2005**, *122* (12), 124904. DOI: 10.1063/1.1860531.

[99] Kreer, T. Polymer-brush lubrication: a review of recent theoretical advances. *Soft matter*, **2016**, *12* (15), 3479–3501. DOI: 10.1039/C5SM02919H.

[100] Yang, W.; Zhou, F. Polymer brushes for antibiofouling and lubrication. *Biosurface Biotribology*, **2017**, *3* (3), 97–114. DOI: 10.1016/j.bsbt.2017.10.001.

[101] Müllner, M. Molecular Polymer Brushes in Nanomedicine. *Macromol. Chem. Phys.*, **2016**, *217* (20), 2209–2222. DOI: 10.1002/macp.201600086.

[102] Kim, W.; Jung, J. Polymer brush: a promising grafting approach to scaffolds for tissue engineering. *BMB Reports*, **2016**, *49* (12), 655–661. DOI: 10.5483/BMBRep.2016.49.12.166.

[103] Engler, A. C.; Lee, H.-i.; Hammond, P. T. Highly efficient "grafting onto" a polypeptide backbone using click chemistry. *Angew. Chem. Int. Ed.*, **2009**, *48* (49), 9334–9338. DOI: 10.1002/anie.200904070.

[104] Foster, J. C.; Radzinski, S. C.; Matson, J. B. Graft polymer synthesis by RAFT transfer ‐ to. *J. Polym. Sci. A Polym. Chem.*, **2017**, *55* (18), 2865–2876. DOI: 10.1002/pola.28621.

[105] Gieseler, D.; Jordan, R. Poly(2-oxazoline) molecular brushes by grafting through of poly(2-oxazoline)methacrylates with aqueous ATRP. *Polym. Chem.*, **2015**, *6* (25), 4678–4689. DOI: 10.1039/C5PY00561B.

[106] Li, Q.; Imbrogno, J.; Belfort, G.; Wang, X.-L. Making polymeric membranes antifouling via "grafting from" polymerization of zwitterions. *J. Appl. Polym. Sci.*, **2015**, *132* (21), n/a-n/a. DOI: 10.1002/app.41781.

[107] Kim, T.; Song, W.; Son, D.-Y.; Ono, L. K.; Qi, Y. Lithium-ion batteries: outlook on present, future, and hybridized technologies. *J. Mater. Chem. A*, **2019**, *7* (7), 2942–2964. DOI: 10.1039/C8TA10513H.

[108] Blomgren, G. E. The Development and Future of Lithium Ion Batteries. *J. Electrochem. Soc.*, **2017**, *164* (1), A5019-A5025. DOI: 10.1149/2.0251701jes.

[109] Tarascon, J. M.; Armand, M. Issues and challenges facing rechargeable lithium batteries. *Nature*, **2001**, *414* (6861), 359–367. DOI: 10.1038/35104644.

[110] Hammami, A.; Raymond, N.; Armand, M. Lithium-ion batteries: runaway risk of forming toxic compounds. *Nature*, **2003**, *424* (6949), 635–636. DOI: 10.1038/424635b.

[111] Goodenough, J. B.; Kim, Y. Challenges for Rechargeable Li Batteries. *Chem. Mater.*, **2010**, *22* (3), 587–603. DOI: 10.1021/cm901452z.

[112] Grey, C. P.; Hall, D. S. Prospects for lithium-ion batteries and beyond-a 2030 vision. *Nat. Commun.*, **2020**, *11* (1), 6279. DOI: 10.1038/s41467-020-19991-4.

[113] Xu, W.; Wang, J.; Ding, F.; Chen, X.; Nasybulin, E.; Zhang, Y.; Zhang, J.-G. Lithium metal anodes for rechargeable batteries. *Energy Environ. Sci.*, **2014**, *7* (2), 513–537. DOI: 10.1039/C3EE40795K.

[114] Asenbauer, J.; Eisenmann, T.; Kuenzel, M.; Kazzazi, A.; Chen, Z.; Bresser, D. The success story of graphite as a lithium-ion anode material – fundamentals, remaining challenges, and recent developments including silicon (oxide) composites. *Sustainable Energy Fuels*, **2020**, *4* (11), 5387–5416. DOI: 10.1039/D0SE00175A.

[115] Cheng, X.-B.; Zhang, R.; Zhao, C.-Z.; Zhang, Q. Toward Safe Lithium Metal Anode in Rechargeable Batteries: A Review. *Chem. Rev.*, **2017**, *117* (15), 10403–10473. DOI: 10.1021/acs.chemrev.7b00115.

[116] Karmakar, A.; Ghosh, A. A comparison of ion transport in different polyethylene oxide–lithium salt composite electrolytes. *J. Appl. Phys.*, **2010**, *107* (10), 104113. DOI: 10.1063/1.3428389.

[117] Zhu, M.; Wu, J.; Wang, Y.; Song, M.; Long, L.; Siyal, S. H.; Yang, X.; Sui, G. Recent advances in gel polymer electrolyte for high-performance lithium batteries. *J. Energy Chem.*, **2019**, *37*, 126–142. DOI: 10.1016/j.jechem.2018.12.013.

[118] Cheng, X.; Pan, J.; Zhao, Y.; Liao, M.; Peng, H. Gel Polymer Electrolytes for Electrochemical Energy Storage. *Adv. Energy Mater.*, **2018**, *8* (7), 1702184. DOI: 10.1002/aenm.201702184.

[119] Winie, T.; Arof, A. K.; Thomas, S. Polymer Electrolytes: Characterization Techniques and Energy Applications; *John Wiley & Sons*, **2019**.

[120] Porcarelli, L.; Shaplov, A. S.; Bella, F.; Nair, J. R.; Mecerreyes, D.; Gerbaldi, C. Single-Ion Conducting Polymer Electrolytes for Lithium Metal Polymer Batteries that Operate at Ambient Temperature. *ACS Energy Lett.*, **2016**, *1* (4), 678–682. DOI: 10.1021/acsenergylett.6b00216.

[121] Georén, P.; Adebahr, J.; Jacobsson, P.; Lindbergh, G. Concentration Polarization of a Polymer Electrolyte. *J. Electrochem. Soc.*, **2002**, *149* (8), A1015. DOI: 10.1149/1.1487832.

[122] Yuan, H.; Luan, J.; Yang, Z.; Zhang, J.; Wu, Y.; Lu, Z.; Liu, H. Single Lithium-Ion Conducting Solid Polymer Electrolyte with Superior Electrochemical Stability and Interfacial Compatibility for Solid-State Lithium Metal Batteries. *ACS Appl. Mater. Interfaces*, **2020**, *12* (6), 7249–7256. DOI: 10.1021/acsami.9b20436.

[123] Zhu, J.; Zhang, Z.; Zhao, S.; Westover, A. S.; Belharouak, I.; Cao, P. ‐ F. Single ‐ Ion Conducting Polymer Electrolytes for Solid ‐ State Lithium ‐ Metal Batteries: Design, Performance, and Challenges. *Adv. Energy Mater.*, **2021**, *11* (14), 2003836. DOI: 10.1002/aenm.202003836.

[124] Monroe, C.; Newman, J. The Impact of Elastic Deformation on Deposition Kinetics at Lithium/Polymer Interfaces. *J. Electrochem. Soc.*, **2005**, *152* (2), A396. DOI: 10.1149/1.1850854.

[125] Chen, L.; Venkatram, S.; Kim, C.; Batra, R.; Chandrasekaran, A.; Ramprasad, R. Electrochemical Stability Window of Polymeric Electrolytes. *Chem. Mater.*, **2019**, *31* (12), 4598–4604. DOI: 10.1021/acs.chemmater.9b01553.

[126] *Batteries LMP® | Blue Solutions*. https://www.blue-solutions.com/en/blue-solutions/technology/batteries-lmp/ (accessed 2020-12-09).

[127] Osada, I.; Vries, H. de; Scrosati, B.; Passerini, S. Ionic-Liquid-Based Polymer Electrolytes for Battery Applications. *Angew. Chem. Int. Ed.*, **2016**, *55* (2), 500–513. DOI: 10.1002/anie.201504971.

[128] Sun, C.; Liu, J.; Gong, Y.; Wilkinson, D. P.; Zhang, J. Recent advances in all-solid-state rechargeable lithium batteries. *Nano Energy*, **2017**, *33*, 363–386. DOI: 10.1016/j.nanoen.2017.01.028.

[129] Staunton, E.; Andreev, Y. G.; Bruce, P. G. Structure and conductivity of the crystalline polymer electrolyte beta-PEO6:LiAsF6. *J. Am. Chem. Soc.*, **2005**, *127* (35), 12176–12177. DOI: 10.1021/ja053249v.

[130] Nair, J. R.; Imholt, L.; Brunklaus, G.; Winter, M. Lithium Metal Polymer Electrolyte Batteries: Opportunities and Challenges. *Electrochem. Soc. Interface*, **2019**, *28* (2), 55–61. DOI: 10.1149/2.F05192if.

[131] Khan, M. S.; Shakoor, A. Ionic Conductance, Thermal and Morphological Behavior of PEO-Graphene Oxide-Salts Composites. *J. Chem. (Hindawi)*, **2015**, *2015*, 1–6. DOI: 10.1155/2015/695930.

[132] Fullerton-Shirey, S. K.; Maranas, J. K. Structure and Mobility of PEO/$LiClO_4$ Solid Polymer Electrolytes Filled with Al_2O_3 Nanoparticles. *J. Phys. Chem. C*, **2010**, *114* (20), 9196–9206. DOI: 10.1021/jp906608p.

[133] Liu, Q.; Peng, B.; Shen, M.; Hu, B.; Chen, Q. Polymer chain diffusion and Li^+ hopping of poly(ethylene oxide)/$LiAsF_6$ crystalline polymer electrolytes as studied by solid state NMR and ac impedance. *Solid State Ionics*, **2014**, *255*, 74–79. DOI: 10.1016/j.ssi.2013.11.053.

[134] Ibrahim, S.; Yassin, M. M.; Ahmad, R.; Johan, M. R. Effects of various $LiPF_6$ salt concentrations on PEO-based solid polymer electrolytes. *Ionics*, **2011**, *17* (5), 399–405. DOI: 10.1007/s11581-011-0524-8.

[135] Croce, F.; Curini, R.; Pantaloni, S.; Passerini, S.; Selvaggi, A.; Scrosati, B. Characteristics of a poly(ethylene oxide)-$LiBF_4$ polymer electrolyte. *J. Appl. Electrochem.*, **1988**, *18* (3), 401–404. DOI: 10.1007/BF01093754.

[136] Sedlaříková, M.; Vondrák, J.; Musil, M.; Mathieisová, H.; Libich, J. Explosivity of lithium perchlorate in gel polymer electrolytes. *Polym. Compos.*, **2013**, *34* (11), 1970–1974. DOI: 10.1002/pc.22604.

[137] Lux, S. F.; Lucas, I. T.; Pollak, E.; Passerini, S.; Winter, M.; Kostecki, R. The mechanism of HF formation in $LiPF_6$ based organic carbonate electrolytes. *Electrochem. Commun.*, **2012**, *14* (1), 47–50. DOI: 10.1016/j.elecom.2011.10.026.

[138] Nagajothi, A. J.; Kannan, R.; Rajashabala, S. Electrochemical performance of plasticized PEO-LiTf complex-based composite gel polymer electrolytes with the addition of barium titanate. *Ionics*, **2018**, *24* (5), 1407–1414. DOI: 10.1007/s11581-017-2307-3.

[139] Wang, W.; Fang, Z.; Zhao, M.; Peng, Y.; Zhang, J.; Guan, S. Solid polymer electrolytes based on the composite of PEO–LiFSI and organic ionic plastic crystal. *Chem. Phys. Lett.*, **2020**, *747*, 137335. DOI: 10.1016/j.cplett.2020.137335.

[140] Maurel, A.; Armand, M.; Grugeon, S.; Fleutot, B.; Davoisne, C.; Tortajada, H.; Courty, M.; Panier, S.; Dupont, L. Poly(Ethylene Oxide)−LiTFSI Solid Polymer Electrolyte Filaments for Fused Deposition Modeling Three-Dimensional Printing. *J. Electrochem. Soc.*, **2020**, *167* (7), 70536. DOI: 10.1149/1945-7111/ab7c38.

[141] Bandara, L.R.A.K.; Dissanayake, M.A.K.L.; Mellander, B.-E. Ionic conductivity of plasticized(PEO)-LiCF3SO3 electrolytes. *Electrochim. Acta*, **1998**, *43* (10-11), 1447–1451. DOI: 10.1016/S0013-4686(97)10082-2.

[142] Nicotera, I. A study of stability of plasticized PEO electrolytes. *Solid State Ionics*, **2002**, *146* (1-2), 143–150. DOI: 10.1016/S0167-2738(01)01003-7.

[143] Fergus, J. W. Ceramic and polymeric solid electrolytes for lithium-ion batteries. *J. Power Sources*, **2010**, *195* (15), 4554–4569. DOI: 10.1016/j.jpowsour.2010.01.076.

[144] Wen, Z. Blend-based polymer electrolytes of poly(ethylene oxide) and hyperbranched poly[bis(triethylene glycol)benzoate] with terminal acetyl groups. *Solid State Ionics*, **2000**, *134* (3-4), 281–289. DOI: 10.1016/S0167-2738(00)00707-4.

[145] Wright, P. V. Polymer electrolytes—the early days. *Electrochim. Acta*, **1998**, *43* (10-11), 1137–1143. DOI: 10.1016/S0013-4686(97)10011-1.

[146] Paranjape, N.; Mandadapu, P. C.; Wu, G.; Lin, H. Highly-branched cross-linked poly(ethylene oxide) with enhanced ionic conductivity. *Polymer*, **2017**, *111*, 1–8. DOI: 10.1016/j.polymer.2017.01.014.

[147] Rolland, J.; Brassinne, J.; Bourgeois, J.-P.; Poggi, E.; Vlad, A.; Gohy, J.-F. Chemically anchored liquid-PEO based block copolymer electrolytes for solid-state lithium-ion batteries. *J. Mater. Chem. A*, **2014**, *2* (30), 11839–11846. DOI: 10.1039/C4TA02327G.

[148] Itoh, T.; Fujita, K.; Inoue, K.; Iwama, H.; Kondoh, K.; Uno, T.; Kubo, M. Solid polymer electrolytes based on alternating copolymers of vinyl ethers with methoxy oligo(ethyleneoxy)ethyl groups and vinylene carbonate. *Electrochim. Acta*, **2013**, *112*, 221–229. DOI: 10.1016/j.electacta.2013.08.124.

[149] Arya, A.; Sharma, A. L. Polymer electrolytes for lithium ion batteries: a critical study. *Ionics*, **2017**, *23* (3), 497–540. DOI: 10.1007/s11581-016-1908-6.

[150] Homann, G.; Stolz, L.; Neuhaus, K.; Winter, M.; Kasnatscheew, J. Effective Optimization of High Voltage Solid‐State Lithium Batteries by Using Poly(ethylene oxide)‐Based Polymer Electrolyte with Semi‐Interpenetrating Network. *Adv. Funct. Mater.*, **2020**, *30* (46), 2006289. DOI: 10.1002/adfm.202006289.

[151] Wetjen, M.; Kim, G.-T.; Joost, M.; Appetecchi, G. B.; Winter, M.; Passerini, S. Thermal and electrochemical properties of PEO-LiTFSI-Pyr_{14}TFSI-based composite cathodes, incorporating 4 V-class cathode active materials. *J. Power Sources*, **2014**, *246*, 846–857. DOI: 10.1016/j.jpowsour.2013.08.037.

[152] Sethuraman, V.; Mogurampelly, S.; Ganesan, V. Ion transport mechanisms in lamellar phases of salt-doped PS-PEO block copolymer electrolytes. *Soft matter*, **2017**, *13* (42), 7793–7803. DOI: 10.1039/c7sm01345k.

[153] Bouchet, R.; Phan, T. N. T.; Beaudoin, E.; Devaux, D.; Davidson, P.; Bertin, D.; Denoyel, R. Charge Transport in Nanostructured PS–PEO–PS Triblock Copolymer Electrolytes. *Macromolecules*, **2014**, *47* (8), 2659–2665. DOI: 10.1021/ma500420w.

[154] Singh, M.; Odusanya, O.; Wilmes, G. M.; Eitouni, H. B.; Gomez, E. D.; Patel, A. J.; Chen, V. L.; Park, M. J.; Fragouli, P.; Iatrou, H.; Hadjichristidis, N.; Cookson, D.; Balsara, N. P. Effect of Molecular Weight on the Mechanical and Electrical Properties of Block Copolymer Electrolytes. *Macromolecules*, **2007**, *40* (13), 4578–4585. DOI: 10.1021/ma0629541.

[155] Wang, C.; Sakai, T.; Watanabe, O.; Hirahara, K.; Nakanishi, T. All Solid-State Lithium-Polymer Battery Using a Self-Cross-Linking Polymer Electrolyte. *J. Electrochem. Soc.*, **2003**, *150* (9), A1166. DOI: 10.1149/1.1593652.

[156] Zhang, B.; Zhang, Y.; Zhang, N.; Liu, J.; Cong, L.; Liu, J.; Sun, L.; Mauger, A.; Julien, C. M.; Xie, H.; Pan, X. Synthesis and interface stability of polystyrene-poly(ethylene glycol)-polystyrene triblock copolymer as solid-state electrolyte for lithium-metal batteries. *J. Power Sources*, **2019**, *428*, 93–104. DOI: 10.1016/j.jpowsour.2019.04.033.

[157] Yuan, R.; Teran, A. A.; Gurevitch, I.; Mullin, S. A.; Wanakule, N. S.; Balsara, N. P. Ionic Conductivity of Low Molecular Weight Block Copolymer Electrolytes. *Macromolecules*, **2013**, *46* (3), 914–921. DOI: 10.1021/ma3024552.

[158] Chintapalli, M.; Le, T. N. P.; Venkatesan, N. R.; Mackay, N. G.; Rojas, A. A.; Thelen, J. L.; Chen, X. C.; Devaux, D.; Balsara, N. P. Structure and Ionic Conductivity of Polystyrene-block-poly(ethylene oxide) Electrolytes in the High Salt Concentration Limit. *Macromolecules*, **2016**, *49* (5), 1770–1780. DOI: 10.1021/acs.macromol.5b02620.

[159] Devaux, D.; Glé, D.; Phan, T. N. T.; Gigmes, D.; Giroud, E.; Deschamps, M.; Denoyel, R.; Bouchet, R. Optimization of Block Copolymer Electrolytes for Lithium Metal Batteries. *Chem. Mater.*, **2015**, *27* (13), 4682–4692. DOI: 10.1021/acs.chemmater.5b01273.

[160] Bergfelt, A.; Rubatat, L.; Brandell, D.; Bowden, T. Poly(benzyl methacrylate)-poly[(oligo ethylene glycol) methyl ether methacrylate] triblock-copolymers as solid electrolyte for lithium batteries. *Solid State Ionics*, **2018**, *321*, 55–61. DOI: 10.1016/j.ssi.2018.04.006.

[161] Gao, H.; Matyjaszewski, K. Synthesis of molecular brushes by "grafting onto" method: combination of ATRP and click reactions. *J. Am. Chem. Soc.*, **2007**, *129* (20), 6633–6639. DOI: 10.1021/ja0711617.

[162] Aoshima, S.; Onishi, H.; Kamiya, M.; Shachi, K.; Kobayashi, E. Role of added Lewis base and alkylaluminum halide on living cationic polymerization of vinyl ether. *J. Polym. Sci. A Polym. Chem.*, **1994**, *32* (5), 879–887. DOI: 10.1002/pola.1994.080320509.

[163] Kerner, M.; Plylahan, N.; Scheers, J.; Johansson, P. Ionic liquid based lithium battery electrolytes: fundamental benefits of utilising both TFSI and FSI anions? *Phys. Chem. Chem. Phys.*, **2015**, *17* (29), 19569–19581. DOI: 10.1039/c5cp01891a.

[164] Lehmann, M. L.; Yang, G.; Nanda, J.; Saito, T. Well-designed Crosslinked Polymer Electrolyte Enables High Ionic Conductivity and Enhanced Salt Solvation. *J. Electrochem. Soc.*, **2020**, *167* (7), 70539. DOI: 10.1149/1945-7111/ab7c6e.

[165] Kim, Y. W.; Lee, W.; Choi, B. K. Relation between glass transition and melting of PEO–salt complexes. *Electrochim. Acta*, **2000**, *45* (8-9), 1473–1477. DOI: 10.1016/S0013-4686(99)00362-X.

[166] Ibrahim, S.; Yasin, S. M. M.; Ahmad, R.; Johan, M. R. Conductivity, thermal and morphology studies of PEO based salted polymer electrolytes. *Solid State Sci.*, **2012**, *14* (8), 1111–1116. DOI: 10.1016/j.solidstatesciences.2012.05.019.

[167] Chowdari, B.; Huq, R.; Farrington, G. Thermal and electrical characterization of PEO-based polymer electrolytes containing mixed Co(II) and Li(I). *Solid State Ionics*, **1992**, *57* (1-2), 49–58. DOI: 10.1016/0167-2738(92)90063-U.

[168] Stolwijk, N. A.; Heddier, C.; Reschke, M.; Wiencierz, M.; Bokeloh, J.; Wilde, G. Salt-Concentration Dependence of the Glass Transition Temperature in PEO–NaI and PEO–LiTFSI Polymer Electrolytes. *Macromolecules*, **2013**, *46* (21), 8580–8588. DOI: 10.1021/ma401686r.

[169] Dreezen, G.; Koch, M.H.J.; Reynaers, H.; Groeninckx, G. Miscible binary blends of poly(ethylene oxide) and an amorphous aromatic polyamide (Aramide 34I): crystallization, melting behavior and semi-crystalline morphology. *Polymer*, **1999**, *40* (23), 6451–6463. DOI: 10.1016/S0032-3861(98)00849-0.

[170] Gorecki, W.; Jeannin, M.; Belorizky, E.; Roux, C.; Armand, M. Physical properties of solid polymer electrolyte PEO(LiTFSI) complexes. *J. Phys.: Condens. Matter*, **1995**, *7* (34), 6823–6832. DOI: 10.1088/0953-8984/7/34/007.

[171] Brooks, D. J.; Merinov, B. V.; Goddard, W. A.; Kozinsky, B.; Mailoa, J. Atomistic Description of Ionic Diffusion in PEO–LiTFSI: Effect of Temperature, Molecular Weight, and Ionic Concentration. *Macromolecules*, **2018**, *51* (21), 8987–8995. DOI: 10.1021/acs.macromol.8b01753.

[172] Chen, X. C.; Sacci, R. L.; Osti, N. C.; Tyagi, M.; Wang, Y.; Palmer, M. J.; Dudney, N. J. Study of segmental dynamics and ion transport in polymer–ceramic composite electrolytes by quasi-elastic neutron scattering. *Mol. Syst. Des. Eng.*, **2019**, *4* (2), 379–385. DOI: 10.1039/C8ME00113H.

[173] Bresser, D.; Lyonnard, S.; Iojoiu, C.; Picard, L.; Passerini, S. Decoupling segmental relaxation and ionic conductivity for lithium-ion polymer electrolytes. *Mol. Syst. Des. Eng.*, **2019**, *4* (4), 779–792. DOI: 10.1039/C9ME00038K.

[174] Shin, J. Ionic liquids to the rescue? Overcoming the ionic conductivity limitations of polymer electrolytes. *Electrochem. Commun.*, **2003**, *5* (12), 1016–1020. DOI: 10.1016/j.elecom.2003.09.017.

[175] Higashimura, T.; Deng, Y.-X.; Sawamoto, M. Synthesis of Living Cationic Poly(N-vinylcarbazole) with Low Molecular Weight. *Polym. J.*, **1983**, *15* (5), 385–388. DOI: 10.1295/polymj.15.385.

[176] Sawamoto, M.; Higashimura, T. Living cationic polymerization of vinyl monomers: Mechanism and synthesis of new polymers. *Makromol. Chem., Macromol. Symp.*, **1986**, *3* (1), 83–97. DOI: 10.1002/masy.19860030108.

[177] Aoshima, S.; Higashimura, T. Living cationic polymerization of vinyl monomers by organoaluminium halides. *Polym. Bull.*, **1986**, *15* (5), 417–423. DOI: 10.1007/BF00265723.

[178] Butzelaar, A. J.; Schneider, S.; Molle, E.; Theato, P. Synthesis and Post-Polymerization Modification of Defined Functional Poly(vinyl ether)s. *Macromol. Rapid Commun.*, **2021**, *42* (13), e2100133. DOI: 10.1002/marc.202100133.

[179] Matyjaszewski, K. Introduction to living polymeriz. Living and/or controlled polymerization. *J. Phys. Org. Chem.*, **1995**, *8* (4), 197–207. DOI: 10.1002/poc.610080403.

[180] Matyjaszewski, K.; Patten, T. E.; Xia, J. Controlled/“Living” Radical Polymerization. Kinetics of the Homogeneous Atom Transfer Radical Polymerization of Styrene. *J. Am. Chem. Soc.*, **1997**, *119* (4), 674–680. DOI: 10.1021/ja963361g.

[181] Butzelaar, A. J.; Gauthier-Jaques, M.; Liu, K. L.; Brunklaus, G.; Winter, M.; Theato, P. The power of architecture – cage -shaped PEO and its application as a polymer electrolyte. *Polym. Chem.*, **2021**, *12* (30), 4326–4331. DOI: 10.1039/D1PY00490E.

[182] Gauthier-Jaques, M. Synthesis of Cage-shaped Polymers by Topological Conversion; *Karlsruher Institut für Technologie (KIT)*, **2021**. DOI: 10.5445/IR/1000136335.

[183] Gauthier-Jaques, M.; Theato, P. Synergy of Macrocycles and Macromolecular Topologies: An Efficient [3_4]Triazolophane-Based Synthesis of Cage-Shaped Polymers. *ACS Macro Lett.*, **2020**, *9* (5), 700–705. DOI: 10.1021/acsmacrolett.0c00248.

[184] Li, X.; Cheng, S.; Zheng, Y.; Li, C. Y. Morphology control in semicrystalline solid polymer electrolytes for lithium batteries. *Mol. Syst. Des. Eng.*, **2019**, *4* (4), 793–803. DOI: 10.1039/C9ME00028C.

[185] Mato, Y.; Honda, K.; Tajima, K.; Yamamoto, T.; Isono, T.; Satoh, T. A versatile synthetic strategy for macromolecular cages: intramolecular consecutive cyclization of star-shaped polymers. *Chemical science*, **2019**, *10* (2), 440–446. DOI: 10.1039/c8sc04006k.

[186] Pesko, D. M.; Jung, Y.; Hasan, A. L.; Webb, M. A.; Coates, G. W.; Miller, T. F.; Balsara, N. P. Effect of monomer structure on ionic conductivity in a systematic set of polyester electrolytes. *Solid State Ionics*, **2016**, *289*, 118–124. DOI: 10.1016/j.ssi.2016.02.020.

[187] Madbouly, S. A.; Wolf, B. A. Equilibrium phase behavior of polyethylene oxide and of its mixtures with tetrahydronaphthalene or/and poly(ethylene oxide-block-dimethylsiloxane). *J. Chem. Phys.*, **2002**, *117* (15), 7357–7363. DOI: 10.1063/1.1507111.

[188] Cimmino, S.; Greco, R.; Martuscelli, E.; Nicolais, L.; Silvestre, C. Blends of poly(ethylene oxide) samples of different molecular weights: thermal and mechanical properties. *Polymer*, **1978**, *19* (9), 1079–1082. DOI: 10.1016/0032-3861(78)90151-9.

[189] Pearce, R.; Vancso, G. J. Imaging of Melting and Crystallization of Poly(ethylene oxide) in Real-Time by Hot-Stage Atomic Force Microscopy. *Macromolecules*, **1997**, *30* (19), 5843–5848. DOI: 10.1021/ma970463y.

[190] Lascaud, S.; Perrier, M.; Vallee, A.; Besner, S.; Prud'homme, J.; Armand, M. Phase Diagrams and Conductivity Behavior of Poly(ethylene oxide)-Molten Salt Rubbery Electrolytes. *Macromolecules*, **1994**, *27* (25), 7469–7477. DOI: 10.1021/ma00103a034.

[191] Vallée, A.; Besner, S.; Prud'homme, J. Comparative study of poly(ethylene oxide) electrolytes made with $LiN(CF_3SO_2)_2$, $LiCF_3SO_3$ and $LiClO_4$: Thermal properties and conductivity behaviour. *Electrochim. Acta*, **1992**, *37* (9), 1579–1583. DOI: 10.1016/0013-4686(92)80115-3.

[192] Butzelaar, A. J.; Röring, P.; Mach, T. P.; Hoffmann, M.; Jeschull, F.; Wilhelm, M.; Winter, M.; Brunklaus, G.; Théato, P. Styrene-Based Poly(ethylene oxide) Side-Chain Block Copolymers as Solid Polymer Electrolytes for High-Voltage Lithium-Metal Batteries. *ACS Appl. Mater. Interfaces*, **2021**, *13* (33), 39257–39270. DOI: 10.1021/acsami.1c08841.

[193] Rieger, J. The glass transition temperature of polystyrene. *J. Therm. Anal.*, **1996**, *46* (3-4), 965–972. DOI: 10.1007/BF01983614.

[194] La Olvera de Cruz, M. Theory of microphase separation in block copolymer solutions. *J. Chem. Phys.*, **1989**, *90* (3), 1995–2002. DOI: 10.1063/1.456042.

[195] Zhang, J.; Yu, X.; Yang, P.; Peng, J.; Luo, C.; Huang, W.; Han, Y. Microphase separation of block copolymer thin films. *Macromol. Rapid Commun.*, **2010**, *31* (7), 591–608. DOI: 10.1002/marc.200900541.

[196] Gartner, T. E.; Kubo, T.; Seo, Y.; Tansky, M.; Hall, L. M.; Sumerlin, B. S.; Epps, T. H. Domain Spacing and Composition Profile Behavior in Salt-Doped Cyclic vs Linear Block Polymer Thin Films: A Joint Experimental and Simulation Study. *Macromolecules*, **2017**, *50* (18), 7169–7176. DOI: 10.1021/acs.macromol.7b01338.

[197] Yu, M.; Tan, J.; Yang, J.; Zeng, Z. Z-type and R-type macro-RAFT agents in RAFT dispersion polymerization – another mechanism perspective on PISA. *Polym. Chem.*, **2016**, *7* (22), 3756–3765. DOI: 10.1039/C6PY00605A.

[198] Cheng, S.; Li, X.; Zheng, Y.; Smith, D. M.; Li, C. Y. Anisotropic ion transport in 2D polymer single crystal-based solid polymer electrolytes. *Giant*, **2020**, *2*, 100021. DOI: 10.1016/j.giant.2020.100021.

[199] Borodin, O.; Smith, G. D. Mechanism of Ion Transport in Amorphous Poly(ethylene oxide)/LiTFSI from Molecular Dynamics Simulations. *Macromolecules*, **2006**, *39* (4), 1620–1629. DOI: 10.1021/ma052277v.

[200] Barai, P.; Higa, K.; Srinivasan, V. Lithium dendrite growth mechanisms in polymer electrolytes and prevention strategies. *Phys. Chem. Chem. Phys.*, **2017**, *19* (31), 20493–20505. DOI: 10.1039/c7cp03304d.

[201] Bai, P.; Li, J.; Brushett, F. R.; Bazant, M. Z. Transition of lithium growth mechanisms in liquid electrolytes. *Energy Environ. Sci.*, **2016**, *9* (10), 3221–3229. DOI: 10.1039/C6EE01674J.

[202] Monroe, C.; Newman, J. Dendrite Growth in Lithium/Polymer Systems. *J. Electrochem. Soc.*, **2003**, *150* (10), A1377. DOI: 10.1149/1.1606686.

[203] Faravelli, T.; Pinciroli, M.; Pisano, F.; Bozzano, G.; Dente, M.; Ranzi, E. Thermal degradation of polystyrene. *J. Anal. Appl. Pyrolysis*, **2001**, *60* (1), 103–121. DOI: 10.1016/S0165-2370(00)00159-5.

[204] Han, S.; Kim, C.; Kwon, D. Thermal degradation of poly(ethyleneglycol). *Polym. Degrad. Stab.*, **1995**, *47* (2), 203–208. DOI: 10.1016/0141-3910(94)00109-L.

[205] Isono, T.; Kawakami, N.; Watanabe, K.; Yoshida, K.; Otsuka, I.; Mamiya, H.; Ito, H.; Yamamoto, T.; Tajima, K.; Borsali, R.; Satoh, T. Microphase separation of carbohydrate-based star-block copolymers with sub-10 nm periodicity. *Polym. Chem.*, **2019**, *10* (9), 1119–1129. DOI: 10.1039/C8PY01745J.

[206] Bendejacq, D.; Ponsinet, V.; Joanicot, M.; Loo, Y.-L.; Register, R. A. Well-Ordered Microdomain Structures in Polydisperse Poly(styrene)−Poly(acrylic acid) Diblock Copolymers from Controlled Radical Polymerization. *Macromolecules*, **2002**, *35* (17), 6645–6649. DOI: 10.1021/ma020158z.

[207] Gilbert, J. B.; Luo, M.; Shelton, C. K.; Rubner, M. F.; Cohen, R. E.; Epps, T. H. Determination of lithium-ion distributions in nanostructured block polymer electrolyte thin films by X-ray photoelectron spectroscopy depth profiling. *ACS nano*, **2015**, *9* (1), 512–520. DOI: 10.1021/nn505744r.

[208] Sharon, D.; Bennington, P.; Webb, M. A.; Deng, C.; Pablo, J. J. de; Patel, S. N.; Nealey, P. F. Molecular Level Differences in Ionic Solvation and Transport Behavior in Ethylene Oxide-Based Homopolymer and Block Copolymer Electrolytes. *J. Am. Chem. Soc.*, **2021**, *143* (8), 3180–3190. DOI: 10.1021/jacs.0c12538.

[209] Gartner, T. E.; Morris, M. A.; Shelton, C. K.; Dura, J. A.; Epps, T. H. Quantifying Lithium Salt and Polymer Density Distributions in Nanostructured Ion-Conducting Block Polymers. *Macromolecules*, **2018**, *51* (5), 1917–1926. DOI: 10.1021/acs.macromol.7b02600.

[210] Lee, D.; Jung, H. Y.; Park, M. J. Solid-State Polymer Electrolytes Based on AB_3-Type Miktoarm Star Copolymers. *ACS Macro Lett.*, **2018**, *7* (8), 1046–1050. DOI: 10.1021/acsmacrolett.8b00474.

[211] Mott, P. H.; Dorgan, J. R.; Roland, C. M. The bulk modulus and Poisson's ratio of “incompressible” materials. *J. Sound Vib.*, **2008**, *312* (4-5), 572–575. DOI: 10.1016/j.jsv.2008.01.026.

[212] Evans, J.; Vincent, C. A.; Bruce, P. G. Electrochemical measurement of transference numbers in polymer electrolytes. *Polymer*, **1987**, *28* (13), 2324–2328. DOI: 10.1016/0032-3861(87)90394-6.

[213] Pesko, D. M.; Timachova, K.; Bhattacharya, R.; Smith, M. C.; Villaluenga, I.; Newman, J.; Balsara, N. P. Negative Transference Numbers in Poly(ethylene oxide)-Based Electrolytes. *J. Electrochem. Soc.*, **2017**, *164* (11), E3569-E3575. DOI: 10.1149/2.0581711jes.

[214] Pożyczka, K.; Marzantowicz, M.; Dygas, J. R.; Krok, F. IONIC CONDUCTIVITY AND LITHIUM TRANSFERENCE NUMBER OF POLY(ETHYLENE OXIDE):LiTFSI SYSTEM. *Electrochim. Acta*, **2017**, *227*, 127–135. DOI: 10.1016/j.electacta.2016.12.172.

[215] Atik, J.; Diddens, D.; Thienenkamp, J. H.; Brunklaus, G.; Winter, M.; Paillard, E. Cation-Assisted Lithium Ion Transport for High Performance PEO-based Ternary Solid Polymer Electrolytes. *Angew. Chem. Int. Ed.*, **2021**. DOI: 10.1002/anie.202016716.

[216] Kim, G.-T.; Passerini, S.; Carewska, M.; Appetecchi, G. B. Ionic Liquid-Based Electrolyte Membranes for Medium-High Temperature Lithium Polymer Batteries. *Membranes*, **2018**, *8* (3). DOI: 10.3390/membranes8030041.

[217] Chen, Z.; Steinle, D.; Nguyen, H.-D.; Kim, J.-K.; Mayer, A.; Shi, J.; Paillard, E.; Iojoiu, C.; Passerini, S.; Bresser, D. High-energy lithium batteries based on single-ion conducting polymer electrolytes and $Li[Ni_{0.8}Co_{0.1}Mn_{0.1}]O_2$ cathodes. *Nano Energy*, **2020**, *77*, 105129. DOI: 10.1016/j.nanoen.2020.105129.

[218] Tang, Y.; Deng, J.; Li, W.; Malyi, O. I.; Zhang, Y.; Zhou, X.; Pan, S.; Wei, J.; Cai, Y.; Chen, Z.; Chen, X. Water-Soluble Sericin Protein Enabling Stable Solid-Electrolyte

Interphase for Fast Charging High Voltage Battery Electrode. *Adv. Mater.*, **2017**, *29* (33). DOI: 10.1002/adma.201701828.

[219] Liu, B.; Zhang, J.-G.; Xu, W. Advancing Lithium Metal Batteries. *Joule*, **2018**, *2* (5), 833–845. DOI: 10.1016/j.joule.2018.03.008.

[220] Wan, J.; Xie, J.; Kong, X.; Liu, Z.; Liu, K.; Shi, F.; Pei, A.; Chen, H.; Chen, W.; Chen, J.; Zhang, X.; Zong, L.; Wang, J.; Chen, L.-Q.; Qin, J.; Cui, Y. Ultrathin, flexible, solid polymer composite electrolyte enabled with aligned nanoporous host for lithium batteries. *Nat. Nanotechnol.*, **2019**, *14* (7), 705–711. DOI: 10.1038/s41565-019-0465-3.

[221] Colombo, F.; Bonizzoni, S.; Ferrara, C.; Simonutti, R.; Mauri, M.; Falco, M.; Gerbaldi, C.; Mustarelli, P.; Ruffo, R. Polymer-in-Ceramic Nanocomposite Solid Electrolyte for Lithium Metal Batteries Encompassing PEO-Grafted TiO_2 Nanocrystals. *J. Electrochem. Soc.*, **2020**, *167* (7), 70535. DOI: 10.1149/1945-7111/ab7c72.

[222] Wetjen, M.; Kim, G.-T.; Joost, M.; Winter, M.; Passerini, S. Temperature dependence of electrochemical properties of cross-linked poly(ethylene oxide)–lithium bis(trifluoromethanesulfonyl)imide–N-butyl-N-methylpyrrolidinium bis(trifluoromethanesulfonyl)imide solid polymer electrolytes for lithium batteries. *Electrochim. Acta*, **2013**, *87*, 779–787. DOI: 10.1016/j.electacta.2012.09.034.

[223] Stolz, L.; Homann, G.; Winter, M.; Kasnatscheew, J. The Sand equation and its enormous practical relevance for solid-state lithium metal batteries. *Mater. Today*, **2021**. DOI: 10.1016/j.mattod.2020.11.025.

[224] Butzelaar, A. J.; Röring, P.; Hoffmann, M.; Atik, J.; Paillard, E.; Wilhelm, M.; Winter, M.; Brunklaus, G.; Theato, P. Advanced Block Copolymer Design for Polymer Electrolytes: Prospects of Microphase Separation. *Macromolecules*, **2021**, *54* (23), 11101–11112. DOI: 10.1021/acs.macromol.1c02147.

[225] Leibler, L. Theory of Microphase Separation in Block Copolymers. *Macromolecules*, **1980**, *13* (6), 1602–1617. DOI: 10.1021/ma60078a047.

[226] Karuppasamy, K.; Theerthagiri, J.; Vikraman, D.; Yim, C.-J.; Hussain, S.; Sharma, R.; Maiyalagan, T.; Qin, J.; Kim, H.-S. Ionic Liquid-Based Electrolytes for Energy Storage Devices: A Brief Review on Their Limits and Applications. *Polymers*, **2020**, *12* (4). DOI: 10.3390/polym12040918.

[227] Liu, K.; Wang, Z.; Shi, L.; Jungsuttiwong, S.; Yuan, S. Ionic liquids for high performance lithium metal batteries. *J. Energy Chem.*, **2021**, *59*, 320–333. DOI: 10.1016/j.jechem.2020.11.017.

[228] Joost, M.; Kim, G. T.; Winter, M.; Passerini, S. Phase stability of Li-ion conductive, ternary solid polymer electrolytes. *Electrochim. Acta*, **2013**, *113*, 181–185. DOI: 10.1016/j.electacta.2013.09.052.

[229] Sakurai, S.; Momii, T.; Taie, K.; Shibayama, M.; Nomura, S.; Hashimoto, T. Morphology transition from cylindrical to lamellar microdomains of block copolymers. *Macromolecules*, **1993**, *26* (3), 485–491. DOI: 10.1021/ma00055a013.

[230] Appetecchi, G. B.; Kim, G. T.; Montanino, M.; Alessandrini, F.; Passerini, S. Room temperature lithium polymer batteries based on ionic liquids. *J. Power Sources*, **2011**, *196* (16), 6703–6709. DOI: 10.1016/j.jpowsour.2010.11.070.

[231] Shin, J.-H.; Henderson, W. A.; Passerini, S. PEO-Based Polymer Electrolytes with Ionic Liquids and Their Use in Lithium Metal-Polymer Electrolyte Batteries. *J. Electrochem. Soc.*, **2005**, *152* (5), A978. DOI: 10.1149/1.1890701.

[232] Elia, G. A.; Bernhard, R.; Hassoun, J. A lithium-ion oxygen battery using a polyethylene glyme electrolyte mixed with an ionic liquid. *RSC Adv.*, **2015**, *5* (27), 21360–21365. DOI: 10.1039/C4RA17277A.

[233] Oldiges, K.; Diddens, D.; Ebrahiminia, M.; Hooper, J. B.; Cekic-Laskovic, I.; Heuer, A.; Bedrov, D.; Winter, M.; Brunklaus, G. Understanding transport mechanisms in ionic liquid/carbonate solvent electrolyte blends. *Phys. Chem. Chem. Phys.*, **2018**, *20* (24), 16579–16591. DOI: 10.1039/c8cp01485j.

[234] Tsurumaki, A.; Kagimoto, J.; Ohno, H. Properties of polymer electrolytes composed of poly(ethylene oxide) and ionic liquids according to hard and soft acids and bases theory. *Polym. Adv. Technol.*, **2011**, *22* (8), 1223–1228. DOI: 10.1002/pat.1931.

[235] Castiglione, F.; Ragg, E.; Mele, A.; Appetecchi, G. B.; Montanino, M.; Passerini, S. Molecular Environment and Enhanced Diffusivity of Li^+ Ions in Lithium-Salt-Doped Ionic Liquid Electrolytes. *J. Phys. Chem. Lett.*, **2011**, *2* (3), 153–157. DOI: 10.1021/jz101516c.

[236] Mereacre, V.; Stüble, P.; Ghamlouche, A.; Binder, J. R. Enhancing the Stability of $LiNi_{0.5}Mn_{1.5}O_4$ by Coating with $LiNbO_3$ Solid-State Electrolyte: Novel Chemically Activated Coating Process versus Sol-Gel Method. *Nanomaterials (Basel)*, **2021**, *11* (2). DOI: 10.3390/nano11020548.

[237] Campbell-Verduyn, L.; Elsinga, P. H.; Mirfeizi, L.; Dierckx, R. A.; Feringa, B. L. Copper-free 'click': 1,3-dipolar cycloaddition of azides and arynes. *Org. Biomol. Chem.*, **2008**, *6* (19), 3461–3463. DOI: 10.1039/B812403E.

11 Appendix

Additional information and spectra for the different projects are given in the following.

11.1 Additional Results for ‘A Systematic Study of Vinyl ether-based Poly(ethylene oxide) Side Chain Polymer Electrolytes’

11.1.1 Cyclic Voltammetry of Poly(cyclohexyl vinyl ether)

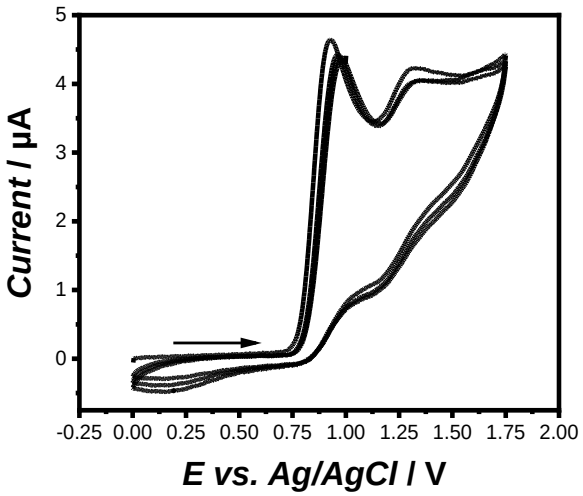

Figure 88. Cyclic voltammogram of poly(cyclohexyl vinyl ether) (0.01 mol L^{-1}) in DCM, using tetrabutylammonium perchlorate (0.1 mol L^{-1}) as electrolyte, glassy carbon as working electrode, platinum-wire as counter electrode and Ag/AgCl as reference electrode at 25 °C on a Metrohm Autolab PGSTAT128N (0 – 1.75 V, 50 mV s^{-1}). Oxidation onset at ~ 0.75 V corresponding to 4.59 V vs $Li|Li^+$.

11.1.2 Calculation of Crystallinity

Table 22. Calculation of the crystallinity of **polymer** series **A** and **B**.

Entry	Polymer	T_m [°C]	ΔH_{melt} [J g^{-1}]	Crystallinity* [%]	Reduction of crystallinity* [%]
1	**Polymer A400**	-1.3	3.92	2.00	98.0
2	**Polymer A550**	14.4	35.8	18.2	81.8
3	**Polymer A750**	27.2	51.9	26.4	73.6
4	**Polymer A1000**	34.3	58.8	29.9	70.1
5	**Polymer A2000**	50.4	102.7	52.3	47.7
6	**Polymer B400**	8.7	50.0	25.4	74.6
7	**Polymer B1000**	38.8	96.4	49.1	50.9
8	**Polymer B2000**	53.3	119.9	61.0	39.0

*Calculated using ΔH_{melt}(PEO) = 196.4 J g^{-1} (169)

11.1.3 Electrochemical Impedance Spectroscopy

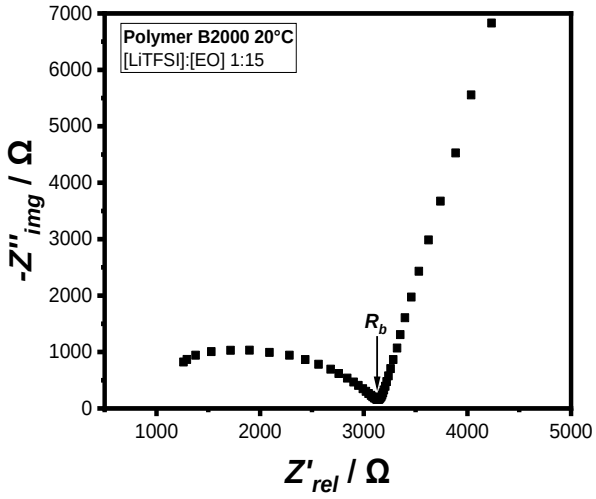

Figure 89. Exemplary EIS spectrum (Nyquist plot) of **polymer B2000** at 20 °C with a [Li$^+$]:[EO] ratio of 1:15.

11.2 Additional Results for 'Synthesis and Post-Polymerization Modification of Defined Functional Poly(Vinyl ether)s'

11.2.1 FT-IR Measurements

Exemplary FT-IR spectra of **P1** and **P2** including all their functionalized polymers were recorded in order to further confirm the successful PPM. As shown below, **P1** and **P2** did show the characteristic signals of their respective functional group (C=C double or C≡C triple bond) before, but not after the PPM, indicating once more their successful quantitative conversion.

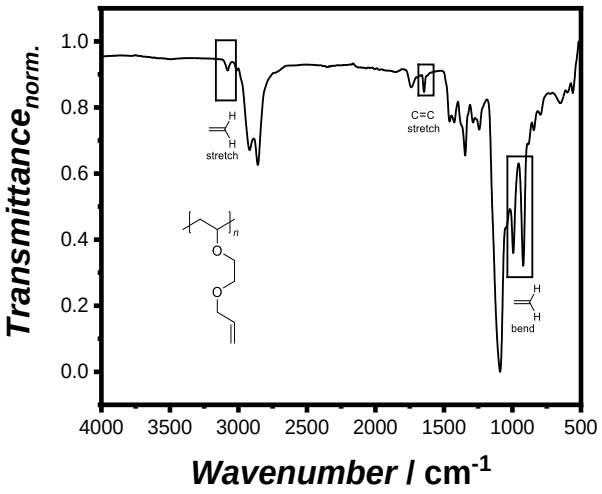

Figure 90. ATR FT-IR spectrum of poly(allyl ethylene glycol vinyl ether) (**P1**).

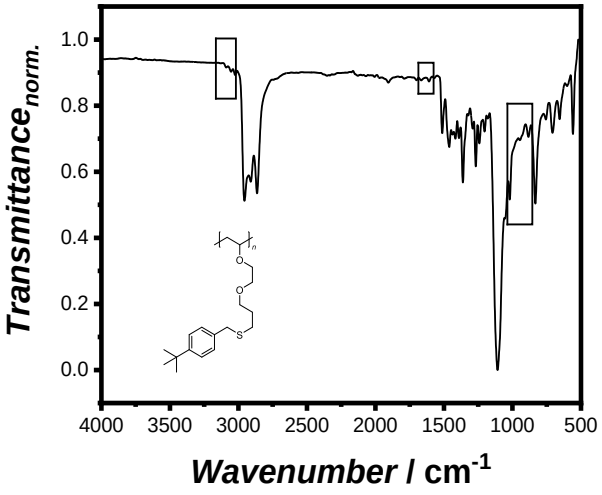

Figure 91. ATR FT-IR spectrum of **P1** after the *thiol-ene* reaction with TBBT.

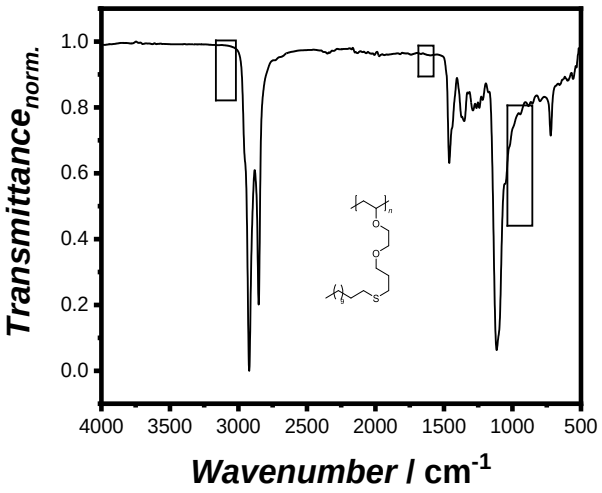

Figure 92. ATR FT-IR spectrum of **P1** after the *thiol-ene* reaction with DDT.

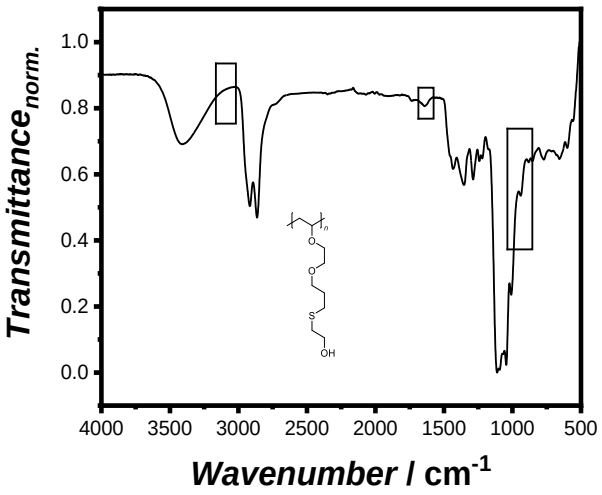

Figure 93. ATR FT-IR spectrum of **P1** after the *thiol-ene* reaction with ME.

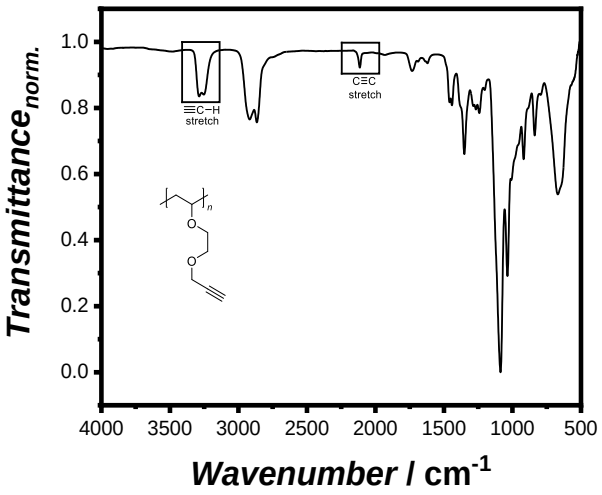

Figure 94. ATR FT-IR spectrum of poly(propargyl ethylene glycol vinyl ether) (**P2**).

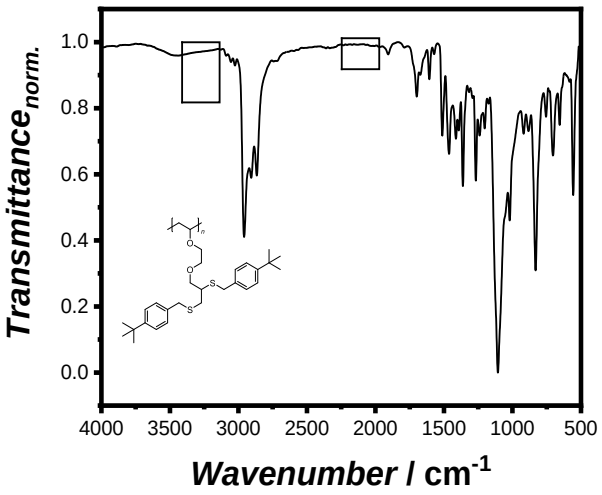

Figure 95. ATR FT-IR spectrum of **P2** after the *thiol-yne* reaction with TBBT.

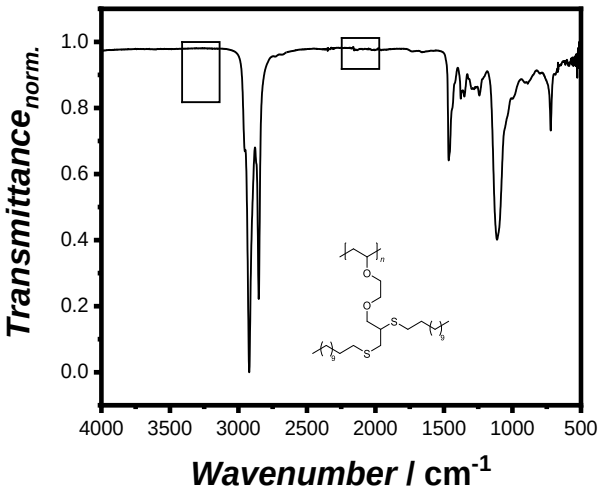

Figure 96. ATR FT-IR spectrum of **P2** after the *thiol-yne* reaction with DDT.

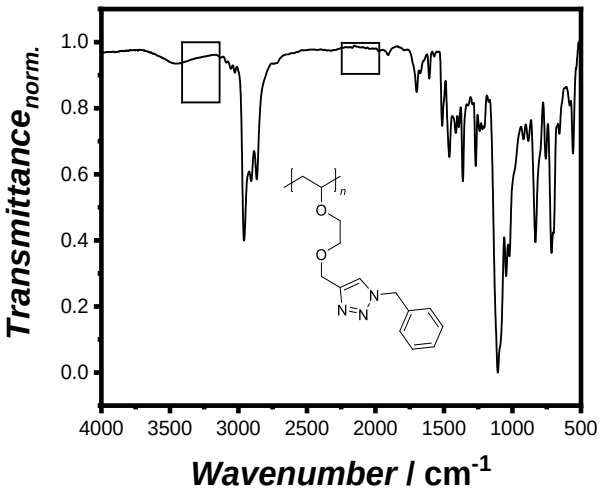

Figure 97. ATR FT-IR spectrum of **P2** after the CuAAC reaction with BzN_3.

11.2.2 ESI-MS Results

Exemplary ESI-MS measurements were conducted to further verify the polymer structure. **P1** before and after functionalization with DDT revealed the appearance of the expected signal spacing. **P2** before functionalization did also show the expected signal spacing, but it was not possible to measure the functionalized polymers, probably because of their exceeding molar mass and/or their insufficient ability to stabilize a sodium ion.

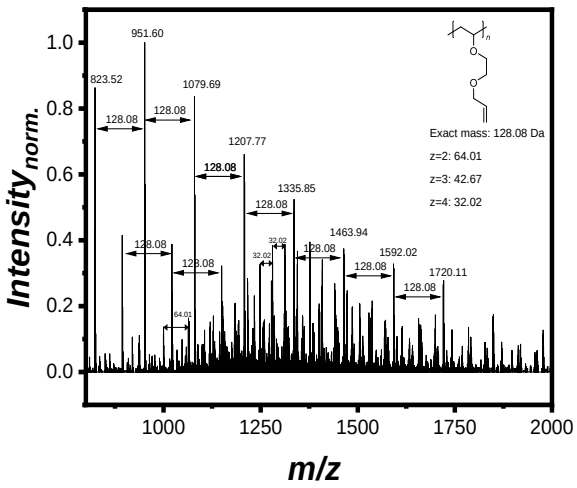

Figure 98. ESI-MS spectrum of **P1**. The signal spacing clearly confirmed the monomer structure. Multiple charged chains could be identified.

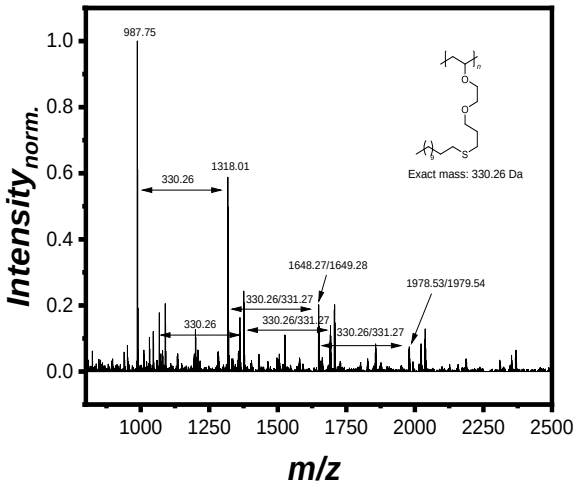

Figure 99. ESI-MS spectrum of **P1** after the *thiol-ene* reaction with DDT. The peak spacing clearly confirmed the successful PPM.

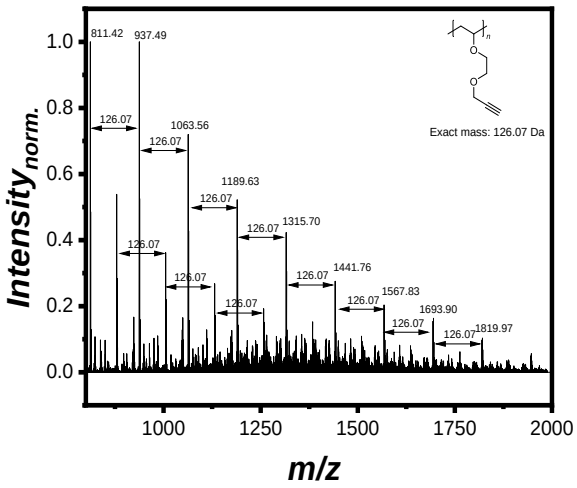

Figure 100. ESI-MS spectrum of **P2**. The peak spacing clearly confirmed the monomer structure.

11.3 Additional Results for 'Styrene-Based Poly(ethylene oxide) Side Chain Block Copolymers as Solid Polymer Electrolyte for High-Voltage Lithium-Metal Batteries'

11.3.1 Additional TGA Thermograms

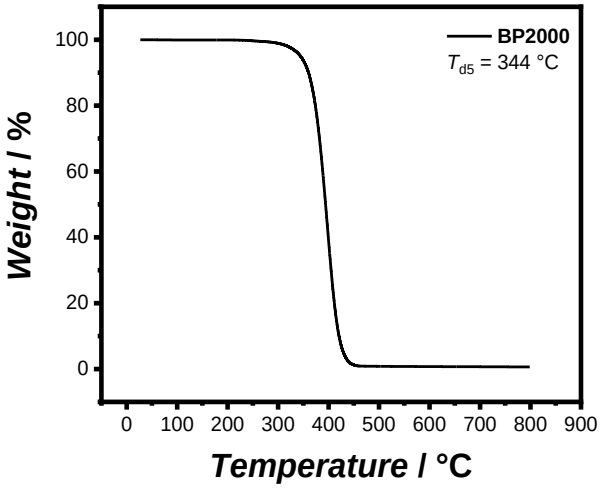

Figure 101. TGA thermogram of **BP2000**. Atmosphere: N_2.

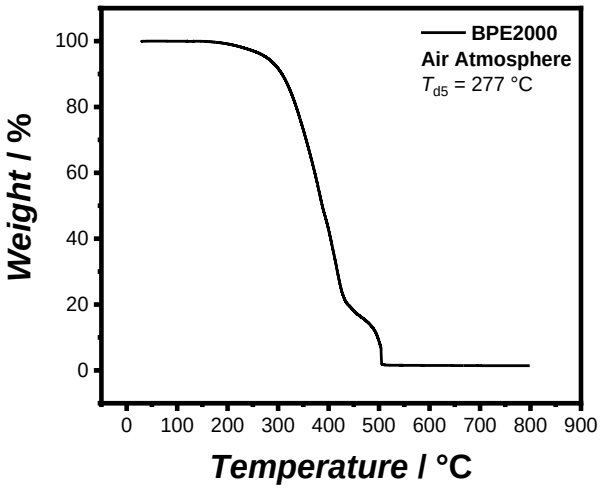

Figure 102. TGA thermogram of **BPE2000**. Atmosphere: Air.

11.3.2 EIS data of Li|BPE2000|Li cells

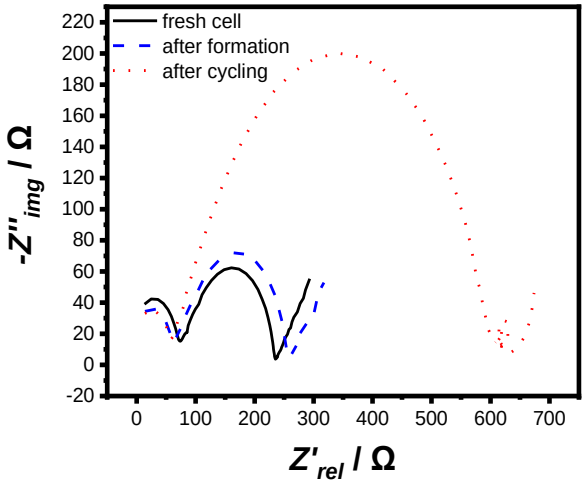

Figure 103. Corresponding EIS data (**Figure 37**) of Li|BPE2000|Li symmetrical cells before cycling, after the initial formation cycles (0.05 mA cm^{-2} for 10 cycles) and after constant plating and stripping with a current density of 0.1 mA cm^{-2} for four hours over a total of 350 hours.

A small decrease in the electrolyte resistance (first intercept) after formation in comparison to the fresh cell was visible, probably as a result of an improved contact. Further, the overall cell resistance (second intercept) was slightly increasing due to SEI formation. After 350 hours of plating and stripping with a current density of 0.1 mA cm^{-2} for four hours, the electrolyte resistance remained constant, whereas the overall cell resistance increased, implying an increasing SEI.

11.3.3 EIS data of Li|BPE2000|NMC622 cells

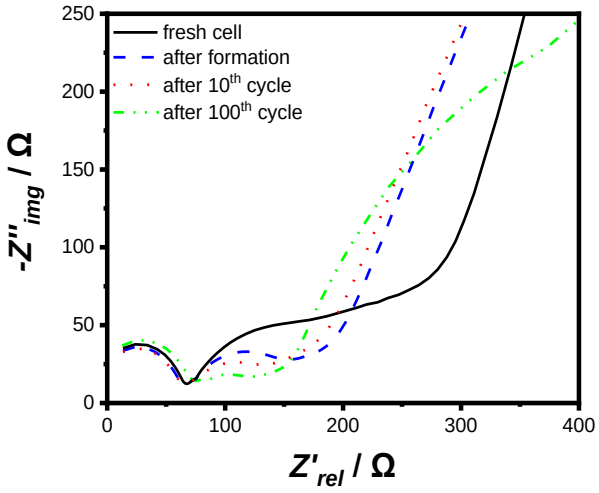

Figure 104. Corresponding EIS data (**Figure 41a**) of Li|BPE2000|NMC622 full cells before cycling, after the initial formation cycles, after 10 cycles and after 100 cycles.

A small decrease in the electrolyte resistance as well as the appearance of the semi-circle attributed to the charge-transfer resistance could be detected after the initial formation cycles probably as a result of the optimized contact after these first cycles. After 10 and even more prominent after 100 cycles, the electrolyte resistance seemed to be slightly increased in comparison to the resistance of the fresh cell and the cell after formation, which is assumed to correspond to minor electrolyte degradation. In contrast, the charge-transfer resistance was barely observable and surprisingly lower than before. Potentially, this behavior can be attributed to a penetration of the cathode by the PE over time (which was also seen by the observation that it is not possible to remove the cathode from the PE after cycling), thus an increased contact area is formed resulting in a better interface and consequently a decreased resistance. However, parasitic processes are possibly present, explaining the decrease in capacity as seen in **Figure 41a**.

11.4 Additional Results for 'Advanced Block Copolymer Design for Polymer Electrolytes: Prospects of Microphase Separation'

11.4.1 Additional SAXS Measurements

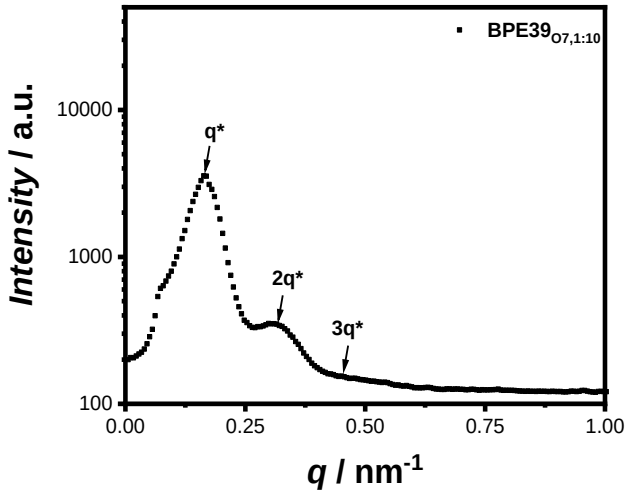

Figure 105. SAXS measurement of **BPE39$_{O7,1:10}$** revealing the microphase separation as well as indicating a lamellar long-range order.

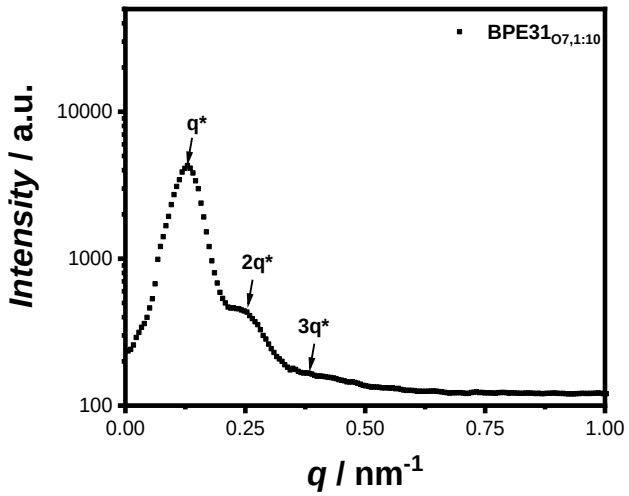

Figure 106. SAXS measurement of **BPE31$_{O7,1:10}$** revealing the microphase separation as well as indicating a lamellar long-range order.

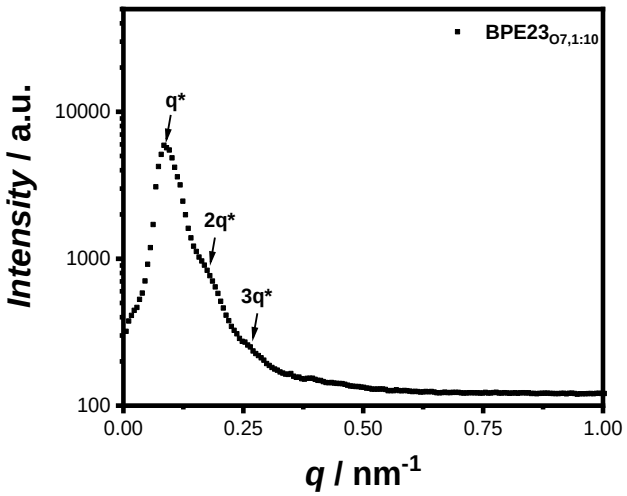

Figure 107. SAXS measurement of **BPE23$_{O7,1:10}$** revealing the microphase separation as well as indicating a lamellar long-range order.

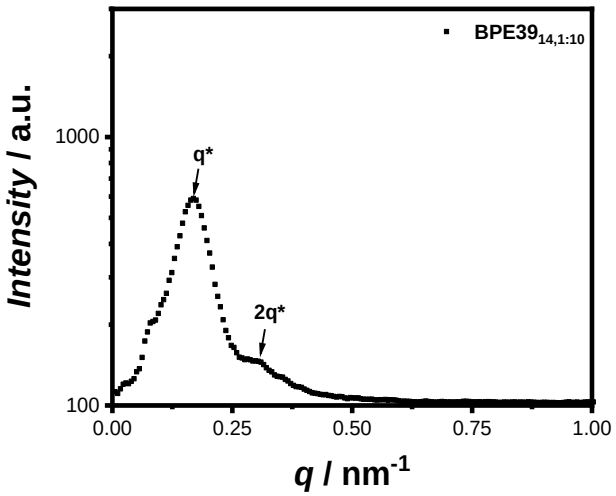

Figure 108. SAXS measurement of **BPE39$_{14,1:10}$** revealing the microphase separation as well as indicating a lamellar long-range order.

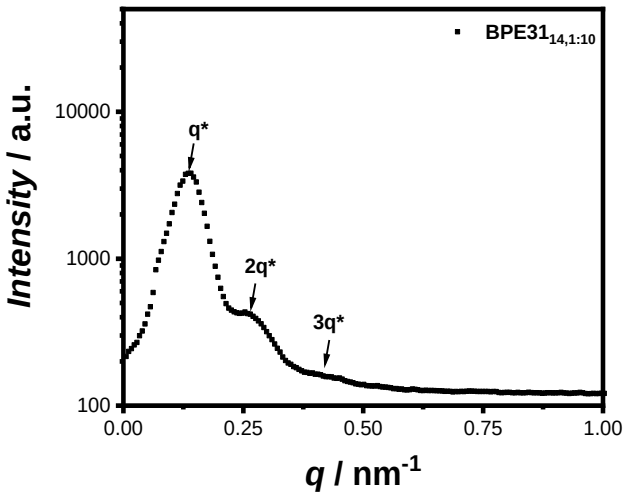

Figure 109. SAXS measurement of **BPE31$_{14,1:10}$** revealing the microphase separation as well as indicating a lamellar long-range order.

11.4.2 Exemplary Measurement of the Li^+ Transference Number

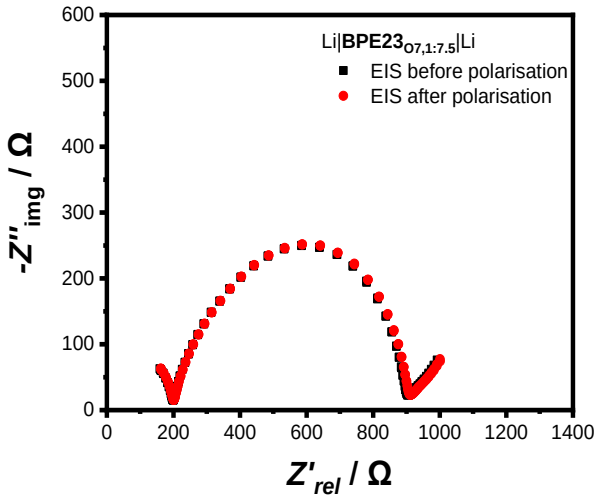

Figure 110. EIS of Li|**BPE23$_{O7,1:7.5}$**|Li before and after applying a potential of 10 mV at 40 °C.

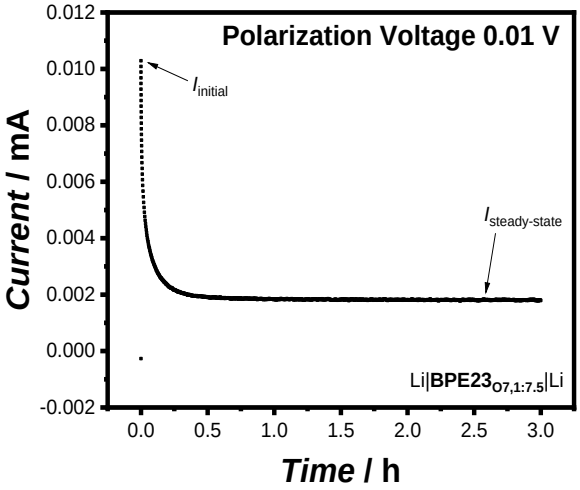

Figure 111. Chronoamperometry of Li|**BPE23**$_{O7,1:7.5}$|Li applying a potential of 10 mV at 40 °C.